

**Optical diagnostics for soot formation
from evaporating fuel films in combustion**

Von der Fakultät für Ingenieurwissenschaften, Abteilung Maschinenbau und Verfahrenstechnik

der

Universität Duisburg-Essen

zur Erlangung des akademischen Grades

eines

Doktors der Ingenieurwissenschaften

Dr.-Ing.

genehmigte Dissertation

von

Niklas Jüngst

aus

Moers

Gutachter: Univ.-Prof. Dr.-Ing. Sebastian Kaiser
Dr. Gilles Bruneaux, HDR

Tag der mündlichen Prüfung: 24.08.2021

Acknowledgment

First of all, I would like to express my sincere gratitude to my supervisor Sebastian A. Kaiser for giving me the opportunity of becoming a PhD student in his group. Sebastian's expertise and contagious passion were invaluable in formulating the research questions and methodology. Your insightful feedback pushed me to sharpen my thinking and provided an important part in creating this work.

Particular thanks also go to Christof Schulz who provided a substantial part of the infrastructure and measurement instrumentation I used in my work. This work was funded by the European Union's Horizon 2020 program in the larger research project "PaREGEn" (Particle Reduced, Efficient Gasoline Engines). In that context, I want to thank Jan Geiler, Roman Grzeszik, and Andreas Manz from Robert Bosch GmbH and Nicolò Frapolli and Yuri M. Wright from the ETH Zürich for lively and motivating discussions and the exchange of research. I want to thank Marshall Long for hardware support. I would like to acknowledge my colleagues from the institute and in particular from our group Patrick Kranz, Daniel Fuhrmann, Ming Zhao, Ali Shahbaz, Syahar Shawal, Kai Banke, and Judith Laichter for their wonderful collaboration, warm hearts, and friendships that grew during the past four years. I also thank Erdal Akyildiz, Jörg Albrecht, Natascha Schlösser, and Joel Albrecht for the intense support on the experiment and the supply with experimental infrastructure. I appreciate the management capabilities and quick purchase-procedures from Barbara Nota.

I want to thank Johannes Kiefer and Heike Glade from the University of Bremen for the encouragement in pursuing a scientific career. Finally, I express my very profound gratitude to my family, my girlfriend Lea, and to my friends for providing me with unfailing support and continuous encouragement through the process of researching and writing this work. This accomplishment would not have been possible without them.

Abstract

Late-evaporating liquid fuel wall-films are considered a major source of soot in spark-ignition direct-injection (SIDI) engines. In this study, a direct-injection model experiment was developed, and optical diagnostics were used to image fuel-film evaporation and soot formation. Fuel is injected by a multi-hole injector into the optically accessible test section of a constant-flow facility. Some of the liquid fuel impinges on a quartz-glass window and forms fuel films. After spark ignition, a turbulent flame front propagates through the chamber, and subsequently sooting combustion arises near the evaporating fuel films.

Laser-induced fluorescence (LIF) of toluene (fluorescent tracer) added to iso-octane (surrogate fuel) in small concentration, excited by laser pulses at 266 nm, is used to image the fuel-film thickness and the air/fuel equivalence ratio in the gas phase. The LIF images of fuel films show that the films remain on the wall surface long after the flame front has passed and that the fuel accumulates to thick fuel blobs in the films throughout the evaporation. Generally, and consistent with results from a Computational Fluid Dynamics (CFD) simulation, the evaporation rate is highest early after start of injection (aSOI) and then decreases and remains on a constant level, with the magnitude strongly depending on the wall temperature. Combustion and thus convective heat transfer show a minor effect on the fuel-film evaporation rate compared to the wall temperature in either CFD or LIF. A low-dimensional model (LDM), developed in this work, shows that the quartz wall only slightly cools down in the impingement region. Consistent with results from the CFD, the fuel-film temperature rapidly approaches the wall temperature, independent of the initial film temperature. Gas-phase LIF finds fuel-rich vapor plumes emerging from the fuel films until late aSOI without combustion. Interestingly, when combustion is initiated fuel vapor plumes are not detected, indicating that the fuel vapor pyrolytically decomposes spatially very close to the fuel films.

The second part of this work deals with the visualization of soot formation from evaporating fuel films by multiple laser-based and high-speed imaging diagnostics. Overlapping laser light sheets at 532 and 1064 nm excited LIF of polycyclic aromatic hydrocarbons (PAH) -potential soot precursors- and laser-induced incandescence (LII) of soot, respectively. For preliminary measurements, the constant-flow facility was replaced with a Santoro or Yale burner, providing a steady, sooting, laminar co-flow diffusion flame. In complementary line-of-sight integrated imaging, the fuel spray, chemiluminescence, and soot incandescence were captured with a high-speed color camera. PAH LIF is found in close vicinity of the evaporating fuel films. Soot is found spatially separated from, but adjacent to the PAH, both with high spatial intermittency. Average images indicate that soot is formed with a much higher spatial intermittency than PAH. Images from the color camera show soot incandescence earlier and in a similar region compared to soot LII. Chemiluminescence downstream of the soot-forming region is thought to indicate the subsequent oxidation of fuel, soot, and PAH. High-speed imaging and the CFD simulation predict the inception of soot pockets to similar times, close to the evaporating fuel films and in consistent spatial extent. Excitation of PAH LIF with 266 and 532 nm and a variation of the detection bandpass-filter show PAH of different size classes systematically in a thin layer between the fuel films and soot.

Kurzfassung

Verdampfende Kraftstoffwandfilme gelten als eine Hauptquelle für Ruß in Motoren mit Benzindirekteinspritzung (BDE). In dieser Arbeit wurde ein Modellversuch entwickelt, um die Kraftstofffilmverdampfung und Rußbildung mit optischer Messtechnik bildgebend zu untersuchen. Ein Mehrloch-Injektor spritzt Kraftstoff in die optisch zugängliche Testsektion eines Windkanals ein, in der der Kraftstoff zum größten Teil in einen kontinuierlichen Luftstrom verdampft. Ein Teil des Kraftstoffs trifft auf eine gegenüberliegende Quarzscheibe und bildet Wandfilme. Nach der Zündung breitet sich eine turbulente Flammenfront durch die Testsektion aus, wodurch sich nahe der verdampfenden Filme Ruß bildet.

Laserinduzierte Fluoreszenz (LIF) von Toluol (fluoreszierender Tracer), das iso-Oktan (Ersatzkraftstoff) in geringer Konzentration zugesetzt und durch Laserpulse bei 266 nm angeregt wird, wird zur bildgebenden Messung der Kraftstoff-Filmdicke und des Verbrennungsluftverhältnisses in der Gasphase verwendet. Die Kraftstofffilme verbleiben noch nach Erlöschen der Flammenfront auf der Wandoberfläche und ziehen sich während der Verdampfung zu dicken Tröpfchen zusammen. In Übereinstimmung mit den Ergebnissen einer CFD-Simulation (Computational Fluid Dynamics) ist die Verdampfungsrate kurz nach Beginn der Einspritzung (aSOI) hoch, nimmt dann ab und bleibt auf einem konstanten Niveau, welches stark von der Wandtemperatur abhängt. Die Verdampfungsrate scheint von der Verbrennung weitgehend unbeeinflusst zu bleiben. Ein niederdimensionales Modell, das im Rahmen dieser Arbeit entwickelt wurde, zeigt, dass sich die Wand nach Ende Einspritzung im Bereich der Flüssigfilme nur geringfügig abkühlt. In Übereinstimmung mit Ergebnissen aus der Simulation zeigt das Modell, dass sich die Flüssigfilmtemperatur schnell der Wandtemperatur angleicht. Kraftstoffdampf-LIF zeigt, dass Kraftstoffdampf während der Verbrennung sehr nah an der Flüssigfilmoberfläche pyrolytisch zerfällt und Rußbildung einleitet.

Der zweite Teil der Arbeit befasst sich mit der Visualisierung der Rußbildung durch LIF, laserinduzierte Inkandeszenz (LII) und Flammenleuchten. Überlappende Laserlichtschnitte bei 532 und 1064 nm regen LIF von polyzyklischen aromatischen Kohlenwasserstoffen (PAK) - potentielle Rußvorläufer - bzw. LII von Ruß an. Für vorläufige Messungen wurde der Windkanal durch einen Santoro- oder Yale-Brenner ersetzt, welche eine gleichmäßige, rußende, laminare Co-Flow-Diffusionsflamme bereitstellen. Bei der komplementären sichtlinienintegrierten Messtechnik wurden Einspritzung, Chemilumineszenz und Rußleuchten mit einer Hochgeschwindigkeits-Farbkamera erfasst. PAK-LIF befindet sich in unmittelbarer Nähe der verdampfenden Kraftstofffilme. Ruß wird räumlich getrennt, aber in angrenzenden Regionen gefunden. Mittelwert-Bilder weisen zusätzlich darauf hin, dass Ruß mit einer viel höheren räumlichen Intermittenz gebildet wird als PAK. Bilder von der Farbkamera zeigen Ruß früher und in einem ähnlichen Bereich im Vergleich zu Ruß LII. Chemilumineszenz stromabwärts weist auf die nachfolgende Oxidation von Brennstoff, Ruß und PAK hin. Die Hochgeschwindigkeitsaufnahmen und die CFD-Simulation zeigen das Entstehen von Ruß zu ähnlichen Zeiten, in der Nähe der verdampfenden Kraftstofffilme und in gleichbleibender räumlicher Ausdehnung. Die Anregung von PAK-LIF mit 266 und 532 nm und eine Variation des Detektionsfilterbandes zeigen, dass PAK verschiedener Größenklassen systematisch in einer dünnen Schicht zwischen Kraftstofffilmen und Ruß lokalisiert sind.

List of symbols

Symbol	Meaning	Unit
a	Thermal diffusivity	m^2/s
a_{air}	Thermal diffusivity of air	m^2/s
a_{w}	Thermal diffusivity of quartz	m^2/s
A	Absorbance	-
A_{f}	Fuel-film area	m^2
A_{iso}	Antoine parameter of iso-octane	-
A_{M}	Tridiagonal matrix	s/m^2
b^n	Vector containing temperatures at the boundaries	K
B_{iso}	Antoine parameter of iso-octane	-
B_{M}	Tridiagonal matrix	s/m^2
B_{λ}	Spectral emissive power per unit area	$\text{W}/(\text{sr}\cdot\text{m}^2\cdot\text{m})$
B_{G}	Background intensity	Counts
c	Concentration	mole/m^3
c_0	Speed of light in vacuum	m/s
c_{iso}	Concentration of iso-octane	mole/m^3
$c_{\text{O}_2,\text{actual}}$	Actual oxygen concentration	mole/m^3
$c_{\text{O}_2,\text{stoich}}$	Stoichiometric oxygen concentration	mole/m^3
c_p	Isobaric specific heat capacity	$\text{J}/(\text{kg}\cdot\text{K})$
c_{tol}	Concentration of toluene	mole/m^3
c_V	Isochoric specific heat capacity	$\text{J}/(\text{kg}\cdot\text{K})$
C_{iso}	Antoine parameter of iso-octane	-
d	Fuel-film thickness	m
d_{cal}	Fuel-film thickness in calibration	
d_{noz}	Nozzle diameter	m
$d_{\text{noz/wall}}$	Nozzle/wall distance	
d_p	Particle diameter	m
D	Diffusion coefficient	m^2/s
$D_{\text{air/fv}}$	Diffusion coefficient for air and fuel vapor	m^2/s
E_1	Energy level 1	J
E_2	Energy level 2	J
E_{measured}	Energy monitor measured	Counts
$E_{\text{reference}}$	Energy monitor reference	Counts
f	Frequency	1/s
f_V	Soot volume fraction	-
FF	Flat-field intensity	Counts
h	Planck constant	$\text{J}\cdot\text{s}$
i	Running variable	-
I_0	Incident intensity	Counts
I_a	Absorbed intensity	Counts

I_{cal}	Background- and flat-field corrected intensity in calibration	-
I_{exp}	Background- and flat-field corrected intensity in measurement	-
I_{f}	Fluorescence intensity	-
I_{FF}	Background-corrected flat-field intensity	Counts
I_{LIF}	Fluorescence intensity	Counts
I_{t}	Transmitted intensity	Counts
k_{B}	Boltzmann constant	J/K
k_{fl}	Rate of spontaneous emission	1/s
k_{IC}	Rate of internal conversion	1/s
k_{ISC}	Rate of intersystem crossing	1/s
k_{Q}	Rate of intramolecular quenching	1/s
l	Absorption path length	m
L	Characteristic length	m
Le	Lewis number	-
$m_{\text{air,actual}}$	Actual mass of air	kg
$m_{\text{air,stoich.}}$	Stoichiometric mass of air	kg
m_{f}	Fuel-film mass	kg
m_{inj}	Mass of injected fuel	kg
\dot{m}	Evaporation rate	kg/(m ² ·s)
\dot{m}_{f}	Time derivative of fuel-film mass	kg/s
M	Modul value	s/m ²
M_{iso}	Molar mass of iso-octane	kg/mole
M_{tol}	Molar mass of toluene	kg/mole
n	Conversion factor in Reynolds analogy	-
Nu	Nusselt number	-
p	Pressure	Pa
p_{intake}	Intake pressure	bar
p_{O_2}	Oxygen partial pressure	Pa
p_{sat}	Saturation vapor pressure	
p_{ves}	Vessel pressure	bar
Pr	Prandtl number	-
\dot{q}	Heat flux	W/m ²
\dot{Q}_{C}	Convective heat flow	J/s
\dot{Q}_{T}	Conductive heat flow	J/s
\dot{Q}_{abs}	Absorptive-heating rate	J/s
\dot{Q}_{rad}	Radiative-cooling rate	J/s
\dot{Q}_{cond}	Conductive-cooling rate	J/s
\dot{Q}_{sub}	Evaporative-cooling rate	J/s
\dot{Q}_{ox}	Oxidative-heating rate	J/s
\dot{Q}_{ann}	Heating rate from annealing	J/s

\dot{Q}_{therm}	Thermoionic heating rate	J/s
R	Universal gas constant	J/(mole·K)
Re	Reynolds number	-
Sc	Schmidt number	-
Sh	Sherwood number	-
t	Time	s
T	Temperature	K
T_0	Temperature at $t = 0$	K
T_{air}	Air temperature	K
T_f	Fuel-film temperature	K
T_{piston}	Piston temperature	K
T_{ves}	Vessel temperature	K
T_w	Wall temperature	K
T_{∞}	Temperature in the core of fluid	
U_{int}	Internal energy	J
U_f	Internal energy of fuel-film element	J
V	Volume	m ³
w	Velocity	m/s
w_{rel}	Relative velocity	m/s
We	Weber number	-
Δh_V	Specific enthalpy of vaporization	J/kg
x, y, z	Spatial coordinates	m
$y_{\text{fuel,sat}}$	Fuel-vapor mole fraction at saturation	-
α	Heat transfer coefficient	W/(m ² ·K)
β	Mass transfer coefficient	m/s
δ	Concentration boundary-layer thickness	m
δ_T	Thermal boundary-layer thickness	m
δ_v	Velocity boundary-layer thickness	m
ε^*	Molar extinction coefficient	m ² /mole
η	Detection efficiency	-
λ	Air/fuel equivalence ratio	-
λ_{air}	Thermal conductivity of air	W/(m·K)
λ_c	Thermal conductivity	W/(m·K)
λ_{em}	Emission wavelength	m
λ_{exc}	Excitation wavelength	m
λ_F	Thermal conductivity of fluid	W/(m·K)
λ_w	Thermal conductivity of quartz wall	W/(m·K)
ν	Kinematic viscosity	m ² /s
σ	Surface tension	N/m
ρ	Density	kg/m ³
ρ_s	Mass concentration at phase boundary	kg/m ³
ρ_{sat}	Saturation mass-concentration	kg/m ³
ρ_{∞}	Mass concentration in the core of fluid	kg/m ³

σ	Precision uncertainty	-
σ_{SN}	Precision uncertainty from shot noise	-
σ_{LE}	Precision uncertainty from pulse-energy fluctuations	-
Φ	Fuel/air equivalence ratio	-
Φ_{FQY}	Fluorescence quantum yield	-
Ω	Collection efficiency	-

List of abbreviations

Abbreviation	Description
aEOI	after end of injection
aSOI	after start of injection
BG	Background
BP	Bandpass
CA	Crank angle
CCD	Charge-coupled device
CFD	Computational Fluid Dynamics
CL	Chemiluminescence
CMOS	Complementary metal-oxide semiconductor
COV	Coefficient of variation
DBI	Diffuse back-illumination
FDM	Finite-Difference methods
ETH	Eidgenössische Technische Hochschule
FF	Flat field
FOV	Field of view
FQY	Fluorescence Quantum Yield
GDI	Gasoline direct injection
HAB	Height above burner
HACA	Hydrogen-abstraction/acetylene-addition
HS	High speed
LED	Light emitting diode
IC	Internal combustion
ICCD	Intensified CCD-camera
IR	Infrared
LES	Large Eddy Simulation
Nd:YAG	Neodymium-doped yttrium aluminum garnet
ODE	Ordinary differential equation
PAH	Polycyclic aromatic hydrocarbons
PFI	Port fuel injection
PIV	Particle Image Velocimetry
PM	Particulate Matter
PN	Particle number
QE	Quantum efficiency
LIF	Laser-induced fluorescence
LII	Laser-induced incandescence
LP	Longpass
NPT	National Pipe Thread
RIM	Refractive index matching
ROI	Region of interest
SNR	Signal-to-noise ratio

SIDI	Spark-ignited direct injection
SOI	Start of injection
SRM	Surface-roughness measurement
TDC	Top dead center
TEM	Transmission electron microscopy
UV	Ultraviolet

Table of contents

Acknowledgment	III
Abstract	V
Kurzfassung	VII
List of symbols	IX
List of abbreviations.....	XIII
1 Introduction.....	1
1.1 Motivation.....	1
1.2 Scope and outline of this work.....	2
2 Fundamentals	4
2.1 Gasoline direct injection (GDI)	4
2.1.1 Fuel injection and mixing	4
2.1.2 Charge modes and fuel-film formation	5
2.2 Film evaporation	7
2.2.1 Thermal conduction.....	7
2.2.2 Discretization of the heat equation	9
2.2.3 Convective heat and mass transfer	11
2.3 Soot formation	13
2.3.1 Fuel pyrolysis and formation of polycyclic aromatic hydrocarbons (PAH)	14
2.3.2 Soot nucleation, growth, and oxidation	15
2.4 Optical diagnostics.....	16
2.4.1 Relevant diagnostic techniques	16
2.4.2 Laser-induced fluorescence (LIF)	18
2.4.3 Laser-induced incandescence (LII) of soot	21
2.4.4 Natural flame luminosity	24
2.4.5 Particle image velocimetry (PIV).....	25
2.5 Light sources and detectors.....	26
2.5.1 Nd:YAG lasers and light emitting diodes (LED)	26
2.5.2 Intensified CCD-cameras and high-speed CMOS cameras.....	27
3 State of the art.....	29
3.1 Impact of fuel films on soot formation	29
3.2 Fuel-film formation and evaporation	30
3.2.1 LIF imaging of fuel films	31
3.2.2 Numerical and theoretical investigation of film evaporation	33
3.3 Visualization of fuel vapor, PAH, and soot	36
4 Fuel-film evaporation	41

4.1	Experiment.....	41
4.2	Flow characterization.....	42
4.2.1	Optical layouts for PIV and optical flow	43
4.2.2	Flow fields in steady-state and transient operation	44
4.3	Fuel-film imaging	47
4.3.1	Tracer and surrogate fuel	47
4.3.2	Co-evaporation.....	48
4.3.3	Optical layout.....	50
4.4	Calibration and image quantification	51
4.4.1	Thickness calibration	51
4.4.2	Laser degassing	54
4.4.3	Temperature dependence	55
4.4.4	Image processing and quantification.....	56
4.5	Results and discussion	57
4.5.1	Comparison with CFD simulation	60
4.5.2	Effect of combustion and elevated temperature.....	62
4.5.3	Influence of the injected mass.....	65
4.5.4	Influence of the flow velocity	67
4.5.5	Local evaporation rate.....	69
4.5.6	Shot-to-shot variability of the film mass.....	70
4.5.7	Precision and accuracy.....	71
4.6	Fuel-film and wall temperatures.....	73
4.6.1	Model assumptions	73
4.6.2	Model development.....	74
4.6.3	Solving scheme	76
4.6.4	Results.....	77
4.7	Section conclusions	80
5	Soot formation.....	83
5.1	Experimental facilities	83
5.1.1	Laminar co-flow diffusion-flame burners.....	83
5.1.2	Optically accessible gasoline engine.....	84
5.2	Fuel-vapor and air/fuel-ratio imaging.....	85
5.2.1	Optical layout.....	85
5.2.2	Equivalence-ratio calibration	86
5.2.3	Image processing and quantification.....	89
5.2.4	Results.....	90
5.2.5	Precision and accuracy.....	95
5.3	Flame-front, PAH, and soot-visualization experiments	96
5.3.1	Optical layout.....	96

5.3.2	Spectral characteristics	99
5.3.3	Preliminary measurements	100
5.4	Results and discussion	102
5.4.1	Spray combustion and soot formation	103
5.4.2	Comparison with CFD simulation	106
5.4.3	Influence of injected mass and temperature	107
5.4.4	Size-class dependent PAH-LIF imaging	110
5.4.5	Transparent soot-precursor layer in fuel-film combustion	113
5.4.6	Soot formation in optically accessible gasoline engine	116
5.5	Section conclusions	118
6	Conclusions and future work	121
6.1	Summary and conclusions	121
6.2	Future work	123
7	Bibliography	125
7.1	References	125
7.2	Contributions of the author	140
7.2.1	Journal articles	140
7.2.2	Conference contributions	140
7.2.3	Supervised theses	141
8	Appendices	142

1 Introduction

1.1 Motivation

Growing global road traffic causes increased particulate-matter (PM) emissions. The PM found in air varies in size and composition but mostly consists of a mixture of solid and liquid particles. In cities, the tailpipe emissions of road transport, such as soot, account for around 30% of the PM [1]. Vehicles with an internal combustion (IC) engine still dominate the market for passenger and freight transport due to the versatility, low initial cost, and flexibility of IC engines. In particular in developing countries with rapidly growing economies, the number of vehicles with IC engines is strongly increasing [2]. Also in the near future (until around 2050), vehicles with conventional IC engines and hybrid concepts (comprising an IC engine and an electric motor) are expected to make more than half of the market share among the total amount vehicles with different propulsion technologies [3].

Soot particles emitted by engines have average diameters of 100-500 nm. Significant amounts of organic matter might be adsorbed to the carbonaceous core of the particles. The small size makes soot particles readily respirable while 20-30% of the inhaled particles are expected to deposit in the humans' lungs and airways [4]. Several epidemiological studies report the exacerbation of pulmonary and cardiac problems of people exposed to ambient aerosols, i.e., air and soot, leading to earlier death or increased morbidity. Long-term effects might include cancer and lung or heart diseases. Which effect soot particles and the adsorbed organic matter, mostly polycyclic aromatic hydrocarbons (PAH), in details cause, is focus of discussion and debate [5].

In the last decades, mostly compression ignition engines, e.g. Diesel engines, were subject to strict limitations on the emission of PM since the diffusion-controlled combustion is likely to produce soot. In the last years, it became clear that not only the amount of soot but also the size of the soot particles determines the risks for human health. Therefore, in 2011 also the particle number (PN) emitted by Diesel engines was limited with the Euro 5b norm. In the following years, also engines with gasoline direct injection (GDI) were observed to cause significant emission of PM and PN. Since the introduction of Euro 6b in 2014, PN emitted by engines with GDI are limited. GDI is a promising technology for future engine concepts where the fuel is injected at high pressure directly into the combustion chamber [6]. This allows for an operation with a stratified fuel/air-mixture, ignitable around the spark electrodes, and globally lean [7]. Together with reduced pumping and heat losses, this contributes to reduced fuel consumption (up to 20%) and thus an increased thermal efficiency and decreasing CO₂ emissions compared to Port Fuel Injection (PFI) engines [7]. Further, the vaporization of the fuel within the cylinder cools the charge (air and fuel) and thus lowers the peak temperature during compression. This in turn significantly lowers the tendency for knocking, enables higher compression ratios, and thus a higher thermal efficiency. The latter can be realized by turbocharging the engine (increased mass of intake air) and either inject more fuel to generate more power or downsize the engine and keep the current power [7]. Injecting the fuel directly into the cylinder additionally provides an accurate control of the metered fuel and the air/fuel ratio in every combustion event resulting in an improved response under transient operation [8].

However, the drawback of GDI compared to conventional gasoline PFI engines is the increased emission of soot while the cause and effect relationship of soot formation is barely understood. Most of the soot in GDI operation is formed under cold-start conditions, during catalyst heating modes, and during dynamic engine modes. Injection systems have been improved over the last years to avoid soot formation under these operating conditions by varying the number of injections or the timing and amount of each injection. Nevertheless, insufficient mixing of fuel and air and in particular liquid fuel adhering to in-cylinder surfaces are currently considered sources of soot-particle formation in modern GDI engines [6]. Liquid fuel films evaporating from in-cylinder surfaces cause fuel-rich regions in the emerging fuel/air-mixture near these films. If those fuel-rich regions persist into the expansion stroke, they might produce soot.

1.2 Scope and outline of this work

The aim of this work is to investigate the impact of evaporating fuel films on soot formation by illuminating the entire process chain from fuel-film formation over evaporation, emergence of fuel vapor, combustion, formation of PAH, to eventually soot particles. The work was mainly done in a simplified direct-injection model experiment which provided large optical access with multiple optical diagnostics. The project was part of a large research project, funded by the European Union's program Horizon 2020, named Particle Reduced, Efficient Gasoline Engines (PaREGEn). The main objective of this project was the development of cleaner and more fuel economic GDI engines.

In the first part of this work, the fuel-film formation and evaporation were investigated. In this context, the experiment was first characterized in terms of boundary conditions which are relevant for fuel-film formation and evaporation. The flow field within the direct-injection model experiment was determined with particle image velocimetry (PIV). Then, the fuel-film formation and in particular evaporation were quantitatively investigated by imaging tracer laser-induced fluorescence (LIF) of liquid fuel films. The signal was calibrated versus the fuel-film thickness so that the film mass and eventually the evaporation rate could be calculated under varying operating conditions. Here, of particular interest were the influences of combustion, the wall temperature, and the flow velocity on the film evaporation-rate. The results were also compared with a semi-empirical, low-dimensional model (LDM), which was developed in the scope of this work, and a 3D-Computational Fluid Dynamics (CFD) simulation. The CFD simulation was done by the ETH in Zurich as a partner in the PaREGEn project.

The second part then deals with imaging the emerging fuel vapor near the fuel films, the propagation of a premixed flame front, and the formation of PAH and soot. With tracer LIF, the air/fuel ratio of the mixture was imaged until the flame front burns out the fuel. Then, different excitation wavelengths were used to visualize LIF of different size classes of PAH and thus visualize the transition region from fuel vapor to soot. Simultaneously, soot was visualized by laser induced incandescence (LII). In complementary experiments, high-speed combustion imaging was used to visualize the fuel injection, chemiluminescence of the flame front, and natural soot luminosity. In the context of the project, the laser-based diagnostics were also

applied in an optically accessible spark-ignited direct-injection (SIDI) engine together with the project partner Bosch in Renningen.

2 Fundamentals

2.1 Gasoline direct injection (GDI)

In GDI, the fuel is injected directly into the combustion chamber. Different operating principles regarding the charge and the injection modes are applied in modern GDI engines. In the following, the principles of fuel injection, spray breakup, mixing, and the effect of fuel-film formation on in-cylinder surfaces are discussed. Figure 1 summarizes these sub processes.

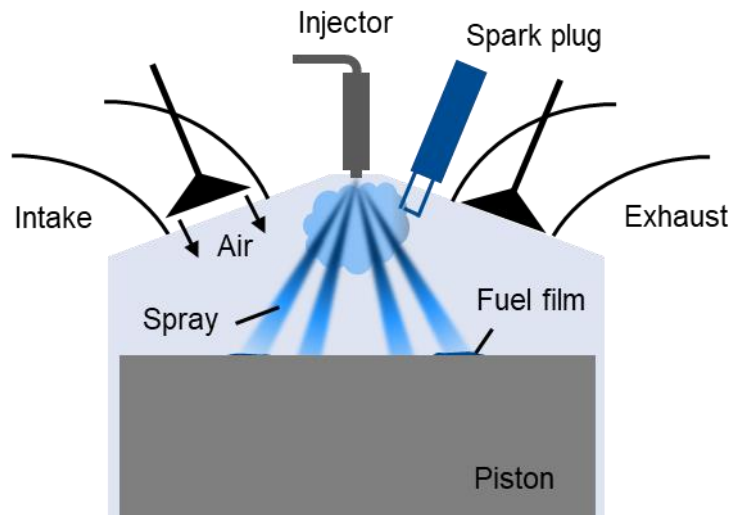


Figure 1: Schematic of gasoline direct injection.

2.1.1 Fuel injection and mixing

An injector sprays the fuel within multiple spray cones at high pressure into the combustion chamber. Fast evaporation of the fuel droplets and mixing with air is required in particular under part-load conditions. Small droplets are required for this purpose, which possess a high specific surface area, enhancing heat and mass transfer with the surrounding. Physical properties that enhance fuel atomization are [3]:

- Low fuel throughput in each nozzle hole (small nozzle diameter)
- High injection pressure (high nozzle-exit velocities)
- High ambient density (high compression ratio)
- Low viscosity of the fuel
- Low surface tension of the fuel

The velocity gradient between the gas and the liquid jet causes shear between the two phases that initiates the jet breakup. The jet breakup is depending on the jet velocity and is divided into three major regimes: Raleigh breakup zone, wind-induced breakup zone, and atomization zone. Atomization requires the highest jet velocities and thus causes the smallest droplets among these regimes. In the context of GDI, atomization is the present regime. The level of atomization is determined by the relative velocity between the liquid jet and the surrounding medium w_{rel} , the density ρ of the liquid, the nozzle diameter d_{noz} , and the surface tension σ of the liquid. These parameters are summarized in the jet Weber number which can be thought of as the ratio of the liquid jet's inertia and surface tension [3]:

$$We = \frac{\rho w_{rel}^2 d}{\sigma} \quad (1)$$

The critical Weber number at which a transition from wind-induced breakup to atomization takes place is around 10-12 [3].

Figure 2 visualizes the different stages of jet atomization during injection. In the nozzle near region, the liquid jet disintegrates into large droplets and ligaments in the primary breakup zone. Further away, entrainment of air from the surrounding dilutes the droplet density and related aerodynamic forces initiate the secondary breakup. Momentum transfer with the surrounding gas phase decelerates the spray's propagation. At the same time, enhanced heat and mass transfer lead to significant evaporation of the droplets. The detailed atomization pathway of single droplets depends on many physical parameters in the environment such that the droplet size usually follows a distribution. Generally, high injection pressures are beneficial since they cause a fine atomization and a high relative velocity between droplets and air which enhances the convective heat and mass transfer and thus mixing between the two [3].

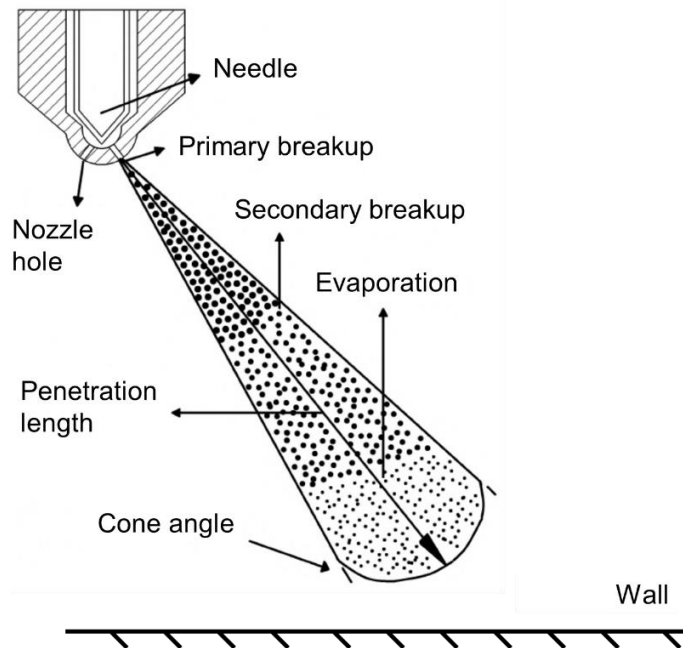


Figure 2: Regimes of jet breakup during fuel injection [9].

2.1.2 Charge modes and fuel-film formation

In GDI engines, the charge (fuel/air-mixture) is either distributed homogeneously or stratified within the combustion chamber, depending on the injection time and mixing properties [3]. An important measure to assess the mixture and the subsequent combustion is the air/fuel equivalence ratio (or air/fuel ratio):

$$\lambda = \frac{m_{air,actual}}{m_{air,stoich.}} \quad (2)$$

where $m_{air,actual}$ is the actual mass of air within the combustion chamber and $m_{air,stoich.}$ is the stoichiometric mass of air. Stoichiometric conditions mean that the amount of air within the

combustion chamber is exactly the amount needed for an entire oxidation of fuel. Then λ equals one. Fuel-lean mixtures are characterized by an excess of air, with $\lambda > 1$. Fuel-rich mixtures indicate incomplete oxidation of the fuel due to a lack of oxygen, indicated by $\lambda < 1$ [10].

For operation with a homogeneous and near-stoichiometric fuel/air-mixture throughout the combustion chamber, the fuel is injected early in the intake stroke so that the time is long enough for a complete mixing of fuel and air until before ignition. That provides globally stoichiometric combustion even under extremely low- or high-load and low- or high engine-speed conditions. In spite of the ongoing development in injection technologies, the operation with a stratified charge under part-load conditions is still unstable such that the operation with a homogeneous mixture remains the dominating mode [3].

However, under certain part-load conditions the operation with a stratified mixture can cause an enhanced engine efficiency. Here, the fuel is injected during or at the end of the compression stroke, temporally close to the ignition. Since the time before ignition then is too short to entirely mix the fuel homogeneously with the air, the fuel is present stratified throughout the combustion chamber. It needs to be guaranteed that an ignitable fuel/air-mixture (usually slightly fuel rich but close to $\lambda = 1$) is present around the spark plug where the flame propagation is initiated. Further away from the spark plug, the fuel/air-mixture becomes leaner towards the walls of the combustion chamber. The spatially averaged λ -values are then on the order of 3-5 [3].

Generally, the injection mode to promote fuel/air-mixing is differentiated into

- Wall-guided direct injection
- Air-guided direct injection
- Spray-guided direct injection

which are schematically shown in Figure 3.

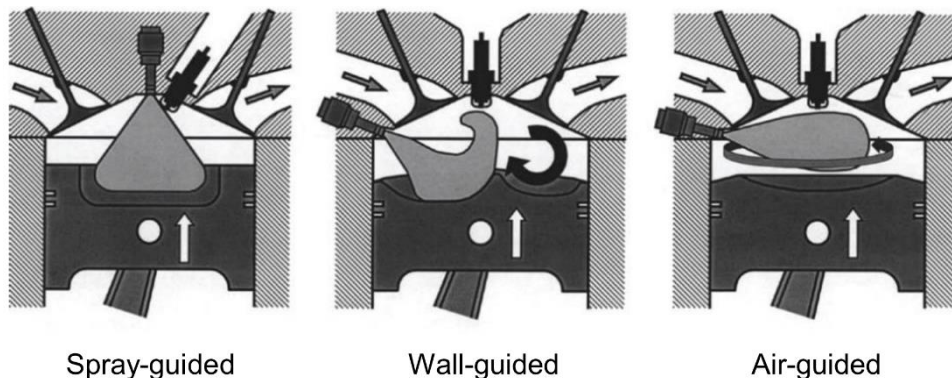


Figure 3: Injection modes for direct injection. Adapted from [11].

Under wall-guided and air-guided operation, the distance between the injector and the spark plug is long and the mixture formation and transport to the spark plug are driven by either the interaction of the spray with the piston or with the in-cylinder air motion, respectively. In spray-guided injection, the injector is close to the spark plug so that an ignitable fuel/air-mixture forms at the spark plug becoming significantly leaner towards the walls. To realize an ignitable

fuel/air-mixture around the spark plug under stratified conditions, the injection mode of choice is usually spray-guided [3, 11].

The targeting of the spray towards the piston surface in wall-guided injection may cause liquid fuel films on the piston. This is in particular relevant under cold-start conditions when the saturation vapor-pressure of the fuel is comparatively low [3, 12]. Also, during spray-guided operation, the close distance between injector and piston might cause significant fuel-film formation. As a consequence of fuel-film formation, the films evaporate throughout the compression and exhaust strokes, cause fuel-rich inhomogeneities in the fuel/air-mixture nearby, and thus a likelihood for soot formation [12]. Since the investigation of the fuel-film evaporation was a major subject of this work, the fundamentals of this phenomenon are described in the following.

2.2 Film evaporation

The multi-dimensional heat transfer by conduction and convection plays an essential role in the evaporation of thin liquid films while radiation can mostly be neglected. The coupling of heat and mass transfer makes the analytical mathematical description of this problem challenging and thus often requires suitable assumptions to simplify the problem [13].

2.2.1 Thermal conduction

Energy transferred from hot to cold regions within a body is called heat. Resting fluids and in particular solids at moderate temperatures transfer heat mainly via conduction. The heat flow cannot be measured directly but it is mathematically connected to the scalar quantity temperature. Fourier's law states the relation between the heat flux and the temperature gradient

$$\dot{q}(x, t) = -\lambda_c \nabla T(x, t) \quad (3)$$

where $\dot{q}(x, t)$ is the heat flux at position x and time t , λ_c is the thermal conductivity of the material, a positive scalar quantity, and $T(x, t)$ is the temperature at x and t . Therefore, when knowing the spatial temperature distribution of a body at any time, the heat flux can be computed from the temperature gradients [13, 14]. Analog to equation (3), the heat flux along the spatial coordinates y and z is calculated. Under stationary conditions, the heat flux through a body is constant such that the temperature profile through the body is linear and the temperature gradient constant [15].

Under non-stationary conditions, the spatial temperature field of a body varies in time and is obtained by solving a partial differential equation, the heat equation [13]:

$$\frac{\partial T}{\partial t} = a \nabla^2 T = a \left(\frac{\partial^2 T}{\partial x^2} + \frac{\partial^2 T}{\partial y^2} + \frac{\partial^2 T}{\partial z^2} \right) \quad (4)$$

Here, a is the thermal diffusivity which describes how fast the temperature diffuses within a body [14]

$$a = \frac{\lambda}{\rho c_p} \quad (5)$$

where ρ is the body's density and c_p is the body's isobaric heat capacity. Equations (3) and (4) hold for a body with constant, temperature-independent properties, and without external heat sources. In the simplest form, equation (4) describes the temperature field solely along the x -coordinate with a one-dimensional heat flux [13]:

$$\frac{\partial T}{\partial t} = a \frac{\partial^2 T}{\partial x^2} \quad (6)$$

Figure 4 visualizes the proportionality of the first derivative of temperature with respect to time and the second derivative with respect to space, as indicated in equation (6), for one-dimensional non-stationary heat conduction. If the change in the spatial temperature gradient (second derivative) is positive, more heat is flowing towards x from the right than heat flows away from x to the left, thus heat accumulates at x causing a temperature increase. Analog, the temperature decreases if the change in the gradient is negative while the temperature remains unaffected if the gradient is constant (stationary heat conduction) [13].

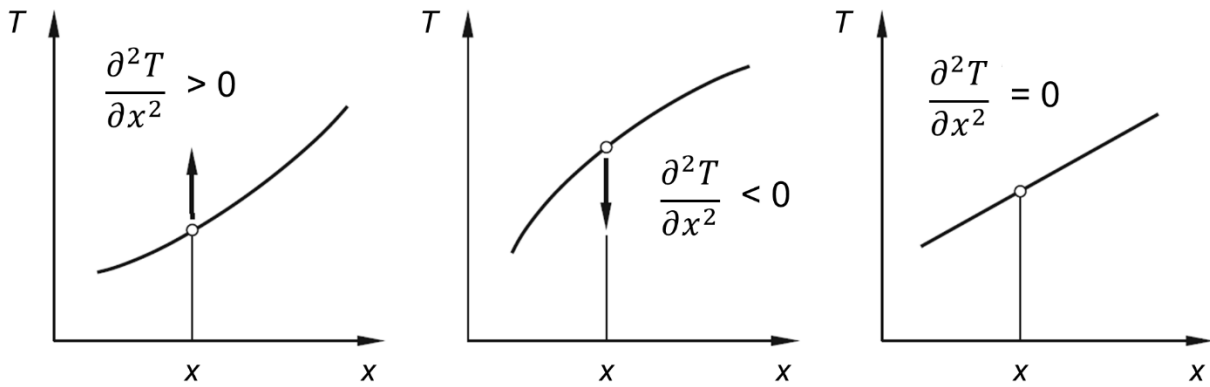


Figure 4: Relation between curvature of the temperature profile and the temporal temperature change according to equation (6). Adapted from [13].

Solving equation (6) analytically requires an initial condition and two boundary conditions. The initial condition is that the temperature profile along the x -coordinate is known at t_0 [13]:

$$T(x, t_0) = T_0(x) \quad (7)$$

The boundary conditions are divided into three sections [14]:

- The temperatures at $x = x_0$ and $x = x_L$ are known at any time t .
- The heat fluxes at $x = x_0$ and $x = x_L$ are known at any time t .
- Heat is exchanged with a surrounding fluid with a known temperature by convection or radiation.

Typical analytical methods for solving equation (6) are separation of variables and Laplace transformation. If the body's properties are non-stationary or if the boundary conditions are

complex, solving the heat equation analytically is sometimes impossible so that numerical methods are needed [13].

2.2.2 Discretization of the heat equation

Often finite-difference methods (FDM) are used to numerically solve the one-dimensional heat equation since they are numerically simple compared to finite-element or finite-volume methods. The basis of this method is to approximate the spatial and temporal derivatives in equation (6) with finite differences. This is done by discretizing the continuous quantities time and space into a finite number of coordinates, called grid [16]. Increasing the number of grid points increases the quality of approximation of the exact solution but also increases the numerical effort required [17].

Under the initial condition that the temperature at $t = t_0$ is known at every coordinate x and the boundary conditions that the temperatures at $x = x_0$ and $x = x_L$ are known any time t , the grid is discretized along $x_0 \leq x \leq x_L$ and $t_0 \leq t$ with the distances Δx and Δt between two neighboring spatial and temporal coordinates, respectively. Then, a grid point has the coordinates

$$x_i = x_0 + i \Delta x \text{ with } i = 0, 1, 2, \dots \quad (8)$$

and [17]:

$$t_n = t_0 + n \Delta t \text{ with } n = 0, 1, 2, \dots \quad (9)$$

The discretization schemes follow either an explicit scheme, an implicit scheme, or a combination of the two such as the Crank-Nicholson scheme. Figure 5 shows grid stencils of the different discretization schemes. When using explicit methods for solution, the first-order time derivative is approximated by a forward differencing formula and the second-order derivate with respect to the spatial location is approximated by a central difference [18]:

$$\frac{T_i^{n+1} - T_i^n}{\Delta t} = \frac{T_{i-1}^n - 2T_i^n + T_{i+1}^n}{\Delta x^2} \quad (10)$$

Then the temperature at $i, n+1$ is explicitly calculable from the known temperatures at every spatial location at the previous time step n while the temperatures at x_0 and x_L come from the boundary conditions. The simplicity of the explicit differencing scheme is countered by the fact that it requires relatively short time steps to make it numerically stable. This may become inappropriate if the calculation needs to be done over a large period of time [18]. The implicit method is numerically more stable at decreased spatiotemporal resolution by employing the central difference of the second-order spatial derivative at $n+1$ instead of n . The drawback of this approach is that a set of linear equations needs to be solved for every time step [16].

$$\frac{T_i^{n+1} - T_i^n}{\Delta t} = \frac{T_{i-1}^{n+1} - 2T_i^{n+1} + T_{i+1}^{n+1}}{\Delta x^2} \quad (11)$$

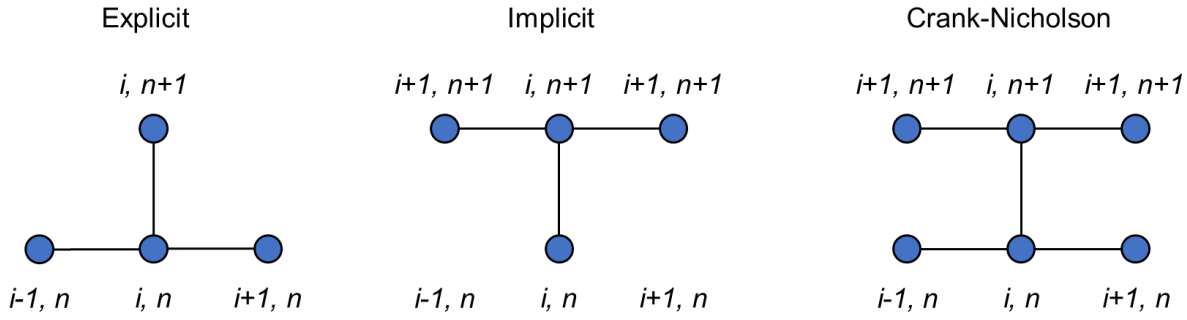


Figure 5: Grid sections showing explicit, implicit, and the combined Crank-Nicholson discretization schemes. Adapted from [18].

In this work, the Crank-Nicholson method is used, a comparatively accurate implicit differencing scheme. Here, an average of the second-order spatial differences (equations (10) and (11)) at (x_i, t_n) and (x_i, t_{n+1}) , thus the combination of Euler forward and Euler backward methods, is applied. Therefore, the spatial derivative is in fact discretized at the time $t_{n+\frac{1}{2}}$. By that, also the first-order temporal derivative is discretized at $t_{n+\frac{1}{2}}$ with the more accurate centered difference approximation [16]. Applying the Crank-Nicholson method to equation (6) gives:

$$\frac{T_i^{n+1} - T_i^n}{\Delta t} = \frac{1}{2} a \left[\left(\frac{T_{i-1}^{n+1} - 2T_i^{n+1} + T_{i+1}^{n+1}}{\Delta x^2} \right) + \left(\frac{T_{i-1}^n - 2T_i^n + T_{i+1}^n}{\Delta x^2} \right) \right] \quad (12)$$

Rearranging equation (12) and summarizing the constants to

$$M = a \frac{\Delta t}{\Delta x^2} \quad (13)$$

gives the following equation:

$$-MT_{i-1}^{n+1} + (2 + 2M)T_i^{n+1} - MT_{i+1}^{n+1} = MT_{i-1}^n + (2 - 2M)2T_i^n + MT_{i+1}^n \quad (14)$$

Given that for every grid point an equation like equation (14) can be formed, results in a tridiagonal problem, which can be described by the following system of equations [17]:

$$A_M T^{n+1} = B_M T^n + b^n \quad (15)$$

Here, A_M and B_M are spherical tridiagonal matrices, shown in A1, and contain the coefficients from equation (14), T^{n+1} and T^n are the temperatures at all grid positions x_i , and b^n contains the temperatures at the edges of the domain x_0 and x_L , as boundary conditions (Dirichlet). From that system of equations, where all temperatures on the right-hand side of equation (15) are known, the temperatures T^{n+1} are calculated. The implicit approach guarantees the numerical stability of the Crank-Nicholson method. Also, the second-order discretization in space and time according to the Crank-Nicholson scheme gives second-order stability. Thus, independent of the stability the time-step distance Δt can be increased to minimize computational effort. The

error from discretization is proportional to (Δx^2) so that it quadratically reduces with reducing spatial distance grid points [16, 17].

2.2.3 Convective heat and mass transfer

Heat transfer

In moving fluids, heat is not only transported by conduction but also by the macroscopic transport of the fluid. In this case, the mechanism is called convection and comprises the transport of the fluid energy and conduction within the boundary layer between the moving fluid and the abutting medium at rest [19].

Figure 6 shows exemplarily the velocity, $w(x)$, and temperature, $T(x)$, profiles in a fluid flow parallel to a wall (or body at rest) where y is the distance from the wall. Here, T_w is the temperature at the wall and T_F is the temperature in the core of the fluid. The regions close to the wall with large temperature and velocity gradients are called velocity and thermal boundary layers (thicknesses δ_w and δ_T), respectively.

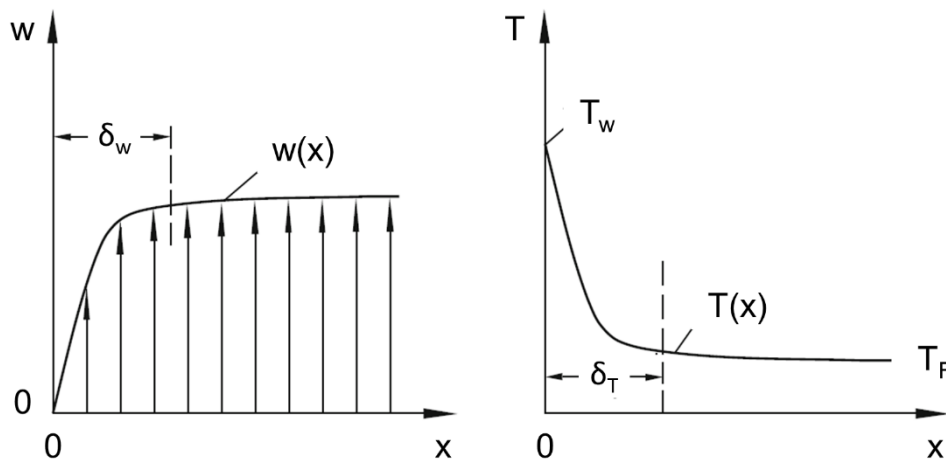


Figure 6: (left) Velocity and (right) temperature profiles of a flow close to a wall. Adapted from [19].

The mathematical description of the transport within the boundary layers is quite complex and was described by Ludwig Prandtl in 1904 with the boundary layer theory. Here, the global heat transport throughout the boundary layer towards the core of the fluid is considered. In this case, with $T_w > T_F$ as indicated in Figure 6, heat is convectively transported from the wall to the fluid. The heat flux from the wall to the fluid perpendicular to the wall is described by Newton's law according to [20]:

$$\dot{q} = \alpha (T_w - T_F) \quad (16)$$

The complex dependency of the heat flux of the three-dimensional flow and temperature field are summarized in the heat transfer coefficient α . To calculate the heat transfer coefficient, a fluid element very close to the wall ($x \rightarrow 0$) is considered where the fluid is considered to be at rest. Thus, heat transfer is solely described by conduction, equation (3), which under stationary conditions is then equal to the local convective heat transfer [19]:

$$\alpha = -\lambda \frac{\left(\frac{\partial T}{\partial x}\right)_w}{(T_w - T_F)} \quad (17)$$

However, in most applications the temperature profile close to the wall is not known and the average heat-transfer coefficient is required and calculated from correlations. Those were produced for technical relevant cases by measuring \dot{q} and $T_w - T_F$. The correlations are formulated in dimensionless numbers which contain geometric and material properties, velocities, and temperatures of the particular physical problem. According to the principle of similarity, temperature and velocity fields are similar in different physical problems if the dimensionless numbers coincide [19]. In dimensionless form, the heat transfer coefficient is formulated in the Nusselt number, Nu , [20]:

$$Nu = \frac{\alpha L}{\lambda_F} \quad (18)$$

Here, L is the characteristic length of the problem and λ_F is the thermal conductivity of the fluid. Correlations for the Nusselt number are separated into whether the heat transfer occurs under free or forced convection. The latter describes the case where the flow is caused by external forces while the former occurs due to temperature or density gradients within the fluid. For forced convection, the Reynolds number, Re , characterizes the flow field:

$$Re = \frac{w L}{\nu} \quad (19)$$

Here, w is the velocity and ν the kinematic viscosity. The Reynolds number can be thought of as the ratio of inertial forces and frictional forces. Exemplarily, pipe flows with $Re > 2300$ are considered turbulent while those with a lower Re number are laminar. The temperature field is described by the Prandtl number, Pr , which is the ratio of the kinematic viscosity and the thermal diffusivity:

$$Pr = \frac{\nu}{a} \quad (20)$$

Correlations for the Nusselt number are always a function of Re and Pr [20]:

$$Nu = f(Re, Pr) \quad (21)$$

Mass transfer

The mass transfer between a medium at rest (e.g. a liquid film) and a flowing medium (e.g. air) is explained via convection. Analog to the definition of convective heat transfer in equation (16), convective mass transfer is formulated:

$$\dot{m} = \beta (\rho_s - \rho_\infty) \quad (22)$$

Here, \dot{m} is the mass flux between the two media (in the following called evaporation rate), β is the mass transfer coefficient, ρ_s is the concentration of the transported species at the phase boundary between the two media, and ρ_∞ the concentration in the core of the fluid. Also, analog to the Nusselt number, the convective heat transfer coefficient is calculated from correlations of a dimensionless number:

$$Sh = \frac{\beta L}{D} = f(Re, Sc) \quad (23)$$

Here, Sh is the Sherwood number, which is the ratio of the convective mass transfer rate and the diffusion rate, D is the diffusion coefficient of the transported species, and Sc is the Schmidt number:

$$Sc = \frac{\nu}{D} \quad (24)$$

which is analog to equation (20) the ratio of momentum diffusivity (kinematic viscosity) and mass diffusivity. The Sherwood number and hence the mass transfer coefficient are calculated from correlations of Reynolds and Schmidt numbers.

If one of the two transfer coefficient or its particular dimensionless number is known, the other can be calculated from Reynolds analogy

$$\frac{Sh}{Nu} = \left(\frac{Sc}{Pr}\right)^n \quad (25)$$

where in good approximation n is equal to 1/3 [21].

2.3 Soot formation

A fundamental physicochemical understanding of soot formation is still evolving and is important to further control soot formation and its hazardous effects [22]. Under ideal conditions, in a combustion device such as a gas turbine or an IC engine, fuel and oxidizer are homogeneously mixed at $\lambda = 1$ so that the entire fuel and oxidizer are converted into carbon dioxide and water under the maximum release of heat. However, regions with a locally fuel-rich mixture ($\lambda < 1$) and high temperatures (> 1500 K) can cause the formation of soot. The community agrees on a general pathway in soot formation which is presented in Figure 7 and will be described in the following [23].

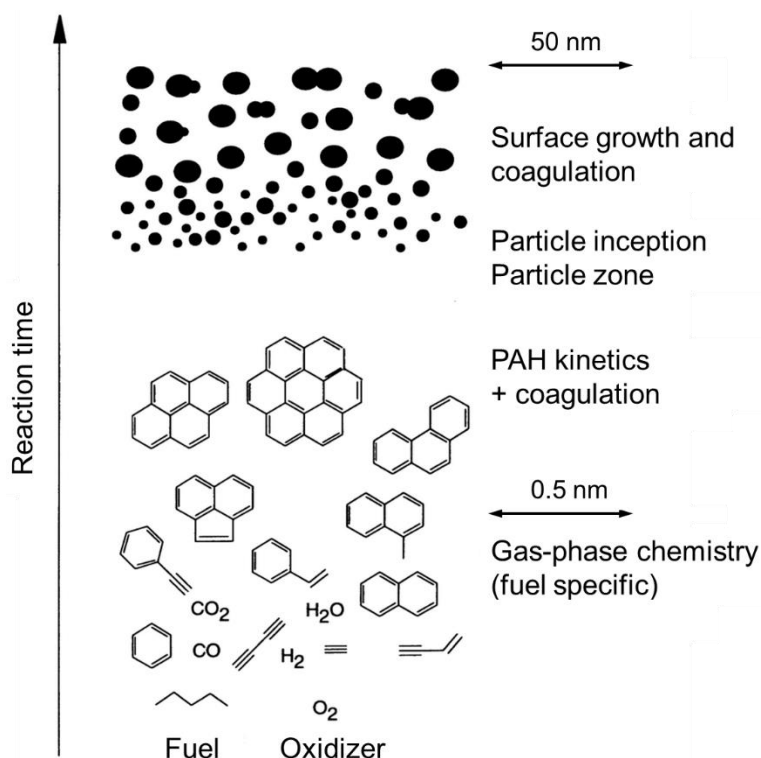


Figure 7: Soot formation under fuel-rich and premixed conditions. Adapted from [24].

2.3.1 Fuel pyrolysis and formation of polycyclic aromatic hydrocarbons (PAH)

Nowadays, it is widely accepted that PAH act as precursors in soot formation. A hydrocarbon is considered a PAH if it consists of at least two fused connected aromatic rings. The smallest PAH is naphthalene [25]. The reaction pathway to the formation of the first aromatic ring in PAH formation certainly depends on the structure of the fuel [26]. Nonaromatic fuels pyrolytically decompose and form acetylene in high concentrations recombining to a first aromatic ring, which further grows by acetylene addition to PAH. In contrast to this, in fuels that contain aromatic species the emergence of PAH is dominated by direct collisions and coagulation of the petrogenic aromatics [22, 26]. The bottom of Figure 7 shows the initial step in soot formation under premixed fuel-rich conditions of an aliphatic fuel. The fuel is partially oxidized by molecular oxygen which causes heat release and the pyrolysis of non-oxidized fuel. Besides products from complete and incomplete combustion such as CO, H₂, CO₂, and H₂O, mainly acetylene (C₂H₂), diacetylene (C₄H₂), and other, higher polyacetylene radicals are present in the reaction zone. An important reaction mechanism of benzene formation in aliphatic flames is the chain-lengthening of acetylene to unsaturated C₄, C₆, C₈, etc. radical species. Those, then either stabilize to polyacetylenes or form benzene with a side chain (i.e., C₆-C₂) via cyclisation or formation of a branched radical with ring-closure [23, 27]. Many different reaction pathways are discussed in literature towards the formation of the first aromatic ring during pyrolysis of aliphatic fuels. However, most of them consider acetylene, diacetylene and their radicals as the initial key species [22].

Further growth of benzene to naphthalene and higher PAH occurs via the hydrogen-abstraction/acetylene-addition (HACA) mechanism and to lesser extent by the coagulation of

aromatic rings and PAH. Figure 8 shows the reaction paths leading to the formation of PAH with two and more aromatic rings.

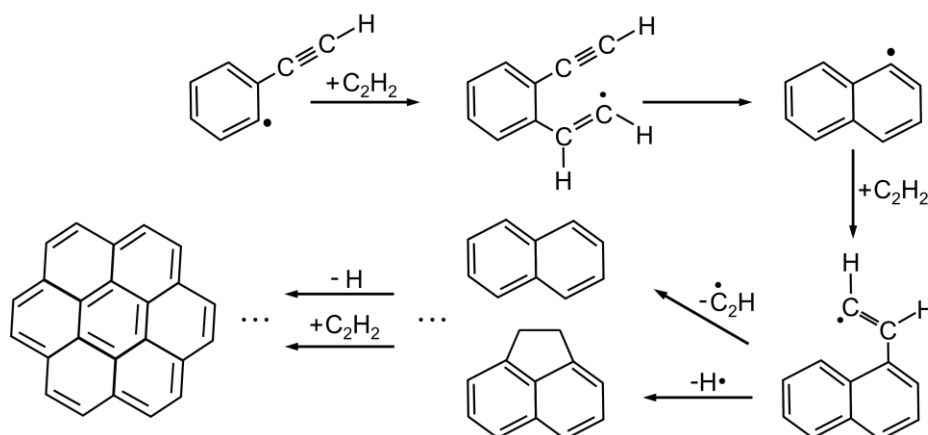


Figure 8: Reaction pathways towards naphthalene and higher PAH formation. Adapted from [28].

Here, acetylene attacks an aromatic ring with a radical site and a side chain. The radical site was created by the abstraction of a hydrogen atom. This step is followed by ring closure and the formation of a naphthalene radical. By acetylene addition to the reactive site of the molecule and subsequent removal of a hydrogen radical or ethynyl radical, acenaphthylene or naphthalene is formed, respectively. Acenaphthylene is a PAH containing a five-membered ring [27]. After several more reaction steps of the HACA mechanism large PAH such as coronene will be formed. Further growth and coagulation of large PAH will result in soot nucleation. Photophysical properties of different PAH size-classes are presented in Section 2.4.2.

2.3.2 Soot nucleation, growth, and oxidation

The reaction mechanisms responsible for growth of PAH in the third dimension and their contribution to the formation of soot nuclei is probably the least understood part in the soot-formation scheme in Figure 7. Sophisticated studies nowadays consider fullerenes as precursors in soot nucleation. Fullerenes are all-carbon, polyhedral, closed shells. Different reaction pathways appear to contribute to the growth from PAH to fullerenes. Aromers are hydrogen-rich PAH resulting from reactions between PAH and are considered as fullerene precursors. Their geometrical structure however is unsuitable for fullerene formation. Therefore, also acetylene is believed to contribute to the formation of a molecule that is suitable for cage closure and thus fullerene formation. A few approaches consider free radical mechanisms as PAH formation to be too slow to explain the rapid soot formation in flames and consider ionic mechanisms. However, conclusions are limited due to the current knowledge of thermodynamic and kinetic data for ionic species [27].

Small soot particles form after, temporally or spatially, the gas-phase chemistry, and have sizes in the range of about 3 nm. They are characterized by being single particles, their small polydispersity, and spheroidal geometry. They also exhibit transparency in measurements in transmission electron microscopy (TEM), thus they are called young or non-mature soot [22].

The further growth of soot in combustion can be divided into two regimes. First, the growth of small soot nuclei is dominated by coalescence with large aromatic structures and surface growth by the HACA mechanism. Both mechanisms remain the spherical shape of the primary particles. Second, in most combustion devices the primary particles are then transported into cooler regions where the temperature is too low for coalescence but high enough for coagulation. Coagulation is the dominant growth mechanism in such cooler region while also surface growth is present to lesser extent. By that, the particles form chain- or grape-like aggregates with fractal structures [29]. Therefore, surface growth by the HACA mechanism determines the final particle concentration while coagulation determines the final size distribution of the soot [23].

At all the previously discussed stages in soot formation as fuel pyrolysis, PAH, and soot growth, destruction of the particular matter may occur by oxidation. Manufacturers of combustion devices are usually most concerned with the oxidation of soot since in e.g. jet and Diesel engines about 90% of the soot is eventually destroyed. Oxidation occurs by reaction with molecular oxygen (O_2), the oxygen radical (O), and the hydroxyl radical (OH). Under most conditions, oxidation by OH is the dominant mechanism compared to oxidation by O_2 and O . Soot aggregates being attacked by oxidizing species may undergo an increase in the specific surface area by a structural change or even fragmentation of the aggregates. This causes enhanced soot burnout rates and illustrates the transient character of soot oxidation [22].

In turbulent and non-premixed combustion (such as fuel-film combustion in SIDI engines), the coupling of chemical reactions and fluid mixing make the quantitative investigation of soot formation very challenging. Here, the governing quantities for the process such as the equivalence ratio, temperature, and fuel concentration might vary significantly in time and space [30].

2.4 Optical diagnostics

In this chapter, the optical methods that were used to investigate the fuel-film formation and evaporation as well as the formation of soot precursors and soot are described. The techniques comprise laser-based and passive diagnostics.

2.4.1 Relevant diagnostic techniques

An overview among the most common optical diagnostic techniques for the properties that were measured in the scope of this work is given in Table 1. The table indicates the physical property of interest, the diagnostic techniques that can be applied, the working principle of each technique as well as an application example for each technique.

Table 1: Prominent optical diagnostic techniques for the properties discussed in this work.

Property measured	Diagnostic technique	Principle	Example application
Film thickness	LIF	Spontaneous emission of light (fluorescence) of a molecule	SIDI engine [31]

		excited by laser-photon absorption.	
	Refractive index matching	Illumination of roughened surface. Change in refractive index and fraction of backscattered light when liquid adheres to surface.	Fuel-spray impingement [32]
	Light absorption	Attenuation of light propagating through absorbing medium.	Urea-water solutions [33]
Mixture fraction	LIF	See above.	Two-stroke engine[34]
	Light absorption	See above.	SI engine [35]
	Raman scattering	Inelastic scattering of light. Frequency shift of scattered light is representative of species, intensity of concentration.	SIDI engine [36]
	Raleigh scattering	Elastic scattering of light on molecular level. Signal intensity is representative of concentration.	Diesel jet [37]
Gas velocity	PIV	Particles seeded to a fluid flow scatter light. Particle shift between two frames yields gas velocity.	Swirl flame [38]
	Optical flow	Movement of brightness patterns between two frames yields gas velocity.	Diesel engine [39]
Flame-front location	Chemiluminescence	Emission of light from radicals, being electronically excited as a consequence of a chemical reaction.	Swirl flame [40]
	OH LIF	Spontaneous emission from OH-molecules after laser excitation.	Hydrogen-fuelled spark-ignition engine [41]
PAH location	LIF	See above.	Gas-turbine model combustor [42]
	Light absorption	See above.	Premixed flame [43]

Soot location	LII	Laser heats soot particles to near sublimation temperature. Consequently, particles emit intense thermal radiation.	Diffusion flame [44]
	Diffuse back-illumination (DBI)	Attenuation of light by the extinction (absorption and scattering) from soot.	Compression-ignited fuel spray [45]
	Soot luminosity	Thermal radiation of hot soot particles in flames.	Diesel engine [46]
	Elastic light scattering (ELS)	Elastic scattering of light by soot particles. Particle size is comparable with the wavelength of the light → Mie scattering.	Premixed flame [47]

2.4.2 Laser-induced fluorescence (LIF)

The transition of a molecule or atom from an electronically excited state to the electronic ground state by emission of light is called luminescence. If the excitation of the molecule occurs via laser energy and the excited state is short-lived, the subsequent emission is called laser-induced fluorescence (LIF) [48, 49]. The total internal energy-state of a molecule is the sum of the electronic, vibrational, and rotational energies of the molecule. Since each of these energies occurs in discrete levels, the molecule's energy levels are also discrete. If the molecule interacts with incident light (e.g. from a laser), the corresponding photon is absorbed if its energy fits the difference of two energy levels of the molecule [50]:

$$E_1 - E_2 = h f \quad (26)$$

where E_1 and E_2 are two distinct energy states, h is the Planck constant, and f is the frequency of the incident light which is connected to the wavelength via the speed of light. Generally, in a molecule each electronic state is subdivided into a multitude of vibrational sublevels where each sublevel again has different rotational states. Figure 9 shows a Jablonski diagram that illustrates electronic excitation of an atom or molecule and the subsequent depopulation mechanisms. Also, the vibrational states within each electronic state are schematically indicated [51]. Here, the arrow length in the vertical dimension is proportional to energy.

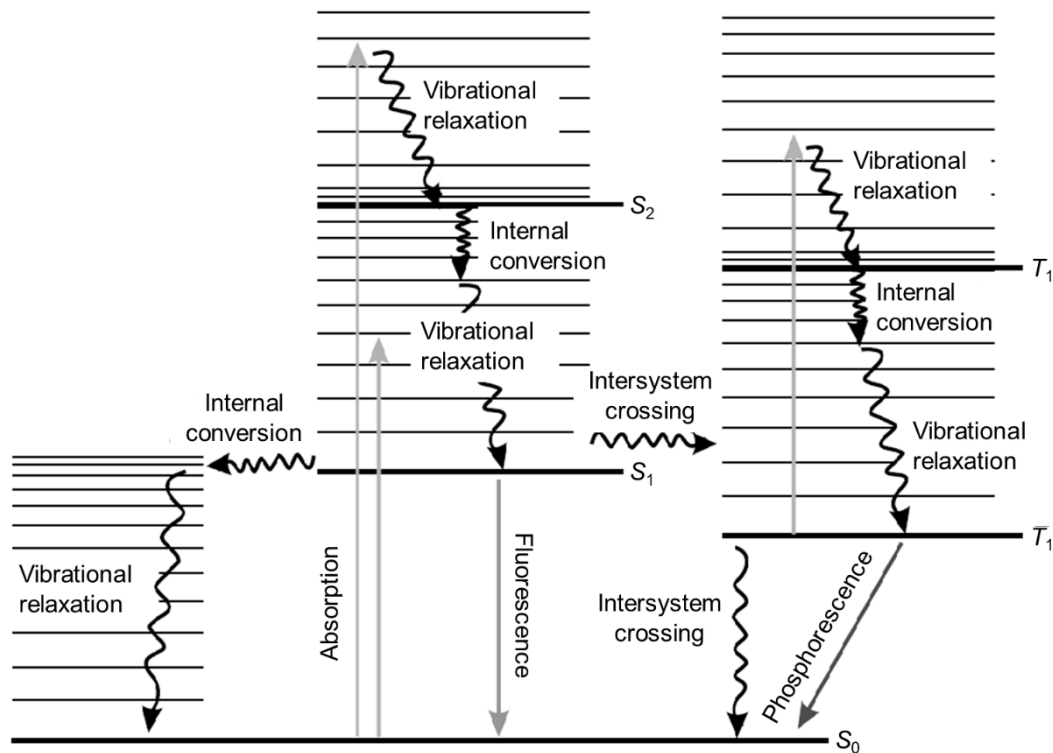


Figure 9: Jablonski diagram of a typical organic molecule showing electronic excitation and depopulation mechanisms including fluorescence [51].

The population of vibrational and rotational energy states within an electronic state is described by the temperature-dependent Boltzmann distribution. Therefore, also the energy difference between two electronic states is a distribution such that a range of photon energies can be absorbed and cause the electronic excitation of a molecule [51].

On a macroscopic, i.e., continuum, scale, the extinction of light when propagating through an absorbing medium at a certain wavelength is described by the Beer-Lambert law [52],

$$I_t = I_0 e^{-\varepsilon^* cl} \quad (27)$$

Here, I_t denotes the transmitted intensity, I_0 the incident intensity, ε^* the molar extinction coefficient, c the molar concentration of the absorbing species, and l the absorption path length. The extinction coefficient describes the extinction of light from absorption, scattering, refraction, and diffraction. In the following, extinction of light is exclusively attributed to absorption. The "absorbed intensity" I_a is equal to the difference between incident and transmitted intensity:

$$I_a = I_0 (1 - e^{-\varepsilon^* cl}) \quad (28)$$

When molecule is electronically excited by photon absorption, it generally first is in a nonequilibrium state from which it relaxes to the thermal equilibrium (for many species the lowest vibrational state at room temperature) of the particular electronic state. At ambient or high-pressure conditions, this vibrational relaxation occurs within picoseconds [51]. If the

vibrational relaxation occurs in the S_1 state, the molecule has a certain probability (the fluorescence quantum yield, FQY) to return to the electronic ground state via emission of a photon. This is fluorescence. After photon emission, the molecule populates a multitude of vibrational and rotational states in the electronic ground state such that the emitted fluorescence intensity covers a spectrum over the wavelength analog to the absorption (mirror symmetry). The transfer of energy to the surrounding during vibrational relaxation causes the fluorescence to be generally of lower photon energy than that of absorption and thus to be spectrally red-shifted (Stokes shift). Therefore, the fluorescence light can easily be distinguished from the excitation light by spectral filtering [51].

Deexcitation mechanisms competing with fluorescence are internal conversion (IC), intersystem crossing (ISC), and collisional quenching. In IC a molecule relaxes from an excited electronic state into a higher vibrational level of the next lower electronic state. From there the molecule relaxes into the electronic ground state by vibrational relaxation. This process is thus non-radiative. If the spin multiplicity of the molecule changes during the electronic transition, the process is called ISC. Then the molecule is left in a triplet state. From the long-lived triplet state the molecule relaxes back to the singlet ground state S_0 by emission of a photon – this is phosphorescence [51, 53]. Collisional quenching is the non-radiative energy transfer of electronic energy from the potentially fluorescing molecule to a surrounding molecule (quencher). This effect is not indicated in Figure 9 since it is not an intra-molecular deactivation mechanism. However, in many cases collisional quenching is the dominant deactivation mechanism. The colliding species can be solvent or bath-gas molecules, but also other molecules of the same species [54]. Taking these depopulation mechanisms into account, the FQY can be written as [55]:

$$\Phi_{\text{FQY}} = \frac{k_{\text{fl}}}{k_{\text{fl}} + k_{\text{IC}} + k_{\text{ISC}} + k_{\text{Q}}} \quad (29)$$

where k_{fl} is the rate for spontaneous fluorescence, k_{IC} and k_{ISC} are the rates of the non-radiative deactivation mechanisms, and k_{Q} is the bimolecular quenching rate coefficient.

The detected fluorescence intensity is proportional to the absorbed intensity, the FQY ϕ ($\frac{\# \text{ photons emitted}}{\# \text{ photons absorbed}}$), and the collection and detection efficiencies $\Omega \eta$ of the imaging system [56]:

$$I_{\text{f}} = \phi \Omega \eta I_{\text{a}} \quad (30)$$

Combining equations (28) and (30), the fluorescence intensity is given by:

$$I_{\text{f}} = \phi \Omega \eta I_0 (1 - e^{-\epsilon^* c l}). \quad (31)$$

When the exponent in equation (31) is small, the fluorescence intensity is in good approximation proportional to the concentration of the fluorescing species and the absorption path length:

$$I_f = \phi(T, p, n_i) \Omega \eta I_0 \varepsilon^*(T) c(T, p) l \quad (32)$$

Equation (32) indicates the dependency of the FQY on ambient pressure, temperature, and bath gas composition. Also, the absorption coefficient may be temperature dependent. Most aromatic molecules, like toluene and anisole, in liquid and gas phase show a significant decrease in the FQY and a red-shift of the fluorescence spectrum with increasing temperature [31, 57-59]. The latter can be exploited to measure temperature with LIF.

A particular group of species that can be excited to fluoresce are PAH. The reaction pathways towards the formation of PAH are presented in Section 2.3.1. Here, their diagnostic treatment by the means of LIF is discussed. According to the Jablonski diagram in Figure 9, the molecule occupies the lowest rovibrational level of the ground electronic state S_0 . According to the Boltzmann distribution, this is the case for most aromatic molecules at room temperature [60]. For PAH, a substantial fraction of the fluorescence light is blue-shifted with respect to the excitation wavelength, in particular at elevated temperatures. This is called anti-Stokes emission [60]. Berlman measured excitation and emission spectra of selected small PAH at room temperature in a liquid solvent [61]. Generally, PAH have a large absorption coefficient and high FQY in the ultraviolet (UV) and visible (VIS) region of the spectrum. As PAH grow in size, their conjugated electronic system increases in size, too, which results in a decreasing energy gap for an electronic transition. Exemplarily, at room temperature benzene, pyrene, and coronene absorb light at up to 270, 370, and 500 nm, respectively [62]. Therefore, larger PAH have red-shifted and broader absorption and fluorescence spectra. This can be exploited to distinguish size classes of PAH via LIF. A quantitative measurement of PAH concentration in flames, however, is almost impossible due to the lack of spectroscopic data for most species at high temperature, such as absorption cross section, quenching efficiencies, and FQY. One option for performing selective measurements of PAH species is to extract them from the flame and cool the sample to reduce the rovibrational temperature [60]. The state of the art in PAH LIF is discussed in more detail in Section 3.3.

2.4.3 Laser-induced incandescence (LII) of soot

In laser-induced incandescence (LII), a laser pulse heats soot particles to well above flame temperatures, such that according to Planck's law (see Section 2.4.4) the particles' broadband emission is much more intense and at shorter wavelengths than the "natural" soot incandescence. Mostly, the LII signal is detected point-wise or two-dimensionally and is an approximate measure of relative soot concentrations or soot volume fraction (f_v). Time-resolved LII might also be used to determine particle sizes based on the signal decay [63]. Figure 10a shows an energy balance around a single soot aggregate after light irradiation.

$$\frac{dU_{\text{int}}}{dt} = \dot{Q}_{\text{abs}} + \dot{Q}_{\text{rad}} + \dot{Q}_{\text{cond}} + \dot{Q}_{\text{sub}} + \dot{Q}_{\text{ox}} + \dot{Q}_{\text{ann}} + \dot{Q}_{\text{therm}} \quad (33)$$

Here, U_{int} is the particle's internal energy, t is the time, \dot{Q}_{abs} is the absorptive-heating rate, \dot{Q}_{rad} is the radiative-cooling rate, \dot{Q}_{cond} is the conductive-cooling rate, and \dot{Q}_{sub} is the evaporative-

cooling rate, \dot{Q}_{ox} is the oxidative-heating rate, \dot{Q}_{ann} is the heating rate from annealing, and \dot{Q}_{therm} is the thermoionic heating rate.

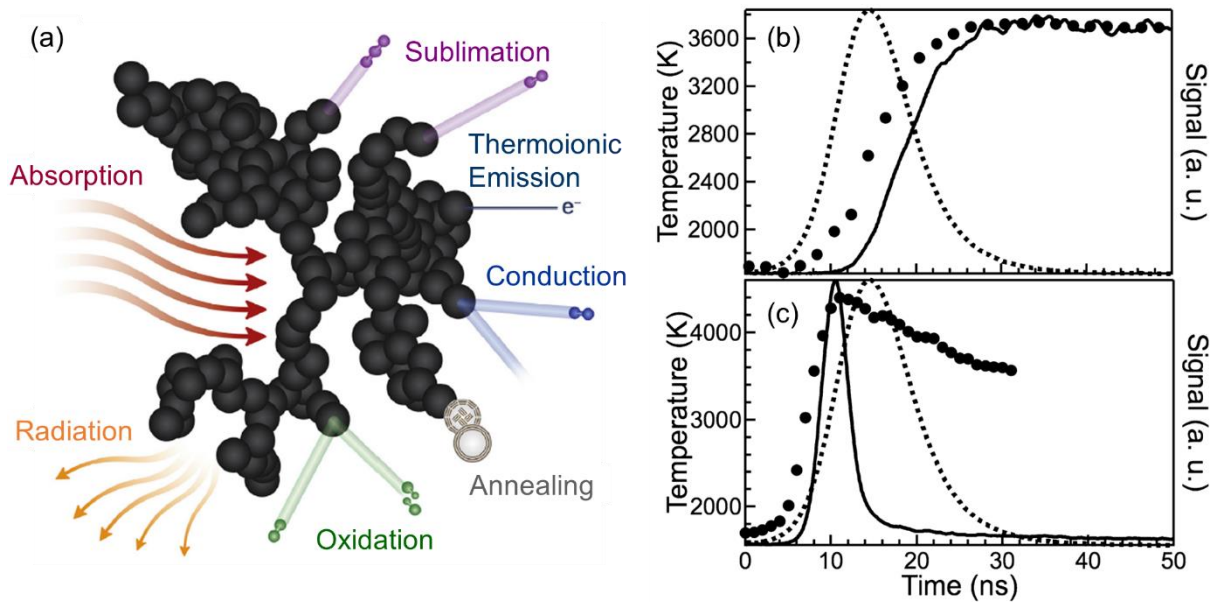


Figure 10: (a) Heat flows around soot aggregate. (b) Temporal evolutions of temperature, signal, and laser pulse for laser fluences of (b) 0.1 and (c) 1.45 J/cm². Adapted from Michelsen et al. and Goulay et al. [64, 65].

The most important processes here are absorption of the incident laser light, which heats up the particle, and the radiation, known as LII. Conduction is the dominating cooling mechanism at moderate laser fluences. At high laser fluences, sublimation becomes the governing mechanism among heat losses which causes particle cooling and mass loss. Oxidation of the particle can cause particle heating and mass loss while the latter is much slower than during sublimation. Annealing of particles is considered an exothermic process, thus heats the particle, but, its rate, energetics, and how it affects other physical parameters is barely understood. Thermoionic emission generally has very little influence on the particle cooling rate and is thus often neglected [66]. Figure 10b and c show the soot particle temperature (solid line), the LII signal (symbols), and the temporal profile of an incident laser pulse (dotted line) at 1064 nm for two laser fluences of 0.1 and 1.45 J/cm², respectively. The particle temperature was derived from emission spectra and the LII signal was detected with a 681.8 nm bandpass filter. Measurements were done on mature soot in an atmospheric co-flow diffusion flame [67]. At a fluence of 0.1 J/cm², the incident laser energy is completely absorbed and heats the particles. Thus, the particles reach the maximum temperature at the end of the laser pulse and then slowly cool down with time. If the fluence were increased further within this low-fluence regime, the signal and temperature decays would accelerate due to the increasing temperature gradient between soot and the ambient. The delay between the maximum particle temperature and LII signal is caused by the non-linear relationship between the two quantities ($\dot{Q}_{\text{rad}} \sim T^4$ [68]). For a laser fluence of 1.45 J/cm², the particles reach the sublimation temperature of around 4600 K during the laser pulse irradiation, around 10 ns after start of the laser pulse. Significant sublimation and enhanced conduction lead to a sharp decrease in the particle temperature and LII signal with progress in time [64].

Figure 11 shows the influence of different excitation laser spatial-profiles on gated LII signals for varying laser fluences. The signal was integrated over an 18 ns gate starting 20 ns after the laser pulse.

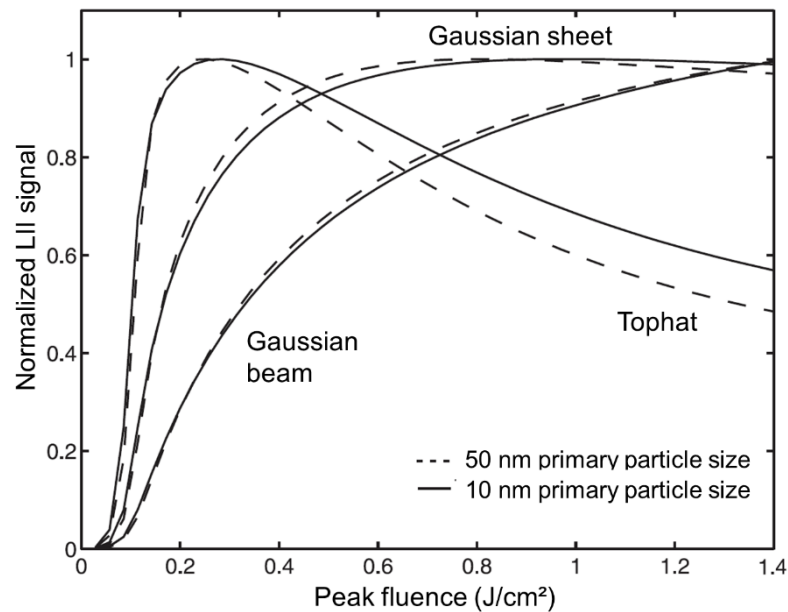


Figure 11: Dependence of gated LII-signals on the peak laser fluence for different spatial laser profiles and primary particle sizes [69].

In particular when imaging the LII signal it is important to have a homogeneous or known fluence distribution throughout the laser spatial profile when quantifying the signal in terms of f_V or relative soot concentration. For this purpose a top-hat profile is the easiest since all particles irradiated by the laser pulse are exposed to the same laser fluence. For a top-hat profile, the LII signal increases up to a laser fluence of about 0.2 J/cm^2 and then decreases due to sublimation. However, a top-hat profile is not simple to generate in practice. Most lasers generate a Gaussian or quasi-Gaussian beam profile. With a Gaussian (i.e., radially symmetric) beam, the LII signal monotonically increases with a decreasing slope above fluences of 0.15 J/cm^2 . Here, soot in the high-fluence center of the beam sublimates while particles irradiated by the broad low-fluence wings of the beam are still heated [70, 71]. In a Gaussian sheet, these two effects may compensate. This compensation is responsible for the fluence-independent region above about 0.5 J/cm^2 , as shown in Figure 11 [64, 72]. LII imaging in this “saturation regime” is less sensitive to shot-to-shot variations in laser energy and inhomogeneities in the local laser fluence.

Typical wavelengths from Nd:YAG (neodymium-doped yttrium aluminum garnet) lasers for LII measurements are 532 and 1064 nm. In particular, 1064 nm is a favorable wavelength since it avoids exciting LIF from PAH, evaporated species, or other combustion intermediates [64]. However, even when exciting LII with 1064 nm and fluences above 0.5 J/cm^2 , Swan-band emission from excited C_2 and can be interfering with LII in the visible and even near-infrared (IR) spectrum [73, 74]. With laser fluences above 1 J/cm^2 at 1064 nm, Swing-band emission from C_3 can also interfere with the LII signal from 360-440 nm [75, 76]. Interference-

free wavelength regions for detection are 400 – 456, 490 – 500, and 580 – 820 nm when exciting with laser fluences below 1 J/cm [64].

2.4.4 Natural flame luminosity

The visualization of combustion luminosity was extensively applied in the research and development of advanced combustion processes in IC engines. The rapid development in the field of high-speed cameras made high-speed imaging of combustion luminosity a simple and cheap technique compared to laser-based measurements. The emission of light in combustion can mainly be separated into the banded chemiluminescence from gas-phase species (blue) and the broadband thermal radiation of soot particles (bright yellow-white) [50].

Chemiluminescence (CL)

CL is the emission of light as a consequence of a chemical reaction [77]. In hydrocarbon flames, exothermic reactions electronically excite specific molecules. From there they rapidly relax to the electronic ground state via emission of light, which is known as CL [78]. The emission occurs in a multitude of wavelength bands where each band is molecule-specific and allows an identification of certain molecules in combustion. The main emitters are CH^* , OH^* , C_2^* , CO_2^* , and to lesser extent HCO^* , CO^* , and CH_2O^* . Chemiluminescence is a marker for oxidation reactions. Detected integrated along the line of sight, it can be used to indicate local stoichiometry and heat release rates [78, 79]. Typical flame markers are CH^* and OH^* . Figure 12 shows the spectral locations of the CL from the diatomic radicals OH^* , CH^* , and C_2^* as well as CO_2^* .

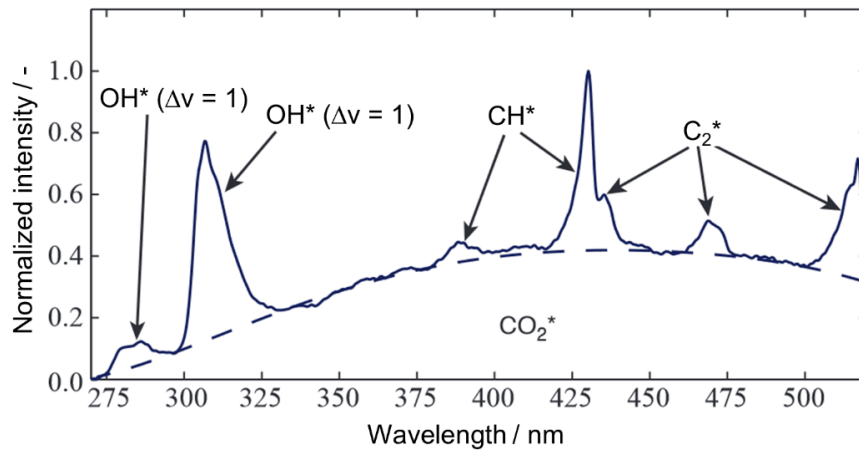


Figure 12: Chemiluminescence spectrum from a methane/air flame. Adapted from [80].

The strongest peaks for OH^* and CH^* CL are at 309 and 431 nm, respectively. The most important reaction mechanisms that cause the formation of OH^* , CH^* , and CO_2^* are [40, 81]:



Soot incandescence

Soot particles form at high temperature and fuel-rich conditions via incomplete oxidation of the fuel. The hot soot particles emit thermal radiation according to Planck's law [50]. The properties of soot are very close those of a blackbody. A blackbody perfectly absorbs all the radiation incident on it and is thus colorless or black. According to Kirchhoff's law a blackbody is also a perfect emitter of radiation. Planck's law describes the spectral emissive power per unit area B_λ [82]:

$$B_\lambda(\lambda, T) = \frac{2hc_0^2}{\lambda_{em}^5} \cdot \frac{1}{e^{\frac{hc}{\lambda k_B T}} - 1} \quad (37)$$

Here, h is the Planck constant, c_0 is the speed of light in vacuum, λ_{em} is the emission wavelength, k_B is the Boltzmann constant, and T is the body's temperature. The equation shows that the intensity of the thermal radiation at a certain wavelength is solely dependent on temperature. Figure 13 shows calculated spectra of a radiating blackbody for temperatures ranging from 1400 – 2200 K. The figure shows the two most important features of blackbody radiation with variation in temperature. First, the emitted intensity becomes much more intense with increasing temperature. Second, the peak of the spectrum blue-shifts with increasing temperature (Wien's displacement law) [82].

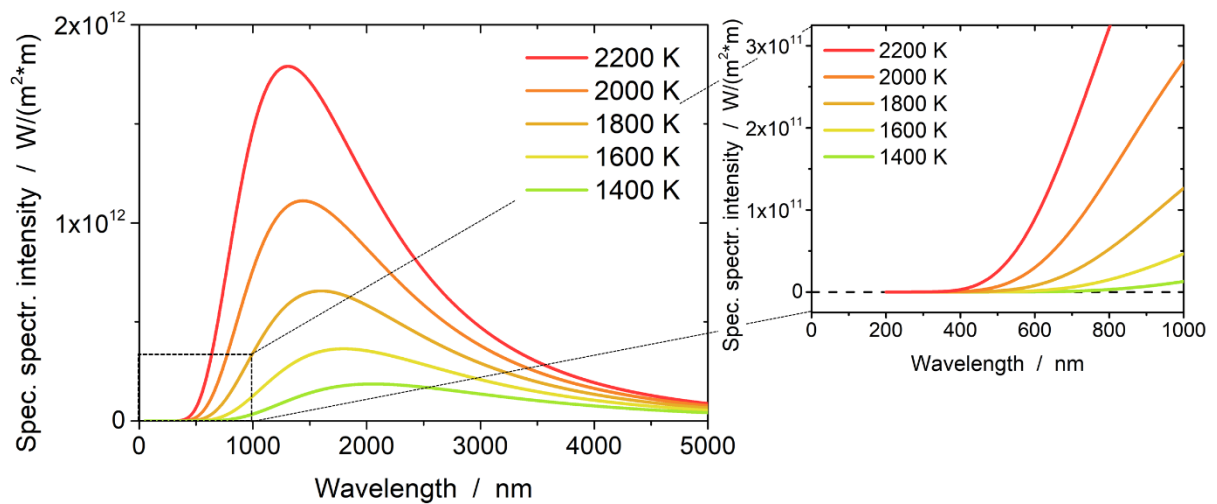


Figure 13: Blackbody-radiation spectra for different temperatures.

2.4.5 Particle image velocimetry (PIV)

Particle image velocimetry (PIV) is a powerful technique for wide-field velocity measurements. Figure 14a shows a typical experimental arrangement for a PIV measurement. Here, two laser pulses with a fixed temporal delay between each other are formed into light. The light sheets illuminate the flow that is seeded with solid or liquid particles. To accurately determine gas velocities from PIV, the particles need to follow the flow since eventually the particles' velocity is considered the fluid velocity. When seeding particles to a gas flow, where the density difference between gas and particles is large, the particles need to be sufficiently small such that the relaxation time is short, and the Stokes number becomes smaller than one. The particles scatter the incident laser light. This Mie-scattered laser light from the two laser pulses is

detected on two frames on a camera. The acquired images are clustered into interrogation windows (small subareas) of user-defined size. The displacement of the particles within an interrogation window between the two laser illuminations is then used to derive a displacement vector for each interrogation window. The length of this vector divided by the time between the two frames gives the velocity magnitude for the interrogation window [83].

The displacement vector of the particles is computed via cross-correlation [84]. In this procedure, the two interrogation windows are shifted pixelwise relative to each other along the x and y coordinates. For each shift the intensity values of overlapping pixels are multiplied. Then, the intensity products of all pixel pairs are summed. Doing this along the total lengths of the x and y axes, s_x and s_y , respectively yield a map as shown in Figure 14b. Here, the peak R_D indicates the displacement along x and y where the maximum correlation between the two frames is found. The maximum correlation means that the particle pattern from the first frame is found in the second frame with highest probability. A main assumption in PIV post-processing with cross-correlation is that all particles have moved homogeneously between the two illuminations [83].

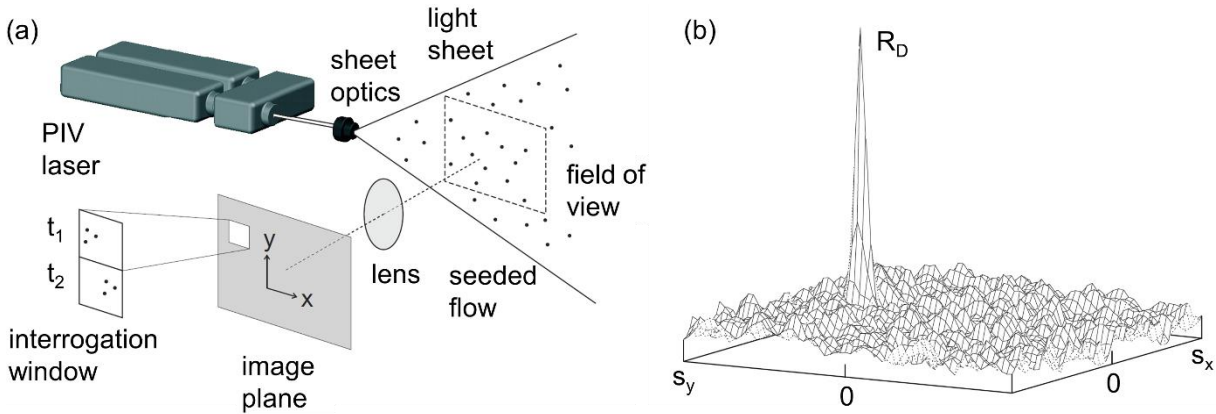


Figure 14: (a) Optical layout for a PIV measurement [84]. (b) Map of peaks from cross-correlation [85].

Optical flow is another technique to derive fluid velocities based on the movement of brightness patterns. Here, the detected light is not necessarily Mie-scattered light from particles but LIF or natural flame luminosity from combustion species [86].

2.5 Light sources and detectors

This chapter discussed the light sources and detectors that were used in this work. As light sources, Nd:YAG-lasers and light emitting diodes (LED) were used. Image intensifiers and cameras with charge-coupled devices (CCD) or complementary metal-oxide semiconductor (CMOS) sensors were used for detection.

2.5.1 Nd:YAG lasers and light emitting diodes (LED)

Nd:YAG laser

In an Nd:YAG laser, Neodymium ions, Nd^{3+} , doped at around 1% into the host material yttrium aluminum garnet (YAG), are the radiating laser medium. In flashlamp pumped Nd:YAG lasers,

a gas-discharge lamp is positioned parallel to the laser rod and optically pumps the laser medium. The flashlamp light at wavelengths between approximately 700-800 nm is absorbed by the Nd^{3+} ions and causes a population inversion between ground and excited state. The latter is a requirement for the operation of a laser. Therefore, the excited state needs to be sufficiently long lived to achieve the population inversion by pumping. At some point, the first Nd^{3+} ions relax to the ground state by spontaneous emission of light. Other excited Nd^{3+} ions interact with the incident photons by also relaxing to the ground state by emission of light. This process is called stimulated emission. The two light waves are coherent, that is, equal in frequency, phase, polarization, and direction of propagation [87]. A resonator, consisting of two parallel mirrors encloses the laser medium. The resonator causes the spontaneous and stimulated emission, the laser light, to propagate multiple times through the laser medium until the amplification reaches the lasing threshold. Then, laser light at 1064 nm is emitted by one of the resonator mirrors which is partially transmitting light of this wavelength [49].

Short laser pulses on the order of 10 ns with high instantaneous power are achieved by Q-switching. By an optical switch within the resonator the losses are kept high so that the lasing threshold is initially not reached. Therefore, a large population inversion builds up. Once the optical switch is turned on the losses become small because of the instantaneously increasing resonator quality/reflectivity, and an intensive short laser pulse depopulates the inversion [49]. This high-intensity laser pulse can be frequency-converted to 532 nm or higher harmonics at 355 and 266 nm in birefringent crystals downstream of the resonator [87].

LEDs

Light emitting diodes (LEDs) consist of semiconducting materials where electrons recombine with electron holes in a p-n junction under the emission of a photon when an electric current is applied. The wavelength of the emitted light depends on the band-gap energy of the semiconducting material. For example, in gallium arsenide, the band-gap energies correspond to light with wavelengths in the near IR, VIS, and near UV [88]. LEDs usually have much broader emission spectra than lasers and may be operated in a pulsed mode with pulse lengths in the microsecond range.

2.5.2 Intensified CCD-cameras and high-speed CMOS cameras

Intensified CCD camera

A CCD image sensor is a two-dimensional array of pixels in which each pixel contains a photo-sensor which consists of a semiconducting material. The photo-sensors convert incident light into electric charge. For the detection of light in the VIS, silicon (Si) is often used as a semiconductor. When silicon is irradiated with visible light, electrons and holes are created. The greater the number of photons incident on a pixel, the greater the number of electrons that accumulate on that pixel. After the exposure of the CCD, the electrons are transported to the read-out circuit by a network of gates (electrodes) on top of the semiconducting layers. The pixels are read out one after another, which makes the frame rate of CCD cameras comparatively slow. Since the absorption coefficient of the semiconducting material differs with the wavelength of the light, the quantum efficiency (QE) of the sensor is a function of the

wavelength [89]. Sources of noise are the dark-current and read-out noise. Electron-hole pairs that form thermally create dark-current noise. It can be reduced by cooling the sensor to low temperatures. Read-out noise appears in the charge-to-voltage conversion. It increases with the readout frequency [90].

Intensified relay optics consist of a gateable image intensifier and relay optics. They may be used in front of the camera for several reasons. The image intensifier has an electronic shutter that enables nanosecond exposure times. This is useful in applications where a temporally short signal needs to be discriminated against a stationary background light such as flame luminosity. The light is focused by a camera lens onto a photo cathode at the entrance window of the image intensifier where it is converted into electrons. The electrons are accelerated towards a phosphor screen in an electric field in a micro-channel plate. In these micro channels the electrons hit the walls several times and release many more electrons, thus amplifying the signal. The amplification factor is controlled by the voltage across the micro channel plate. The phosphor screen then emits light in the VIS spectrum that is imaged by the relay optics onto the CCD sensor. Since conventional photo cathodes are often sensitive in the UV, the image intensifier is sometimes used to convert signal from the UV to the VIS and make it detectable for conventional CCD sensors. An image intensifier becomes also necessary if the signal is very low and in the range of the CCD sensor's read noise. However, the intensifier always adds additional noise so that the final signal-to-noise ratio (SNR) is worse than with only a CCD camera [91].

High-speed CMOS camera

In an CMOS sensor, in contrast to a CCD each pixel in the pixel array has an entire read-out circuit. This circuit consists of a photosensor, a photosensor reset, signal amplification, and output circuits [92]. The parallel structure of CMOS sensors enables much higher read-out rates than CCD sensors can achieve, which makes the former suitable for high-speed imaging. CMOS sensors also have the advantage that only a small sub window of the entire sensor may be read out at even higher frame rates but reduced spatial resolution [93]. CMOS sensors have individual signal amplifiers on each pixel, which increases the fixed-pattern and read-out noise compared to CCD sensors [92].

CCD and CMOS sensors can be equipped with a "Bayer pattern" to acquire color images. Then, each pixel is equipped with a color-filter for either red, green, or blue (RGB). The filter pattern consists of 50% green, 25% red, and 25% blue filters since the human eye is most sensitive in the green. Each pixel is only covered with one filter, thus it only senses one of the three colors. The missing color intensities in each pixel are calculated according to the intensity values of neighboring pixels with different color filters. The image thus becomes a "full color" image for the human visual system [94, 95].

3 State of the art

In the following the current state of the research on fuel-film imaging and evaporation as well as visualization of PAH and soot formation is discussed. Parts of the content were published in Jüngst et al. [96-98] and Shahbaz, Jüngst, and Kaiser [99]. The crank-angle convention in this thesis is that 0° crank angle (CA) is at compression top-dead center (TDC), i.e., crank angles during intake and compression are negative.

3.1 Impact of fuel films on soot formation

The correlation between evaporating fuel films on the piston and engine-out soot emissions was investigated by Waley et al. [100], Drake et al. [101], Ortmann et al. [102], and Stevens and Steeper [103]. Waley et al. measured particulate mass and size distributions stemming from piston fuel-films for different fuels [100]. Drake et al. imaged evaporating fuel films by refractive index matching (RIM) and identified pool fires above those by high-speed imaging of the combustion luminosity in an optically accessible SIDI engine [101], see Figure 15a. They found first soot formation from fuel-rich pockets soon after the spark. However, most of this soot was oxidized in the cylinder during the remainder of the cycle. In contrast, soot formed in pool fires was not burned out due to low turbulent mixing rates and low temperatures close to the walls and was detected in some cycles until exhaust valve opening.

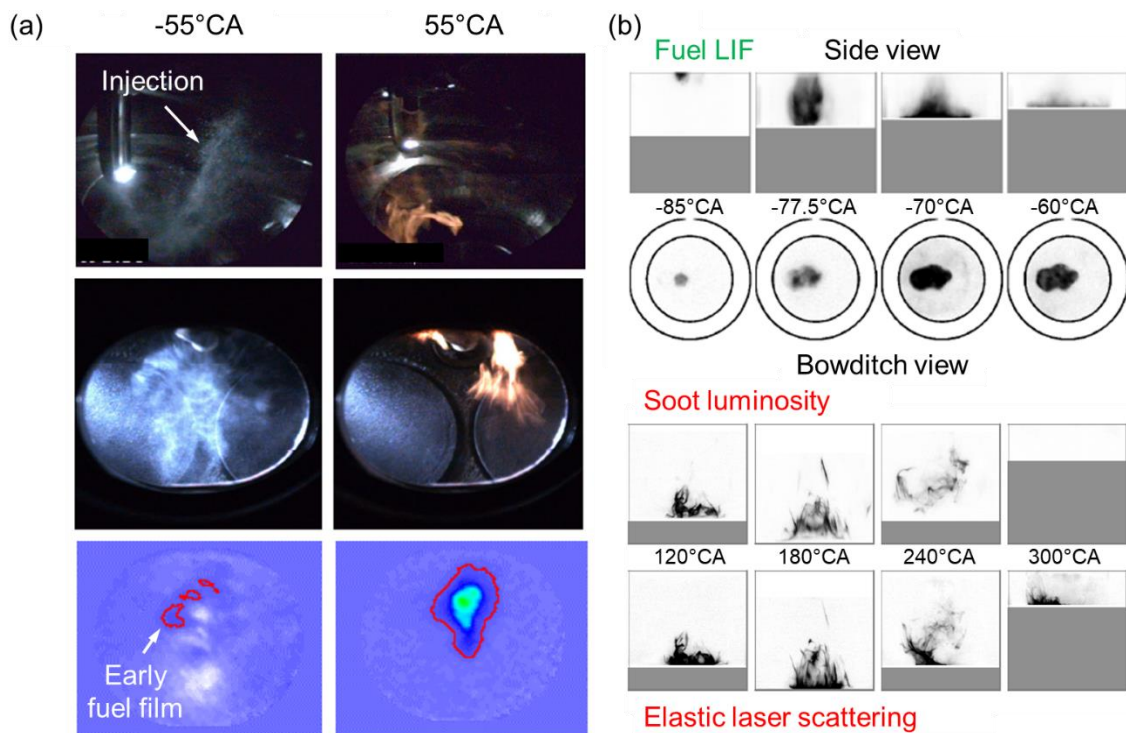


Figure 15: (a) (left) Injection, flame chemiluminescence, and early fuel film at 55°CA. (right) Soot luminosity and late fuel film 55°CA. Adapted from [101]. (b) (top) Gasoline LIF of liquid fuel in the spray and on the piston and (bottom) soot luminosity and elastic laser scattering of soot above the piston. Adapted from [103].

Stevens and Steeper [103] used LIF to show that for late injection (start of injection (SOI) - 90°CA), where the piston is close to the injector, significant amounts of fuel impinge on the

piston, see Figure 15b. High-speed imaging of flame luminosity and elastic laser scattering of soot revealed that under these conditions soot may exist into the exhaust stroke because there is not enough time for film evaporation. Stojkovic et al. [104] also found two distinct stages of soot formation in a SIDI engine, operating with a stratified fuel/air-mixture, by simultaneously imaging OH^* CL and LII of soot. They found that early soot originates from regions with partially premixed combustion close to the electrodes, indicated by OH^* CL, and is oxidized later due to high temperatures (2000 - 2400 K) and turbulent mixing. Soot formation from pool fires occurs later and becomes significant when 80% of the heat has already been released. Temperatures then are much lower (about 1700 K), so that oxidation is unlikely, causing soot engine-out emissions. In a wall-guided GDI engine, Ortmann et al. visualized the formation of fuel films and measured the engine-out emissions of soot and unburned hydrocarbons [102]. When fuel films persist into the exhaust stroke and the local temperature is too low to cause soot formation, unburned hydrocarbons are emitted [105-108].

Recently, the author was involved in a study on the simultaneous visualization of fuel-film LIF and soot incandescence in an all-metal SIDI engine through endoscopic access [99]. Fuel was excited with 266 nm laser pulses and the imaging was done with an intensified double-frame CCD camera. The first frame was laser-synchronous and mainly captured fuel-film LIF while the second frame (2.1 μs later) captured soot incandescence. While for the iso-octane/toluene-mixture fuel films appear as distinct spots, gasoline fuel-films spread more connected over the piston surface, see Figure 16. Soot incandescence is found adjacent to the fuel films close and in particular for gasoline downstream of the films following the tumble flow.

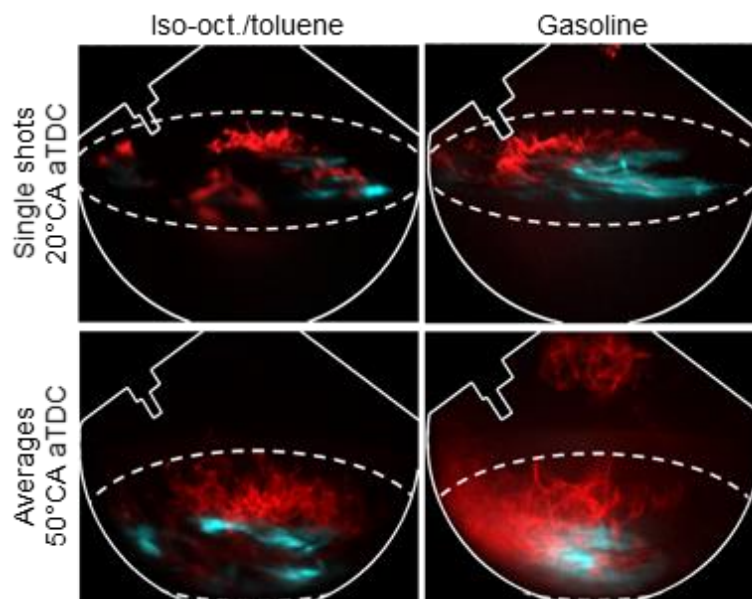


Figure 16: (top) Single shots and (bottom) ensemble-average images of simultaneous fuel-film LIF (turquoise) and soot incandescence (red) for (left) iso-octane + 5% toluene and (right) gasoline. Adapted from [99]. The engine temperature was 353 K, the injection pressure was 100 bar.

3.2 Fuel-film formation and evaporation

Evaporating liquid films are important in nature and engineering. In particular under non-boiling conditions, they are relevant in diverse applications such as falling-film evaporators,

seawater desalination, nanoparticle coating processes, cooling of chemical reactors and gas-turbine blades, exhaust aftertreatment. In spark-ignited (SI) direct-injection (DI) engines, liquid fuel evaporating from the piston surface during combustion is known to cause soot formation. Avoiding this in engine design and operation requires physical understanding and accurate numerical tools and models. However, the mass-transport limitation during evaporation under non-boiling conditions and the coupling of heat and mass transfer makes film evaporation depend on many factors.

3.2.1 LIF imaging of fuel films

Experimentally, Mizomoto et al. [109] determined the lifetime of evaporating fuel droplets on a hot surface with a temperature higher than the liquid's boiling point already in the 70s. Stanglmaier et al. [110] manually measured the vaporization time of single and multi-component droplets on a heated surface under a variation of ambient pressure and excess temperatures (temperature difference between solid surface and boiling point of the liquid). They found that an increasing ambient pressure reduces the droplet vaporization time of single-component fuels when the excess temperature is positive due to a compression of the insulating fuel vapor layer between the liquid and the solid (Leidenfrost regime). For a negative excess temperature, the vaporization time increases with increasing pressure due to an increasing partial pressure of the fuel, limiting the convective mass transport. Measuring the vaporization time manually requires evaporation times above 0.5 s, which is unsuitable for thin films. To experimentally investigate the evaporation of thin films, evaporating rapidly, optical diagnostics become necessary. Schulz and Beyrau determined the lifetime of fuel films via high-speed visualization and investigated the effect of rail and ambient pressure on the evaporation duration of liquid fuel films in a pressure vessel [111].

To investigate the impact of evaporating fuel films in combustion as a source of soot formation, instantaneous two-dimensional detection of the film thickness is desirable. Candidate techniques for the imaging of thin liquid films are RIM and LIF. In RIM, a roughened transparent surface, such as a quartz window, is illuminated from the bottom and the backscattered light is captured with a camera. When a liquid, such as fuel, adheres to the top of the rough surface, the change in the refractive index and hence the intensity of backscattered light is less than when no fuel adheres to the surface. However, at a certain thickness the technique becomes insensitive to thickness because the film covers the surface roughness and scattered light is not detected anymore [101]. Typical detectable thicknesses are in the range of 0.03 to 3 μm . Maligne and Bruneaux compared the measured fuel-film thicknesses in a high-pressure cell via RIM and LIF (see below) and found results from the two techniques to be in a good agreement [112]. They also found the film to consist of "discrete structures" causing a faster evaporation of the film than without discrete structures.

Quantitative imaging of the film thickness with LIF requires the use of a fluorescent tracer added to a liquid surrogate fuel in small concentration. By judicious choice of the tracer concentration the dynamic range of the experiment can be adjusted to the expected range of film thicknesses. Lin and Sick compared the fluorescence properties of 3-pentanone and toluene as potential tracers dissolved in iso-octane as a surrogate [113]. They found that toluene co-

evaporates better with iso-octane and has higher FQY, which makes it more suitable for quantitative imaging. The general applicability of LIF for liquid film-thickness imaging has already been shown in several model experiments at atmospheric pressure [114-116]. The influence of ambient pressure and temperature, fuel temperature, rail pressure, and nozzle/wall-distance on fuel-film formation was investigated in further model experiments [117-123]. Figure 17a shows single shot images of the film thickness from different injection events and the evolution of the derived film mass on the right. The images clearly show the accumulation of fuel in the outer part of the wetted area due to the momentum of the impinging spray. The empirically observed hyperbolic dependency of the film mass versus time after start of injection (aSOI) was attributed to a decrease in the film area, reduced heat flux into the film due to cooling of the wall, and saturation of the ambient gas with fuel vapor.

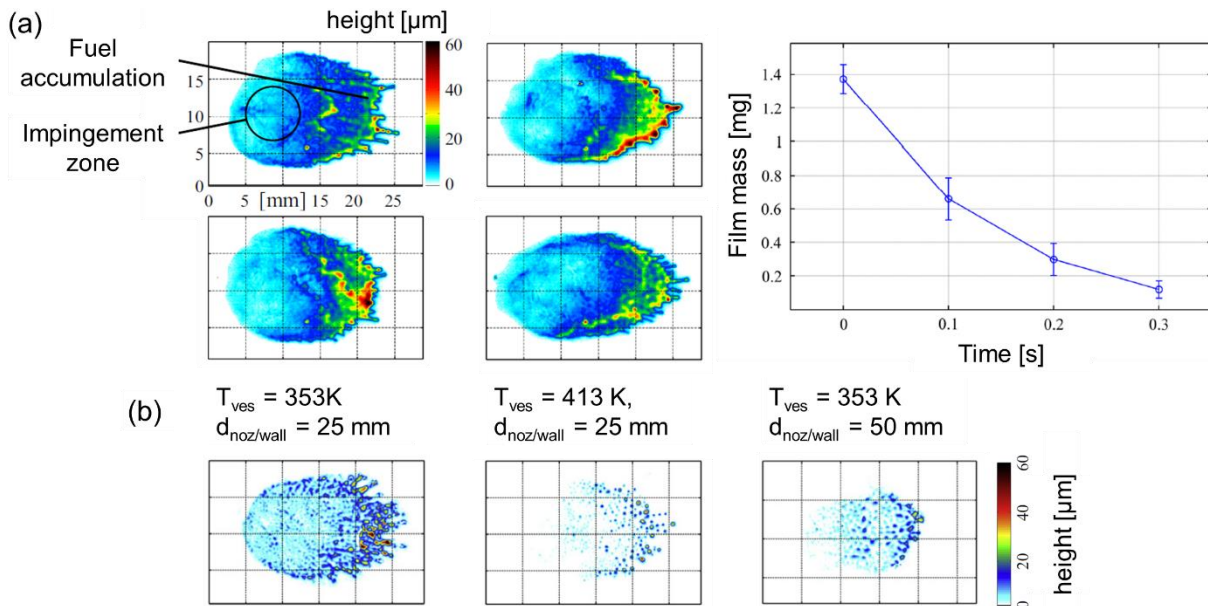


Figure 17: (a) Single shots of fuel-film thickness 3 ms after start of injection (aSOI) and fuel-film mass evolution. Vessel pressure 1 bar, vessel temperature 313 K, and rail pressure 150 bar. Error bars indicate the shot-to-shot fluctuations in the film mass. Adapted from [117] (b) Effect of vessel temperature and nozzle/wall distance on fuel-film formation for a rail pressure of 150 bar and a vessel pressure of 3 bar. Adapted from [118]. The fuel was iso-octane with 12% of 3-pentanone.

They found the fraction of fuel adhering to the wall significantly decreasing with increasing vessel temperature and nozzle/wall-distance, as shown in Figure 17b. Consistent with Senda et al. [56], they state that when reducing the impingement angle (the angle between a spray-cone's center axis and the wall plane) the film mass shrinks and the film area increases, resulting in decreased lifetime of the film compared to large impingement angles. Zheng et al. and Senda et al. investigated the effect of injection duration, impingement angle on the fuel-film thickness, area, and mass by RIM and LIF on flat surfaces, and compared the results to simulations [56, 124]. Li et al. imaged the film thickness with high-speed LIF to quantitatively investigate the formation of wave patterns and the secondary breakup of liquid films during spray impingement, as shown in the top of Figure 18. Here, a wave in the liquid film moves from 1300 to 1500 μs aSOI towards the leading edge of the liquid film and instead of completely spreading onto the wall, and the wave breaks up with detached liquid droplets splashing from

the liquid film. The bottom row of Figure 18 shows the propagation of a second wave which does not breakup under the detachment of droplets but simply expands the film due to the lack of a significant co-flow of air. This phenomenon brings the potential to reduce the film mass by the secondary atomization.

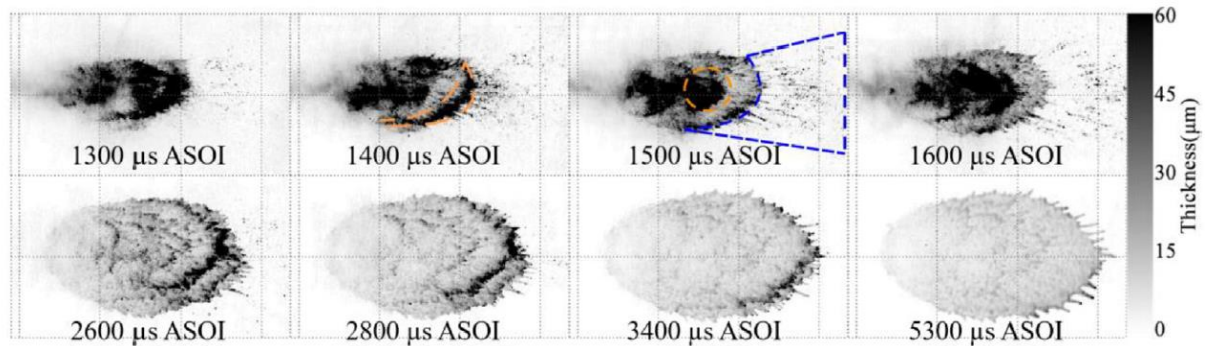


Figure 18: Fuel-film dynamics at different times aSOI (top) with film breakup from wave entrainment and (bottom) and without film breakup but wave propagation. Yellow markings indicate the first and second wave, blue marking indicates the wave-breakup region. Figure from [125].

Pointwise LIF measurements of the fuel-film-thickness were carried out under a variety of process parameters [126] and in the intake or combustion chamber of metal engines [127, 128]. Park et al. conducted simultaneous single-point measurements of fuel-film temperature and thickness in a SIDI engine by means of LIF [129]. The LIF-based temperature measurement exploited the red-shift of the fluorescence spectrum with increasing temperature. They found that the film temperature follows the piston temperature quite well during the cycle.

Quantitative LIF fuel-film imaging on the piston window of an optically accessible SIDI engine was recently performed by Geiler et al. [31]. An important outcome was that in LIF imaging of the liquid fuel-film, the interfering LIF signal from the gas phase is effectively suppressed by quenching by oxygen, unless stratification is extremely strong, like just after end of injection (aEOI). The LIF signal from the liquid toluene/iso-octane mixture was found to decrease with increasing temperature. Geiler et al. also systematically identified the determining parameters influencing the LIF of liquid toluene and other potential tracers [31, 130].

3.2.2 Numerical and theoretical investigation of film evaporation

Few multidimensional numerical studies exist on the quantitative prediction of fuel-film formation and evaporation [131-133]. Consistent with experimental studies, CFD simulations showed that a small impingement angle increases the fuel-film area and hence the evaporation rate [131]. The spray-wall contact and the formation of liquid fuel films were simulated and compared to measurements [132, 133]. Fuel-film area and thickness throughout the fuel film were in good agreement in measurement and simulation. In our previous work, results from CFD simulations and LIF imaging of the fuel films in an optically accessible SIDI engine were compared for sweeps in the operating conditions, including start of injection, injection pressure, as well as engine speed and load [134].

Karlsson and Heywood compared results from CFD with high-speed images of fuel-film formation and evaporation in an optically accessible SIDI engine [135]. Only 1% and 4%, depending on the piston temperature, of the injected fuel remained on the piston surface. Figure 19 compares the measured and simulated thickness distributions throughout fuel films from (a) Köpplé [136] for two different injection pressures and (b) Zhang et al [133]. The comparison shows that fuel-film thickness distributions are both qualitatively and quantitatively very similar in simulation and experiment. However, both simulations fail to predict the accumulation of fuel into thick fuel droplets.

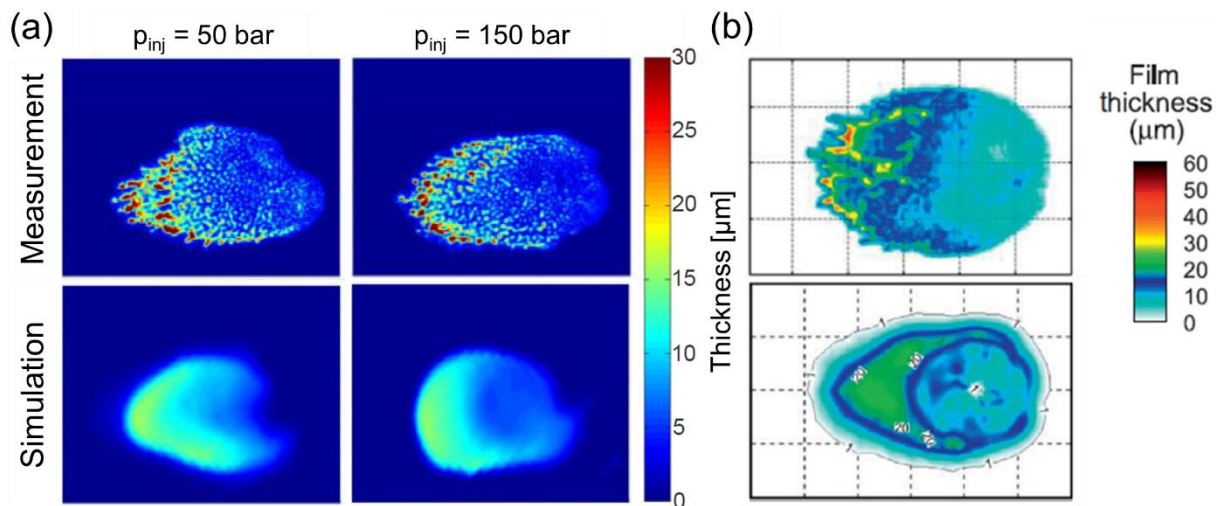


Figure 19: Comparison of measured and simulated fuel-film thickness images from (a) Köpplé [136] and (b) Zhang et al. [133].

Knowing the fuel-film temperature is essential for a quantitative analysis since both the evaporation rate and most tracers' photophysical properties depend on temperature. In this context, a low-dimensional model (LDM) was developed here, building on number of numerical and experimental investigations of wall-film heat transfer. The temperature of water films, ranging from 0.1 to 1 mm in thickness and with temperatures far below the boiling point was modelled one-dimensionally. Assuming the wall as adiabatic yielded a strong decrease of the film temperature until it reaches the wet-bulb temperature [137]. In a one-dimensional model of evaporating methanol films under engine-relevant conditions, the wall temperature was considered constant. This may be expected to yield an overprediction of the heat flux between wall and film and consequently the evaporation rate [138]. Assuming laterally uniform but time-dependent heat flux through the wall allowed for one-dimensionally modelling of a Diesel films' temperature and evaporation rate [139, 140]. Such models have also included the spray-wall interaction as well as the subsequent wall-film formation and evaporation, where the film temperature was calculated zero-dimensionally and was found to rapidly approach the surface temperature [133]. Evolutions of the temperature and evaporation rate of iso-octane fuel films were calculated. The gas phase was modelled one-dimensionally considering the diffusive flux of fuel into the concentration boundary layer and limiting heat transfer with the gas phase to conduction. In this model, the wall temperature that was considered constant strongly constrained the film temperature and thus the evaporation rate [141]. In terms of experiments, via infrared emission imaging the surface temperature of a plate was measured to decrease by

up to 14 K during spray impingement, converging rapidly towards a constant value aEOI [142]. The evaporation cooling of a wall as a consequence of spray impingement was further examined with phosphor thermometry. In some cases, the local temperature depression correlated well with local fuel-film thickness, indicating that (lateral) heat transfer parallel to the wall is low early aEOI [143]. A combination of CFD simulation and schlieren and Mie-scatter imaging was used to investigate the transient heat transfer during fuel-spray impingement on a hot wall [144-146]. A conclusion relevant for the current work was that is necessary to solve the transient conductive heat transfer within the wall instead of assuming a constant wall temperature in the boundary region (Dirichlet boundary condition) [146]. In a CFD simulation, Köpple found that the heat transfer between the impinging droplets and the wall is crucial for the initial fuel-film temperature and validated the predicted wall-temperature trace experimentally with thermocouples mounted slightly under the piston surface in an optically accessible engine [136]. The model from this work expands on those in the literature in simultaneously calculating the wall temperature (one-dimensionally) and film temperature (zero-dimensionally) throughout the film evaporation.

Table 2 summarizes the boundary conditions and findings of the discussed models. Indicated is the fuel, the initial film thickness d , the initial wall and air temperatures, T_w and T_{air} , the ambient pressure p , the heat transfer coefficient α as well as the range of temperature gradients ΔT_f through the fuel film between the wall and the gas/liquid-interface with a note on whether the film is being heated or cooled.

Table 2: Initial and operating conditions of low-dimensional film-evaporation models as well as calculated fuel-film temperature gradients.

Model	Fuel	$d / \mu\text{m}$	$T_w/T_{air} / \text{K}$	p / bar	$\alpha / \text{W}/(\text{m}^2\cdot\text{K})$	$\Delta T_f(t) / \text{K}$
Min and Tang	Water	100-1000	300/300	1	50-200	0.2-2 Cooling
Oliveira and Hochgreb	Methanol	100-500	361/317	3.75	-	~20-25 Cooling
Liye et al.	Diesel	30	400/1000	-	2000	24-78 Heating
Yan et al.	Diesel	20-50	350-500/ 800-1100	30-70	1000-2500	30-120 Heating
Zhang et al.	<i>n</i> -tridecane	~10	343/833	30	1000-10000	0 Heating
Tao et al.	Iso-octane	10	363/330	1-15	-	0 Heating

While most previous studies investigate the fuel-film formation characteristics and derive evaporation tendencies based on that, this work expands on previous work by using LIF

imaging and a CFD simulation to determine the film-thickness two-dimensionally as a function of time. Film mass and evaporation rate were determined from the results, compared, and analyzed for varying boundary conditions. Complementing that, an LDM of gas/film/wall heat transfer was developed. It yields the fuel-film temperature, which allows assessing some aspects of measurement uncertainty in the LIF measurement, and it gives additional insight into the heat transfer mechanisms near the fuel film.

3.3 Visualization of fuel vapor, PAH, and soot

As the fuel films evaporate, fuel-rich regions arise near the films. The visualization of the nearby gaseous fuel is desirable, since soot formation is most likely in these regions. Tracer LIF imaging of the gas phase is much more common than of the liquid phase, and an overview of the technique can be found in [53] and photophysical properties of selected tracers in [147, 148]. When pressure and temperature vary, quantitative LIF imaging becomes more difficult due to the dependencies of the LIF signal on these parameters. In isobaric and isothermal systems, tracer LIF in a gaseous flow gives information on the local fuel concentration [53]. A qualitative visualization of the fuel/air-mixing above evaporating fuel films was carried out by Alger et al. in an optical SIDI engine [108]. Schlieren imaging, a qualitative line-of-sight imaging technique, visualizes the mixing of the denser gaseous fuel with the surrounding air. Montanaro et al. visualized both the liquid and the gaseous fuel during spray-wall interaction in a quiescent chamber for different wall temperatures by schlieren and Mie-scatter imaging [144, 145].

When the premixed flame front reaches the fuel-rich regions in the fuel/air-mixture near the fuel films, it may turn into a non-premixed flame, producing soot. Several studies report an increased flame-quenching distance when the flame front approaches a fuel-wetted wall compared to a dry wall [149-151]. Tao et al. state that a flame propagating towards a vaporizing wall film is likely to be quenched due to locally high equivalence ratios and heat loss to the vaporization boundary layer. They found the quenching distance to be on the order of 20 to 200 μm for ambient pressures between 7 and 15 bar. Generally, higher ambient pressure and lower wall and film temperatures result in smaller quenching distances. Flame quenching occurred at a constant equivalence ratio throughout the investigated operating conditions [150]. As a result of flame quenching, temperatures in the quenched region might not be enough for a complete conversion from fuel vapor to soot but to PAH. Further away from the wall PAH are consumed to form soot.

However, even in simpler model experiments, how exactly solid-phase soot is formed from PAH, i.e., gas-phase species, is still barely understood. Some common optical diagnostics for soot are based on light extinction, elastic light scattering, and LII [152]. The LII signal is detected point-wise or two-dimensionally and is an approximate measure of the relative soot concentration f_v . In laminar diffusion flames, LII has been used to characterize soot and measure particle sizes or f_v [44, 153, 154]. Geigle et al. investigated the influence of turbulence on soot formation via LII imaging of f_v in a gas-turbine model combustor [155]. They found soot to be formed with high spatio-temporal intermittency.

Previous investigations of soot formation in IC engines mainly focused on Diesel engines. Notably, Dec et al. investigated the soot formation in Diesel engines with 2-D imaging of soot by LII [156, 157]. Dec conceived a conceptual model of the different combustion stages [158]. The cause-and-effect chain leading to engine-out soot emissions in a SIDI engine is much less investigated. Two-dimensional measurements of f_v [159] and particle size [160] were performed in SIDI engines by LII. In a spray-guided SIDI engine, de Francqueville et al. [159] measured a sharp decrease of f_v during the expansion stroke, most likely due to oxidation.

Most PAH have broadband optical absorption and fluorescence spectra that shift to longer wavelengths as PAH increase in the number of benzene rings [61]. This allows for size-dependent detection of PAH based on the excitation and detection wavelengths [152, 161]. While most of the PAH can be excited in UV, only a limited pool of PAH can be excited in the visible [162, 163]. However, the large variety of PAH, their broad spectra, and the dependency of these on temperature and local bath-gas composition so far have prevented a quantification of PAH concentration based on LIF [42, 152]. A species selective measurement of PAH is possible with ex-situ techniques like photoionization coupled with mass spectrometry or jet-cooled LIF [42, 152, 162]. Bejaoui et al. [162] found a shift of the PAH-LIF spectra to longer wavelength with increasing height above burner (HAB) in a Diesel spray flame, see Figure 20.

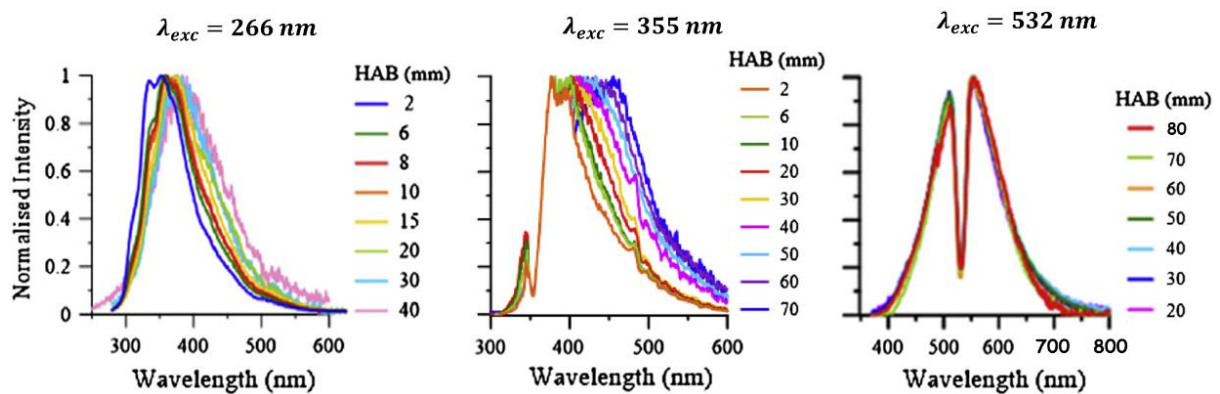


Figure 20: PAH-LIF spectra at different heights above the burner (HAB) in a Diesel spray-flame, excited at (left) 266 nm, (center) 355 nm, and (right) 532 nm. Figure from [162].

When exciting with 266 nm, the spectrum red-shifts around 40 nm from 2 to 40 mm HAB. At the same time, the absolute LIF signal decreases with increasing HAB (indicated by the noisy shape of the spectra at high HAB). That is caused by the consumption of small PAH and an overall decreasing PAH number-concentration. Interestingly, the spectra do not shift with increasing HAB in a premixed flame (not shown here) such that the shift is definitely not temperature induced. Sgro et al. states that the fluorescence around 250 to 380 nm upon excitation at 266 nm is attributed to aromatic species with 2-3 aromatic rings [164]. Ciajolo et al. attribute the broadband fluorescence emission in the VIS upon excitation at 266 nm to PAH with higher molecular weight or even condensed species [165]. Large PAH are expected to be excited to higher electronic states after excitation with 266 nm ($S_0 \rightarrow S_3$ or $S_0 \rightarrow S_4$ and fluorescence from $S_1 \rightarrow S_0$ around 500 nm [162]). The red-shift of the spectrum is more pronounced with excitation at 355 nm where PAH LIF is detected even at 70 mm HAB. Therefore, it is assumed that small PAH with 3-4 aromatic rings are detected at low HAB and large PAH at 70 mm HAB. Excitation with 532 nm does not show a significant shift of the

spectrum with increasing HAB. Predominantly similar (and large) PAH species are being detected when exciting with 532 nm [162], indicated by the similar fluorescence spectra. Nevertheless, according to the existing literature, excitation at 532 nm leads to the emission of a multitude of different PAH. Long chain PAH with more than five aromatic rings [162], incipient particles [152], being condensed matter or small solid particles, 5-membered ring PAH [163, 165, 166], which occur at high concentrations, and dimers of PAH [161] may contribute to the signal. However, Wang [167] stated that dimers of PAH are unstable at flame temperatures. In the 90s, D'Alessio et al. [43] and Dobbins et al. [168] observed the existence of 2-4 nm non-soot nanoparticles in a rich premixed ethylene/oxygen and in a nonsmoking ethene diffusion flame, respectively. D'Alessio et al. reported that those particles are strong absorbers in the UV but transparent in the visible and described them as polymer-like structures containing sub-structures with aliphatic aromatic (2-3 ring) bonds. Dobbins et al. described them as layers of fully condensed large PAH and stated that they are supposed to absorb in the visible.

Several studies report the visualization of PAH LIF and soot LII in laminar diffusion flames [169-173]. Figure 21 shows (a) images and (b) axial profiles of OH LIF, soot LII, and PAH LIF, excited with a laser light-sheet at 248.5 nm, in the center plane of a laminar propane diffusion flame (see caption for excitation and detection details).

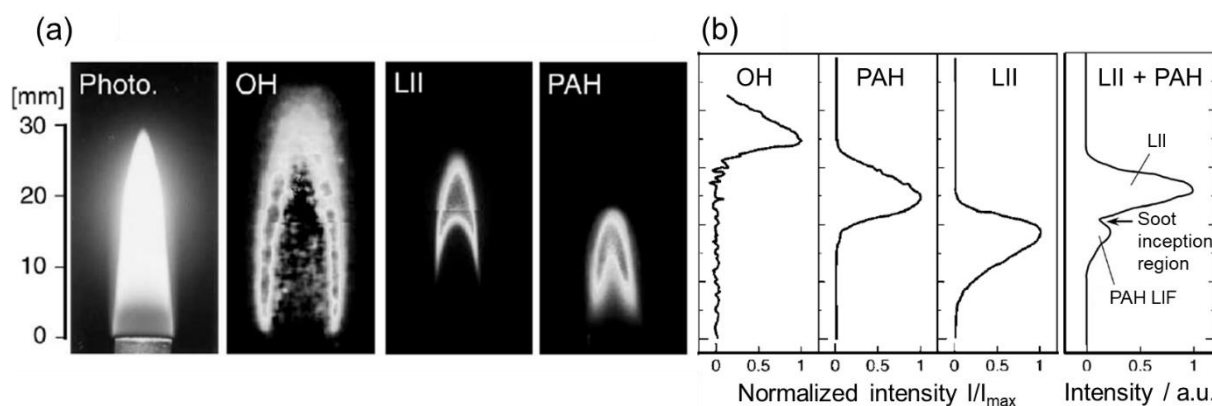


Figure 21: (a) Photography of flame luminosity and images of OH LIF, soot LII, and PAH LIF. (b) Axial profiles of OH LIF, soot LII, PAH LIF, and LII + PAH LIF. Excitation of OH LIF, soot LII, and PAH LIF with 248.457 nm and detection with a bandpass filter 296.5/10. Excitation of soot LII and PAH LIF additionally with 248.469 nm with delayed and prompt detection with a longpass filter. Global intensity correction and suitable image subtraction results in isolated images of OH LIF, soot LII, and PAH LIF. Adapted from [171].

PAH are generated close to the nozzle exit and found completely inside the flame within in the fuel-rich region. The peak of PAH LIF coincides with the region where soot LII begins to appear and diminishes when soot LII peaks. LII disappears when OH LIF peaks. The results indicate that PAH form in the fuel-rich region, that their concentration increases towards the soot inception region. OH is detected around the outer edge of the flame and oxidizes the soot. The radial distribution of the three signals is analog to the axial distribution. Vander Wal et al. found a similar gradation of PAH LIF and soot LII in an ethylene diffusion flame and also attributed the local minimum or “dark zone” in the overlay of the two signals to the soot inception region [170]. By changing the detection bandpass-filter from 400 to 500 to 600 nm (each with 70 nm

bandwidth), they found the PAH-LIF region approaching the soot-LII region. The explanation is the increasing size of PAH being detected at longer detection wavelengths.

In a non-premixed laminar co-flow flame, Bennett et al. [174] visualized the stratification of PAH LIF, excited with 282.85 nm, by spectral variation of the detection filter, see Figure 22a. An increase in pressure from 8 to 16 bar clearly shows a compression of the soot-precursor region towards the burner nozzle due to the increasing fuel-pyrolysis rate [174, 175]. At the same time, the overlap with the region of soot luminosity shrinks. Therefore, in particular a high-pressure applications it is expected that different size classes of PAH can be visualized by varying the detection filter-band with little interference from soot luminosity or LII.

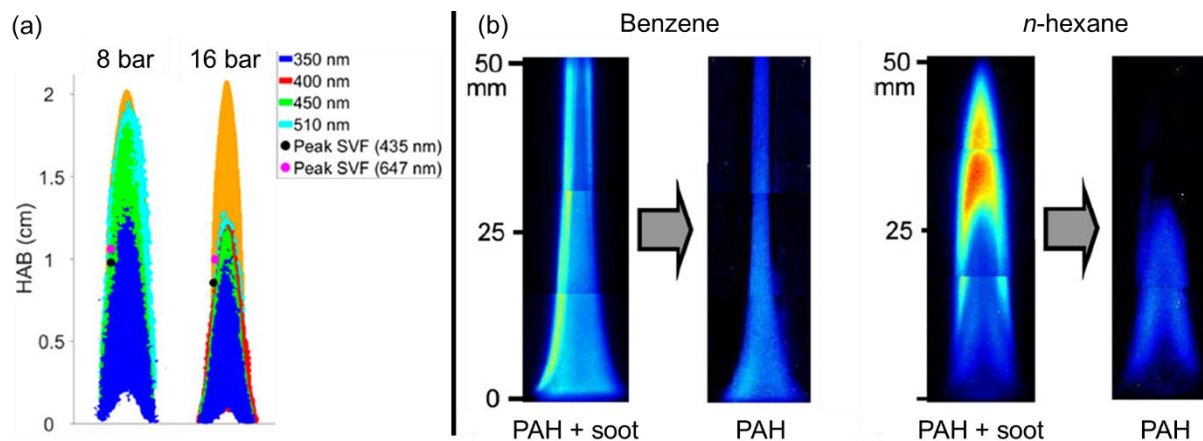


Figure 22: (a) Zones of different PAH LIF and maximum soot volume fraction (Peak fV) by varying the detection wavelength at 8 and 16 bar ambient pressure. Orange shows area of soot luminosity. Adapted from [174]. (b) PAH LIF in diffusion flames above liquid fuel pools of (left) benzene and (right) hexane. Adapted from [176].

Kobayashi et al. [176] excited PAH LIF and soot LII with 248.5 nm in laminar diffusion flames above liquid pools of aromatic and aliphatic fuels, see Figure 22b. For the aromatic fuel, in this case benzene, soot formation starts right on the liquid's surface due to the rapid growth of PAH from petrogenic benzene. The soot-inception zone, the overlap of PAH and soot, is shaped as an inverted cone which exceeds the top of the image. In contrast to this, the hexane flame shows a flame with a closed tip, which indicates the complete oxidation of PAH and soot by high OH concentrations (there are twice as many H atoms per C atom in hexane as in benzene).

Other studies simultaneously visualized PAH and soot in turbulent combustion. Hayashi et al. demonstrated simultaneous imaging of Mie scattering, PAH LIF, and soot LII in a laboratory-scale pulverized coal flame [177]. Bouvier et al. imaged OH LIF, PAH LIF, and soot LII in a swirl burner with stratified premixed flame [38]. Geigle et al. visualized PAH excited at 283 nm and soot LII excited at 1064 nm, in a turbulent, pressurized flame in a gas-turbine model combustor [42]. They identified PAH clouds well isolated from soot filaments. Lemaire et al. [178] found soot precursors excited at 532 nm and soot excited at 1064 nm spatially separated in turbulent combustion of Diesel vaporized into a methane flame. In the central fuel-rich region of Diesel combustion, Aizawa et al. [179] found PAH LIF excited at 355 nm after the premixed combustion and before soot LII, surrounding the PAH. In an optically accessible Diesel engine, soot LII excited at 1064 nm was simultaneously visualized with different size-

classes of PAH by varying the excitation wavelength from 266 to 355 to 532 to 633 nm [180-182]. Li et al. found that the region where presumably large PAH were excited at 532 and 633 nm partially overlapped with the soot region. Figure 23 shows typical results [182]: The ensemble-average images of PAH LIF and soot LII indicate soot with a higher spatial intermittency compared to the more homogeneously distributed PAH. PAH LIF excited with 633 nm spatially overlaps with soot LII more than PAH LIF excited with 355 nm. This indicates that large PAH (> 10 aromatic rings) excited with 633 nm directly participate in soot nucleation in contrast to small PAH (2-4 aromatic rings) excited with 355 nm [182]. Most of the soot is already oxidized at 366°CA, thus 14°CA or 2 ms before EOI, whereas the spatial extent and the intensity of the PAH-LIF cloud, in particular for excitation with 633 nm, remain unchanged.

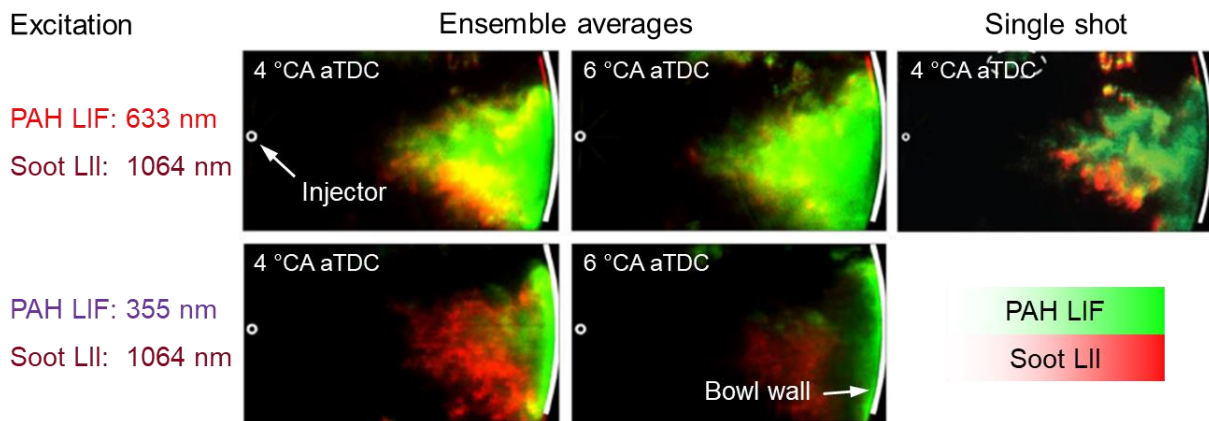


Figure 23: Ensemble averages and a single shot of PAH LIF (green, excited with 355 or 633 nm) and soot LII (red, excited with 1064 nm) at 364 and 366°CA. n-heptane was injected at 800 bar from 350 to 380°CA. Adapted from [182].

The current work expands on these previous studies by combining PAH LIF and soot LII in the context of GDI and evaporating fuel films. To obtain complementary information, high-speed color imaging of the spray, chemiluminescence, and soot luminosity was performed. The experiments were mainly conducted in a constant-flow chamber at atmospheric pressure, with some preliminary measurements in a sooting laminar co-flow flame.

4 Fuel-film evaporation

This chapter discusses methods and results of fuel-film imaging and evaporation. The diagnostics were developed and applied in a constant-flow facility with an optically accessible test section, which is considered a direct-injection model experiment. First, the experimental apparatus is introduced. The flow-field characterization and preliminary measurements on the co-evaporation and photophysical properties of the fuel are discussed. Then, results from LIF on fuel-film thickness imaging are presented from which fuel-film masses and evaporation rates are calculated. Some of these experimental results are compared to results from a CFD simulation. A LDM is presented which yields the transient fuel-film and wall temperatures. The model gives additional insight into the heat transfer mechanisms near the fuel film. Parts of the content was published by Jüngst et al. [96-98], in particular Sections 4.1, 4.3.1, 4.3.3, 4.4.1, 4.5.1, 4.5.2, 4.6, and 4.7.

4.1 Experiment

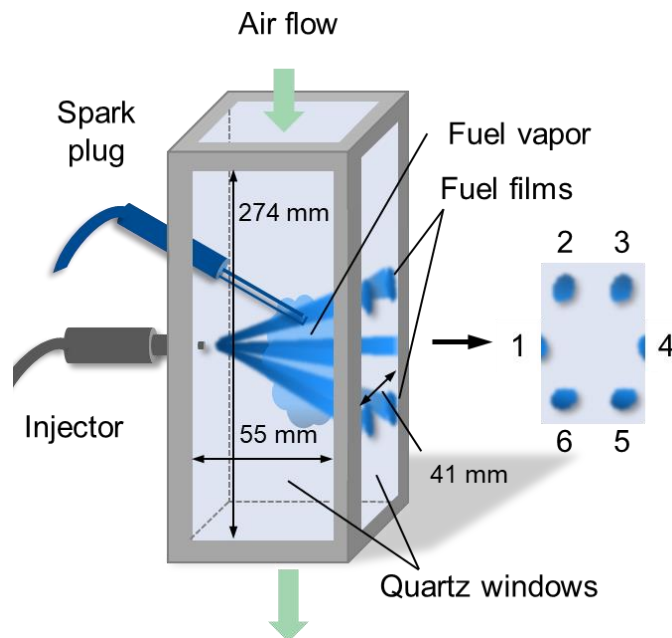


Figure 24: Optically accessible test section of the constant-flow facility with the insert on the right showing the numbering scheme for the fuel films. Figure published in [97].

The optically accessible part of the constant-flow facility is shown in Figure 24. Hot air at atmospheric pressure flows from top to bottom with a mean velocity of 1.8 m/s. A stack of perforated plates and fine wire meshing (approximate hole or mesh size 2 mm × 2 mm) upstream between the air heater and the test section creates small-scale turbulence and a more uniform bulk flow. The test section has a square cross-section of about 5.5 · 5.5 cm². Three of the side walls are from quartz, while the fourth one is from aluminum. A six-hole injector protrudes through this wall, with four of the six sprays impinging on the window on the opposite side, forming fuel films number 2, 3, 5, and 6. The remaining two sprays impinge mainly on the metal frame next to the quartz window. The impingement distance (the distance between the nozzle tip and the wall along the spray axis) is 39 mm for films 5 and 6, and 47 mm for films 2 and 3. However, most of the fuel evaporates into the air, forming a fuel/air-mixture.

Spark electrodes above the injector (see Figure 24) ignite the fuel/air-mixture 0.7 ms aEOI). Therefore, the experiment employs a combination of a spray-guided and wall-guided direct-injection strategy. The latter is known to potentially lead to increased soot formation [183].

Table 3 gives an overview of the operating conditions in the fuel-film imaging experiments. Iso-octane was chosen as a surrogate fuel since it is non-fluorescing and has a boiling point roughly in the middle of the boiling curve of gasoline. Parameters that were varied in the experiments are the flow-facility temperature, the air flow velocity, the injection duration, and whether the film evaporates in a combusting environment or not. The air, wall, and injector temperatures cannot be controlled independently but follow the air temperature as given in Table 3. The average flow-velocity was determined as follows. The flow velocity at the entrance of the constant-flow facility, far upstream of the test section, was measured with an anemometer. From that, the volume flow was calculated. By taking volume conservation into account and neglecting pressure loss over the distance to the test section, the average flow-velocity within the test section was calculated and is indicated in Table 3.

Table 3: Operating conditions for the flow-facility experiments.

Fuel	Iso-octane + 1%/10% toluene
Injector	Six holes
Rail pressure	100 bar
Injector/fuel temperature	361 K (339 K, 350 K, 300 K)
Injection duration	0.5 ms (4.6 mg), 1 ms (9.3 mg)
Air temperature	381 K (340 K, 361 K, 300 K)
Air flow velocity	1.8 m/s (3 m/s, 6.5 m/s, 10 m/s)
Back pressure	1 bar
Quartz wall temperature	352 K (332 K, 342 K, 300 K)

This model experiment has some of the salient features of SIDI engine combustion but is also simplified and thus less realistic in others. It mimics part-load conditions of a SIDI engine with a stratified mixture, i.e., injection during or at the end of compression, temporally close to the ignition, resulting in substantial fuel-film formation. The combustion strategy of the experiment can be considered a combination of spray-guided and wall-guided direct injection. Obviously, the main difference in our model experiment is that the pressure is atmospheric, and therefore lower than in real engine combustion, and constant. Bulk flow velocities are also somewhat lower. The temperature range was chosen to investigate the evaporation of liquid films under non-boiling (mass-transport limited) conditions. Although piston temperatures are expected to be higher in SIDI engines, also pressures are, the fuel-film temperature is most likely also below the fuel's boiling point.

4.2 Flow characterization

To characterize the flow within the test section more precisely than with average velocities, and for a more informed interpretation of the upcoming results on fuel-film evaporation and soot formation, results on the gas-velocity fields in steady-state and transient operation are

presented. The steady flow, induced by the laboratory exhaust system, was measured with PIV. Separately, transient flow velocities at times short aEOI were measured by optical flow of fuel-vapor LIF.

4.2.1 Optical layouts for PIV and optical flow

Figure 25 shows the optical layouts for PIV and optical-flow measurements. It should be considered that PIV and optical flow were performed in separate experiments. The stack of perforated plates with fine wire meshing (in the following simply called grid) is indicated above the test section. Laser pulses from an Nd:YAG-laser (Litron, Nano L PIV Series) at 266 nm and 532 nm were horizontally focused by a positive cylindrical lens ($f = 400$ mm) and vertically opened up by a negative cylindrical lens ($f = -25$ mm) into light sheets. To also capture the three-dimensionality of the flow field, both techniques were applied within three distinct planes in the test section. The light sheets intersected the fuel films 2 and 6 in plane A and films 3 and 5 in plane C. Plane B was the central plane.

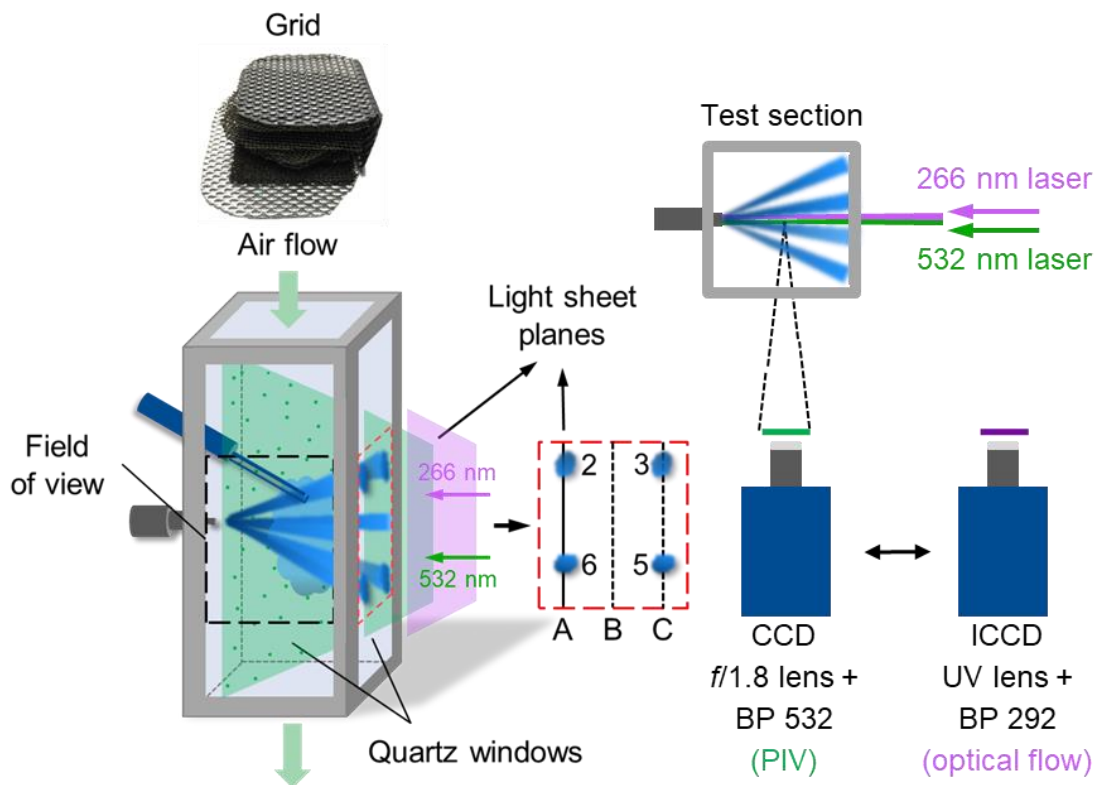


Figure 25: Optical layouts for flow-velocity measurements with PIV (green) and LIF (purple). Light-sheet planes are also indicated.

For PIV measurements, particles were generated with an aerosol generator (LaVision). In that device, pressurized air flows over a liquid pool of oil (Bis(2-ethylhexyl) sebacate) and entrains droplets following the air flow. The particle-laden flow was seeded to the constant-flow facility around 0.5 m upstream between the air heaters and the test section. A CCD camera with a $f/1.8$ lens (Nikon) and a bandpass filter centered at 532 nm (Semrock, 532/18 nm BrightLine) captured Mie-scattered light from the droplets. The temporal delay Δt between the two images was 250 μ s such that particles moved around 10 px between the two frames. 200 image pairs were acquired for each plane with a repetition rate of 15 Hz.

For optical-flow measurements, iso-octane was used as a surrogate fuel and doped with 10 vol.-% of toluene. Laser pulses at 266 nm excited LIF of the toluene. An intensified CCD camera with a UV lens (Cerco, $f = 45$ mm, $f/1.8$) and a bandpass filter BP 292/27 centered at 292 nm (Semrock 292/27 BrightLine HC) captured LIF of the fuel vapor. The fast decay time of the image intensifier's phosphor screen (P46) enabled a minimum delay time of 220 μ s between two frames. The temporal delay between the two laser pulses and frames was set to 300 μ s which was still long enough for the comparatively slow timescales in the test section. Again, 200 image pairs were acquired for each plane. The time between two image pairs was 2.5 s, long enough to flush the fuel vapor from the test section. For the two measurement techniques, PIV-postprocessing in the software DaVis 8 (LaVision) was used with the parameters given in appendix A2.

4.2.2 Flow fields in steady-state and transient operation

Steady-state operation

Figure 26 shows ensemble averages of 200 velocity fields and a single velocity-field in planes A, B, and C in steady-state operation, measured via PIV. For plane A, the velocity fields are shown with and without the grid inserted. Locations of the injector, the spark electrodes and the quartz wall on the opposite side are also indicated. The background color denotes the velocity magnitude. The vector length is uniform and indicates the direction of the flow.

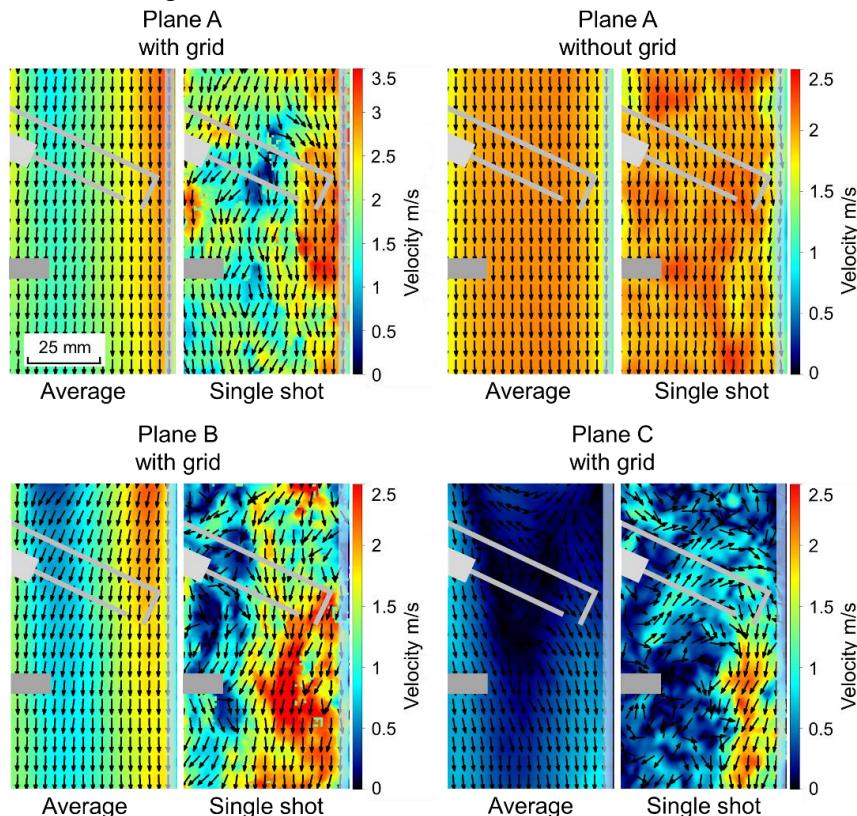


Figure 26: (Left) Ensemble averages of 200 velocity fields and (right) single velocity-field in planes A, B, and C. In plane A with and without grid.

Ensemble averages indicate the downstream directing flow, especially in planes A and B. The images acquired without grid suggest an axisymmetric plug flow, which is according to the

average Reynolds number of 5500 in the transition regime between laminar and turbulent. Here, the single shot shows only slight variation in the flow direction and velocity magnitude throughout the flow field compared to the average. With the grid inserted, the single shots reveal that the flow has much small-scale structure and strong variations in direction and magnitude of the flow velocity. Generally, the small-scale structure is desired for presumably enhanced mixing of the air flow with the injected fuel. The standard deviation of the velocity in plane A (not shown here) indicates an increase from 0.2 to 0.6 m/s when inserting the grid.

The ensemble average velocity-fields from different planes indicate the following features in the flow. Maximum average velocities are in the range of 3.2, 2.3, and 1.1 m/s in planes A, B, and C, respectively. Apparently, the pressure loss at the grid increases from plane A to C, inducing the observed large-scale velocity gradient. In planes A and B, the maximum velocities are reached around 7 mm from the quartz wall on the right side. In plane C, the velocities are of comparatively small magnitude and a recirculation zone is detected in the top of the test section. In conclusion, the turbulence grid appears to cause an additional pressure loss and thus an on average slower flow through the test section. However, the grid fulfills its purpose of sustaining comparatively high flow velocities near the wall in plane A (1.9 and 2 m/s with and without grid, respectively) while presumably enhancing fuel/air-mixing by inducing small-scale turbulence at the same time. The results discussed below were obtained with the grid inserted.

Transient operation

Figure 27 shows results from the optical-flow measurements, acquired from 1.2 to 15 ms aSOI without combustion. The injection ends 1 ms aSOI. Ensemble averages and single shots (from individual injections) of the velocity fields in plane A are shown and ensemble averages from planes B and C. Here, the color and the length of the arrows indicate the velocity magnitude. The LIF signal from fuel vapor and films is indicated in grayscale in the background.

At 1.2 ms aSOI, the injection has just ended, and the sprays still propagate through the test section. At that time, a reliable calculation of velocities is prevented by the propagation of the sprays transverse to the imaging plane and the comparatively long Δt between the two image frames. At 3 ms aSOI, flow velocities of above 5 m/s are detected above film 2 in plane A. The fuel-vapor plume rebounds from the wall and is transported downstream convectively by the background flow. In plane B, the flow appears to form a vortex close to film 2 with a mean velocity of 2-2.5 m/s. The vortex forms from the vapor moving upstream very close to the wall but then being entrained towards the core of the flow, eventually moving downstream. At the same time, in the bottom of the test section velocities are on average lower and prominent in the wake of sprays 5 and 6 in all three planes. At 6 ms aSOI, the vapor plumes propagate towards the core of the test section, and velocities are significantly higher in the top than in the bottom throughout all planes. In plane A, the flow direction on average homogenizes in the top due to the incoming flow while the vortex in plane B persists. At 9 ms aSOI, the constant flow more and more “flattens” the injection-induced flow and eliminates the fluctuations in the velocity, resulting in a mostly downstream directed flow in all three planes. At 15 ms aSOI, the magnitude of the flow velocities again approach those measured with PIV in steady state in all planes. However, near the wall the flow velocities are slow. In contrast to the steady-state

operation, in plane A the highest velocities in the top are now measured near the left edge of the image. Additionally, the recirculation region in the top of plane C, detected with PIV (see Figure 26), seems not to have evolved yet.

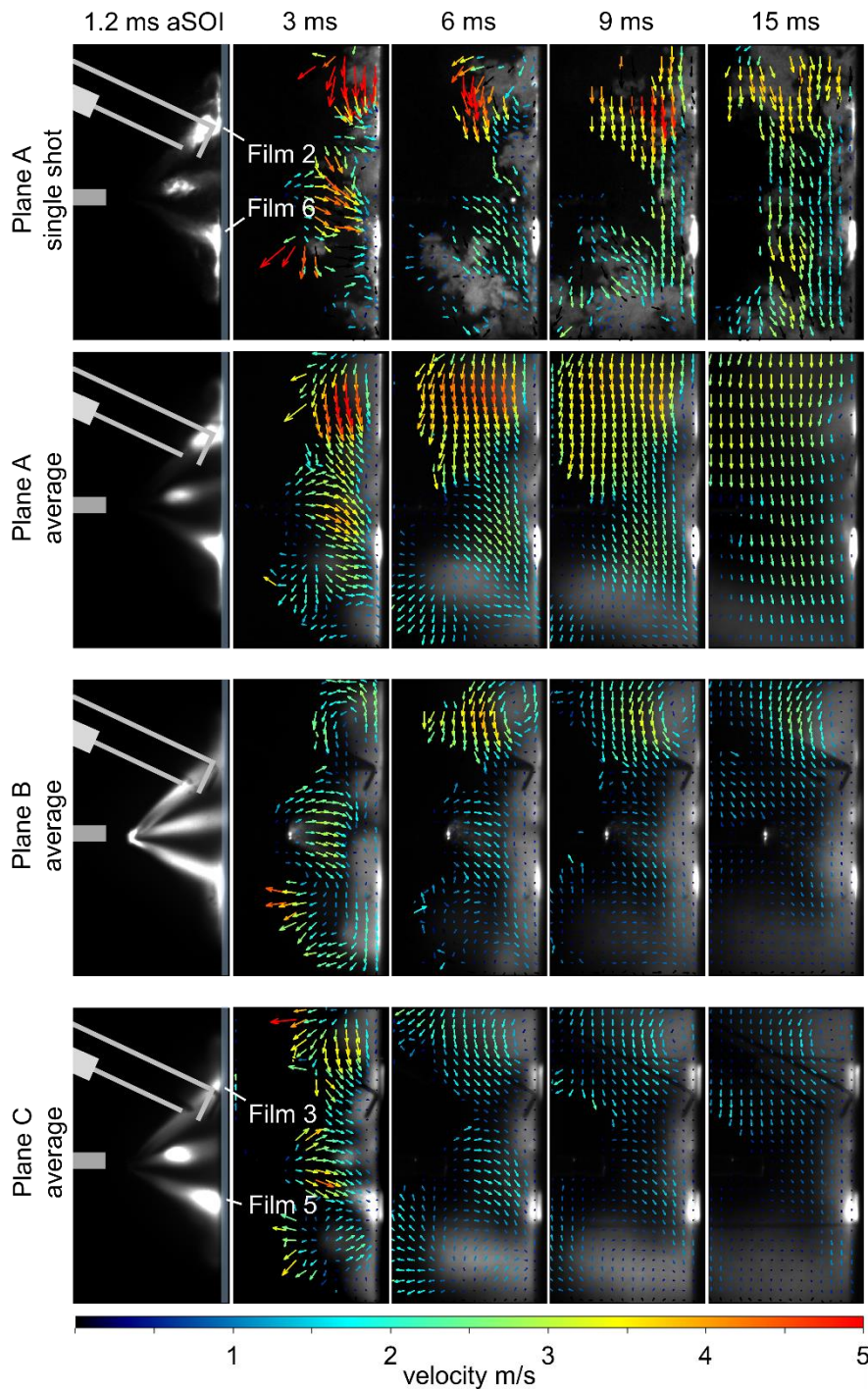


Figure 27: Ensemble averages of 200 velocity fields and single velocity-fields in planes A, B, and C without combustion at different times aSOI. $T_w = 352$ K, $v_{\text{air}} = 1.8$ m/s, $m_{\text{inj}} = 9.3$ mg, without combustion.

Figure 28 shows a time series of ensemble averages and single shots of velocity fields in plane A when combustion is initiated. Ignition of the fuel/air-mixture was 1.7 ms aSOI. The lack of vectors around the spark electrodes at 3 ms aSOI is attributed to the emerging flame front in

this region, burning the fuel vapor and evaporating the seeding droplets. Apart from that, flow velocities are of similar magnitude in the top and bottom compared to the case without combustion. At 6 ms aSOI, the spatial extent of the flame front increases such that the region without vectors further grows. From 9 to 15 ms aSOI, the flow velocities are significantly higher compared to the case without combustion. Also, highest velocities are here detected in the center and bottom of the field of view (FOV). Apparently, at 9 ms aSOI, the rapidly emerging flame front pushes the remaining fuel vapor towards the core of the test section from where it is accelerated to up to 6 m/s downstream. The velocities again decrease at 15 ms aSOI, approaching the steady state flow-velocities.

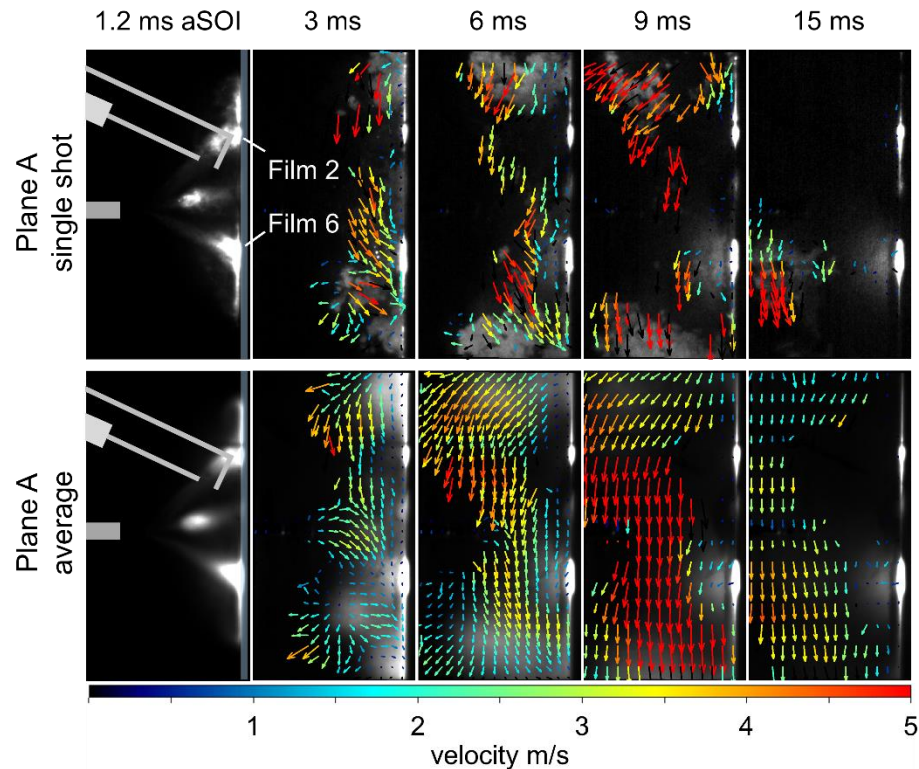


Figure 28: Ensemble averages of 200 velocity fields and single velocity-fields in plane A at different times aSOI. $T_w = 352$ K, $v_{\text{air}} = 1.8$ m/s, $m_{\text{inj}} = 9.3$ mg, with combustion.

4.3 Fuel-film imaging

The physical properties of tracer and surrogate fuel for fuel-film imaging as well as their co-evaporation characteristics are subject of this section. The optical layout for fuel-film LIF is presented.

4.3.1 Tracer and surrogate fuel

Commercial fuels contain many different components that fluoresce when excited by UV lasers. Every component has different photophysical properties, meaning that the LIF signal of each component depends among others on temperature, pressure, and bath gas composition. Therefore, it is very difficult to derive quantitative information, such as species concentration, from the total detected signal, which is the sum of the individual contributions. For quantitative LIF imaging of fuels, a mixture of a fluorescent marker and a non-fluorescing surrogate is

usually chosen [53]. In this work iso-octane (boiling point: 372 K) was chosen as the non-fluorescing surrogate, and toluene (boiling point: 384 K) as the fluorescent tracer. The tracer should co-evaporate with the surrogate and exhibit similar properties in terms of viscosity, diffusivity, and surface tension [53]. Co-evaporation is required so that the fraction of the tracer is same in liquid and gaseous fuel. Also, the spectral properties of the tracer, the dependence of the LIF signal on temperature, pressure, and bath-gas composition need to be known for quantitative measurements [59]. Toluene mostly fulfills these requirements. For LIF imaging, the volume fraction of toluene in iso-octane was 1 vol.-%. Since the tracer number density was about 2500 times lower in the gas phase and quenching by oxygen also leads to strong signal decrease in fuel-vapor imaging, here the tracer volume fraction was 10 vol.-%. Figure 29 shows the fluorescence spectrum of toluene dissolved in liquid cyclohexane and upon excitation at 266 nm [61]. Also, the transmission of the LP 266 (Semrock 266 nm RazorEdge), blocking laser stray light, and BP 292/27, isolating the toluene fluorescence from background fluorescence, are shown [184, 185].

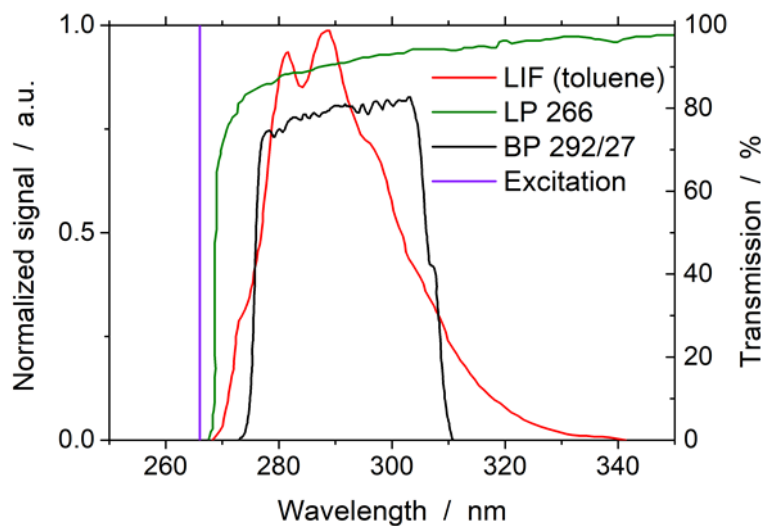


Figure 29: Fluorescence spectrum of liquid toluene, excited at 266 nm [61], and transmission of filters used for LIF (toluene) [184, 185]. Figure published in [96].

4.3.2 Co-evaporation

In preliminary experiments, the co-evaporation of iso-octane and toluene was investigated. An ideal co-evaporation would be obtained if the two species evaporated to equal fractions (as present in the liquid fuel). The difference in the boiling temperatures of iso-octane (372 K) and toluene (384 K) at ambient pressure is 12 K. That might promote the preferential evaporation of iso-octane which would alter the composition of the remaining liquid fuel. Here, mixtures with 1 vol.-% toluene/99 vol.-% iso-octane and 10 vol.-% toluene/90 vol.-% iso-octane, as used for fuel-film and fuel-vapor imaging, respectively, were investigated. Figure 30a shows the experimental setup. A glass cylinder with 400 ml of the iso-octane/toluene-mixture was magnetically stirred on a heated plate at a temperature of 353 K (almost equal to the quartz-wall temperature). The evaporation rate in that experiment was slightly lower compared to the one in thin film-evaporation such that the effect of toluene enrichment in the remaining liquid is expected to be stronger here. The laboratory exhaust system constantly removes the emerging

fuel vapor about 1 m above the experiment. A sample was taken from the remaining liquid after 25, 50, 75, and 95% of the liquid fuel had evaporated. The samples were diluted with iso-octane by a factor of 1000. Then, their UV transmission I_t was measured in a cuvette with an absorption path length l of 10 mm in a UV/VIS-spectrophotometer (Varian, Cary 400). According to Beer-Lambert law, see equation (27), the absorbance A of the samples was calculated:

$$A = -\ln\left(\frac{I_t}{I_0}\right) = \varepsilon^* c l \quad (38)$$

Since the extinction coefficient and the absorption path length are constant throughout all samples, the absorbance is a measure of the relative change in toluene concentration. Figure 30b shows the resulting absorption spectra of the two mixtures in the UV.

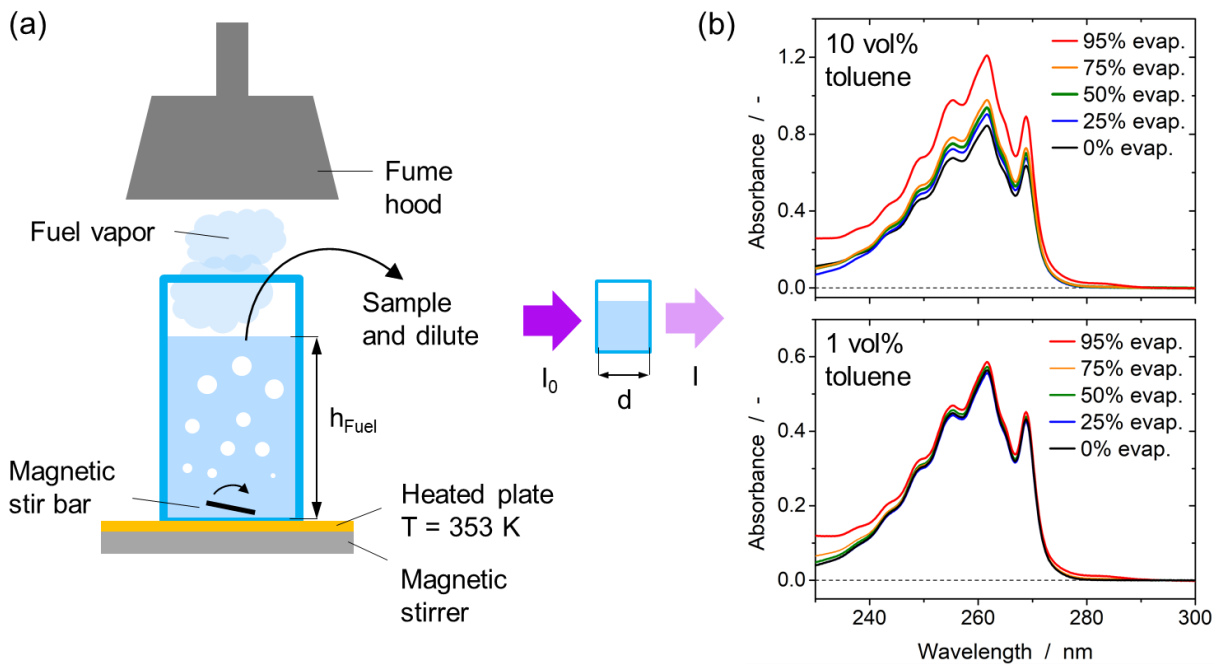


Figure 30: (a) Experimental setup for mixture evaporation on a heated plate. (b) Absorbance spectra of toluene/iso-octane samples after 0, 25, 50, 75, and 95% have evaporated.

The absorbance spectra of each mixture were normalized by the spectrum of the sample in which 0% had evaporated. The normalized absorbances were averaged from 250 to 270 nm since the absorbance changes about the same factor at every wavelength. The result is shown in Figure 31. The relative change in the average absorbance then equals the relative change in the toluene concentration. The mixture with 1 vol.-% toluene, which is used for fuel-film imaging, does not show a significant change up to an evaporated volume of 75%. When 95% of the liquid have evaporated, the toluene concentration has increased by 5% compared to the initial mixture. For the mixture with 10 vol.-% of toluene, the toluene concentration linearly increases about 6, 10, and 15% with the 25, 50, 75% evaporated, respectively. When 95% of the mixture have evaporated, the toluene concentration has increased by 43%.

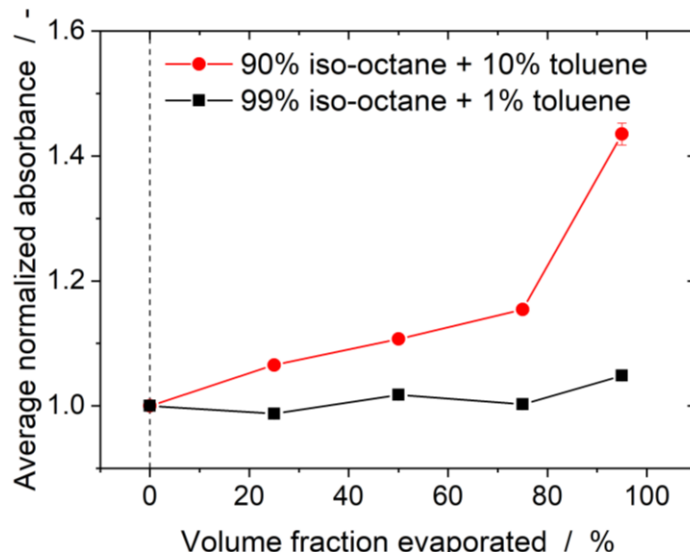


Figure 31: Normalized absorbance, averaged from 250 to 270 nm, after 0, 25, 50, 75, and 95% have evaporated of mixtures with initially 1 vol.-% toluene and 10 vol.-% toluene. Error bars indicate the standard deviation in the normalized absorbance among 250 to 270 nm. For most data points the standard deviation is less than the size of the data points

4.3.3 Optical layout

The experiment for fuel-film imaging is shown in Figure 32. A Pellin-Broca prism separated the fourth harmonic (266 nm) from an Nd:YAG laser (Litron, Nano L PIV Series) from the remaining second harmonic (532 nm).

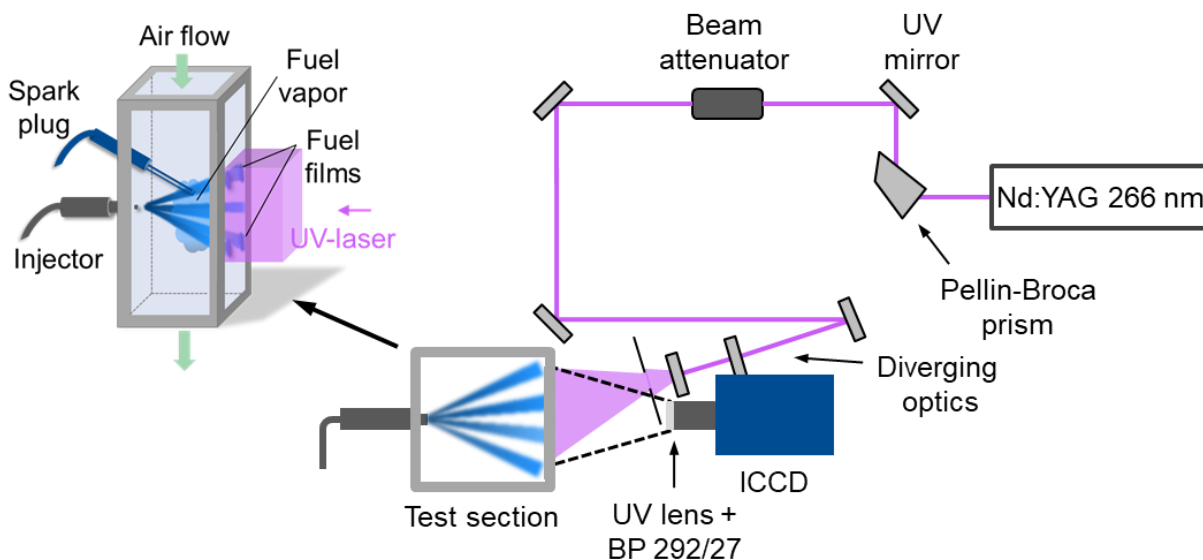


Figure 32: Optical layout for fuel-film LIF. Modified versions of this Figure published in [96, 98].

The pulse energy was adjusted by a dielectric beam attenuator. Two UV mirrors deflected the beam towards the test section. A negative spherical lens ($f = -100$ mm) and a negative cylindrical lens ($f = -120$ mm) expanded the beam vertically and horizontally. An aperture clipped the UV laser so that only the region of interest (ROI) of the quartz wall was illuminated. The fluorescence was imaged by a UV lens (Cerco, $f = 85$ mm, $f/4$) on an intensified CCD camera (LaVision, Intensified Relay Optics + Imager Intense), indicated by the dashed lines in

Figure 32. A bandpass filter, BP 292/27, blocked laser stray light and spectrally further narrowed the detection region to suppress background fluorescence from the aluminum back plate of the test section, the injector tip, and the electrodes. The projected pixel size was 0.09 mm/pixel. The time between two images was 2.5 seconds and hence long enough to entirely evaporate the fuel film and flush the fuel vapor from the test section, such that each image shows an individual injection at a certain time aSOI.

4.4 Calibration and image quantification

Strategies on the in-situ calibration of the LIF signal versus the film thickness, the correction of influences from temperature and dissolved gases on the tracers' photophysics, and on the image quantification are presented in this section.

4.4.1 Thickness calibration

For absolute calibration, fuel films with a range of thicknesses were established in a purpose-built thin-film cuvette (calibration tool), shown in Figure 33a. Thin precision shims created a gap of known distance between a black back wall and a quartz plate, shown in the sectional view in Figure 33a. The gap was filled with the iso-octane/toluene mixture and a quartz plate pushed onto the precision shims and an O-ring (Viton gasket) surrounding the cavity by the silver holder plate. Thus, a fuel film of known thickness was created between the two shims. This calibration tool was mounted just behind the quartz-wall to perform an in-situ calibration with excitation, collection, and detection efficiencies locally equal to those in fuel-film imaging. The image in Figure 33b shows the detected LIF intensity from a fuel layer with 40 μm thickness after background-correction. The spatial standard deviation in the corrected image was 2.6%.

To account for the spatially inhomogeneous excitation, detection, and collection efficiencies in fuel-film LIF imaging, a sample was illuminated giving a uniform LIF response to laser excitation. Such a "flat-field" was acquired by illuminating a plate of quartz glass of inferior quality, which fluoresced homogeneously (homogeneous distribution of impurities) in the UV when excited at 266 nm. The flat-field plate was located behind the quartz wall that the fuel films are on. Figure 33d shows the LIF signal from the quartz plate when the laser light partially passes through the plate and is reflected at the aluminum back wall, where injector and electrodes are mounted. This flat-field was used to correct the fuel-film images. Since in the calibration images with a thin-film cuvette these reflections do not occur, the flat-field shown in Figure 33e was acquired within the calibration tool and was used to correct the calibration images. Errors from inhomogeneities in the spatial distribution of impurities in the flat-field quartz-glass material were estimated by acquiring flat-field images with the glass rotated or turned. The average spatial standard-deviation in the LIF signal throughout different regions of the flat-field material was about 1.5%.

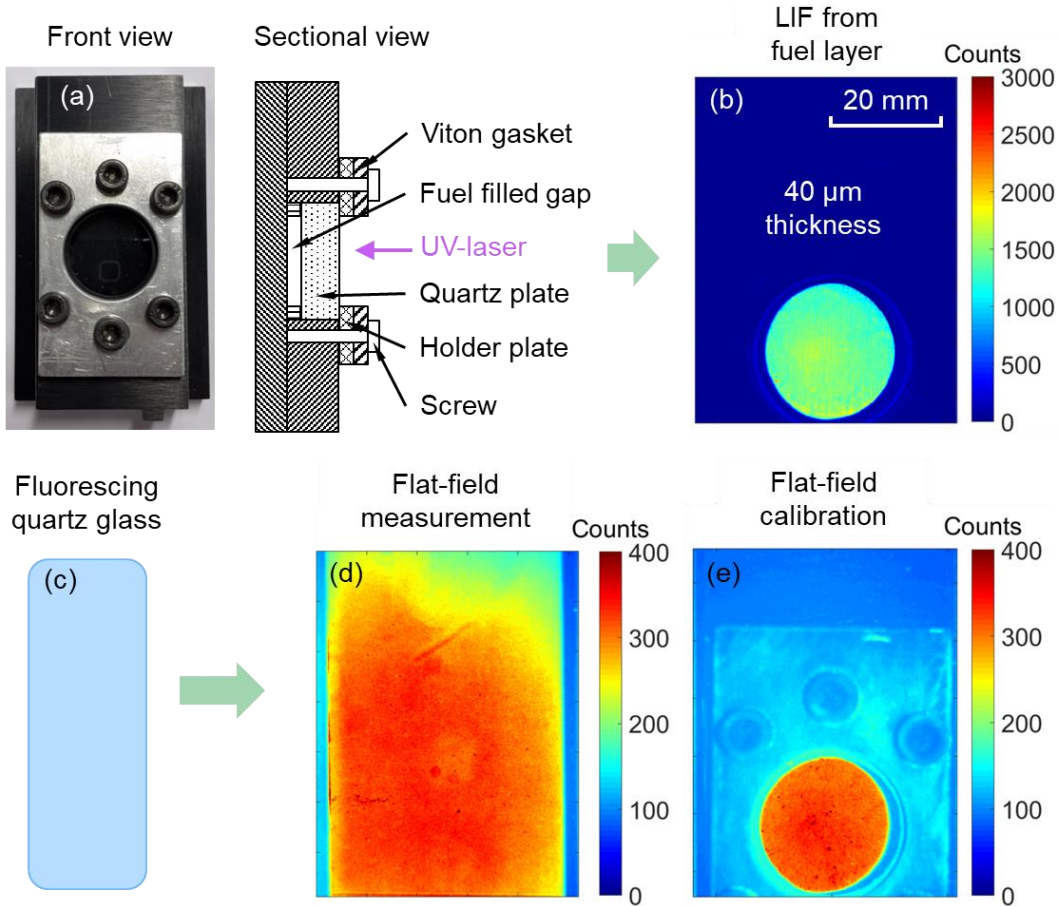


Figure 33: (a) Calibration tool, (b) fuel-film image for a thickness of 40 μm after background correction, (c) quartz glass of inferior quality, (d) flat-field for measurement, (e) flat-field for calibration. Modified version of this Figure published in [98].

The raw images of the fuel layer in the calibration tool were ensemble averaged and then background- and flat-field-corrected according to:

$$I_{\text{cal}} = \frac{\langle I_{\text{cal,raw}} \rangle - \langle BG_{\text{cal}} \rangle}{\langle FF \rangle - \langle BG_{\text{FF}} \rangle} \quad (39)$$

Here, $\langle I_{\text{cal,raw}} \rangle$ is an uncorrected ensemble average of 50 single shot images, $\langle FF \rangle$ is an ensemble average of 50 single shots of the flat-field in calibration, and $\langle BG_{\text{cal}} \rangle$ and $\langle BG_{\text{FF}} \rangle$ are ensemble averages of the background in calibration and flat-field imaging, respectively. In the calibration, the background was acquired by imaging the calibration tool without precision shims but with fuel between the black back plate and the quartz window (thus showing the surface roughness of the black back plate), see Section 4.5.7. The background in flat-field imaging was acquired by illuminating the device without flat-field material. Figure 34 on the left shows the raw and corrected images of a 30 μm thick film and the flat-field. Correcting raw images according to equation (39) for shim thicknesses ranging from 10 to 100 μm and spatially averaging the signal in the indicated ROI gives the data shown in Figure 34 on the right. Each data point is the average of three individual measurements, each comprising the ensemble average of 50 background- and flat-field corrected single shots. In Figure 34 the deviation from the linear approximation between the LIF signal and the fuel-film thickness becomes

pronounced a calibration thickness of 100 μm . However, measured fuel-film thicknesses did not exceed 50 μm such that the linear fit function $I_{\text{cal}} = 0.16 \frac{1}{\mu\text{m}} \cdot d_{\text{cal}}$ was used to calculate the film thicknesses from the LIF signal. The fit approximates the data points between 0 and 50 μm very well, indicated by a coefficient of determination of 99.2%.

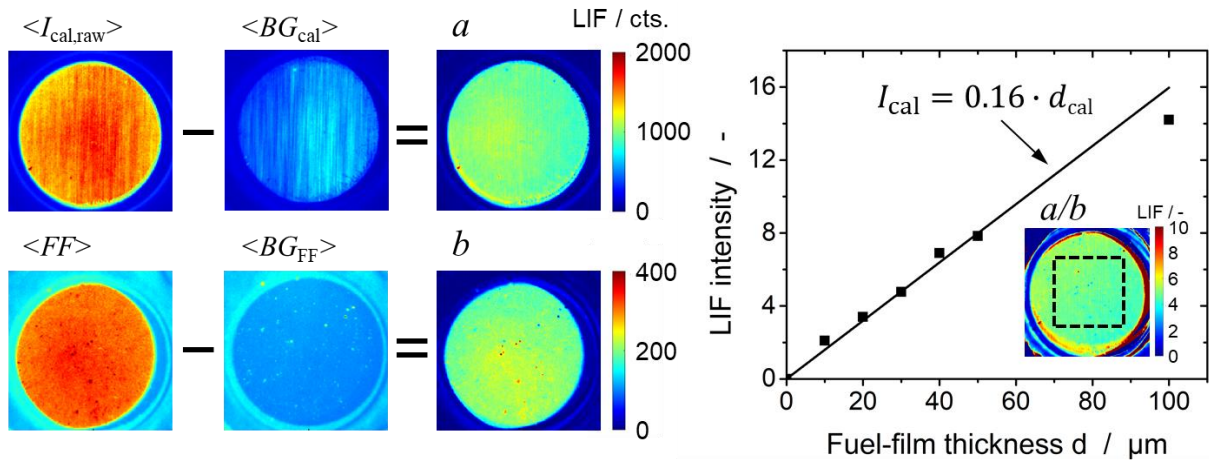


Figure 34: (left) Image post-processing according to equation (39). (right) Calibration data of LIF signal versus fuel-film thickness at 298 K. The standard deviation among three individual measurements is less than the size of the data points.

For the flat-field correction it is important that both the LIF signal of toluene and the LIF signal of the flat-field material are proportional to the laser fluence. Laser pulse-energies were measured downstream of the aperture, indicated in Figure 32, with a laser energy sensor (Coherent, J-50MB-YAG), and were varied with the beam attenuator between 2 and 5 mJ. The pulse energies were divided by the illuminated area on the quartz window of 30 cm^2 . This results in an average laser fluence to which the fuel films are exposed. Figure 35 indicates a linear relation between the laser fluence and the LIF of toluene and flat-field glass material.

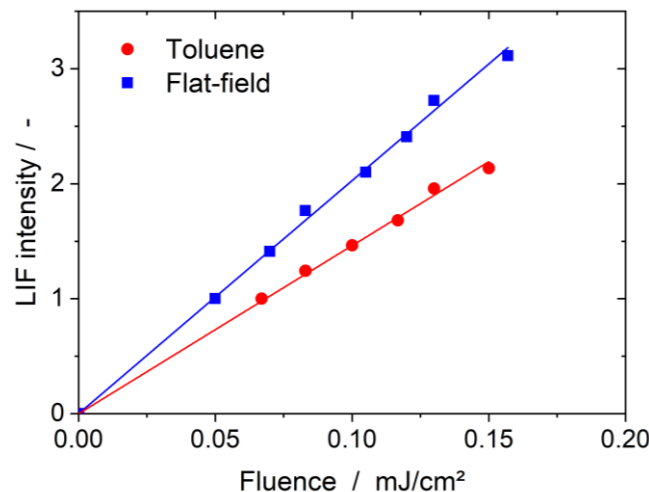


Figure 35: LIF signal versus laser fluence for iso-octane/toluene-mixture and flat-field glass material.

4.4.2 Laser degassing

Prompted by Geiler [130] experiments with UV laser illumination repeated over thousands of pulses were performed. It was found that for an iso-octane/toluene fuel-layer of constant thickness the signal increased with time. Figure 36a shows the LIF signal of a fuel film of 100 μm thickness and 1 vol.-% toluene and 99 vol.-% iso-octane after 1 and 2000 laser pulses irradiation. Figure 36b shows the spatial mean throughout the ROI which indicates that the LIF signal has increased by a factor of about 3.7 after the irradiation with 2000 laser pulses (pulse energy: 35 mJ, laser repetition-rate: 10 Hz). Geiler [130] is qualitatively consistent with this finding, reporting a signal increase about a factor of 3.5 for a 100 μm thick fuel film of 99 vol.-% iso-octane and 1 vol.-% toluene after the illumination with 1000 laser shots (pulse energy: 36 mJ, laser repetition-rate 5 Hz). In both traces, the data was normalized by the spatial average after the first laser pulse. The steeper signal increase in the case from Geiler most probably results from a higher laser fluence in the irradiated region of the fuel layer. Geiler additionally showed that the maximum signal is independent of the laser fluence which solely affects the speed of the signal increase. Also, he showed that this signal increase does not occur for ketones such as acetone, butane, and 3-pentanone. Most probably, the laser energy, partially absorbed by the fuel film, leads to locally hot regions within the fuel film. In these regions the oxygen thermally degases from the liquid film and presumably forms gas bubbles. That leads to a reduced oxygen concentration, a reduced quenching rate, and a higher signal. Oxygen quenching is widely known from gas-phase LIF where the presence of oxygen strongly decreases the LIF signal due to collisional signal quenching [55]. Geiler found the effect for aromatic tracers in a non-fluorescing surrogate fuel. During fuel-film thickness measurement every fuel-film is exposed to only a single laser shot such that a laser degassing is not likely. As a consequence of the investigations discussed above, in the following the fuel layers in the calibration tool were exposed to only 50 laser pulses to make the signal increase from laser degassing negligible.

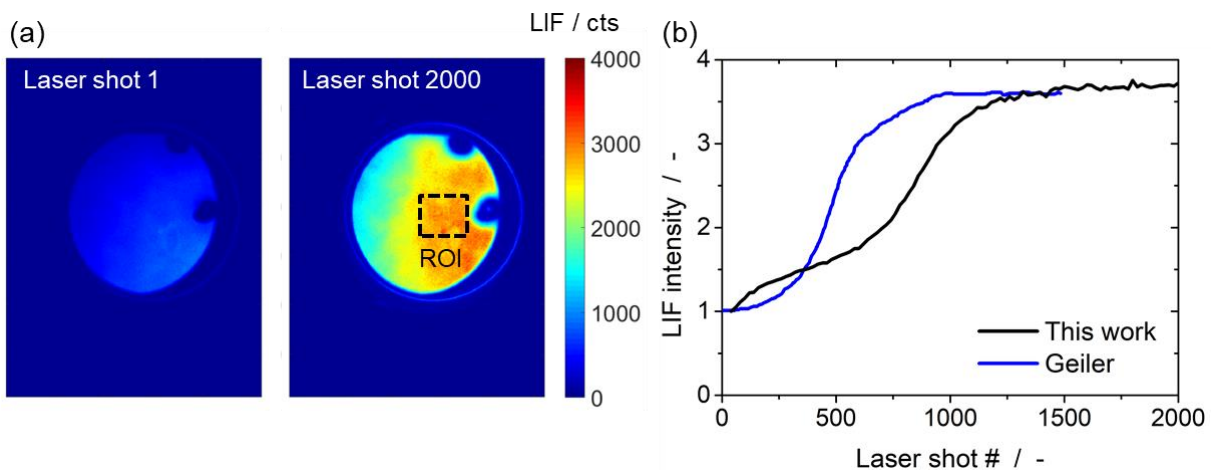


Figure 36: (a) LIF image of 100 μm thick fuel film (1 vol.-% toluene) after 1 and 2000 laser pulses. (b) Spatially averaged LIF signal versus number of laser pulses from of 100 μm thick fuel film (iso-octane + 1 vol.-% toluene) from this work and from Geiler [130].

4.4.3 Temperature dependence

To investigate the influence of temperature on liquid-film fluorescence, the calibration tool was put onto a plate heated by “heating cartridges” from the inside, as indicated in Figure 37a. A channel was drilled through the side of the holder plate of the calibration tool into the fuel-filled gap. Then, a sheathed thermocouple (Type K, NiCr-Ni), indicated by the green wire in Figure 37a, was glued into the channel, measuring the temperature within the fuel layer. The heating cartridges were controlled such that the fuel film reaches the desired temperature. Here, the fuel film of 100 μm thickness was heated to temperatures ranging from 305 to 365 K. The measurement was done with two different strategies. In the first measurement, 10 images were acquired every 10 K between 305 and 365 K to investigate the effect of temperature in a non-degassed condition of the fuel film (low-signal region in Figure 36b). In the second measurement, 100 images were acquired every 10 K after the probe was exposed to 2000 laser shots to investigate the temperature effect under degassed conditions. Figure 37b shows ensemble average images of 100 single shots after background correction for (left) 315 and (right) 365 K under degassed conditions.

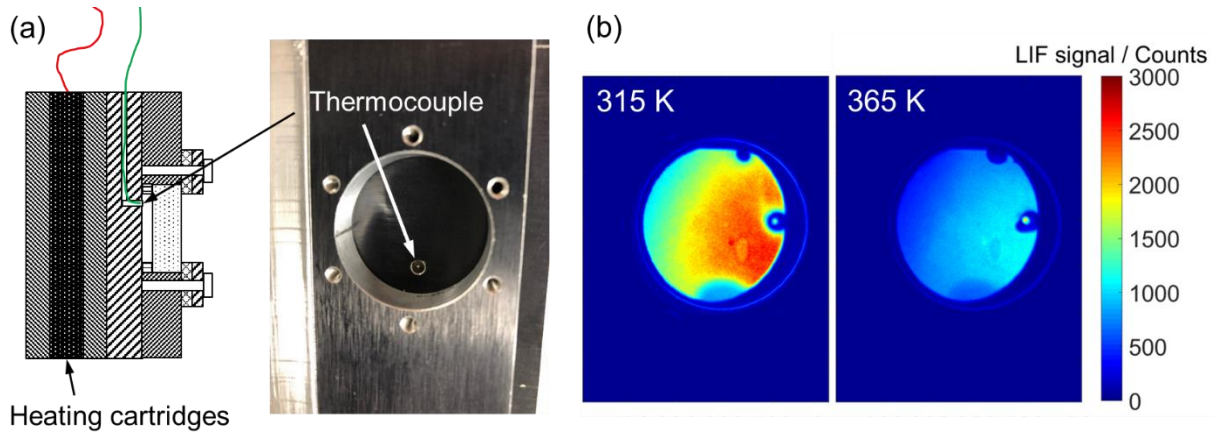


Figure 37: (a) Sectional view of modified calibration tool on a heated plate and with thermocouple within the fuel layer. (b) Images of a fuel film of 100 μm thickness at 315 K and 365 K.

The signal from the ROI, indicated in Figure 36a, was spatially averaged and plotted versus the temperature as shown in Figure 38 for a degassed and non-degassed sample on the left and right, respectively. Under degassed conditions, the LIF signal decreases approximately linearly about a factor of 3 from 315 to 365 K. Consistent with this, Geiler et al. measured an approximately linear decrease in the LIF signal about a factor of 2.6 from 303 to 373 K [31]. The data from this work and from Geiler et al. were normalized by the signals at 305 and 303 K, respectively. During the actual fuel-film measurement, every film is exposed to only one laser shot so that the dependency of the LIF signal under non-degassed conditions is of interest. The result of the non-degassed sample indicates that the LIF signal decreases only about a factor of 2.3 from 305 to 365 K. Also, the signal does not decrease linearly but comparatively stronger at low temperatures. Thus, the signal of the non-degassed sample is less sensitive to temperature variations at around 350 K. The ad-hoc power-law fit approximates the data and was used to correct the LIF signal as given in equation (41). Any potential spectral shift in the toluene fluorescence with temperature is implicitly taken into account by using the same detection filter (BP 292/27) in the fuel-film imaging and the temperature variation used for signal correction.

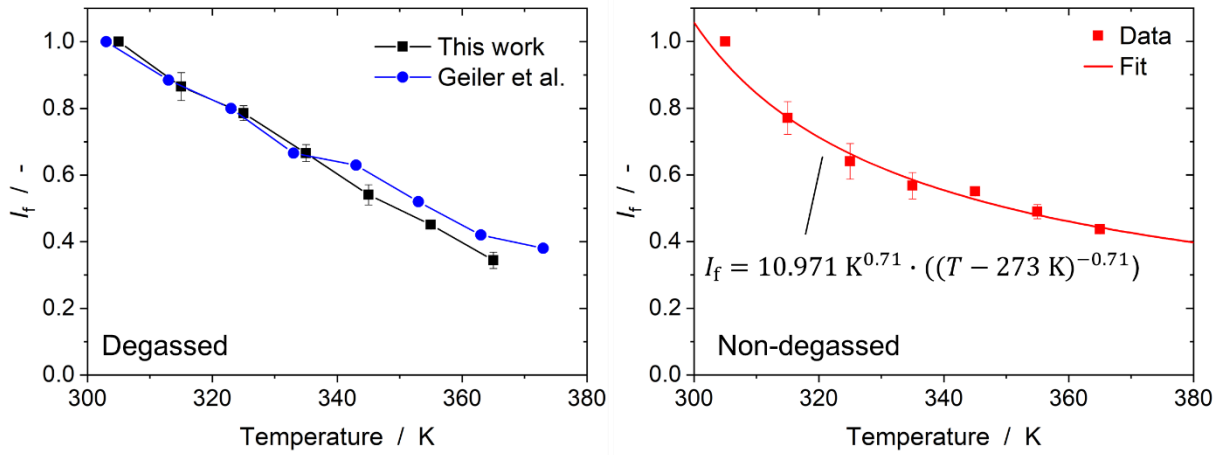


Figure 38: LIF signal of liquid toluene versus temperature in (left) degassed condition from this work and from Geiler et al. [31] and (right) non-degassed condition. Error bars indicate the standard deviation among three individual measurements. Modified version of this Figure published in [98].

4.4.4 Image processing and quantification

Single shot images of fuel-film LIF were post-processed analogously to equation (39)

$$I_{\text{exp}} = \frac{I_{\text{exp,raw}} - \langle BG_{\text{exp}} \rangle}{\langle FF \rangle - \langle BG_{\text{FF}} \rangle} \quad (40)$$

with the corresponding background and flat-field images, as shown in Figure 39.

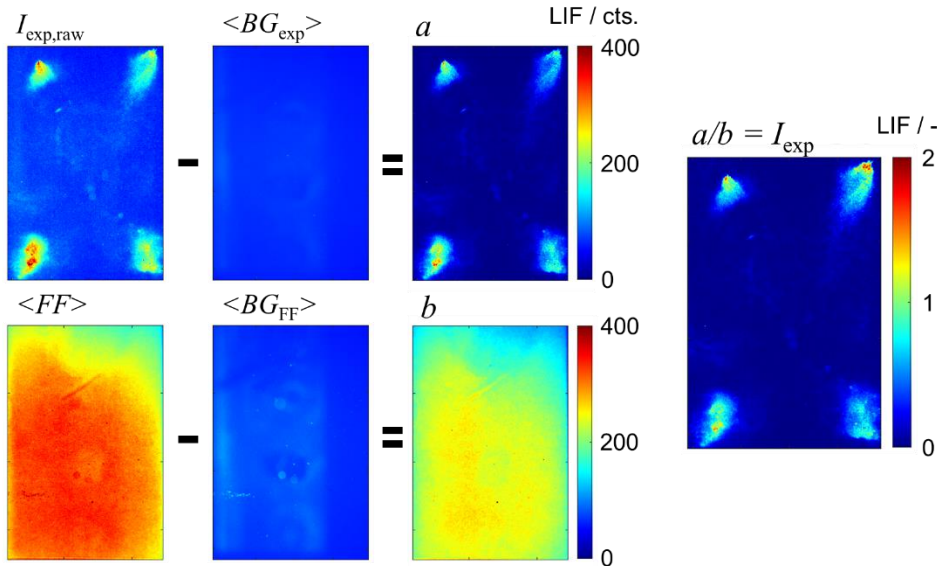


Figure 39: Image post-processing of fuel-film LIF images: Background subtraction and flat-field division.

With the calibration constant $\frac{d_{\text{cal}}}{I_{\text{cal}}} = 6.25 \mu\text{m}$, indicated on the right in Figure 34, the fuel film thickness was calculated pixel-wise according to:

$$d(x, y) = \frac{I_{\text{exp}}(x, y)}{I_{\text{cal}}} d_{\text{cal}} \frac{I_f(298 \text{ K})}{I_f(T_w)} \quad (41)$$

The background and flat-field corrected fluorescence intensity of the fuel films is I_{exp} , while the one in the calibration is denoted as I_{cal} . The ratio $\frac{d_{\text{cal}}}{I_{\text{cal}}}$ results from the calibration function. The fuel-film temperature was approximated as the quartz-wall temperature. The CFD simulation and the LDM (see Section 4.6.4) show that once the fuel adheres to the wall, it rapidly approaches the temperature of the quartz wall, and that the latter does not cool down much due to the fuel impingement. Park and Ghandhi also stated that the fuel-film temperature reaches the wall (in their case, piston) temperature [129]. Therefore, the acquired image was corrected by the ratio $\frac{I_f(298 \text{ K})}{I_f(T_w)}$, where $I_f(298 \text{ K})$ is the LIF signal at 298 K (the temperature during calibration, see Figure 34), and $I_f(T_w)$ that at the quartz-wall temperature in the experiment.

4.5 Results and discussion

Figure 40 shows film-thickness images as a single shot, an ensemble average of 50 single shots at 3 ms aSOI, and single shots of film 6 at 9, 20, and 30 ms aSOI (see caption for operating conditions).

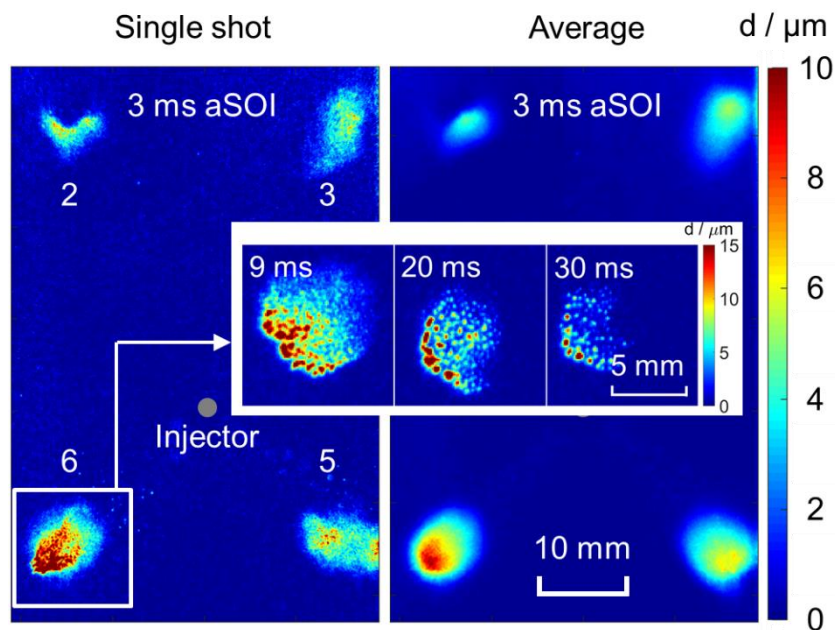


Figure 40: Fuel-film imaging: (left) Single shot and (right) ensemble average of 50 single shots of the film thickness at 3 ms aSOI and overlaid single shots of film 6 at 9, 20, and 30 ms aSOI. $T_w = 352 \text{ K}$, $v_{\text{air}} = 1.8 \text{ m/s}$, $m_{\text{inj}} = 4.6 \text{ mg}$, with combustion.

The propagation of the turbulent flame front through the mixture happens between 3 and 15 ms aSOI. Fuel films 1 and 4 entirely adhere to the metal frame around the quartz wall and are thus not visible in the images. The injector tip is indicated in the lower part of the FOV. For sprays 2 and 3, the impingement angle (the angle between the spray cone axis and the wall) is approximately 50° . For sprays 5 and 6 the impingement angle is approximately 70° . The

orthogonal distance from the injector nozzle to the wall is about 32.5 mm. Thus, the impingement distance along the spray axis is 39 mm for films 5 and 6 and 47 mm for films 2 and 3. The spray forming film 2 collides with the spark electrodes such that the quantity of fuel reaching the wall is smaller than for fuel film 3. The temporal evolution of film 6 clearly shows that the fuel film consists rather of a randomly distributed multitude of individual fuel droplets, leading to a wavy structure in the film thickness. This becomes even more pronounced during evaporation when the fuel accumulates in small regions into discrete fuel "blobs" or droplets. Schulz et al. also observed the contraction of the fuel film in some regions into such small, thick droplets [117]. In some images (not shown here), those regions appear to be even thicker, e.g. around 9, 15, or 45 ms aSOI, than the thickest parts of the film at 3 ms aSOI. The explanation for this is that the fuel volume on the wall tends to minimize the surface area exposed to the air flow by contracting into droplets, providing the minimum area/volume-ratio. Single shots and, in particular, the ensemble average show the systematic accumulation of fuel in the outer regions of the wetted area. The momentum of the spray in the vertical direction pushes the fuel into these areas. Previous studies also reported that the fuel film is thin throughout much of the spray impact area and accumulates towards the film tip [31, 118, 124].

Figure 41 shows averages and single shots of the thickness of film 2, which completely evaporates much earlier than films 5 and 6.

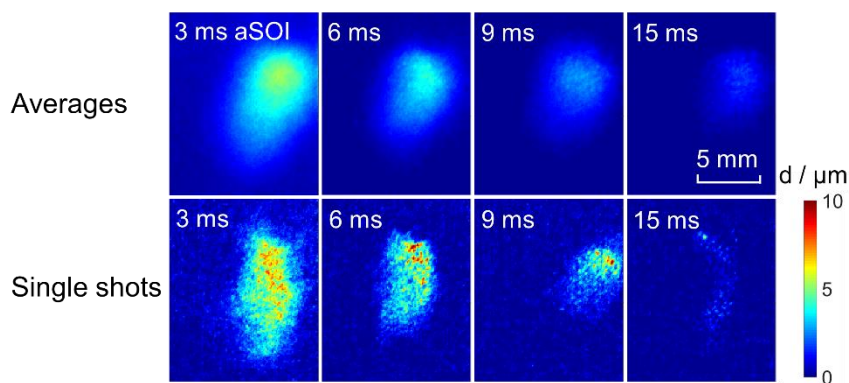


Figure 41: Evolution of fuel-film 6. $T_w = 352$ K, $v_{air} = 1.8$ m/s, $m_{inj} = 4.6$ mg, with combustion.

For the calculation of the total film area and volume, the thickness images were thresholded at $1 \mu\text{m}$ film thickness. Integration of the film thickness over the thresholded area and multiplication with the projected pixel results in the total film volume. Multiplying the result with the density of iso-octane of 0.69 mg/mm^3 yields the fuel-film mass. Figure 42 shows the evolutions of fuel-film mass and area of the four fuel films under the aforementioned conditions. For better visibility, error bars are only shown for films 2 and 6. Assuming that the total injected fuel mass of 4.6 mg splits evenly onto the six single sprays, each spray contains around 0.77 mg. Thus, about 18 and 22% of the injected fuel adhere to the wall for films 5 and 6 (impingement angle 70° , impingement distance 39 mm, 100 bar fuel pressure), respectively. For films 2 and 3 (impingement angle 50° , impingement distance 47 mm), only 6% and 15% of the injected mass adhere to the wall, respectively. Figure 42 indicates that the area of film 3 is 10% higher than that of film 6 although the film mass is 33% lower. Therefore, the average thickness of film 3 is $2.7 \mu\text{m}$ and around 38% below that of film 6. Although the boundary conditions are same, film 5 has a 18% lower initial mass than film 6. When looking at Figure

40, it seems that the thickness of film 5 appears to predominantly deviate in the thicker regions of the films where the fuel accumulates while it is similar in the surrounding region. That is supported by the fact that the thresholded area of film 5 is only 4% lower than that of film 6, shown on the right in Figure 42. The mean film thicknesses over the thresholded areas are 4.4 and 3.7 μm at 3 ms aSOI for films 6 and 5, respectively. Apparently, a higher fraction of the injected fuel is convectively transported with the gas flow downstream for spray 5 than for spray 6. Also, clipping of film 5 in some images and slight deviations in the mass flow of fuel between the injector orifices might contribute to the deviation in the initial film masses. Nevertheless, the evaporation rates of films 5 and 6 appear to be very similar throughout the film evaporation (not shown here).

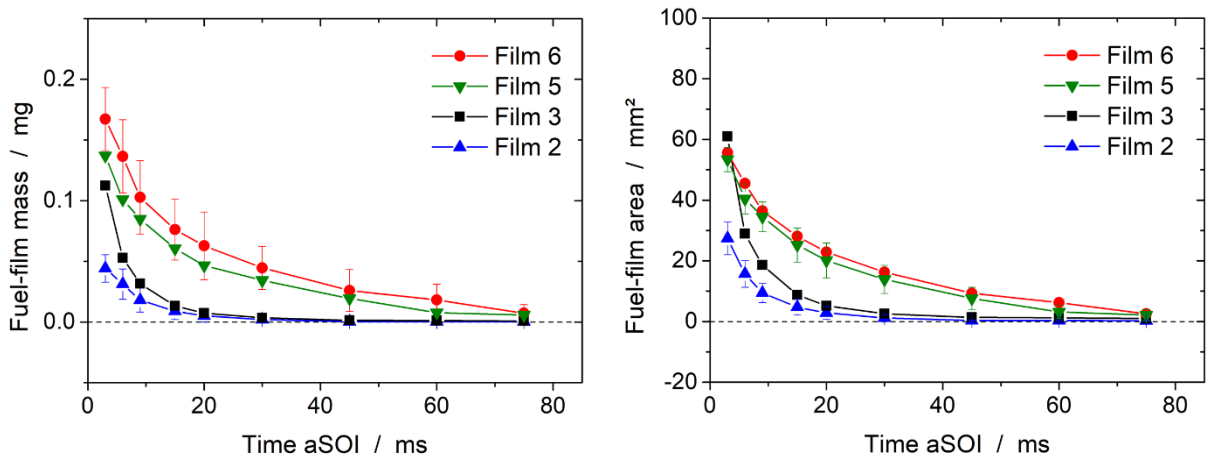


Figure 42: Fuel-film mass and area versus time aSOI of fuel films 2, 3, 5, and 6. $T_w = 352\text{ K}$, $v_{\text{air}} = 1.8\text{ m/s}$, $m_{\text{inj}} = 4.6\text{ mg}$, with combustion. Error bars indicate the standard deviation among 50 individual injections.

Consistent with the work from Senda et al. [56], the area remains constant for different impingement distances and angles such that the mean film thickness significantly decreased for an increasing impingement distance. This becomes apparent from the comparison of film 3 with films 5/6 in Figure 40 and from the evolution of the film area in Figure 42. Also, Cheng et al. found the film area at 3 ms aSOI to be only slightly dependent on the impingement distance. They stated that with an injection pressure of 3 bar and an impingement angle of 90° , the film area was 150 and 135 mm^2 for 50 and 60 mm distance, respectively [126].

Consistent with Schulz et al. [117], slopes of the film-mass evolutions are greatest early aSOI for all fuel films. This originates from enhanced convective transport coefficients because of strong turbulence after the end of injection and from the initially large film area. Additionally, the fuel-film area available for heat and mass transfer shrinks dramatically early aSOI, as shown on the right in Figure 42. While the fuel accumulates to thick droplets in the outer part of the fuel film and remains until the end of evaporation, the thin parts of the film where the jet impinges on the wall evaporate first.

In the following discussion, first a comparison of LIF imaging and CFD simulation for fuel-film thickness determination is presented. Then, the influence of different operating parameters on the evaporation characteristics, found by LIF and partially by CFD, is given. The investigation will focus on film 6 which is entirely optically accessible for all operating

conditions and provides the highest SNR. However, similar evolutions are found for films 2, 3, and 5. The CFD simulation was done by the ETH in Zurich. For completeness, a brief summary of the simulation methods is included here, while details can be found in [98, 134].

Turbulence was treated with a Large Eddy Simulation (LES) approach, where only large-scale turbulent motions are resolved, whereas the smaller scales are modelled with the k- ϵ sub-model. The liquid phase dispersed into the gas phase was treated with a Lagrangian approach [186]. Additional processes which account for an accurate representation of the spray include droplet evaporation, condensation, and droplet/wall-interaction modelled according to Sirignano [187], Torres et al. [188], and Bai and Gosman [189], respectively. For the fuel film, conservation equations for mass, momentum, and energy were employed [190]. The fixed time steps had a base duration of 10^{-3} ms, while in the reacting case, this was reduced to $0.5 \cdot 10^{-3}$ ms for the first 10 ms. The geometry represented in Figure 24 was meshed with around 1.5 million cells with a base cell size of 4 mm refined three times to 0.5 mm in the spray and spark-plug regions. Film-thickness images were smoothed in post-processing.

4.5.1 Comparison with CFD simulation

Figure 43 shows images of the four fuel films' thickness at 8.5 ms aSOI from the CFD simulation and LIF imaging. Results from LIF imaging are shown as an ensemble average of 20 single shots and a single shot of the film thickness. The CFD simulation showed very little shot-to-shot variation in film thickness and area such that the film-evaporation analysis is based on single realizations. Here, the temperature was that of the laboratory (about 300 K) and the experiment was operated in quiescent air and without combustion. This was realized by closing a throttle in the air flow during the measurements and opening it between two injections to flush the test section. These operating conditions were chosen to compare the two methods under simple boundary conditions. First, the error in LIF imaging of the film thickness from temperature variations in the fuel film is very low since wall, air, and injector are at ambient temperature as during calibration. Second, in CFD, errors in the calculation from complicated interaction of the fuel films with the flow and the combustion are avoided.

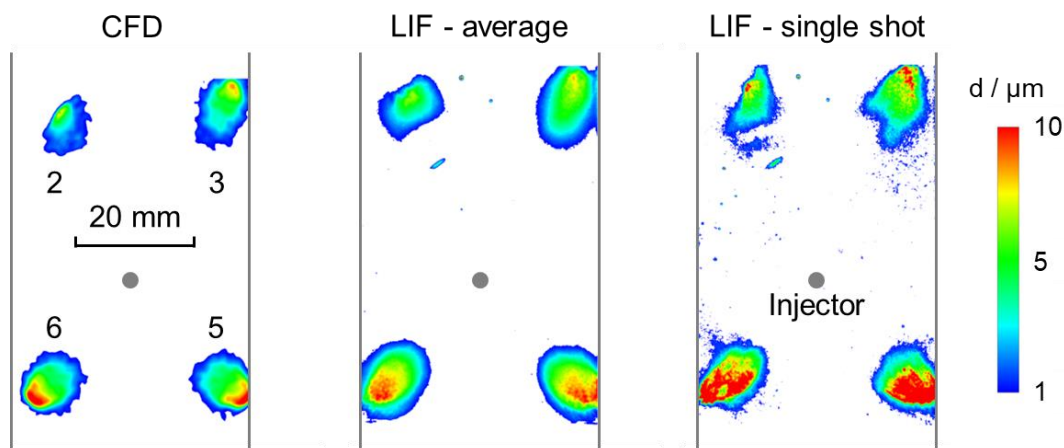


Figure 43: Fuel-film thickness at 8.5 ms aSOI in CFD simulation and LIF imaging. $T_w = 300$ K, $v_{\text{air}} = 0$ m/s, $m_{\text{inj}} = 4.6$ mg, without combustion. Figure published in [98].

The fuel films represent the parts of the films that exceed a threshold of $1 \mu\text{m}$ in thickness. The gray stripes to the right and left of each image indicate the edges of the quartz window. Visually, film-thickness distribution and area are in very good agreement between LIF and CFD. The collision of the spray with the spark electrodes and the lower quantity of film 2 compared to film 3 is also captured by the simulation. Also, the similarity in film area of film 3 compared to films 5 and 6 is captured by the CFD simulation.

Figure 44 compares the temporal evolution of the evaporating film 6 from CFD and LIF. The fuel-film thickness distributions are both qualitatively and quantitatively very similar in simulation and experiment throughout the entire evaporation process. However, the images show that the fuel-film area thresholded at $1 \mu\text{m}$ is larger in the measurement. The single shots indicate in contrast to the ensemble average and the simulation that the fuel film has many locally thick regions (“fuel blobs”).

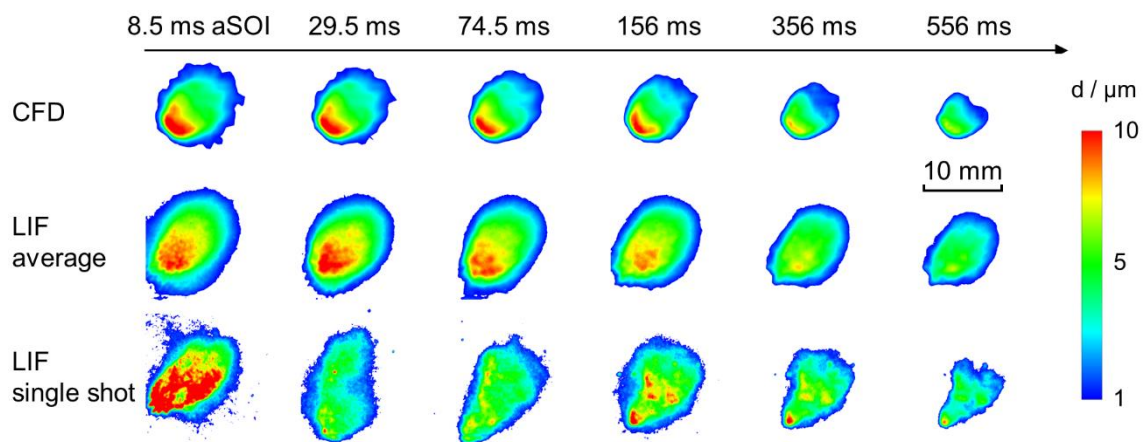


Figure 44: Evolution of fuel-film 6 thickness from CFD simulation and LIF imaging. $T_w = 300 \text{ K}$, $v_{\text{air}} = 0 \text{ m/s}$, $m_{\text{inj}} = 4.6 \text{ mg}$, without combustion. Figure published in [98].

Figure 45 shows the corresponding fuel-film mass evolutions of the four fuel films from CFD and LIF. The first LIF datapoint is at 8.5 ms aSOI, when the LIF signal from any remaining droplets in the air interfering with the LIF signal from fuel films becomes negligible. The evolutions from LIF of films 3 and 5 show slightly increasing film mass early aSOI. This is unphysical, since droplets have vanished by this time, but it results to some extent from only averaging 20 single shots such that the indicated mean film-mass has not completely converged. Also, reflections of laser light and LIF within the gap between the quartz window and the metal frame where parts of the fuel film flow into, contribute to the high fluctuations in the average mass early aSOI. However, with ongoing evaporation and in particular for films 2 and 6, the film mass is monotonically decreasing with an approximately constant slope. As opposed to the experiment, the simulation also quantitatively captures the impingement, indicated by the accumulation of fuel mass in Figure 45 starting at 1 ms aSOI and peaking around 1.6 ms aSOI for the four films. At 8.5 ms aSOI, the masses of films 2, 3, and 6 are around 65, 41, and 51% higher in the measurement than in the simulation, respectively. The CFD simulation shows higher slopes than LIF early aSOI until around 50 ms aSOI. Beyond this time, similar evaporation rates of 10 and $8.9 \text{ mg}/(\text{m}^2 \cdot \text{ms})$ were observed in LIF and CFD, respectively.

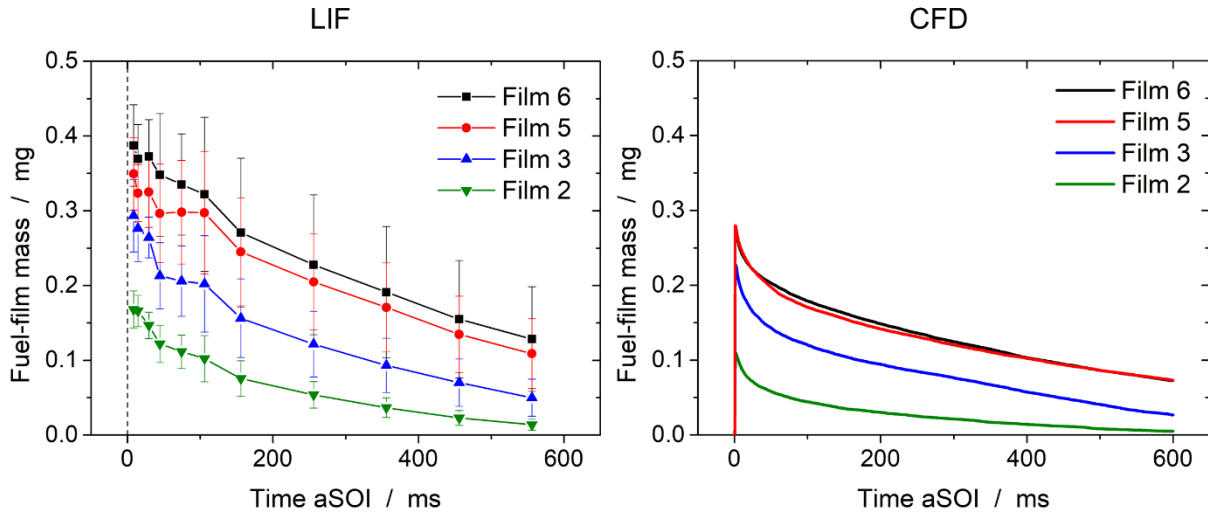


Figure 45: Fuel-film mass versus time aSOI from (left) LIF imaging and (right) CFD simulation. $T_w = 300$ K, $v_{air} = 0$ m/s, $m_{inj} = 4.6$ mg, without combustion. Error bars indicate the standard deviation among 20 individual injections. Figure published in [98].

4.5.2 Effect of combustion and elevated temperature

Figure 46 shows the evolution of film 6 from CFD and LIF during combustion and with a wall temperature of 352 K. In contrast to the comparison at room temperature, here both the film's initial area and thickness agree in simulation and experiment. However, the former predicts faster evaporation such that the film has completely evaporated around 45 ms aSOI, while some fuel is still left in the LIF images at 60 ms aSOI.

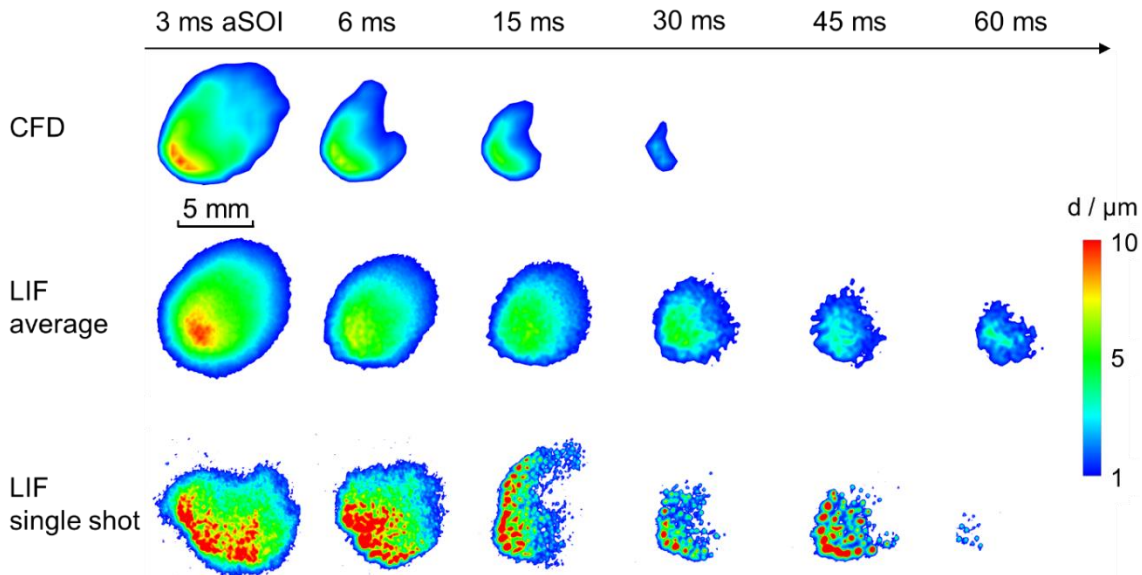


Figure 46: Evolution of fuel-film 6 thickness from CFD simulation and LIF imaging. $T_w = 352$ K, $v_{air} = 1.8$ m/s, $m_{inj} = 4.6$ mg, with combustion. Figure published in [98].

The single shots clearly show the fuel accumulating in discrete regions during evaporation. Comparing the single shots in Figure 46 ($T_w = 352$ K) with the single shots in Figure 44 ($T_w = 300$ K) shows that the formation of “blobs” is more pronounced at elevated wall temperature. Most probably, the higher diffusivity and lower viscosity of the liquid fuel favor

the local film contraction. This blob formation is not predicted by the CFD simulation but also there a slight variation in thickness within the thick region of the fuel film at 3 ms aSOI is apparent. Although surface tension is considered in the CFD simulation, the cell size in the film region is too coarse for it to have a significant effect. Köpple [132] also found that their CFD simulation failed to predict the formation of thick fuel blobs throughout evaporation. With the same injector, in an optically accessible engine, Frapolli et al. [134] found mean film thicknesses around 5 to 6 μm in a 3D-CFD simulation and the film thickness decreasing from 14 to 4 μm in a LIF measurement throughout evaporation ($m_{\text{inj}} = 24 \text{ mg}$, $p_{\text{intake}} = 1 \text{ bar}$, $T_{\text{piston}} = 365 \text{ K}$, $p_{\text{inj}} = 100 \text{ bar}$, $\text{SOI} = -330^\circ\text{CA}$, 1200 rpm). Figure 47 shows the mass and evaporation rate of fuel film 6 from CFD and LIF for wall temperatures of 332 and 352 K, for the latter with and without combustion.

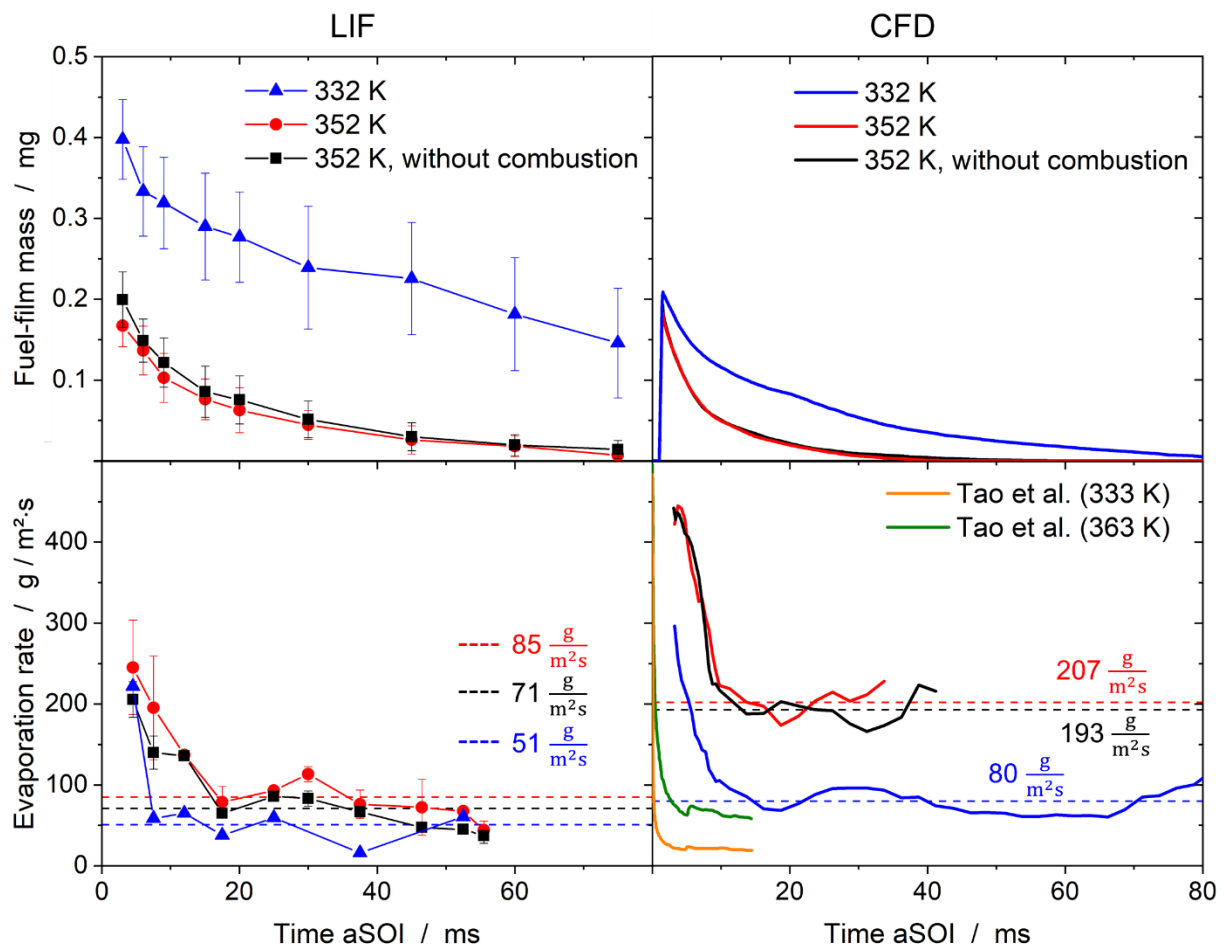


Figure 47: (Top) Fuel-film mass and (bottom) evaporation rate versus time aSOI of film 6 from (left) LIF imaging and (right) CFD simulation and Tao et al. [141]. $v_{\text{air}} = 1.8 \text{ m/s}$, $m_{\text{inj}} = 4.6 \text{ mg}$. Error bars in the film mass indicate the standard deviation among 50 individual injections. Where shown, error bars in the evaporation rate indicate the standard deviation among three experimental runs performed several days apart. Dashed horizontal lines indicate the mean evaporation rates between 10 ms aSOI and the end of evaporation. Figure published in [98].

Note that in the experiment, a higher wall temperature is achieved by a higher air flow temperature, also raising the injector temperature (and the corresponding values were given to the simulation). Thus, less fuel reaches the wall resulting in decreased fuel-film mass and area.

Therefore, the bottom row of Figure 47 plots the evaporation rate as the time derivative of the fuel-film mass, \dot{m}_f , divided by the fuel-film area, A_f . This rate is calculated between two time steps t_n and t_{n+1} according to:

$$\left(\frac{\dot{m}_f}{A_f}\right)_{\frac{1}{2}(t_{n+1}+t_n)} = \frac{m_{f,t_n} - m_{f,t_{n+1}}}{\left(\frac{A_{f,t_n} + A_{f,t_{n+1}}}{2}\right) (t_{n+1} - t_n)} \quad (42)$$

Here, m_{f,t_n} , $m_{f,t_{n+1}}$ and A_{f,t_n} , $A_{f,t_{n+1}}$ are the fuel-film masses and areas, respectively, at the corresponding times t_n and t_{n+1} .

Figure 47 shows that experimentally the fuel-film mass adhering to the wall at 3 ms aSOI strongly increases with decreasing temperature. Assuming that similar fractions of the masses of sprays 1 and 4 adhere to the wall as for sprays 5 and 6, around 16 and 19% of the injected mass adhere to the wall for LIF and CFD, respectively, at elevated temperature ($T_w = 352$ K). The maximum fuel-film masses increase about 125 and 10% when decreasing the wall temperature from 352 to 332 K in experiment and simulation, respectively. In contrast to this, the effect of combustion on the film mass appears to be rather small in the experiment and almost non-existent in the simulation. In general, the simulation shows similar trends but generally lower fuel-film masses than the experiment. In both LIF and CFD, the evaporation rate is highest in the beginning, then decreases and becomes quasi-steady from around 10-15 ms aSOI onward at all conditions, as indicated by the dashed lines in Figure 47. The generally high evaporation rates early aSOI most likely result from the highly turbulent flow (high Re numbers thus high mass transfer coefficients $\beta = f(Re Sc)$) after the end of injection. The increase in wall temperature increases the quasi-steady evaporation rates by 66 and 158% in LIF and CFD, respectively. According to equation (47), constant evaporation rates imply constant mass transfer coefficients and fuel-vapor concentration gradients. Since the fuel vapor in the core of the test section is constantly convected away by the air flow, the concentration gradient is mostly dependent on the saturation vapor concentration on the film surface, which is determined by the fuel-film temperature. From LIF imaging, evaporation rates are derived that are much more similar for the three conditions examined here than they are in the CFD. However, the experimental data are quite noisy. In contrast to LIF, the CFD shows a large difference in the evaporation rate already in the beginning. In the study of Tao et al. [141], modelling the fuel film (iso-octane, initial thickness of 25 μm) and gas phase (ambient temperature 330 K, ambient pressure about 1 bar) one-dimensionally, a qualitatively similar evolution of the evaporation rate was observed. The calculated fuel-film surface temperatures and evaporation rates were found to depend predominantly on the wall temperature. In their case, the increasing concentration boundary-layer thickness of fuel vapor in the gas phase caused the evaporation rate to quickly decrease towards a constant level strongly depending on the wall temperature, as indicated in Figure 47.

Both techniques show very little influence of combustion on the evaporation rate which increases in the quasi-steady period by 20 and 7% on average in LIF and CFD, respectively, with combustion. The turbulent flame front propagates through the test section from 5 to 15 ms aSOI, greatly increasing the temperature gradient between gas and film, but this appears not to have a significant influence on the evaporation rate in experiment and simulation. The small

influence of convective heat transfer compared to conduction is also reflected in the LDM as discussed in Section 4.6.4. In contrast to this, the experimental evaporation rate has a local maximum around 30 ms when substantial soot luminosity is found near the wall in the lower part of the test section. Low uncertainties in the evaporation rate between 20 and 40 ms aSOI indicate the reproducibility of the local maximum and thus the statistical significance. The long-lasting consumption of fuel vapor near the film surface by the non-premixed flame is an additional sink in the fuel-vapor mass balance on the film surface and thus disturbs the equilibrium between mass diffusion and convection in the concentration boundary layer. This in turn results in an increased diffusive flux of fuel from within the film [21].

4.5.3 Influence of the injected mass

Figure 48 shows the mass evolution and the evaporation rate of film 6 with and without combustion for an injected mass of 9.3 mg (injection duration of 1 ms). In contrast to the case with an injected mass of 4.6 mg, here the combustion seems to significantly influence the evaporation of film 6. Again, in the mass evolution, the case with combustion shows a lower initial mass, about 14%, than the case without combustion. The mass evolution with combustion shows a steeper slope early aSOI until 9 ms aSOI and late aSOI between 30 and 45 ms aSOI. These regions appear as local maxima in the evolution of the evaporation rate. Eventually, later than 45 ms aSOI, the evaporation rate of the case with combustion decreases again towards the magnitude of the case without combustion. The single shots from individual injections on the right in Figure 48 show that at 45 ms aSOI that for the case with combustion the flame predominantly has burnt away the thin regions, where the spray impinges.

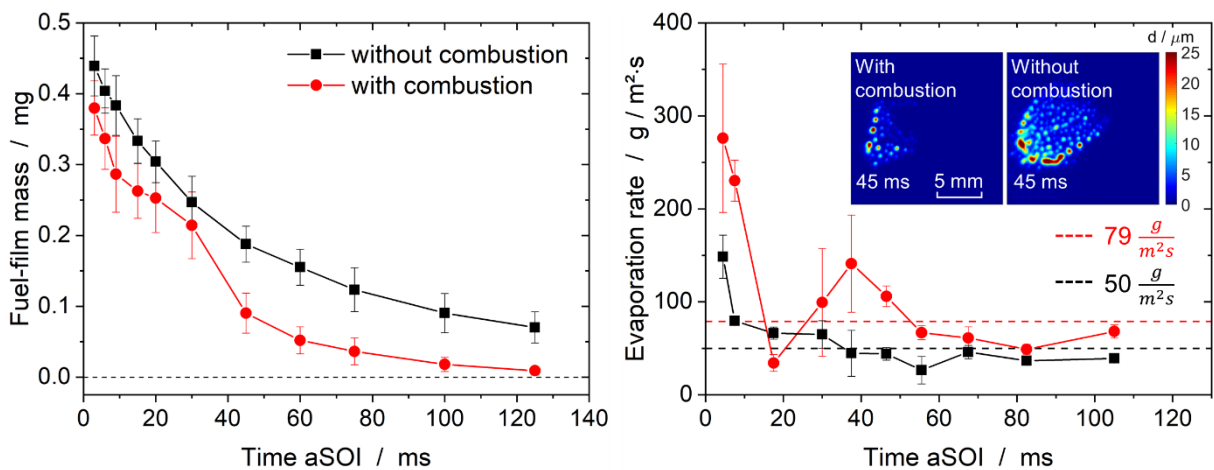


Figure 48: Fuel-film mass and evaporation rate versus time aSOI of film 6. $T_w = 352$ K, $v_{\text{air}} = 1.8$ m/s, $m_{\text{inj}} = 9.3$ mg. Error bars in the film mass indicate the standard deviation among 50 individual injections. Error bars in the evaporation rate indicate the standard deviation among three experimental runs performed several days apart. Dashed horizontal lines indicate the mean evaporation rates between 15 ms aSOI and the end of evaporation.

Possibly, the propagation of the turbulent flame front early aSOI causes the first peak in the evaporation rate. Increased gas flow velocities during flame propagation, as determined in optical-flow measurements result in increased heat and mass transfer coefficients compared to the case without combustion, see Figure 27 and Figure 28. This in turn might additionally cause

a slight heat up of the fuel film. Compared to an injection duration of 0.5 ms, here the chemiluminescent region/flame front indicates a greater spatial extent, as discussed in Section 5.4.1 (Figure 82), which can be thought of as an increased absolute heat released. The second peak in the evaporation rate might be attributed to the formation of soot from fuel film 6. Between 24 and 36 ms aSOI, as discussed in Section 5.4.1, strong PAH formation is detected close to film 6. This is linked to the consumption of fuel vapor on the film surface and thus an increased mass flux of fuel from the liquid film towards the surface compared to an injected mass of 4.6 mg, as described above. The dashed lines in Figure 48 indicate the quasi-steady evaporation rates beyond 17 ms. They are 7% and 30% lower with and without combustion, respectively, than for an injected mass of 4.6 mg.

Comparing the cases with combustion in Figure 47 and Figure 48, shows that the initial film mass (3 ms aSOI) increases from 0.17 to 0.38 mg (0.2 to 0.44 mg without combustion) when increasing the injected mass from 4.6 to 9.3 mg (0.5 and 1 ms). Figure 49a compares the mean fuel-film thickness and area for the two injected masses. Figure 49b shows the results from previous work [96] and compares the effect of even higher injected masses in the same experiment, under very similar conditions (50 mm impingement distance, 100 bar injection pressure, $T_w = 365$ K), and with a different injector.

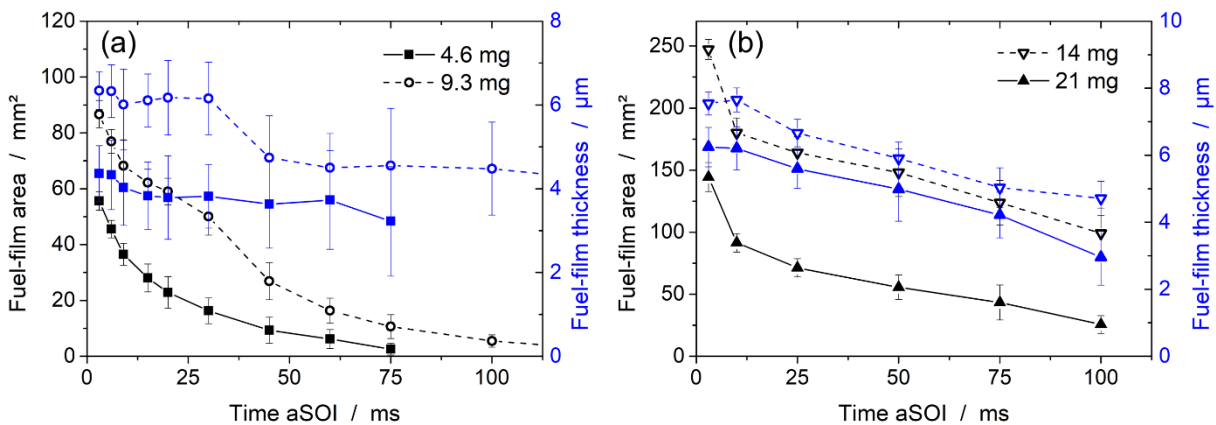


Figure 49: (a) Evolutions of film area and mean thickness of fuel film 6 for the injected masses 4.6 and 9.3 mg. $T_w = 352$ K, $v_{\text{air}} = 1.8$ m/s, with combustion. (b) Evolutions of film area and thickness from previous work [96]. $T_w = 365$ K, $v_{\text{air}} = 1.8$ m/s, with combustion. Error bars indicate the standard deviation among 50 individual injections. Modified version of this Figure published in [96].

The corresponding fractions of fuel adhering to the wall are 22% and 24%. The initial film area increases about 55%, while the film thickness increases about 45% when increasing the injected mass from 4.6 to 9.3 mg. The film thickness remains approximately constant throughout the evaporation for both injected masses. The initial area increases about 71%, while the film thickness increased only about 21% when the injected mass was increased from 14 to 21 mg (2.1 and 2.6 ms). This is in good agreement with the results from Senda et al. who found the mean film thickness to be constant around 21 μm when increasing the injected mass from 7 to 14 mg (increasing the injection duration from 4 to 8 ms), while the area increased about 90% [56]. This trend changes for very thin films. Maligne and Bruneaux investigated fuel films with thicknesses below 1 μm and observed that the film thickness increases about 67% when

increasing the injected mass by 50% [112]. Apparently, the results shown in Figure 49a are in the transition zone between the two regimes since fuel-film area and thickness increase by about similar fractions. In contrast to the present work (Figure 49a), during most of the evaporation the mean film thickness decreases approximately linearly with a similar slope for both injection durations in Figure 49b. Also, the fuel-film area decreases with a similar slope in both cases. Only from 3 to 10 ms aSOI the film thickness remains almost constant in both cases. In the same time span the area decreases by 28% and 42% for 14 and 21 mg, respectively. The sharp decrease in the covered area from 3 to 10 ms aSOI corresponds to the complete evaporation of the thin parts of the fuel films, which is why the average thickness does not change much, despite ongoing evaporation from the entire film. The fractions of the injected fuel-mass adhering to the wall are 28 and 38% for the injected masses 14 and 21 mg, respectively. This is in good agreement with Schulz et al. [117] who also found 38% of the injected mass adhering to the wall in a constant-pressure vessel under similar conditions ($m_{inj} = 21.7$ mg, $p_{ves} = 1$ bar, $T_{ves} = 365$ K, $p_{inj} = 150$ bar, $d_{noz/wall} = 35$ mm). In longer injection events, the late portions of the spray propagate through a bulk gas with a higher fuel/air ratio than that seen by the early portions. This leads, according to equation (22), to a lower evaporation rate of the fuel droplets, and thus to larger fractions of liquid fuel reaching the wall.

Figure 50 shows a sequence of single shots of the film from individual injections of 9.3 mg. The film looks blurry at the boundary at 3 ms aSOI but exhibits a comparatively sharp boundary from 6 ms aSOI onward. Again, the fuel film indicates a very prominent contraction of fuel into thick blobs, even more pronounced than for an injection duration of 4.6 mg.

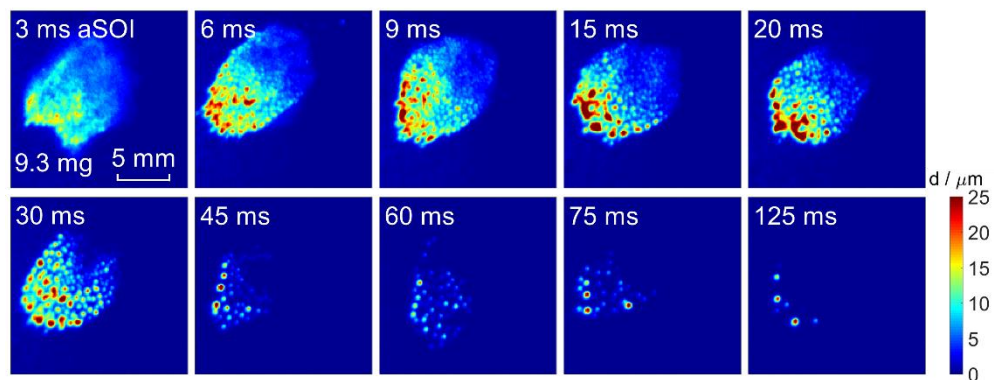


Figure 50: Film evaporation: Single shots of the thickness of film 6 for an injected mass of 9.3 mg. $T_w = 352$ K, $v_{air} = 1.8$ m/s, with combustion.

4.5.4 Influence of the flow velocity

The influence of an increasing flow velocity on the evolutions of mass and evaporation rate of film 6 are shown in Figure 51. Controlling the gas temperature to a fixed value while varying the flow velocity would result in different wall and injector temperatures. Therefore, this investigation was done at ambient temperature and without combustion. To achieve flow velocities of 3 and 10 m/s, the grid (see Figure 25) needed to be removed. To achieve 6.5 (with grid) and 10 m/s (without grid), a fan far upstream of the test section was turned on to further increase the pressure differential across the test section. The left side of Figure 51 shows that the initial fuel-film masses, at 3 ms aSOI, are 0.44, 0.43, 0.55, and 0.59 mg for the gas

velocities 6.5, 1.8, 10, respectively. Apparently, the grid affects the initially adhering fuel-film mass more than the absolute velocity magnitude since the initial masses are lowest for 6.5 and 1.8 m/s. Most probably, the small-scale structure in the flow with the grid inserted enhances the fuel evaporation, as described in Section 4.2.2, and thus causes less fuel reaching the wall. The fuel film has evaporated first for a flow velocity of 6.5 m/s and last for 3 m/s.

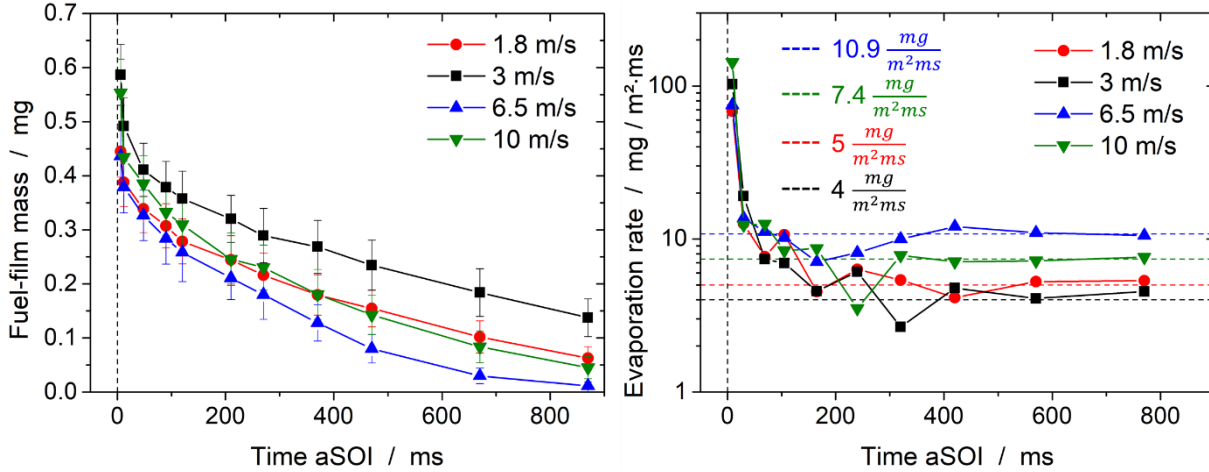


Figure 51: Fuel-film mass and evaporation rate versus time aSOI of film 6 for the flow velocities of 1.8, 3, 6.5, and 10 m/s. Error bars indicate the standard deviation among 50 individual injections. $T_w = 300$ K, $m_{inj} = 4.6$ mg, without combustion. Dashed horizontal lines indicate the mean evaporation rates between 300 ms aSOI and the end of evaporation. Note the logarithmic scale for the evaporation rate.

For all four velocities and consistent with the results from Sections 4.5.1-4.5.3, the films evaporate fastest between 6 and 12 ms aSOI, as indicated on the right in Figure 51. Around 300 ms aSOI the fuel films approach quasi-steady evaporation rates that depend on the particular flow velocity. The quasi-steady evaporation rates become 10.9, 7.4, 5, and 4 $\text{mg}/(\text{m}^2\cdot\text{ms})$ for 6.5, 10 m/s, 1.8, and 3 m/s, respectively. Like the initial film mass, the quasi-steady evaporation rates are also more affected by the grid (enhanced mass transfer coefficient near film 6 due to small-scale turbulence) than by the velocity magnitude, as exemplarily indicated by the evaporation rates 10.9 and 7.4 $\text{mg}/(\text{m}^2\cdot\text{ms})$ for velocities 6.5 and 10 m/s, respectively.

Figure 52 shows single shots of the thickness of film 6 for 3 and 6.5 m/s flow velocity. The images reveal that the fuel film forms in a more oval shape for the higher flow velocity. During evaporation, the higher flow velocity seems to flatten thick regions in the film more efficiently. This, in turn, leads to a larger film area on the wall and an eventually shorter lifetime, as also seen in Figure 51.

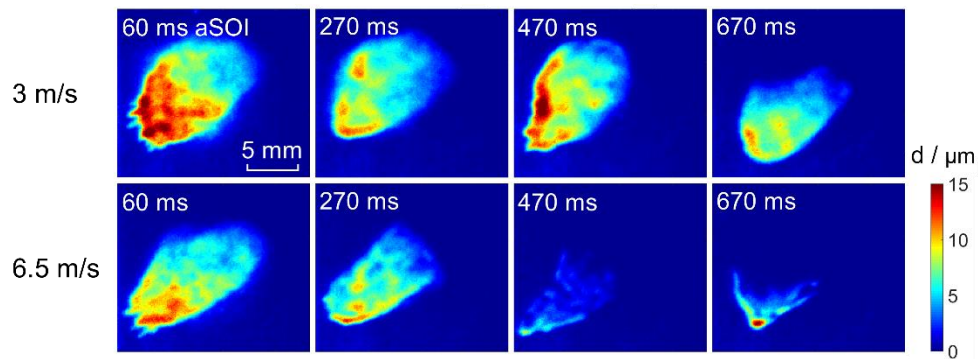


Figure 52: Film evaporation: Single shots of the thickness of film 6 for 3 and 6.5 m/s flow velocity. $T_w = 300$ K, $m_{inj} = 4.6$ mg, without combustion.

4.5.5 Local evaporation rate

In the previous sections, the evaporation rate was calculated based on the mass decrease of the entire fuel film (regions with thicknesses above $1 \mu\text{m}$) between two time-steps. This section investigates whether the local evaporation rate, calculated from the mass decrease in a small ROI of the film-thickness image, is different from the global one. Figure 53 compares the evolution of the local and global evaporation rates of film 6. The local evaporation rate was calculated within a small area (10×10 px) in the thick center of the film, as indicated in the ensemble average images in Figure 53.

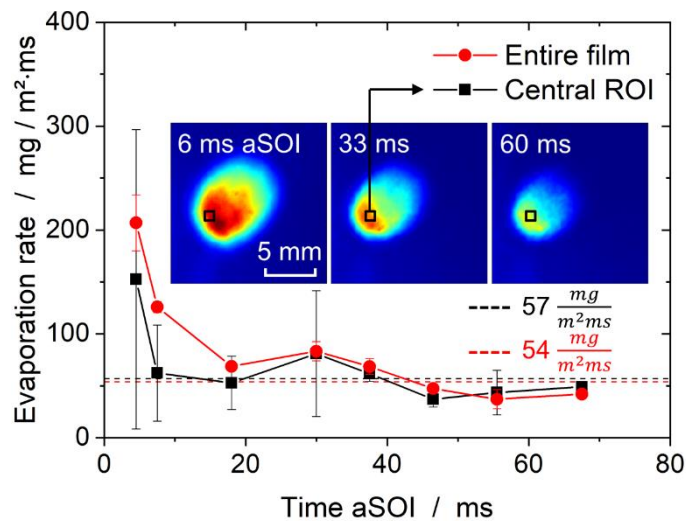


Figure 53: Evaporation rate of film 6 calculated over the entire thresholded film area and over a 10×10 px region in the thick center of the film. $T_w = 352$ K, $v_{air} = 1.8$ m/s, $m_{inj} = 4.6$ mg, with combustion. Error bars in the evaporation rate indicate the standard deviation among three experimental runs performed several days apart. Dashed horizontal lines indicate the mean evaporation rates between 15 ms aSOI and the end of evaporation.

Early aSOI, the local evaporation rate is around 50% below the global evaporation rate. The difference in the early evaporation might be due to two reasons. First, the contraction of the continuous fuel film into discrete fuel droplets is pronounced early aSOI, e.g. between 3 and 20 ms aSOI, and presumably leads to a mass flow of fuel parallel to the wall towards the thick central region of the film. This counteracts the mass loss due to evaporation and thus results in

an underestimation of the evaporation rate. Second, the large areas of thin regions in the film might approach the wall temperature faster than the thick regions in the center. The high standard deviations at 4.5 and 7.5 ms aSOI indicate the insignificance of the observed difference in the two rates. Beyond 15 ms aSOI, the two evaporation rates approach similar values of 57 and 54 mg/(m²·ms) for the entire film and the central ROI, respectively. This indicates that the film has reached a uniform temperature and is exposed to uniform heat and mass-transfer conditions.

4.5.6 Shot-to-shot variability of the film mass

The error bars in the fuel-film mass evolutions in the previous sections indicate a significant shot-to-shot variation in the single-shot film mass. Figure 54 shows histograms of the fuel-film mass for different operating conditions and different times aSOI. Each histogram shows 200 film masses distributed among bins with a width of 0.01 mg. Also indicated is the coefficient of variation (COV, c_v), which is the relative standard deviation in the single-shot film mass.

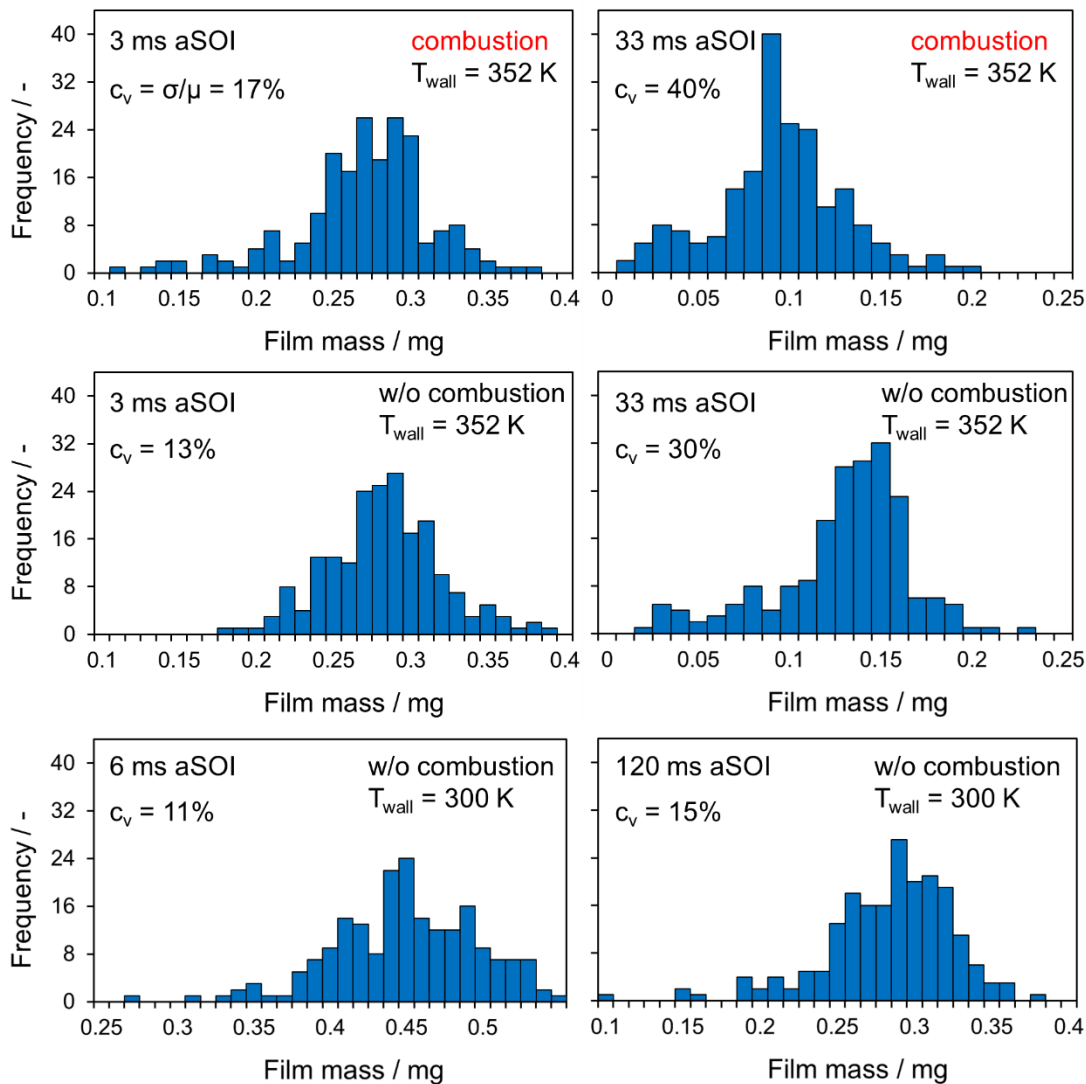


Figure 54: Histograms of the film mass at various times aSOI and under different operating conditions.

A part of the fluctuation in the film mass comes from fluctuations in the laser pulse energy, around 4.5% (see Section 4.5.7), while the major part results from stochastic variations in the physics related to fuel-film formation and evaporation. Spatial noise is not expected to affect the film mass since the mass is calculated from a region of around 10000 pixels such that variations in the film thickness are expected to even out by summing up the film thickness of all pixels.

For a wall temperature of 352 K, the film mass is subject to around three times higher fluctuations late aSOI, at 33 ms aSOI, compared to the film mass at 3 ms aSOI. The COVs are 40% and 30% at 33 ms aSOI and 17% and 13% at 3 ms aSOI with and without combustion, respectively. Most likely, the extent to which the fuel film contracts into thick droplets, i.e., size and number of fuel “blobs”, throughout the evaporation varies significantly between individual evaporation events. This, in turn, affects the total fuel-film area adhering to the wall and thus the film mass that has evaporated until that time aSOI. Therefore, with time the different contraction properties of the fuel film become more pronounced in the film mass. If the fuel is injected at ambient temperature and the wall is also at ambient temperature, the COVs in the film mass are only 11 and 15% at 6 and 120 ms aSOI, respectively. Compared to the high wall-temperature case, the higher viscosity and lower diffusion coefficient of the liquid fuel cause reduced local contraction of the film into thick droplets and thus a less fluctuating single-shot film mass. All histograms indicate a relatively symmetric distribution of the film mass around the mean.

4.5.7 Precision and accuracy

Uncertainty in the measured fuel-film thickness results from temperature differences between the fuel and the wall, changes in the composition of dissolved gases in the fuel, insufficient co-evaporation of iso-octane and toluene, and non-uniformities in the film thickness distribution in the calibration tool. The precision uncertainty is dominated by shot noise. A more in-depth discussion of the measurement uncertainty follows.

Since in the actual measurement the fuel was injected with nitrogen as pressurizing gas, the oxygen concentration in the liquid film might be different than that of the fuel layer in calibration. To test whether the fuel's oxygen saturation in the injector and supply system is affected by the pressurizing gas, fuel-film LIF was imaged from 3 to 80 ms aSOI with air and nitrogen as pressurizing gases. Before each measurement, the fuel was pressurized with air or nitrogen in the fuel supply system for two hours as it was the case during the measurements. Figure 55a shows the LIF signal of film 6 spatially integrated and normalized by the signal at 3 ms aSOI after injecting with air and nitrogen. The results show that the deviations between the two curves are mostly within one standard deviation. This implies that the oxygen concentration of the pressurized fuel does either not change with the type of pressurized gas or the fuel immediately saturates with oxygen at ambient air pressure when travelling through the test section during injection.

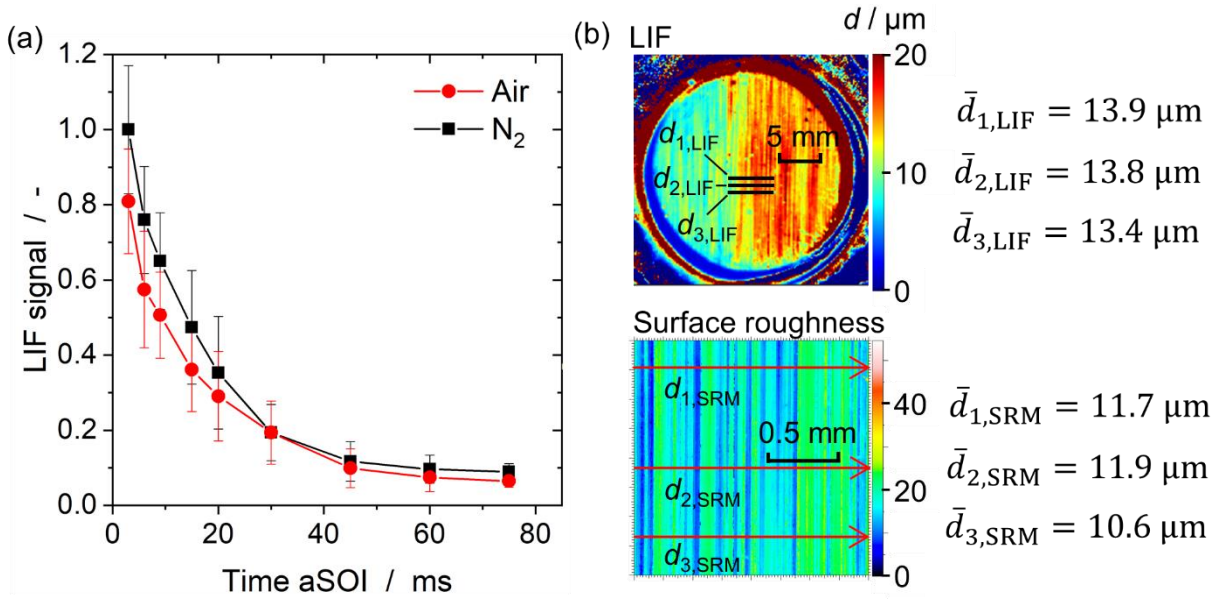


Figure 55: (a) Evolution of LIF signal, spatially integrated throughout fuel film 6 for air and nitrogen as pressurizing gases at different times aSOI. Error bars indicate the standard deviation among 50 single shots. (b) Surface roughness of calibration tool from a calibrated background LIF image and a surface-roughness measurement (SRM).

Figure 55b shows a flat-field corrected and calibrated background image of the calibration tool in the top and the result of a surface roughness measurement (SRM) of a small, central region ($1.6 \times 1.6 \text{ mm}^2$) in the calibration tool in the bottom. The SRM was done by the Institute of Metals Engineering at the University of Duisburg-Essen. Note that the exact location of the SRM is not known and also that the spatial resolution is 30 times higher than in LIF. The background image in the film-thickness calibration was acquired by illuminating the calibration tool filled with fuel and without precision shims inserted (nominal thickness zero). By that, the surface roughness of the black back plate is imaged. The image shows maximum thicknesses of $15 \mu\text{m}$. This is consistent with the results in Figure 34, where the signal/background-ratio of a $30 \mu\text{m}$ thick fuel layer is around 2:1 in the thick regions. The thickness was averaged along three different lines, each with a length of 5 mm in the center of the image, as indicated in Figure 55b. The average thickness is $13.7 \mu\text{m}$ in that region. The SRM finds the average surface roughness of $11.4 \mu\text{m}$ also in the central region of the calibration tool. The two methods find the magnitude in good agreement such that the SRM additionally verifies the calibration of the LIF signal versus the absolute fuel-film thickness as shown in Figure 34.

Concerning the fuel film temperature, the films were assumed to be at the initial wall temperature during evaporation such that the LIF signal of the fuel films was corrected with the ratio $\frac{I_f(298 \text{ K})}{I_f(T_w)}$ as given in equation (41). Therefore, a deviation in the film temperature from the initial wall temperature would result in an error in the predicted film thickness. As discussed in Section 4.6, the uncertainty in the fuel film temperature is estimated to be about $\pm 10 \text{ K}$. Figure 38 shows that at 352 K this corresponds to an uncertainty of 9% in the measured film thickness

Geiler et al. observed the effect of self-quenching for LIF of liquid toluene [130]. For a fuel-film layer of $100 \mu\text{m}$ thickness, he found the effect to be negligible up to toluene concentrations

in iso-octane of around 10 vol.-% and laser fluences of 1.5 mJ/cm². In this work, the toluene concentration was 1 vol.-% and the laser fluence below 0.2-0.3 mJ/cm².

The precision uncertainty was calculated from flat-field corrected single shots of the flat-field. The deviation of the signal from unity then is partly spatial noise, dominated by shot noise. The relative standard deviation in a region of 33 × 33 pixels (3 × 3mm²) is $\sigma_{\text{SN}} = 5.7\%$. The flat-field corresponds to a film thickness of 6.25 μm such that 5.7% is the precision uncertainty for that thickness. Shot-to-shot fluctuations in the laser pulse-energy and variation in spatial energy distribution of the laser profile might also result in signal fluctuations between single shots. The standard deviation of the spatially averaged signal from the 33 × 33 pixels ROI among 50 single shots of the flat-field was found to be $\sigma_{\text{LE}} = 4.5\%$. According to Gaussian error propagation, the overall precision uncertainty is $\sigma = \sqrt{\sigma_{\text{SN}}^2 + \sigma_{\text{LE}}^2} = 7.3\%$ (SNR = 13.8) at a film thickness of 6.25 μm and a resolution of 0.09 mm/px. Assuming that the noise is shot-noise dominated (SNR follows the \sqrt{N} -law), the spatial SNR is 5.5 (precision uncertainty of 18%) and 39 (precision uncertainty of 2.5%) for the minimum and maximum measured film thicknesses of 1 and 50 μm, respectively. Thus, the total precision uncertainty in the film thickness is between 18.5% and 5%. However, the film mass and thus evaporation rate are not affected by precision uncertainty since the film thicknesses from several thousand pixels are summed up such that fluctuations even out.

4.6 Fuel-film and wall temperatures

This section presents the development of a low-dimensional model (LDM) to determine transient fuel-film and wall temperatures. By means of the LDM, transient zero-dimensional fuel-film and one-dimensional wall temperatures were calculated throughout the course of fuel-film evaporation whose mass evolution was taken from the LIF measurements.

4.6.1 Model assumptions

In light of the literature results discussed in Section 3.2.2, thermal conduction in the 8 mm thick quartz wall was considered one-dimensional, perpendicular to the wall. Convective heat and mass transfer between the film and the gas were considered zero-dimensional. Then, the zero-dimensional fuel-film temperature, T_f , results from an energy balance, as shown in Figure 56a. Assuming a uniform temperature throughout the film perpendicular to the wall is consistent with Min and Tang [137] who found a maximum temperature gradient of 0.2 K in a 100 μm thick water film during evaporation from an adiabatic wall. The current work considers heat transfer between wall and film. Before spray impingement, heat is transferred conductively in steady-state through the wall resulting in a linear temperature profile. The inner wall temperature at $x = 0$ is 352 K and the outer temperature at $x = w$ is 344 K, both determined with a sheathed thermocouple (Type K, NiCr-Ni) temporarily attached to the wall with thin heat-resistant tape. As boundary conditions, the temperature on the outside was considered constant while the one on the inside was updated with the film temperature from the previous time step throughout calculation. The air temperature, T_{air} , of 381 K was measured in the core the air flow with a thermocouple under steady-state conditions and was considered constant.

The temperature profile in Figure 56b schematically shows the temperature through wall, film, and air. The energy balance was considered around a fuel-film element (green rectangle in Figure 56a) of 10×10 pixel cross section ($A_f = 0.77 \text{ mm}^2$). The film in this element had an approximately uniform thickness d ($10.4 \mu\text{m} \pm 0.4 \mu\text{m}$ at 3 ms aSOI) in the thickest region of fuel film 6, generated by spray 6. This neglects lateral heat transfer (parallel to the wall, in the y - and z -axis) between the thin outer parts of the film and the thick central parts. In principle, the local change in thickness and thus total heat capacity between these two regions would cause a lateral temperature gradient parallel even with uniform conductive and convective heat transfer everywhere on the fuel-film area.

Figure 56b shows images of film 6 with the fuel-film element indicated as well as the mass evolution of the film element. The polynomial fit function $m_f(t)$ approximates the data.

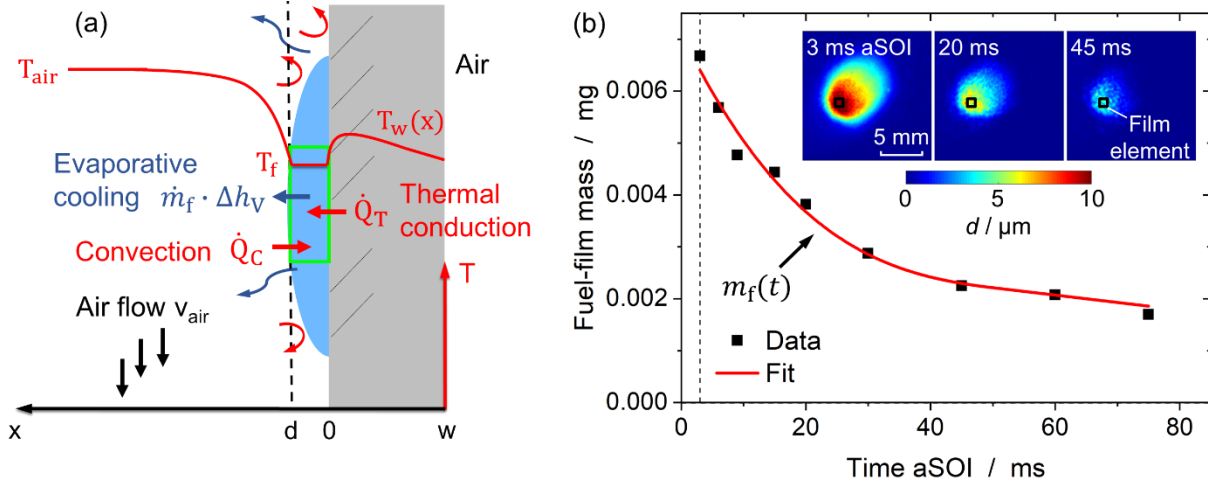


Figure 56: (a) Sketch of the evaporating fuel-film on the quartz wall with an energy balance around a fuel-film element (green rectangle) and a qualitative temperature profile through wall, film, and gas. (b) Mass evolution of fuel-film element (data and fit) of the case with $T_w = 352 \text{ K}$, $v_{air} = 1.8 \text{ m/s}$, $m_{inj} = 4.6 \text{ mg}$, without combustion. Figure published in [98].

4.6.2 Model development

Convectively, the heat flow \dot{Q}_C is transferred between the bulk air flow ($T_{air} = 381 \text{ K}$) and the fuel film. Between the quartz wall and the fuel film, heat is transferred via thermal conduction, \dot{Q}_T . Then, the change in internal energy of the fuel film, U_f , is expressed as:

$$\frac{\partial U_f}{\partial t} = m_f(t) c_V \frac{\partial T_f}{\partial t} + \frac{\partial m_f}{\partial t} c_V T_f = \dot{Q}_T + \dot{Q}_C \quad (43)$$

Considering the change in enthalpy during evaporation, equation (43) becomes

$$\frac{\partial U_f}{\partial t} = m_f(t) c_V \frac{\partial T_f}{\partial t} + \frac{\partial m_f}{\partial t} (h_g - h_l) = \dot{Q}_T + \dot{Q}_C \quad (44)$$

with h_g and h_l being the specific enthalpies of gaseous and liquid fuel, respectively, with the difference being the heat of vaporization Δh_V :

$$\frac{\partial U_f}{\partial t} = m_f(t) c_V \frac{\partial T_f}{\partial t} + \frac{\partial m_f}{\partial t} \Delta h_V(T_f) = \dot{Q}_T + \dot{Q}_C \quad (45)$$

Inserting expressions for the heat flows according to the assumptions discussed above yields a first-order partial differential equation for the fuel-film temperature:

$$\frac{\partial T_f}{\partial t} m_f(t) c_V = -\lambda_w A_f \left. \frac{\partial T_w}{\partial x} \right|_{x=0} + \alpha A_f (T_{\text{air}} - T_f) - \dot{m}_f(t) \Delta h_V(T_f) \quad (46)$$

As shown in Figure 56b, the mass evolution of the fuel-film element measured with LIF was fitted with a polynomial function to determine $m_f(t)$ and $\dot{m}_f(t)$ as inputs for the model. The heat capacity of iso-octane, c_V was considered constant with a value of 241 J/(mole K) [191]. A temperature-dependent correlation for Δh_V of iso-octane was taken from [192].

To determine the convective heat flow between the air and the fuel film, an equation for the heat transfer coefficient α is required. The latter is obtained via the Reynolds analogy from the mass transfer coefficient contained in equation (47):

$$\dot{m}_f(t) = \beta A_f (\rho_{\text{sat}}(T_f) - \rho_{\infty}). \quad (47)$$

Here, $\rho_{\text{sat}}(T_f)$ is the fuel-vapor concentration on the film surface, which was calculated from the saturation vapor pressure, p_{sat} , of the fuel (under the assumption of constant total pressure) with the Antoine parameters of iso-octane, A_{iso} , B_{iso} , and C_{iso} , from Willingham et al. [193]:

$$p_{\text{sat}} = 10^{\left(A_{\text{iso}} - \frac{B_{\text{iso}}}{C_{\text{iso}} - T_f}\right)} \quad (48)$$

The fuel-vapor concentration in the bulk of the air flow, ρ_{∞} , was considered zero (see Section 5.2). Rearranging the Reynolds analogy [21]

$$\frac{Nu}{Pr^n} = \frac{Sh}{Sc^n} \quad (49)$$

and replacing $Nu = \frac{\alpha L}{\lambda_{\text{air}}}$ and $Sh = \frac{\beta L}{D_{\text{air/fv}}}$, where λ_{air} is the thermal conductivity of air (0.032 W/(m·K) at 380 K [194]) and $D_{\text{air/fv}}$ is the diffusion coefficient between air and fuel vapor (0.152·10⁻⁴ m²/s at 381 K [195]), gives an expression for the heat transfer coefficient:

$$\alpha = \frac{\lambda_{\text{air}} \beta}{D_{\text{air/fv}} Le^n} \text{ with } Le = \frac{Sc}{Pr} = \frac{a_{\text{air}}}{D_{\text{air/fv}}} \text{ and } n = \frac{1}{3} \quad (50)$$

Here, a_{air} is the thermal diffusivity of air, which was calculated from λ_{air} as 3.47·10⁻⁵ m²/s. To determine the conductive heat flux between the wall and the fuel film, the temperature gradient $\left. \frac{\partial T_w}{\partial x} \right|_{x=0}$ in the wall at $x = 0$ is obtained by discretizing the one-dimensional heat equation of the wall

$$\frac{\partial T_w}{\partial t} = a_w \frac{\partial^2 T_w}{\partial x^2} \quad (51)$$

in time and space. The thermal diffusivity, a_w , of the wall was calculated from the thermal conductivity λ_w of 1.5 W/(m·K), taken from [196]. The implicit finite difference method according to Crank-Nicholson was used for discretization [82, 197, 198], see Section 2.2.2, with the centered difference approximation for the temporal derivative at $(x_i, t_{n+\frac{1}{2}})$ and an average of the second-order spatial differences at (x_i, t_n) and (x_i, t_{n+1}) , see equation (12). Figure 57 schematically shows a section of the temperature grid-points distributed along the wall while the vertical and horizontal axes indicate the temporal and spatial dimensions, respectively. Spatially, the quartz wall was discretized into 500 grid points with a distance of $\Delta x = 16 \mu\text{m}$ between two grid points. The evaporation time of 75 ms was discretized into 1000 time steps, resulting in a temporal resolution of $\Delta t = 75 \mu\text{s}$. Therefore, the space-time mesh had a total number of 500,000 grid points. At the beginning (t_0), the temperature in every grid point along the x-axis was known from the stationary thermal conduction (linear temperature profile) through the wall before spray impingement. The temporal and spatial differences in temperature between grid points yield difference quotients which are used to approximate the derivatives in equation (51). With the discretized temperature gradient $\left. \frac{\Delta T_w}{\Delta x} \right|_{x=0}$ equation (46) is simplified to an ordinary differential equation (ODE) from which the fuel-film temperature was determined numerically with Python 2.7. For solving, an initial condition for the fuel-film temperature is required. Since this temperature is unknown, in an *a-posteriori* sensitivity analysis a range of physically plausible temperatures was considered, as will be discussed in Section 4.6.4.

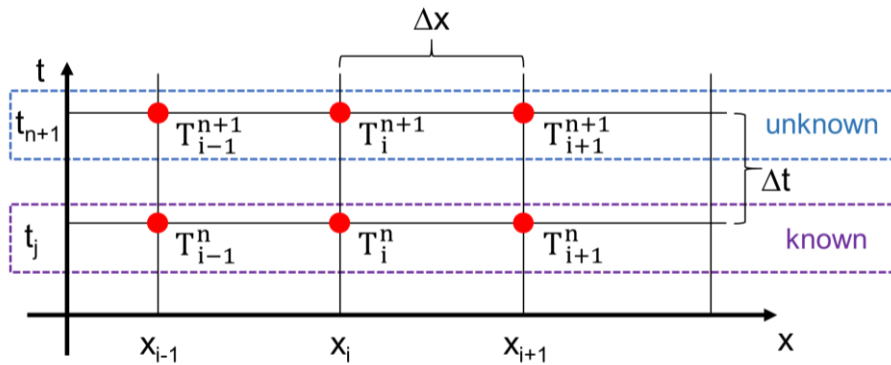


Figure 57: Wall-temperature grid points for temporal and spatial discretization.

4.6.3 Solving scheme

Figure 58 shows the flow chart of the film and wall-temperature calculation. The simulation starts at 3 ms aSOI, when most of the spray dynamics have disappeared and a stable fuel film has formed. The film is considered to instantaneously change the wall-temperature at $x = 0$ to the initial fuel-film temperature. Based on that disturbance in the linear wall-temperature profile, the one-dimensional heat equation, equation (51), is solved for the subsequent time step Δt so that an updated wall-temperature profile is obtained. Then, the spatial temperature difference $\frac{\Delta T_w}{\Delta x}$ between the grid points at $x = 0$ and $x = \Delta x$ is used to calculate the heat conductively transferred between wall and fuel film within Δt . From the product of the mass evaporated in Δt and the enthalpy of vaporization, the heat of vaporization, cooling the fuel

film, is calculated. From the Reynolds analogy, an updated heat transfer coefficient is calculated based on the current film temperature which is then used to determine the heat convectively transferred within Δt . The resulting terms for \dot{Q}_T , \dot{Q}_C , and $\dot{m}_f \Delta h_V$ are then used to solve the ODE determine the film temperature after Δt . Then, the new film temperature again is replacing the current wall temperature at $x = 0$ and the calculation of \dot{Q}_T , \dot{Q}_C , and $\dot{m}_f \Delta h_V$ throughout the next time interval is processed. Therefore, the heat equation of the wall and the differential equation of the film temperature are solved successively.

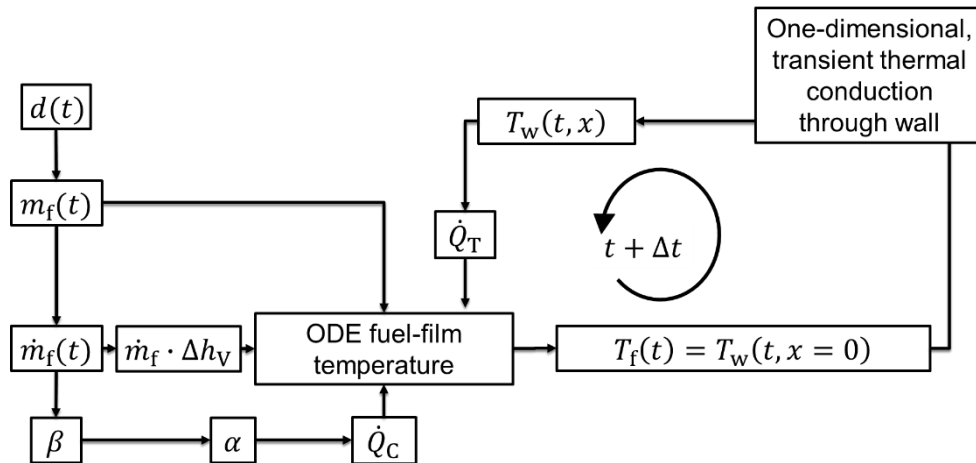


Figure 58: Schematic procedure for calculating the film and wall temperatures throughout the time step Δt .

4.6.4 Results

The results from the LDM in Figure 59 show the heat fluxes between the fuel-film element and its surrounding, as well as the resulting film and wall temperature evolutions. The conductive and convective heat fluxes are considered negative if they flow out of the film element. The enthalpy flux due to vaporization is always negative, since it is cooling the film element. The change in the internal energy of the film is considered positive if the film temperature increases.

Here, the initial film temperature (361 K) was set equal to the injector temperature, which is 9 K above the initial wall temperature (352 K). The resulting thermal conduction from the film to the wall and the evaporative cooling cause the high rate of change in internal energy. At 4.1 ms aSOI the film temperature has decreased below the adjacent wall's temperature such that thermal conduction becomes positive and increases in magnitude. The decrease in film temperature also increases the differential driving the convective heat transfer, but at the same time the heat transfer coefficient decreases because turbulence from the injection dissipates. However, the conductive and convective heat fluxes, the latter being 10 times smaller than the former, do not compensate for the evaporative cooling such that the film temperature further decreases -although more slowly- from 4.1 to 18 ms aSOI. From 18 ms aSOI on, the sum of thermal conduction and convection slightly exceed the evaporative cooling, the change in internal energy becomes positive, and the film temperature slowly increases from the minimum of 347 K to eventually 349 K at 75 ms aSOI. Figure 59b shows that already at a depth of 1.5 mm the wall temperature is almost unaffected by the film evaporation. Eventually, the mean film temperature becomes constant with a value of about 350 K, close to the initial wall temperature

of 352 K, which explains the quasi-steady evaporation rates determined from LIF and CFD, shown in Figure 47.

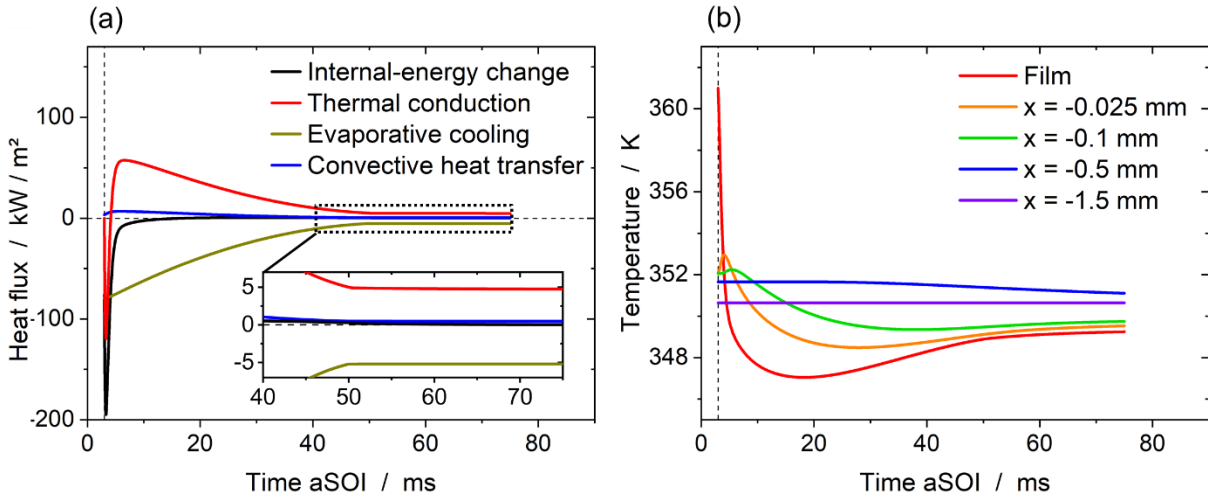


Figure 59: (a) Heat fluxes from the fuel-film element determined from the LDM. (b) Fuel-film and wall temperatures at different depths of the quartz wall versus time. $T_w = 352$ K, $v_{air} = 1.8$ m/s, $m_{inj} = 4.6$ mg, without combustion. Dashed vertical lines indicate the time 3 ms aSOI. Figure published in [98].

In a CFD simulation, Zhang et al. [133] found a positive peak in the conductive heat flux at the end of injection and during the evaporation of n-tridecane. As in the present study, they report the highest heat transfer coefficient during the injection and a decrease in that coefficient by about a factor of 14 (17 in this work) when the gas motion is becoming slower. Min et al. [137] numerically determined the heat fluxes around 100 μ m thick evaporating water films on an adiabatic wall and found the convective heat flux of 300 W/m² to be about 10 times smaller than the thermal conduction of 2900 W/m² within the film, mainly compensating for evaporative cooling. This ratio is consistent with the current results, since during the late evaporation stage (long after the end of injection, $t > 45$ ms aSOI), the heat fluxes for convection and conduction are 0.5 and 5 kW/m², respectively. Overall, it is clear that at the conditions examined here the heat flux between wall and film has a much greater influence on the film temperature and evaporation rate than the convective heat flux resulting from e.g., the elevated temperature in combustion.

To analyze the impact of the unknown initial film temperature, that parameter was varied. Figure 60 shows fuel-film temperature evolutions from the LDM for three different initial film temperatures and from the CFD. Since the film-mass data is available only from 3 ms aSOI onward (see Figure 56b), calculations from the LDM also start at that time. In contrast to that, the CFD simulation yields the film temperature already from around 1 ms aSOI when impinging droplets initiate the fuel-film formation. An initial temperature of 352 K corresponds to the case that the spray droplets on the wall assume the wall temperature of 352 K very fast. Setting the initial temperature to 346 K assumes that the spray droplets undergo significant evaporative cooling in flight such that the initial film temperature is below the injector temperature (361 K). The CFD results were not known when the LDM part of this study was conducted and the evaporation-induced temperature differential was set to 15 K. In fact, the CFD simulation

predicts the initial film temperature (at 1 ms aSOI) to be 342 K, 19 K below the injector temperature due to that effect, which is qualitatively consistent with Hildenbrand et al. [199]. Finally, the simulation with 361 K consider the case that the fuel droplets do not undergo substantial cooling or heating before impinging on the wall.

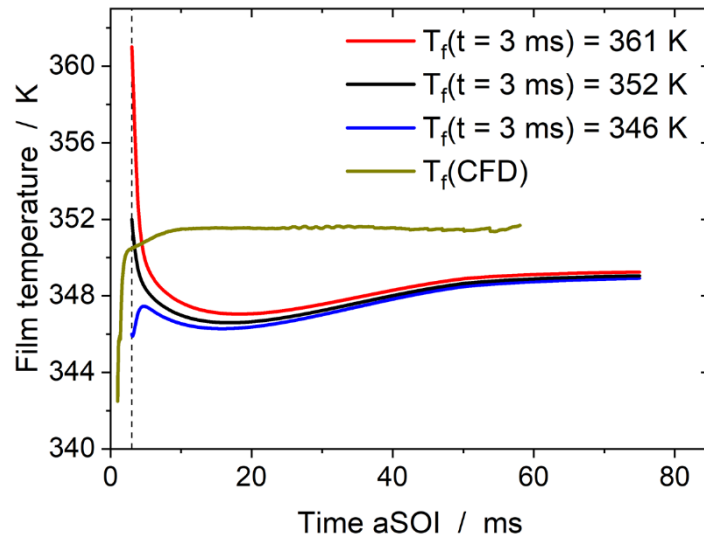


Figure 60: Film-temperature evolution for different initial temperatures calculated in LDM and CFD simulations. Figure published in [98].

Regardless of the initial film temperature, the LDM here predicts very similar temperature traces after around 5 ms aSOI throughout evaporation with a minimum in temperature around 18 ms aSOI and eventually approaching the initial wall temperature. In the CFD simulation, a quasi-steady film temperature of around 351 K is already approached at 3 ms aSOI. This suggests a higher heat flux between film and wall in the CFD than in the experiment and also explains the difference in evaporation rates already seen at early times aSOI for wall temperatures 332 and 352 K in the simulation in Figure 47. Both the LDM and CFD agree in that the fuel film rapidly approaches the wall temperature, which does not decrease much throughout evaporation.

Figure 61 shows the wall temperature traces between $x = 0$ mm and $x = -0.9$ mm at different times aSOI. Before spray impingement, the temperature profile in the wall is linear with a slope of 1 K/mm. At 3 ms aSOI, the fuel film with a temperature of 361 K adheres to the left side of the quartz wall at $x = 0$ mm. The black dashed line indicates the interface between the air flow and the quartz wall and thus the fuel-film position. The fuel film is considered the first grid point of the wall. Therefore, the wall temperature at $x = 0$ mm indicates the film temperature, highlighted by the blue dots. With the start of the simulation at 3 ms aSOI, the steep temperature gradient is being reduced by the evaporative cooling of the film and the conductive transport of heat towards the inner of the wall. At 4.4 ms aSOI the film temperature has decreased below the highest wall temperature (at $x = -0.016$ mm), such that in part of the domain the direction of thermal conduction reverses, and the wall conductively heats the fuel film. The temperature gradient between surface and temperature maximum first steepens further, but then decreases again. Even at 50 ms aSOI, when most of the fuel has evaporated, only the first 0.6 mm of the

8 mm thick wall are significantly affected by the temperature depression on the surface, validating the initial assumption of a semi-infinite wall.

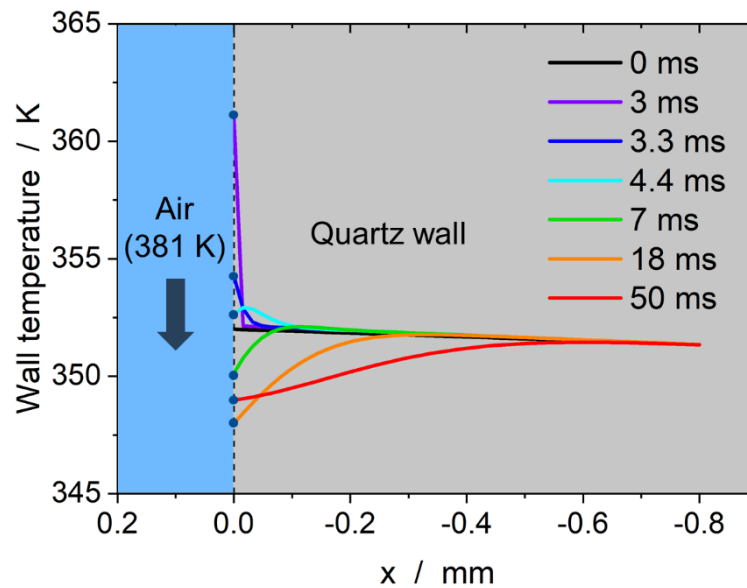


Figure 61: Wall temperature traces at different times aSOI.

4.7 Section conclusions

Quantitative tracer-LIF of an iso-octane/toluene-mixture was used to image the thickness of fuel films evaporating from a hot quartz wall. The fuel films form on the window after high-pressure injection of fuel into the test section of the constant-flow facility. Prior to fuel-film imaging, PIV and optical flow were used to characterize the flow field in the test section under steady-state and transient operation. Under steady-state operation, the results show that the inserted grid upstream of the test section breaks the symmetry of the plug flow, which is an undesired effect, but as intended causes small-scale turbulence, thus enhancing fuel/air-mixing. In transient operation, i.e., shortly aEOI, increased gas velocities are observed near the spray/wall impingement-region. Even higher gas velocities are found when the fuel is combusted, and the volume dilatation caused by combustion pushes some of the fuel-vapor cloud of the test section.

Preliminary measurements were done to investigate the photophysical and physicochemical properties of the iso-octane/toluene-mixture which was used for fuel-film imaging. Despite the slightly different boiling points of the two species, it was found that for this composition they co-evaporate very well such that significant enrichment of toluene is not observed (error < 5% with 95% of the fuel evaporated). Consistent with Geiler [130], the toluene LIF signal was found to be dependent on temperature and the number of laser pulses irradiating the fuel film was found. The signal of a fuel layer of 100 μm increased by a factor of 3.7 after irradiation with 2000 laser pulses. This was attributed to decreased oxygen quenching resulting from “laser degassing”, postulated to be removal of oxygen from the fuel layer in locally hot regions. However, it was found that in the actual measurement laser degassing was not important because every fuel-film was exposed to only a single laser shot. The fuel layers in the calibration tool were exposed to only 50 laser pulses to make the signal increase from laser degassing

negligible. In contrast to this, the temperature dependency had to be considered, and the acquired data were used to account for the difference in the LIF signal that occurs because the fuel-film temperature is different in calibration and actual measurement. The calibration was done in-situ by creating fuel layers of known thickness in a thin-film cuvette as a calibration tool. In the spray-film measurements, sets of single shot images of the film thickness were acquired at multiple times aSOI. From such images the fuel-film mass and evaporation rate versus time aSOI were determined. Selected LIF results were compared to those of a 3D-CFD simulation

The fuel-film thickness distributions are both qualitatively and quantitatively similar in simulation and experiment throughout the entire evaporation process. Both LIF and CFD find an accumulation of fuel in the outer regions of the four fuel films due to the spray impact. At ambient temperature and without flow and combustion, the CFD predicts approximately 30% less initial fuel-film mass than found in the experiment, while the evaporation rates are very similar. The images show that CFD slightly underpredicts both thickness and area and does not show the formation of “fuel blobs” – local convex bulges within the fuel-film structure – that are clearly seen in single shots in LIF imaging, in particular at elevated wall temperature.

At elevated temperature, the CFD predicts about two times higher evaporation rates than LIF measures, while the fuel-film mass is very similar in LIF and CFD. Generally, the evaporation rate is highest early aSOI for LIF and CFD because of high turbulence and mass transfer coefficients, then decreases and remains quasi-steady from 10-15 ms aSOI onward, with the magnitude strongly depending on the wall temperature. The quasi-steady evaporation rate indicates a constant mass transfer coefficient and fuel-vapor concentration gradient, the latter implying constant film temperature. Combustion has a minor effect on the fuel-film evaporation rate compared to the wall temperature in either CFD or LIF. While there is no effect from the fast-propagating turbulent premixed flame on the early evaporation rate, a local maximum becomes apparent at 30 ms aSOI in LIF, which is attributed to the persistent fuel consumption by the nearby, relatively stationary non-premixed sooting combustion increasing the diffusive flux of fuel towards the film surface. The influence of combustion becomes more prominent for an increased injected mass. The flow velocity and the turbulence in the flow, induced by the grid, were found to increase the quasi-steady evaporation rates.

In the time-dependent LDM, the fuel-film temperature was determined from a heat balance around a fuel-film element, and the wall temperature was determined one-dimensionally by discretizing the wall heat equation. According to this model, the quartz wall only slightly cools down in the impingement region early aSOI as the conductive heat flux from the bulk solid keeps the surface temperature close to the initial temperature. Consistent with results from the CFD, the fuel-film temperature rapidly approaches the wall temperature, independent of the initial film temperature. This validates the assumption that the film is at initial wall temperature and shows that correcting the LIF signal based on the wall temperature is indeed reasonable. Also, it means that the wall temperature determines the fuel-film temperature, thus its saturation vapor pressure, and thereby the evaporation rate. The LDM also shows that the convective heat flux from the gas phase is about 10 times lower than thermal conduction from the wall,

consistent with the finding from CFD and LIF that under the current conditions, combustion has minor effect on the evaporation rate.

5 Soot formation

This chapter presents method and results of the visualization of PAH LIF, soot LII, soot incandescence, and chemiluminescence in the vicinity of evaporating fuel films. The investigations were performed in two laminar co-flow diffusion flames, in the constant-flow facility, and in an optically accessible engine. In the constant-flow facility, also the air/fuel ratio was imaged prior to the flame front burning out the fuel/air-mixture. Parts of the content and data was published in Jüngst et al. [96-98], in particular Sections 5.2.1, 5.3.1, 5.3.2, 5.4.1, 5.4.2, 5.5.

5.1 Experimental facilities

This section presents two experiments, laminar diffusion-flame burners and an optically accessible engine. The constant-flow facility was already introduced in Section 4.1.

5.1.1 Laminar co-flow diffusion-flame burners

Figure 62 shows photos of the two laminar co-flow diffusion-flame burners, the so-called Yale burner [200] and the Santoro burner [63]. Both burners are used in several research institutes with standardized operating conditions and are well characterized. The Yale burner was partially manufactured and assembled within the scope of this work while the Santoro burner was already available to use. Both burners provide stationary sooting flames which are suitable for preliminary measurements in the context of soot LII and PAH LIF. They consist of a central nozzle providing a constant ethylene flow which is surrounded by a honeycomb that provides the air flow. The inner diameters of air and fuel outlets are indicated in Figure 62.

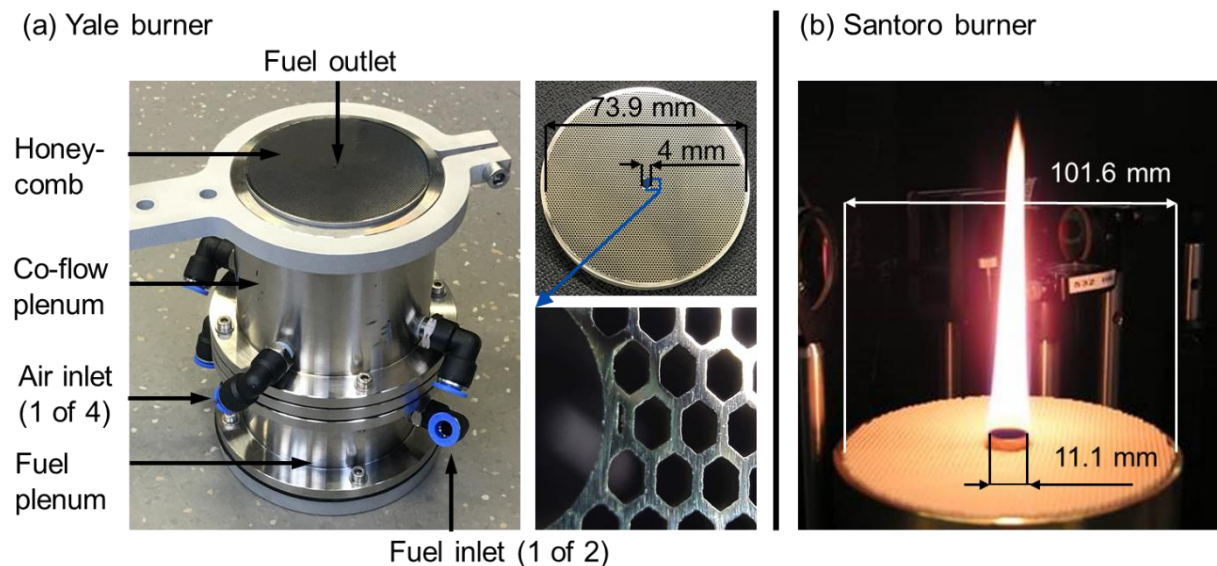


Figure 62: Experimental setup of (a) Yale and (b) Santoro burner [63].

For the Yale burner, the co-flow plenum, the fuel housing, and an intermediate plate between the two elements were already available before assembling burner. Four NPT (National Pipe Thread) connectors were screwed into the co-flow plenum to provide the required air flow. The fuel plenum was equipped with two NPT connectors distributing the fuel flow. A plate between

the two plenums separates fuel from air. The fuel tube protruded through the intermediate plate and the honeycomb and was sealed in the bores against the co-flow plenum. A sintered matrix and a honeycomb reduce turbulence and rectify the air flow. The sintered matrix was placed below the honeycomb within the co-flow plenum. The honeycomb was 3D-printed. Figure 62a shows a close-up view of the honeycomb around the fuel nozzle. Each pore had a diameter of 0.9 mm. The operating parameters of the burners were chosen consistent with the literature [63, 201, 202]. Mass-flow controllers and “rotameters” were used to set the desired flow rates of fuel and air. The gas inputs of the Yale burner allowed for diluting the fuel with 20, 40, 60, or 68% nitrogen to control the soot loading of the flame, as indicated in Table 4.

Table 4: Operating parameters for Yale and Santoro burners.

Burner type	Yale burner	Santoro burner
Fuel	Ethylene/air	Ethylene/air
Fuel/air equivalence ratio Φ	Non premixed	Non-premixed
Fuel flow-rate	0.264 / 0.211 / 0.158 / 0.105 / 0.084 slm	0.23 slm
N ₂ flow-rate	0 / 0.053 / 0.106 / 0.159 / 0.18 slm	-
Co-flow	56.8 slm	43 slm
Fuel flow-velocity	35 cm/s	4 cm/s
Co-flow velocity	35 cm/s	8.9 cm/s

5.1.2 Optically accessible gasoline engine

Simultaneous visualization of PAH and soot was also performed in an optically accessible single-cylinder SIDI engine as an initial more complex application of the diagnostic. The measurements were performed in collaboration with Bosch at their facility in Renningen. Figure 63 shows a cross-sectional view of the combustion chamber and the engine periphery as well as the operating condition. The injector of the four-valve SIDI engine with a pent-roof head was centrally mounted and the piston surface was flat. The cylinder liner and a part of the piston were manufactured from fused silica thus providing optical access. The Bowditch-type piston was extended by a 45°-mirror. The intake pressure was 1 bar and the engine was operated at 1200 rpm skip fired with 20 rest cycles and one working cycle. The skip-fired operation was chosen to not significantly heat up the combustion-chamber walls and the piston. This was necessary to ensure wall wetting by fuel films which then also survive into the exhaust stroke, interact with the flame front, and produce soot. Since iso-octane has a low sooting tendency, the engine was run at ambient temperature. This includes the cooling-water, intake, and oil temperatures. The injection started at -360°CA (the beginning of the intake stroke) and ended at -348°CA such that the piston was close to the injector during injection and significant wall wetting occurred. The engine was run at medium load with an injected mass of 17.1 mg and at globally stoichiometric conditions ($\lambda = 1$). The same injector was used as in the constant-flow experiments discussed in Section 4.1, producing six individual fuel films on the piston surface.

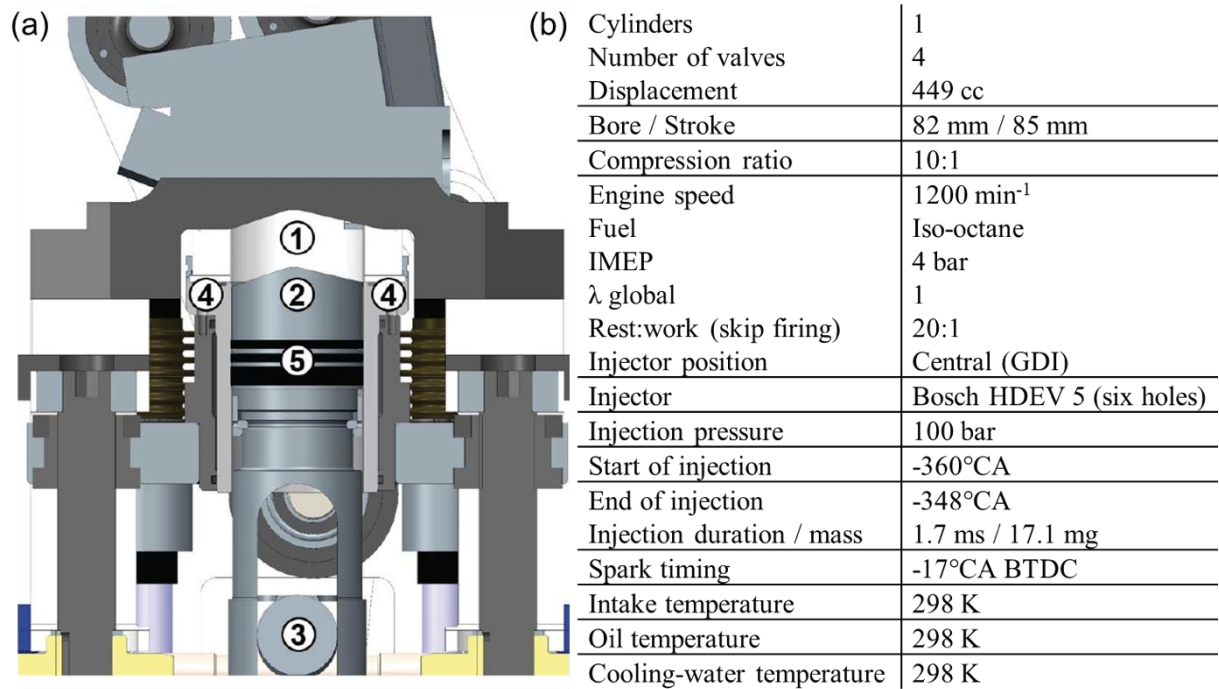


Figure 63: (a) Cross-sectional view of the combustion chamber and engine periphery of the optically accessible SIDI engine. (1) Quartz cylinder-liner, (2) piston, (3) aluminum Bowditch-mirror, (4) liner, (5) graphite piston-rings. Adapted from Geiler [130]. (b) Engine geometry and operating conditions for PAH LIF + soot LII experiments. IMEP: indicated mean effective pressure.

5.2 Fuel-vapor and air/fuel-ratio imaging

The air/fuel ratio was imaged by tracer LIF in the test section of the constant-flow facility to assess the soot formation characteristics of the premixed fuel/air-mixture and the non-premixed fuel/air-mixture near the fuel films. During combustion, the LIF images were used to visualize the fuel vapor near the evaporating fuel films. A mixture of 90 vol.-% iso-octane and 10 vol.-% toluene was used. In the following, the optical layout, the quantification procedure, and the results are shown.

5.2.1 Optical layout

Figure 64 shows a plan view of the optical layout for fuel-vapor imaging. Here, a laser sheet formed a two-dimensional plane within the test section at 266 nm. The beam was deflected towards the test section by the Pellin-Broca prism and mirrors. An energy monitor captured a reflection of every laser pulse and was used to account for shot-to-shot fluctuations in laser energy. A positive cylindrical lens ($f = 400$ mm) focused the laser beam horizontally. A negative cylindrical lens ($f = -25$ mm) expanded the beam vertically to a light sheet. An aperture clipped the light sheet vertically so that the FOV had a height of 100 mm with a laser-sheet thickness of 0.5 mm. The light sheet intersected the fuel films 2 and 6. An intensified CCD camera was equipped with a UV lens (Cerco, $f = 45$ mm, $f/1.8$) and a bandpass filter centered at 292 nm, BP 292/27. The projected pixel size was 0.15 mm/pixel. Again, the time between two images was 2.5 s, long enough to flush the fuel vapor from the test section.

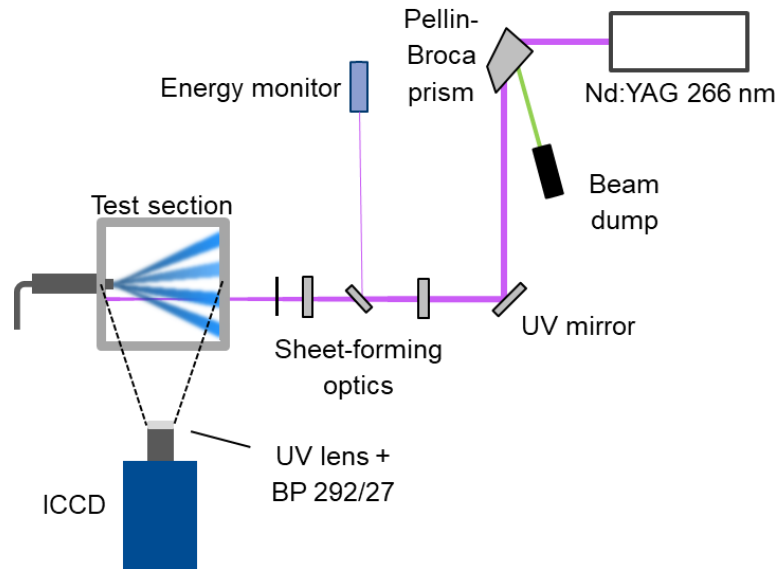


Figure 64: Optical layout for fuel-vapor LIF.

5.2.2 Equivalence-ratio calibration

Calibration of the LIF signal versus the fuel/air equivalence ratio (in the following called equivalence ratio) Φ and acquisition of a corresponding flat-field were done with the same arrangement. With the air heater switched off, i.e., at room temperature ($T = 295$ K), the air flow through the constant-flow facility was interrupted by inserting metal sheets into the top and bottom of the optically accessible section, as indicated in Figure 65a. A known mass of fuel was injected into the closed volume and evaporated while a small fan in the lower part of the section increased the mixing of air and fuel vapor, thus creating a homogeneous fuel/air-mixture with known fuel concentration.

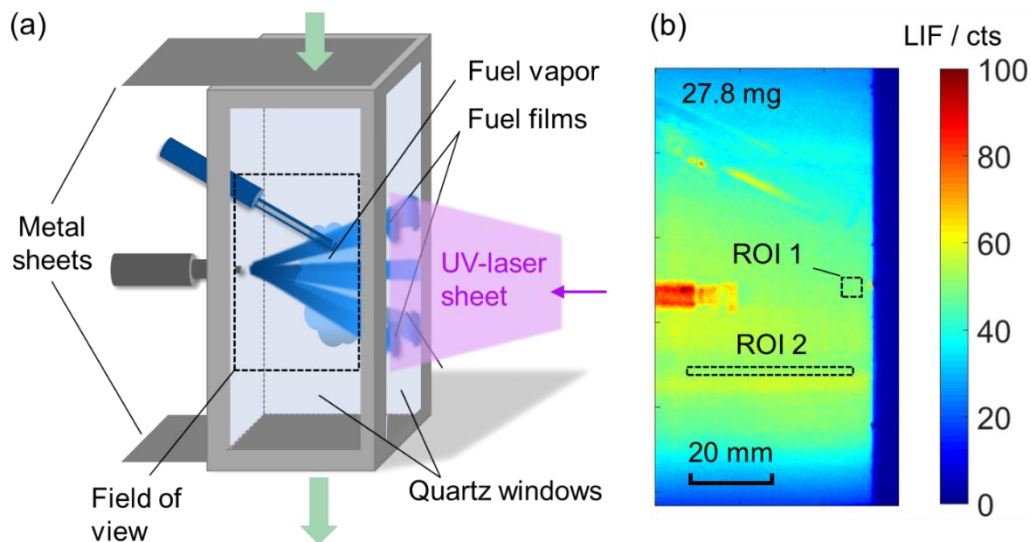


Figure 65: Calibration and flat-field acquisition: (a) covering the top and bottom of test section with metal sheets generates a closed volume. (b) Background-corrected ensemble average of 100 single-shot images of fuel-vapor LIF after 6 injections (each 4.6 mg) into the resulting closed volume.

Figure 65b shows the background-corrected ensemble average image for an injected mass of 27.8 mg. Under the assumption of isochoric mixing, the mole fraction of fuel and the equivalence ratio become 0.35% and 0.2, respectively. The temperature of the fuel/air-mixture was measured with a thermocouple and it was found that the effect of evaporative cooling of the charge was negligible. This is most probably due to two reasons. First, the fan increases convective heat transfer between the charge and the walls. Also, a significant part of the fuel evaporates from the walls and this does not contribute much to the evaporative cooling of the charge.

In the flat-field image the laser sheet enters from the right. The injector is visible on the left side of the image. The electrodes were slightly behind the illumination plane and are visible above the injector. The high intensities at the injector result from the light sheet being reflected by the polished nozzle. The LIF intensity decreases towards top and bottom of the FOV mainly because of the transverse intensity profile of the laser. Also, the field-dependent collection and detection efficiencies of the imaging system cause intensity gradients. First, the flat-field image was used to account for the spatially inhomogeneous excitation, detection, and collection efficiencies in fuel-vapor LIF imaging. Second, the flat-field was used for the absolute calibration of the equivalence ratio.

Figure 66 plots the LIF signal, spatially averaged in ROI 1, versus the injected mass, ranging from 27.8 to 776 mg, and the equivalence ratio. The LIF data shows a non-linear relation with the injected mass. The asymptotic fit onto the data follows the equation:

$$I_{\text{LIF}} = 718.87 \text{ cts} \cdot (1 - e^{-0.00257 \frac{1}{\text{mg}} \cdot m_{\text{inj}}}) \quad (52)$$

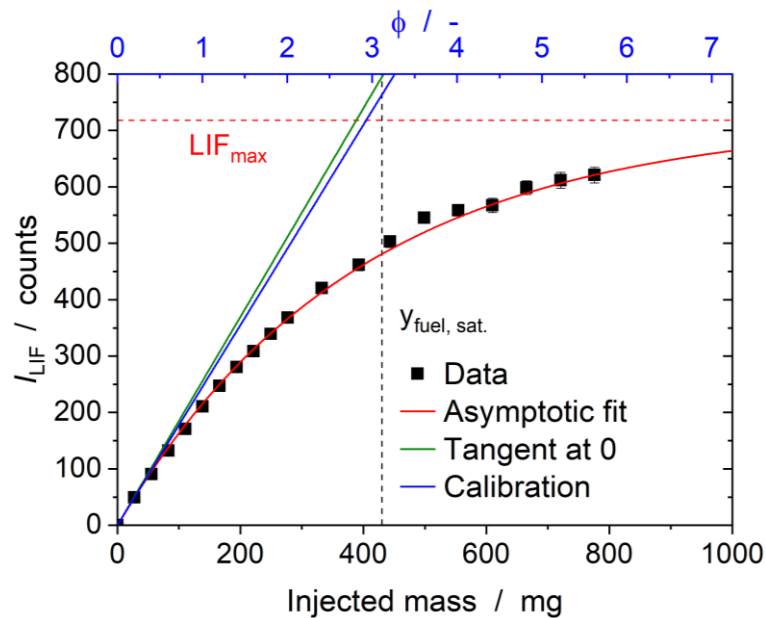


Figure 66: LIF signal versus injected mass of fuel and equivalence ratio. Error bars indicate the standard deviation of the spatially averaged signal in ROI 1 from 100 single shots.

In a next step it was clarified that the non-linear relation between the LIF signal and the injected mass in Figure 66 does not stem from laser absorption in the gas phase. Therefore, LIF signal

was vertically integrated in ROI 2, indicated in the lower part of the image in Figure 65b for the injected mass of 500 mg. The result is a clearly linear relation of the signal with increasing distance from right to left (graph not shown here). This linear relationship over 4 cm path length can be expected. The 700 times lower density and the dilution with air in the test section correspond to a 2500 times lower concentration of toluene in the fuel vapor than in the liquid fuel. Therefore, the absorption of the laser in a 4 cm thick fuel-vapor layer equals that in 16 μm of liquid fuel film where a linear relation between LIF signal and the film thickness was found up to 50 μm thickness. Based on that, a linear relation between LIF and injected mass is expected. Therefore, the non-linearity between LIF and the injected mass is attributed to leakage of fuel/air-mixture through the housings of injector and spark-electrodes. The higher the injected mass, the higher the leakage rate and thus the deviation from linearity. The rise in the LIF signal beyond the saturation mole-fraction, indicated by the dashed line Figure 66, also indicates a leakage and that the saturation concentration has not been reached (The saturation mole-fraction was calculated under the assumption of constant volume). The asymptotic fit function in Figure 66 indicates that the maximum LIF signal is 718 cts, which must correspond to the saturation fuel mole-fraction of 5.16% (injected mass 440 mg).

The nominal equivalence ratio, indicated at the top x-axis in Figure 66, was calculated from the injected mass assuming isochoric (constant volume) mixing as follows. The closed chamber has a height of 0.57 m, and a cross-sectional area of 0.003 m^2 . Thus, the total volume becomes 0.0017 m^3 . From the total injected mass, the concentrations of iso-octane and toluene, c_{iso} and c_{tol} , are calculated:

$$c_{\text{iso}} = \frac{\left(\frac{m_{\text{inj}} \cdot 0.877}{M_{\text{iso}}}\right)}{0.0017 \text{ m}^3} \quad (53)$$

$$c_{\text{tol}} = \frac{\left(\frac{m_{\text{inj}} \cdot 0.123}{M_{\text{tol}}}\right)}{0.0017 \text{ m}^3} \quad (54)$$

Here, m_{inj} is the injected mass while M_{iso} and M_{tol} are the molar masses of iso-octane and toluene, respectively. For a complete oxidation of the fuel, the stoichiometric oxygen concentration $c_{\text{O}_2, \text{stoich}}$ is required:

$$c_{\text{O}_2, \text{stoich}} = 12.5 \cdot c_{\text{iso}} + 9 \cdot c_{\text{tol}} \quad (55)$$

Equation (55) results from 12.5 and 9 molecules of oxygen required for oxidizing a molecule of iso-octane (C_8H_{18}) and toluene (C_7H_8), respectively. The actual oxygen concentration in the closed chamber is calculated from the ideal gas law

$$c_{\text{O}_2, \text{actual}} = \frac{p_{\text{O}_2}}{R T} \quad (56)$$

with the universal gas constant R , the partial pressure of oxygen p_{O_2} , and temperature T . Under the assumption that mixing with the injected fuel is an isochoric process, the partial pressure of

oxygen of 0.21 bar is constant. The temperature was also constant with 295 K. This yields the nominal equivalence ratio Φ :

$$\Phi = \frac{c_{O_2,stoich}}{c_{O_2,actual}} \quad (57)$$

However, according to the results discussed above, significant leakage of the fuel/air-mixture occurs if the injected mass accumulates, as indicated in Figure 66. Then, the mixing is not an isochoric process anymore. For a reliable and accurate calibration, the data point for the least injected mass of 27.8 mg was used for which the error from leakage is smallest. The time between the first injection and the image acquisition is short and the total pressure increases only about 0.35% such that leakage is expected to be negligible. The trace ‘‘Calibration’’ in Figure 66 is a linear function through the origin and the first data point (27.8 mg|49.5 cts). It has with a slope of 1.79 cts/mg and was eventually used to post-process the acquired images. Additionally, a first-order approximation from a Taylor series of the asymptotic fit function, equation (52), at $x = 0$ was used to verify that fuel/air-mixture has not leaked out of the closed chamber when acquiring the first data point, i.e., isochoric mixing:

$$f(x) = \sum_{i=0}^1 \frac{f^{(i)}(x_0)}{i!} (x - x_0)^i \quad (58)$$

$$f(x) = \frac{f^{(0)}(0)}{0!} (x - 0)^0 + \frac{f^{(1)}(0)}{1!} (x - 0)^1 \quad (59)$$

Inserting the solutions for f and f' from equation (52) gives an equation for the tangent at $x = 0$, which is the green line in Figure 66:

$$I_{LIF} = 1.848 \frac{\text{cts}}{\text{mg}} \cdot m_{inj} \quad (60)$$

The green first-order line is about 4% steeper than the blue line such that both lines find a similar proportionality between the LIF signal and the first data point. Additionally, both lines intersect the maximum LIF signal, found by the asymptotic fit, approximately where the fuel-vapor saturation concentration of 5.16% is reached ($\Phi = 3.1$). This further confirms that the mixing of fuel and air is nearly isochoric when acquiring the first data point.

5.2.3 Image processing and quantification

The image processing of the fuel-vapor LIF images is similar to that in fuel-film imaging. A background correction was applied to each fuel-vapor single shot and to the ensemble average flat-field image. Equation (61) comprises the image processing terms. The inverse of Φ gives the relative air/fuel ratio λ (in the following simply called air/fuel ratio):

$$\lambda(x, y) = \frac{1}{\Phi(x, y)} = \frac{1}{\frac{I_{exp}(x, y)}{I_{FF}(x, y)} \Phi_{FF,1} \frac{E_{reference}}{E_{measured}} \frac{I_f(295 \text{ K})}{I_f(T_{air})}} \quad (61)$$

Here, $I_{\text{exp}}(x,y)$ is the background-corrected LIF intensity during the measurement and I_{FF} the background corrected flat-field intensity, which corresponds to the equivalence ratio $\Phi_{\text{FF},1} = 0.2$. The correction of shot-to-shot fluctuations in laser energy was accounted for by $\frac{E_{\text{reference}}}{E_{\text{measured}}}$. Figure 67 shows the image post-processing applied to a single shot acquired at 6 ms aSOI. The difference in temperature of the toluene vapor in calibration and measurement was considered by the ratio $\frac{I_f(295 \text{ K})}{I_f(T_{\text{air}})}$, where $I_f(295 \text{ K})$ and the LIF signal at 295 K, and $I_f(T_{\text{air}})$ that at air temperature in the experiment. It was assumed that the fuel vapor is at the same temperature as the incoming air. The temperature dependence of toluene LIF signal in the gas phase at 1 bar air was taken from Benzler et al. [57]. From this data, the ratio $\frac{I_f(295 \text{ K})}{I_f(T_{\text{air}})}$ becomes 1.287, 1.371, and 1.479 for the air temperatures 345, 361, and 381 K. The impact of temperature fluctuations on the accuracy of the measured fuel/air-ratio is discussed in Section 5.2.5.

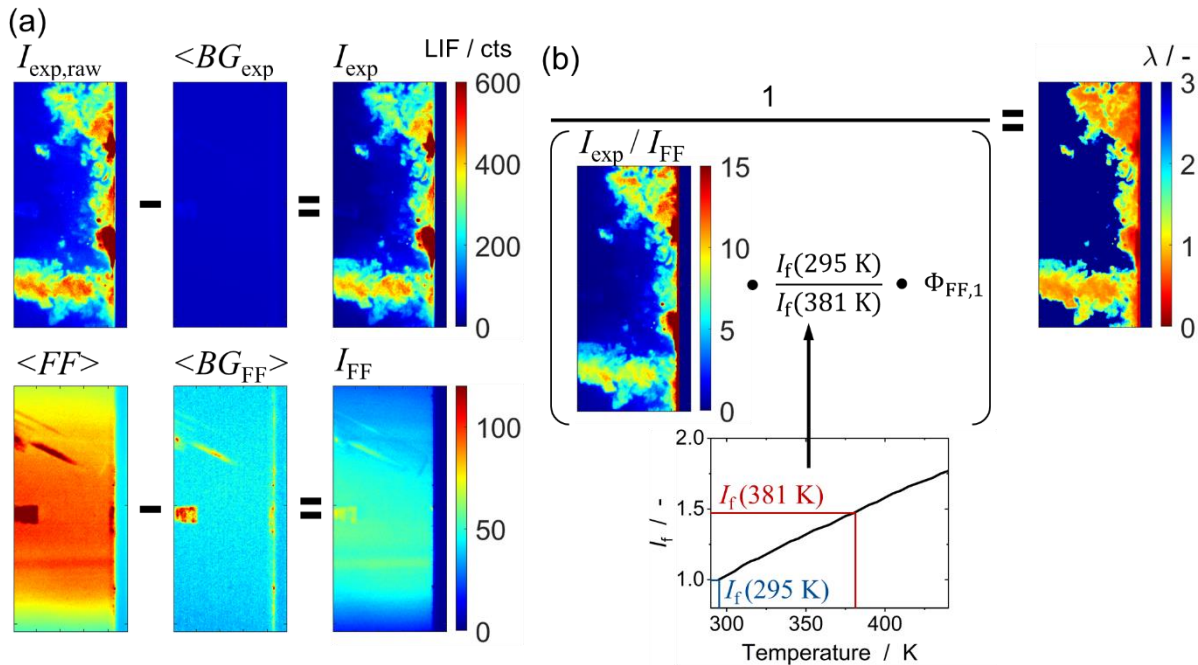


Figure 67: Post-processing of fuel-vapor LIF images: (a) Background and flat-field correction of fuel-vapor LIF single shot. (b) Temperature correction and equivalence-ratio quantification of single shot. Temperature dependence of toluene LIF per volume in air at 1 bar from [57].

5.2.4 Results

Injection and mixture formation

Figure 68 qualitatively shows the injection and the spray-wall impingement in background-corrected single shots of LIF from individual injections. The saturated regions in images at 0.7 and 1.2 ms aSOI indicate where the light-sheet plane intersects with the sprays 1, 2, and 6. The different impingement angles and distances are apparent from the images. The “dark” vertical region on the right-hand side of the images indicates the quartz wall where the fuel films form. At 3 ms aSOI the sprays have collided with the wall. The fraction of fuel droplets that has not evaporated before impingement either sticks to the wall, splashes or rebounds from the wall

into the gas phase. Since the images were recorded at moderate temperature (332 K air temperature), a comparatively large quantity of non-evaporated fuel droplets is still present at 3 ms aSOI. It needs to be noted that the gain of the intensifier was set to 40 for images acquired at 0.7 and 1.2 ms aSOI and to 50 for the image acquired at 3 ms aSOI.

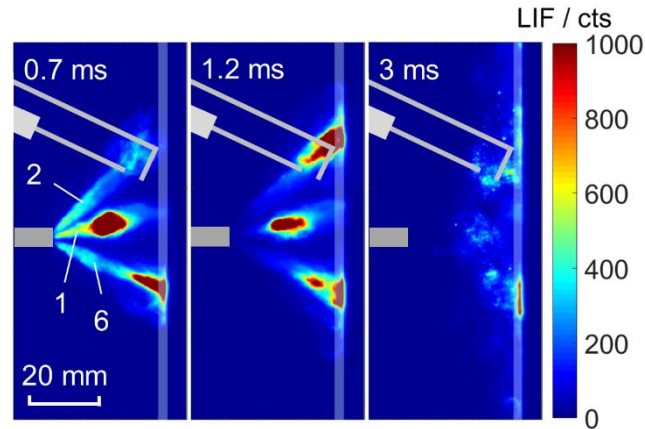


Figure 68: Single shot LIF images of fuel injection and wall impingement. $T_{\text{air}} = 332 \text{ K}$, $v_{\text{air}} = 1.8 \text{ m/s}$, $m_{\text{inj}} = 9.3 \text{ mg}$, without combustion.

Figure 69 shows calibrated images of λ between 6 and 15 ms aSOI and without combustion. The single shots were acquired from individual injection events and the ensemble averages result from 100 single shot images of λ . Fuel films 2 and 6, intersected by the laser light-sheet, and the quartz wall are indicated on the right side within the images.

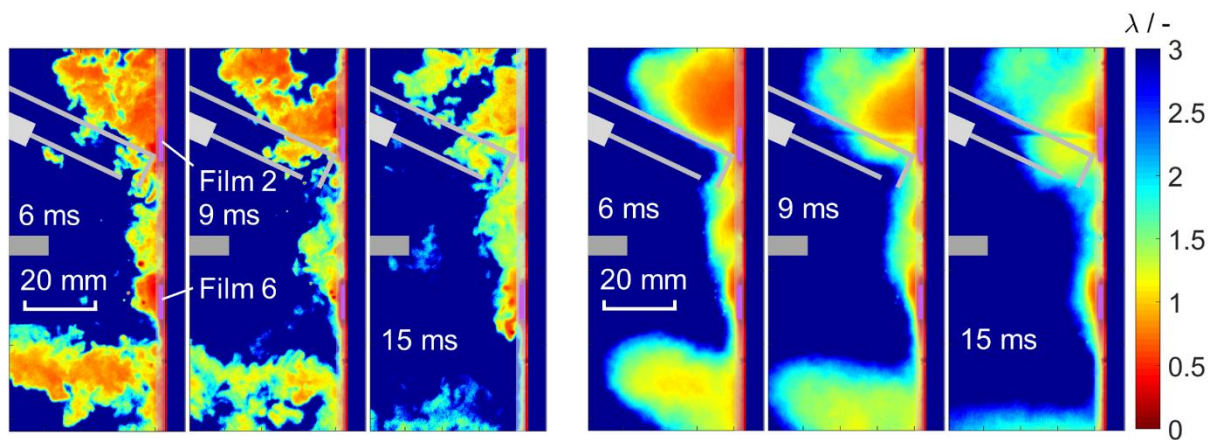


Figure 69: (left) Single shot and (right) ensemble average images of λ between 6 and 80 ms aSOI in a non-reacting environment. $T_{\text{air}} = 381 \text{ K}$, $v_{\text{air}} = 1.8 \text{ m/s}$, $m_{\text{inj}} = 9.3 \text{ mg}$, without combustion.

The spatial distribution of the fuel vapor coincides well between the single shots and the averages, indicating that the single shots are representative. At 6 and 9 ms aSOI, the images show fuel vapor concentrated above film 2 and below film 6 with minimum air/fuel ratios on the order of 0.6-0.8 in the single shots. In the top region, the average images indicate λ gradually increasing from around 0.8-1 near the wall to 1.5-2 within the bulk of the test section. Between the two films, λ ranges from 0.5 to 1.5. At 15 ms aSOI, the fuel-vapor plume below film 6 was transported downstream out of the FOV by the constant plug-flow through the test section. The plume propagates around 20 mm downstream from 6 to 15 ms aSOI which coincides quite well

with the mean velocity in the test section of 1.8 m/s. In contrast to that, the vapor plume in the top does not follow the flow downstream but mixes with the incoming air and becomes leaner.

Figure 70 shows single shots of λ at 3, 6, and 9 ms aSOI during combustion and in regions where the flame front has not burnt the fuel. Two snapshots from different combustion events are shown at each time aSOI. Ignition of the fuel/air-mixture is initiated around 1.7 ms aSOI. In the first single shot at 3 ms aSOI the contour of the emerging flame front is indicated around the spark electrodes. The spark is located around 5 mm behind the light-sheet plane such that the flame has not propagated into the visualized fuel vapor in every single shot. Therefore, the fuel/air-mixture seems unaffected by the flame front in the second single shot at 3 ms aSOI. The fuel/air-mixture seems unaffected by the flame front in the second single shot at 3 ms aSOI. The air/fuel ratio of 1, as indicated in both single shots at 3 ms aSOI, around the spark electrodes indicates locally high flammability of the mixture.

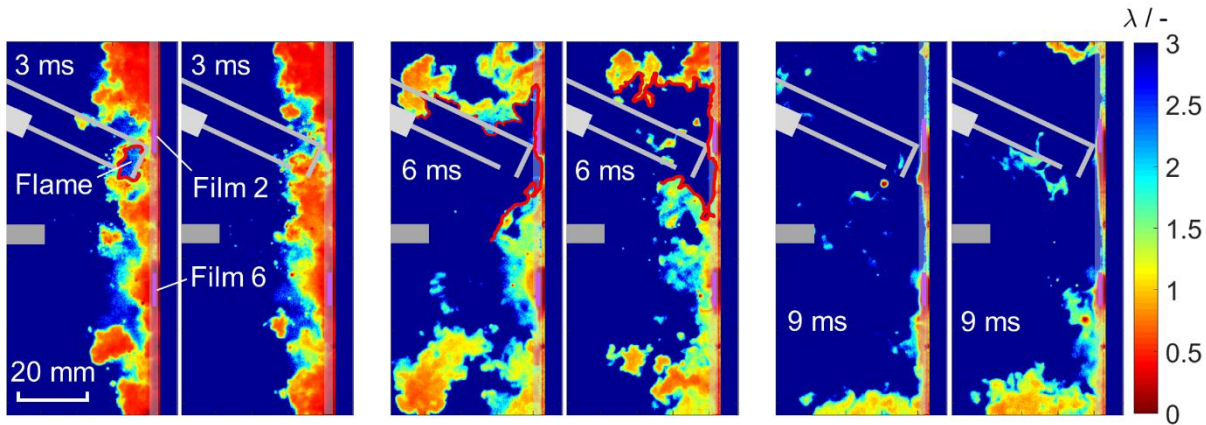


Figure 70: Single shots of λ in a reacting environment. $T_{\text{air}} = 381 \text{ K}$, $v_{\text{air}} = 1.8 \text{ m/s}$, $m_{\text{inj}} = 9.3 \text{ mg}$, with combustion.

At 3 ms aSOI, above film 2 and below film 6, fuel-vapor plumes with λ around 0.5 and thus a high tendency for soot formation are detected. At 6 ms aSOI, these plumes emerge further into the bulk gas, dilute with air while in some regions λ is still around 0.5 – 0.7. The flame front, indicated by the contours around the remaining fuel-vapor regions, reaches some of those fuel-rich regions near film 2 in both single shots at 6 ms aSOI, making soot formation likely. At 9 ms aSOI, the flame front reached also film 6 and burnt most of the fuel vapor in the FOV while some unburnt vapor is pushed out of the test section by the expanding hot gases.

Figure 71 shows single shots of λ during combustion from 3 to 9 ms aSOI for an injected mass of 4.6 mg. Reducing the injection duration to 0.5 ms and the injected mass to 4.6 mg results in a spatially narrower distribution of the fuel vapor close to the wall compared to an injected mass of 9.3 mg. However, λ again is close to 1 around the two electrodes and 0.5 above film 2 and below film 6. At 3 ms aSOI, the flame front propagates among the fuel/air-mixture near the electrodes. In contrast to the images for the injected mass of 9.3 mg, the fuel/air-mixture dilutes to a lesser extent from 3 to 6 ms aSOI. Most probably, the shorter injection duration causes lower turbulent mixing rates of fuel and air and less momentum pushing the rebounding fuel-vapor plumes into the bulk. It should be noted that this is true for most of the single shots. Therefore, despite a globally leaner fuel/air-mixture, regions with low λ , e.g. around film 2, might initiate soot formation when a flame propagates through these regions.

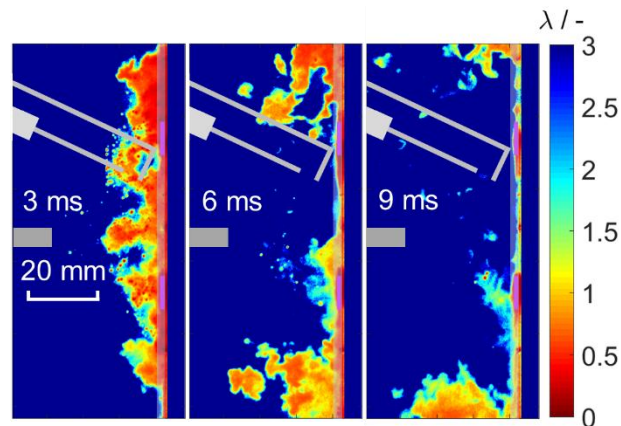


Figure 71: Single shots of λ for an injected mass of 4.6 mg. $T_{\text{air}} = 381 \text{ K}$, $v_{\text{air}} = 1.8 \text{ m/s}$, $m_{\text{inj}} = 4.6 \text{ mg}$, with combustion.

Late film-evaporation

Figure 72 shows the emergence of fuel vapor from the two films into the test section without combustion between 18 and 80 ms aSOI.

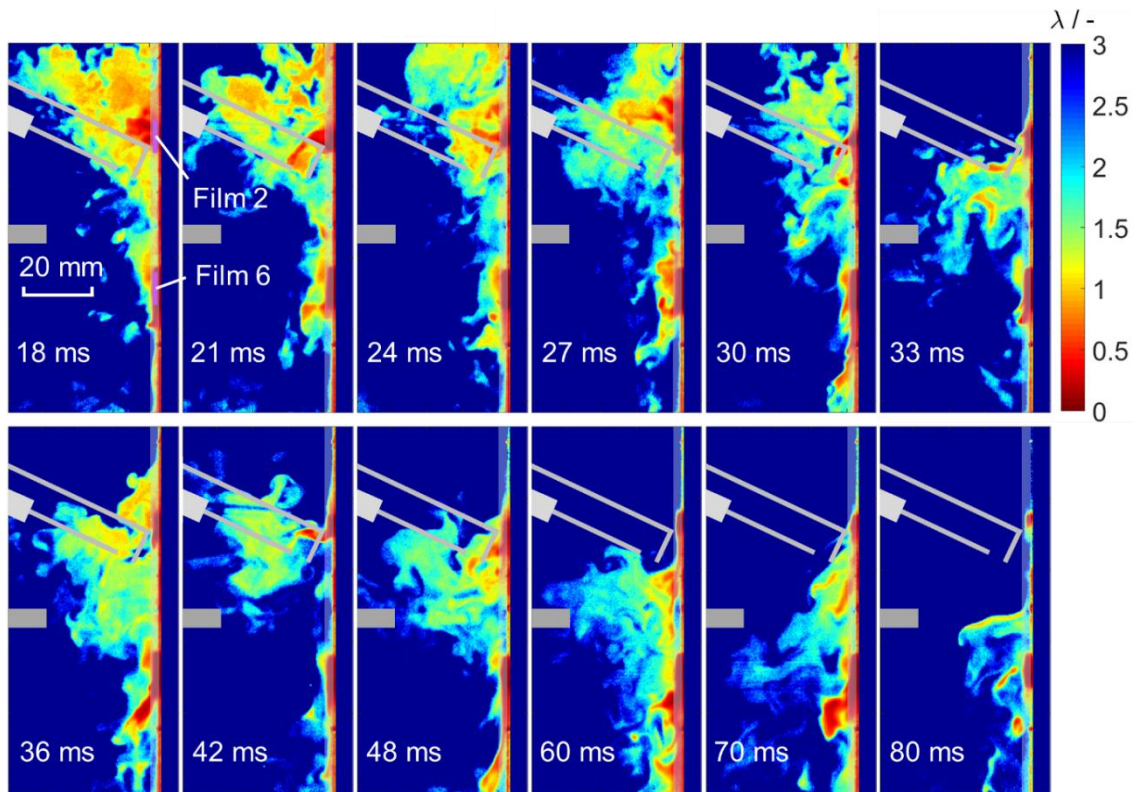


Figure 72: Single shots of λ during late fuel-film evaporation in a non-reacting environment. $T_{\text{air}} = 381 \text{ K}$, $v_{\text{air}} = 1.8 \text{ m/s}$, $m_{\text{inj}} = 9.3 \text{ mg}$, without combustion.

While most of the fuel in the bottom FOV was already transported downstream at 18 ms aSOI, a fuel/air-mixture with λ around 1 is located in the top region. Locally, fumes of fuel vapor with air/fuel ratios of about 0.5 are convected away from film 2 between 18 and 27 ms aSOI into the bulk, providing a high tendency to form soot. Images from 27 to 42 ms aSOI show the transport of fuel-rich regions from above film 2 downstream, further diluting with air, and a concentration

of fuel vapor between the two films at 33 and 36 ms aSOI. With time the fuel/air-mixture is diluted and λ becomes greater than 3. Throughout all images, fuel vapor from film 6 is not transported towards the core of the test section but rather strictly downstream close to the wall. Also, throughout all images, the fuel-richest regions are curved structures originating from the fuel films with λ even below 0.5, thus having a high tendency to form soot.

Figure 73 shows the evolution of the average λ in a region slightly above of film 2 (ROI 1) and below of film 6 (ROI 2), where fuel-rich regions were detected in particular. Early aSOI, from 6 to 18 ms aSOI fuel-rich mixtures with λ around 0.5 persist in the top region near film 2. These regions provide a high tendency for soot formation if they are caught by the flame front. Later than 18 ms aSOI, the mixture dilutes with incoming air, becomes leaner, and λ increases to 3 around 48 ms aSOI. In the bottom, near film 6, the fuel/air-mixture indicates λ around 1 early aSOI. At 9 ms aSOI, λ decreases, apparently due to an enrichment with fuel vapor emerging from film 6. Around 30 ms aSOI, λ of the mixture becomes 0.5 and even lower later aSOI, providing a high tendency for soot formation. Note that these λ -evolutions were measured without combustion. The propagation of the flame front and the formation of non-premixed sooting flames might influence the flow characteristics (e.g., buoyancy, dilation) and thus the spatiotemporal evolution of λ .

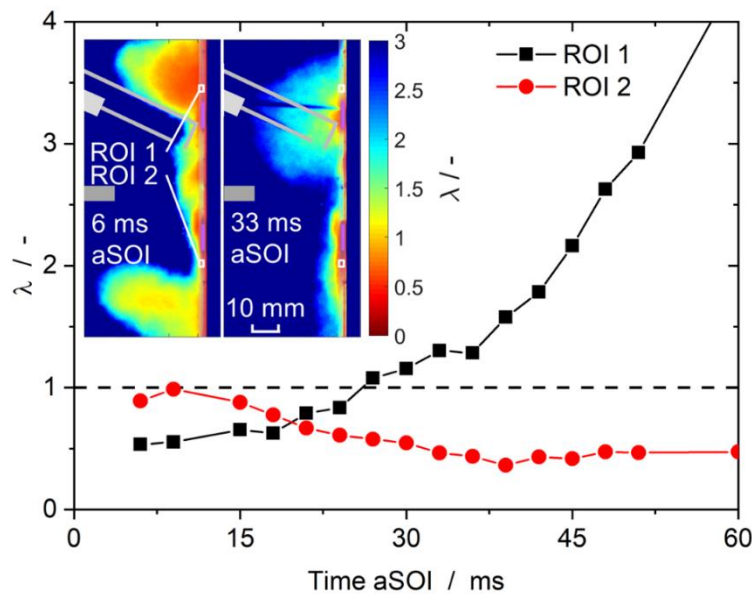


Figure 73: Evolution of λ in two regions, near film 2 and film 6. Also shown are ensemble average images of λ 6 and 33 ms aSOI. $T_{\text{air}} = 381 \text{ K}$, $v_{\text{air}} = 1.8 \text{ m/s}$, $m_{\text{inj}} = 9.3 \text{ mg}$, without combustion.

Figure 74 shows background-corrected single shots of fuel films and vapor from 21 to 36 ms aSOI during individual combustion events. To not saturate the sensor too much, the intensifier gain was reduced to 50. In the oxygen-depleted regions much greater FQY is expected due to the reduced fluorescence quenching. The visualization clearly shows fuel films 2 and 6 on the right side of the images. Surprisingly, fuel-vapor plumes following the flow towards the core of the test section are not detected. This is clearly in contrast to the images acquired without combustion where LIF signal from fuel-vapor plumes is clearly detected in the test section away from the quartz wall, see e.g., Figure 72. However, in all images a low signal of 200-400 cts is detected on the wall below and above film 2. This signal is most likely attributed to PAH LIF,

as further discussed in Section 5.4.5. This indicates that the fuel vapor is pyrolyzing very close to the film surface within the hot burnt gas, initiating soot precursor (PAH) formation.

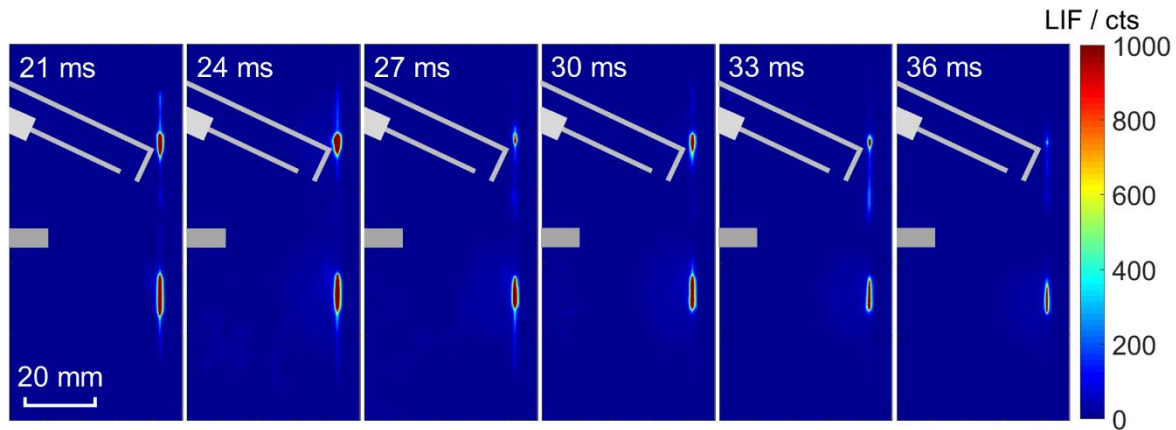


Figure 74: Single shot LIF images during fuel-film evaporation in a reacting environment. $T_{\text{air}} = 381 \text{ K}$, $v_{\text{air}} = 1.8 \text{ m/s}$, $m_{\text{inj}} = 9.3 \text{ mg}$, with combustion.

5.2.5 Precision and accuracy

Inaccuracies in determining the equivalence ratio mainly stem from deviations in the fuel-vapor temperature from the air temperature. However, the LIF signal of gaseous toluene in air is relatively insensitive to temperature (as opposed to the signal in nitrogen, which is strongly temperature dependent) [57]. The insensitivity against temperature variations originates from strong quenching by oxygen, the dominating depopulation mechanism of the excited state at these temperatures. Assuming that the temperature of the fuel vapor is bounded by the air temperature and the wall temperature ($\Delta T = 29 \text{ K}$) yields a maximum inaccuracy of 11% in the equivalence-ratio determination.

The highest equivalence ratios were around 2, corresponding to a fuel-vapor mole fraction of around 3% such that the oxygen partial pressure locally reduced to 0.203 bar while it was 0.21 bar when acquiring the flat-field. The local change in the oxygen partial pressure results in different quenching efficiencies. With a Stern-Volmer coefficient for oxygen quenching of $6.5 \cdot 10^{-24} \text{ m}^3$ at 375 K [55], the LIF signal changes about 2.8% when the oxygen partial pressure decreases from 0.2 to 0.203 bar. Therefore, the LIF signal is in good approximation considered proportional to the tracer number density and thus the equivalence ratio in this experiment [203].

Self-quenching of the LIF signal by the tracer itself is a well-known problem in gas-phase toluene LIF when the bath gas is nitrogen [54]. Then, non-linearities in the signal versus concentration are observed already for toluene concentrations 5-10 times less than the toluene vapor pressure at room temperature (0.5 – 1 vol.-%). The quencher is toluene in the electronically excited state such that the effect of self-quenching additionally depends on the laser fluence. Since the quenching cross section of molecular oxygen is about 50 times larger than the one from toluene, self-quenching is negligible for measurements in air. Therefore, self-quenching is not expected to significantly affect the measurement accuracy here.

The precision uncertainty was calculated from a flat-field corrected single shot of a flat-field. The deviation of the signal from unity stems from spatial noise, dominated by shot noise. The relative standard deviation of the signal in a region of 20×20 pixels ($3 \times 3 \text{ mm}^2$) is $\sigma_{\text{SN}} = 12\%$. The flat-field corresponds to the minimum equivalence ratio of 0.2 ($\lambda = 5$, fuel-vapor mole fraction of 0.35%) such that 12% is the maximum precision uncertainty from shot noise. Changes in spatial energy distribution of the laser profile might also result in signal fluctuations between single shots. The standard deviation of the spatially averaged signal from the 20×20 pixels among 100 single shot images of the flat-field was found to be $\sigma_{\text{LE}} = 2.6\%$. Fluctuations in the absolute laser pulse-energy that were not corrected by the energy monitor might contribute to that standard deviation. According to Gaussian error propagation, the overall precision uncertainty is then $\sigma = \sqrt{\sigma_{\text{SN}}^2 + \sigma_{\text{LE}}^2} = 12\%$ (SNR = 8.3) at a mole fraction of 0.35% and resolution of 0.15 mm/px. Extrapolating the spatial SNR to the maximum measured equivalence ratio of around 2 (fuel-vapor mole fraction of 3%) according to the \sqrt{N} -law of photon noise results in a spatial precision uncertainty of 3.8% and an overall precision uncertainty of 4.6%.

5.3 Flame-front, PAH, and soot-visualization experiments

The measurements on the visualization of PAH, soot, and combustion luminosity were mainly done in the constant-flow facility introduced in Section 4.1. Additionally, PAH, soot, and combustion luminosity were also imaged in the Yale and Santoro-burner flames as well as in the optically accessible SIDI engine. The burners simply replaced the constant-flow facility, and they were used for preliminary in-situ measurements. Measurements in the optically accessible SIDI engine were performed with Bosch in Renningen.

5.3.1 Optical layout

Flow facility and burners

The layout for the laser diagnostics is shown in Figure 75. First, the optical layout for the simultaneous visualization of PAH, soot, and chemiluminescence in Figure 75a is discussed. Pulses from two Nd:YAG lasers were formed into vertical, overlapping sheets at 532 and 1064 nm intersecting fuel films 2 and 6. The delay between the two laser pulses was 500 ns such that a quasi-simultaneous visualization was performed while the 532 nm laser was introduced first with a fluence of 0.008 J/cm^2 . The 1064 nm laser employed a fluence of 0.5 J/cm^2 since the LII signal was found to saturate at that laser fluence of 0.5 J/cm^2 in the Santoro burner, consistent with experiments by Lee et al. [204], see Section 5.3.3. The PAH-LIF and LII signals were spectrally separated and captured on two intensified CCD cameras. A beam splitter, BS 509 (Semrock, HC BS 509), transmitted light with a wavelength above about 509 nm and reflected shorter-wavelength light to separate PAH LIF from soot LII. An intensified CCD camera with a bandpass filter centered at 435 nm (Semrock, 435/40 BrightLine HC) captured soot LII. The gate of the intensifier was set to 60 ns, starting with the laser pulse. A second intensified CCD camera with a Schott-glass longpass filter (OG 550) captured PAH LIF. The gate of this intensifier was set to 30 ns, also starting with the laser pulse. The short gating suppressed most natural flame luminosity. The FOV had a height of 80 mm with a laser-

sheet thickness of 0.5 mm. The projected pixel size was 0.14 mm/pixel. The time between two images was 2.5 s, during which the test section was completely flushed by the air flow. For preliminary measurements, the constant-flow facility was replaced by the Santoro burner, that was used to check how well PAH LIF can be discriminated against soot luminosity and LII, and to optimize the excitation/detection scheme, as further discussed in Section 5.3.3.

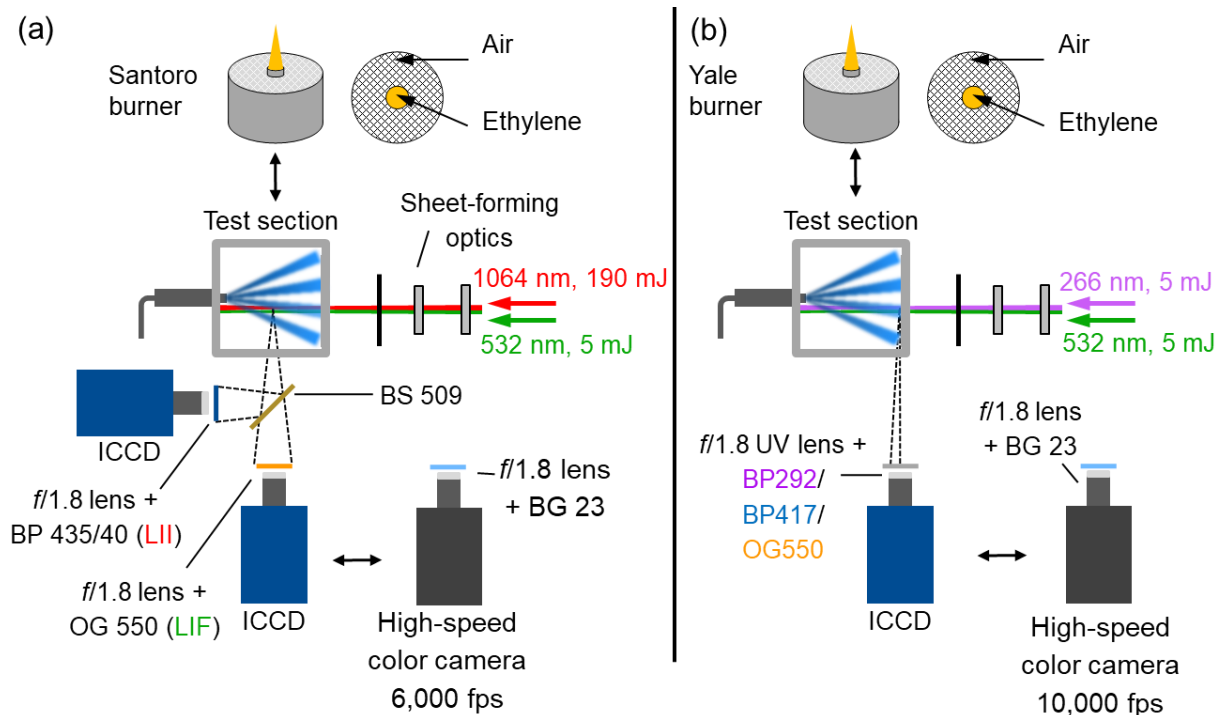


Figure 75: (a) Optical layout for visualizing PAH, soot, and chemiluminescence. Modified version of the Figure published in [97]. (b) Optical layout for the visualization of PAH LIF, excited at 266 or 532 nm and detected with a variety of spectral filter bands, and combustion luminosity.

In separate experiments, a high-speed color camera (Phantom v1612) with a blue Schott-glass filter (BG 23, 2 mm thickness) imaged the spray, chemiluminescence, and natural soot incandescence. The filter was used to partially suppress the strong soot incandescence with respect to presumably blue chemiluminescence. A pulsed LED side-illuminated the sprays and their impingement. The camera was focused on the center plane of the test section and operated with an exposure time of 124 μ s at 6000 frames/second. The f -number was 1.8 yielding an approximate depth of field of 7-10 mm.

The optical layout in Figure 75b was used to visualize solely PAH LIF, excited with 266 or 532 nm and detected with a variety of spectral filter-bands. This arrangement was used to perform size-class dependent imaging of PAH LIF. The two overlapping light sheets, each with a fluence of about 0.008 J/cm², were formed and directed with the same sheet-forming optics, thus also intersecting with films 2 and 6, and had similar dimensions as the ones introduced before. The intensified CCD camera was equipped with a UV lens (Cercor, $f = 45$ mm, $f/1.8$) and varying detection filters, BP 292/27, BP 417/60 (Semrock 417/60 BrightLine HC), and OG 550. The gate again was set to 30 ns. As indicated in Figure 75b, the optical axis of the collection optics was aligned along the quartz wall where the fuel films evaporate from. Again, in separate experiments a high-speed color camera replaced the laser-based experiment to image

combustion luminosity. For a comparison of size-class dependent PAH LIF in the test section, the experiment was here replaced with the Yale burner.

Optically accessible engine

The purpose of the engine measurements was to simultaneously visualize PAH LIF and soot LII in an optically accessible SIDI engine. Three Nd:YAG lasers at 266, 355, and 532 nm were used to excite fluorescence from different size classes of PAH, while one at 1064 nm was used to excite soot LII. The temporal delay between the laser pulses was 2000 ns and they were triggered in the sequence 266, 355, 532, and finally 1064 nm. Figure 76 shows the optical layout for the simultaneous visualization of PAH and soot in the engine. Note that the cameras and the piston are in a different height than the lasers with respect to the paper plane. Also shown is a photo of the quartz piston with visible soot deposits from the six fuel films.

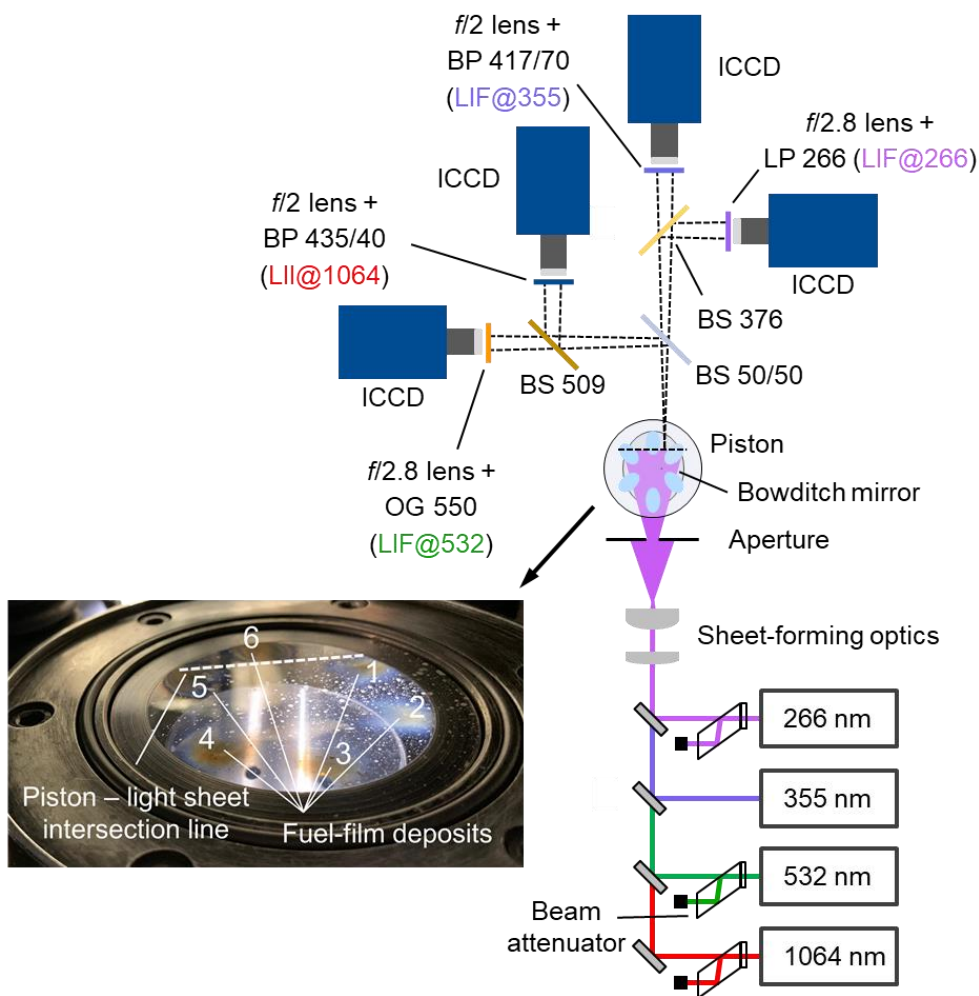


Figure 76: Optical layout for simultaneous PAH LIF and soot LII in the optically accessible SIDI engine.

Polarization-based beam attenuators allowed for energy control of the 266, 532, and 1064 nm laser pulses. A positive spherical lens ($f = 1000$ mm) focused the light, a positive cylindrical lens ($f = 40$ mm) expanded the pulses horizontally. The light sheets were clipped by an aperture, reflected through the piston into the combustion chamber via the Bowditch mirror, and focused in the center of the combustion chamber, between the piston-light sheet intersection line and

the pent roof. The light sheets had a width of about 40 mm, and thicknesses of 0.7, 0.2, 0.8, and 1.5 mm for 266, 355, 532, and 1064 nm, respectively. The signals were first evenly divided by a 50/50 beam splitter (Thorlabs, BPD508-FS – Polka-Dot Beamsplitter). Signals excited at 266 nm and 355 nm were separated by a beam splitter BS 376 (Semrock, Beamsplitter HC BS 376). Signal with wavelengths longer than about 376 nm were transmitted while shorter-wavelength signal was reflected. An intensified CCD camera, equipped with a UV lens (Cercor, $f = 100$ mm, $f/2.8$) and a longpass filter, LP 266, captured reflected PAH LIF, excited at 266 nm, thus between 266 and 376 nm. PAH LIF excited at 355 nm was captured by an intensified CCD camera, equipped with a VIS-lens (Carl Zeiss, $f = 100$ mm, $f/2$) and a bandpass filter, BP 417/60. PAH LIF, excited at 532 nm, and soot LII, excited at 1064 nm, were captured as the reflected part of the 50/50 beam splitter with the same detection optics as for the flow-facility experiments, shown in Figure 75a. The intensifier gates were set to 50, 100, 40, and 2000 ns for signals excited at 266, 355, 532, and 1064 nm, respectively, and started all with the laser pulses. The high gate for the soot LII channel was necessary due to strong jitter of the 1064 nm laser Q-switch. The projected pixel size was 0.13 mm/pixel. A set of 50 images was acquired at crank angle positions of 20, 30, 40, 50, 60, and 70°CA. Compression TDC corresponds to 0°CA. The operating conditions for the engine experiments are introduced in Section 5.1.2.

5.3.2 Spectral characteristics

Figure 77 shows the spectral features of PAH LIF and soot LII excitation and detection as they were used for the simultaneous visualization in the constant-flow facility and engine.

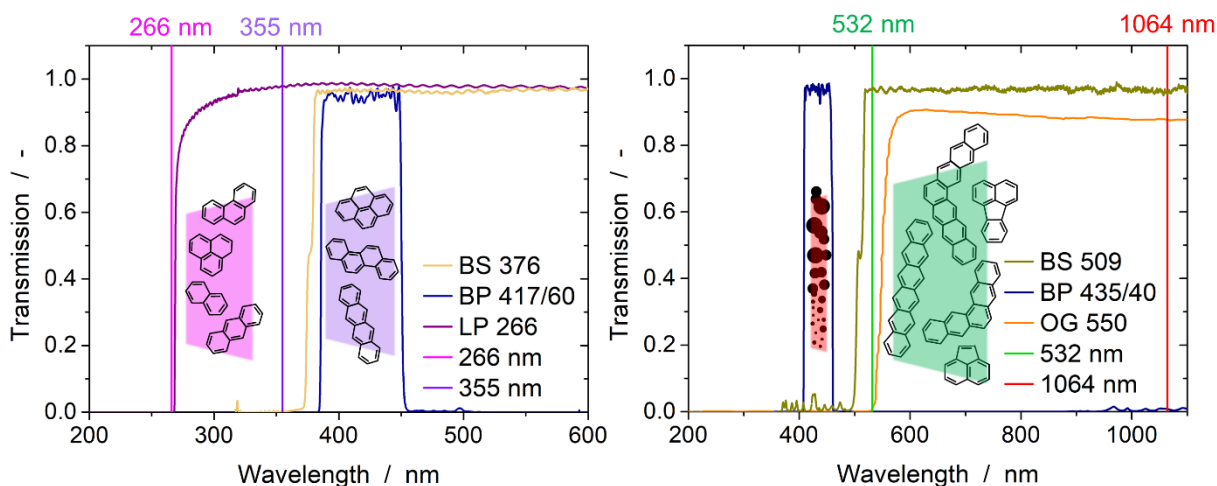


Figure 77 Transmission curves of filters and beam splitter as well as excitation wavelengths and representative species detected in the indicated wavelength range. Modified version of this Figure published in [97].

For a more comprehensive discussion of PAH LIF with different excitation/emission-schemes, the reader is referred back to Section 3.3. The detection of PAH LIF, excited at 266 nm, between 266 and 376 nm comprises mainly small PAH (2-3 aromatic rings). Excitation with 355 nm and detection with a bandpass filter, slightly red-shifted, leads most presumably to the detection of mainly PAH with 3-4 aromatic rings [162, 164]. The excitation with 532 nm and the detection

of the entire red-shifted LIF is expected to result in the detection of long chain PAH with more than five aromatic rings, incipient particles, 5-membered ring PAH, and dimers of PAH [152, 161-163]. Soot LII, excited at 1064 nm, was detected blue-shifted with a bandpass filter centered at 435 nm. The interference from C_2 and C_3 emissions is not expected in this spectral region and with this excitation/emission-scheme [64].

5.3.3 Preliminary measurements

Preliminary measurements were performed in-situ in the Santoro burner before applying the simultaneous laser diagnostics in the constant-flow facility. Figure 78 shows the dependence of the LII and LIF signal on the laser fluence in the Santoro burner. Images were background-corrected by turning off the laser and thus subtracting natural combustion luminosity from the flame. PAH-LIF images were additionally corrected by subtracting an ensemble average LII image to remove the interference of LII signal, excited by the 532 nm laser. However, LII signal was more intense in the image acquired with 1064 nm than in the one acquired with 532 nm such that the PAH LIF regions in Figure 78b appear smaller than they actually are. Figure 78a indicates mean LII signals, excited with 1064 nm, from a central and an outer ROI, presumably representing different maturity states of the soot, and the results from Bladh and Bengtsson in the flame of the Santoro burner versus laser fluence. Figure 78b shows mainly LIF signal, excited with 532 nm, with some LII interference on the right from ROIs in the left and right wings of the flame.

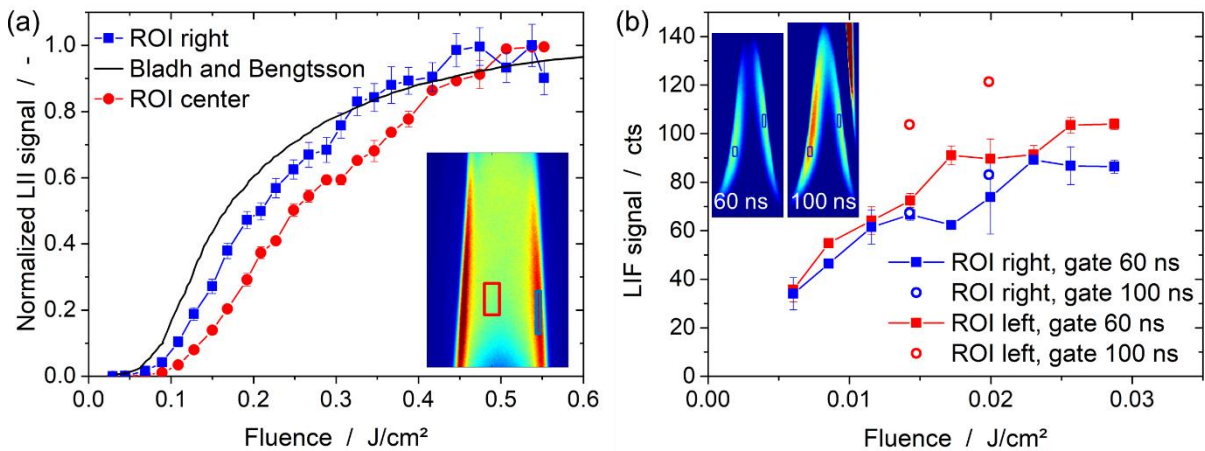


Figure 78: (a) LII signal and (b) predominantly LIF signal versus laser fluence from two regions of interest and LII signal also from Bladh and Bengtsson [69]. Error bars indicate the standard deviation among 3 ensemble averaged images, each comprising 100 single shots.

Bladh and Bengtsson modelled the LII signal as thermal radiation of soot excited by a laser sheet with a Gaussian transverse profile at 1064 nm, captured with a 18 ns gate starting 20 ns after the pulse. For low laser fluences the temperature of the soot particles increases linearly with the laser fluence such that, according to the Stefan-Boltzmann law, the LII signal increases proportionally to T^4 . At a certain fluence, some particles reach the sublimation temperature of soot (about 4000 K). Therefore, a further increase in the laser fluence does not contribute to a further heating of those particles but to vaporization, indicating the turning point of the function in Figure 78a. Solely the particles that have not reached the sublimation temperature contribute to an increase in the LII signal with increasing laser fluence. At a certain fluence, all particles

reach the sublimation temperature such that the LII signal does not increase anymore with increasing laser fluence [64]. As discussed in Section 2.4.3, this plateau region is much more pronounced when exciting with a Gaussian sheet instead of a top-hat profile. At high overall fluence, the signal loss due to sublimation of the particles in the high-fluence center of the sheet is compensated for by the increasing signal in the low-fluence wings [64]. LII imaging in this “plateau regime” is desirable for soot concentration measurements, since then the measurement is less sensitive to shot-to-shot variations in laser energy and inhomogeneities in the local laser fluence. Experimentally, the LII signals in both ROIs begin to saturate at a laser fluence of about 0.5 J/cm^2 , consistent with experiments by Lee et al. [204], hence this value was chosen for LII imaging.

According to the findings from Santoro et al., soot particles in the annular region of the flame are larger than particles in the center region at the same HAB. The explanation is that strong nucleation and growth occur at lower HAB in the annular region of the flame compared to the central region [205]. Since soot particles from both regions are in the Rayleigh regime ($d_p \ll \lambda_{\text{exc}}$ [64]) and thus absorb laser energy proportional to their volume, they are expected to be heated to similar temperatures when exposed to the same laser fluence. However, the normalized LII signal detected in the central region is systematically lower than the one from the right annular region (ROI right) up to a fluence of 0.5 J/cm^2 . The reason for that is that younger soot has a lower absorption function such that it is heated to the sublimation temperature at higher laser fluence than more mature soot [206].

Figure 78b shows PAH LIF excited at 532 nm in thin stripes in the Santoro-burner flame. At two fluences, the gate was increased to test whether the detected signal was solely from short living fluorescence or interfered with LII. LII interference is not apparent in the right flank of the flame. However, in the left flank of the flame the signal increases when the gate is raised to 100 ns, indicating the interference with LII. Most likely, the interference stems from flickering of the flames during image acquisition and the subsequent subtraction of a LII image from the LIF image. For the same reason, an intense stripe of LII signal is visible on the very right of the image with a gate of 100 ns. Nevertheless, the signal saturates around 0.025 J/cm^2 in both ROIs. 0.008 J/cm^2 were chosen to yield maximum LIF signal yet low LII interference.

Figure 79a shows a single shot of simultaneous soot LII and PAH LIF in the Santoro-burner flame. PAH are mainly detected in a hollow-cone region up to 45 mm above the nozzle. Above and to the sides the PAH-LIF cone overlaps with the LII signal, indicating the nucleation region where soot forms from PAH. However, the 532 nm laser excites soot LII in the right flank of the flame up to a HAB of about 50 mm where soot LII is excited not by the 1064 nm light sheet. Figure 79b shows that the LII signal starts to significantly increase at about 35 mm HAB and peaks at about 50 mm. The downstream decrease in the LII signal is attributed to oxidation of soot and -to a lesser extent- to decreasing laser fluence. The LIF signal peaks at around 35 mm where the LII signal increases. This indicates that the nucleation rate of soot becomes larger than the formation rate of PAH. For similar flow conditions, also Santoro et al. [205] found that the f_v strongly increases at 37.6 mm HAB and they reported the beginning of the oxidation region at 50 mm. Smyth et al. and Mannazhi et al. [173, 207] also observed the strongest PAH

LIF at a HAB where the soot LII started to increase in ethylene and methane co-flow diffusion flames, respectively.

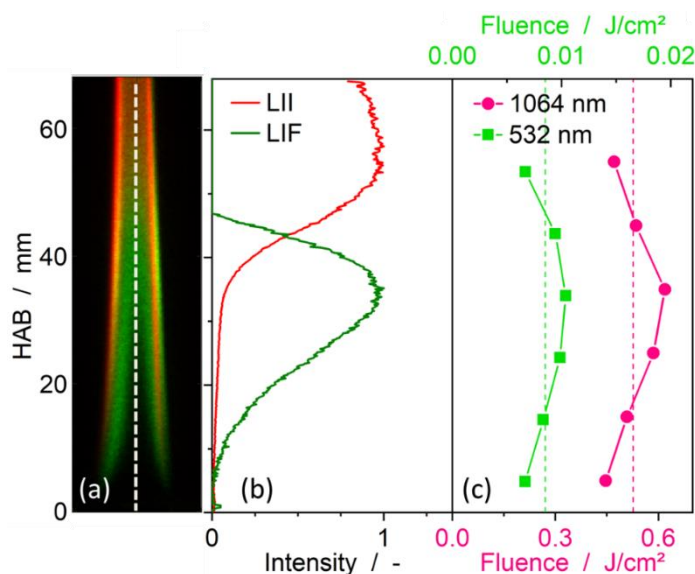


Figure 79: (a) Overlay of simultaneous soot LII (red) and PAH LIF (green) images, (b) LII and LIF signals along the centerline with increasing HAB, (c) vertical profiles of fluence in the light sheets.

In separate experiments, different size classes of PAH were visualized in the Yale burner. Figure 80 shows the natural flame luminosity emitted from the Yale-burner flame, acquired in the scope of this work and from [208], for varying ethylene/nitrogen-ratios of the fuel. Qualitatively, the flame shapes from this work and the ones from Yale appear very similar. The flame appears slightly higher at all dilution ratios in this work. The differences might stem from slight fluctuations in the fuel flow, controlled via a rotameter. For the visualization of PAH LIF, the fuel consisted of 40% ethylene and 60% nitrogen. This dilution was chosen since the then smaller flame was flickering less but still has substantial soot.

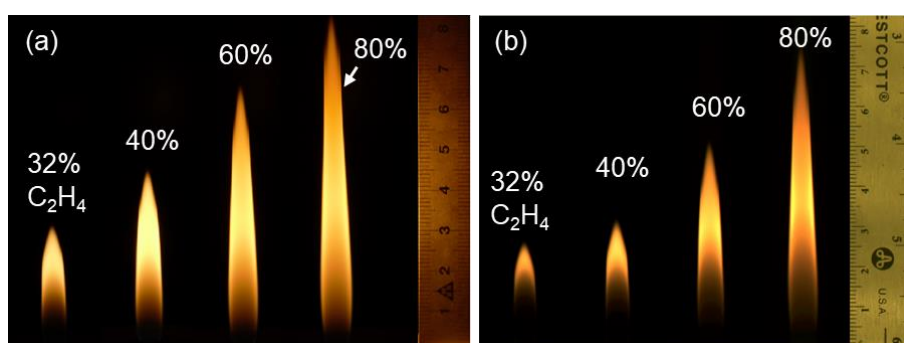


Figure 80: Images of the natural flame luminosity emitted from the Yale burner, (a) captured in Duisburg with a DSLR and (b) captured at Yale [208]. The exposure time in this work was 62.5 ms.

5.4 Results and discussion

In the following, results from the visualization of PAH, soot, and chemiluminescence are presented. First, the simultaneous visualization of PAH LIF and soot LII in the constant-flow facility is shown which is then partially compared to results from a CFD simulation. Then, the

visualization of different size-classes of PAH based on the excitation/detection-scheme is presented. Finally, results from simultaneous PAH LIF and soot LII in the engine are discussed.

5.4.1 Spray combustion and soot formation

Figure 81 shows single shots from simultaneous imaging of PAH LIF (green) and soot LII (red). For each time aSOI, two snapshots from different combustion events are shown, normalized by the maximum signals of PAH LIF and soot LII in each image.

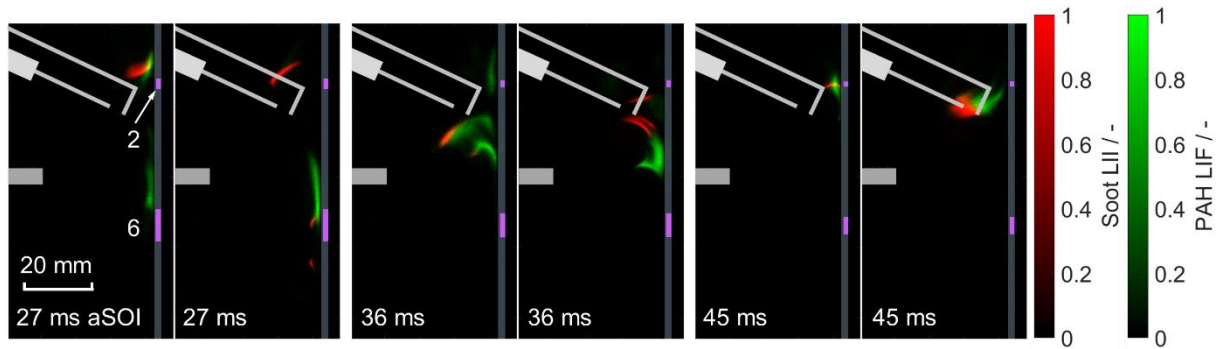


Figure 81: Single shots of PAH LIF and soot LII images from individual combustion events. The vertical magenta lines qualitatively indicate the extent of fuels films 2 and 6, see text for details. $T_{\text{air}} = 381 \text{ K}$, $v_{\text{air}} = 1.8 \text{ m/s}$, $m_{\text{inj}} = 9.3 \text{ mg}$. Figure published in [97].

The quartz wall is indicated in dark gray on the right edge of each image. The two relevant fuel films on that wall (number 2 and 6 in top and bottom, respectively) are indicated by magenta lines, whose vertical extent and thickness are approximately proportional to those of the films. Film 2 has an initial mass of about 0.15 mg and has evaporated completely about 80 ms aSOI, while film 6 has an initial mass of 0.37 mg and has evaporated completely at 125 ms aSOI.

The single shots show PAH and soot mostly in spatially separate -but often adjacent- regions. In contrast to our preliminary experiments in the laminar flame of the Santoro burner but consistent with studies of soot formation in turbulent combustion [42, 204], here the signals excited at 532 and 1064 nm do not overlap significantly. This indicates that the 532-nm light solely excites PAH LIF and not LII. Both signals are detected in intermittent filaments, with the PAH regions appearing more blurred than the sharp-edged ones with soot. At 27 ms aSOI, LII signal is mostly detected around the spark electrodes, probably stemming from both the evaporating fuel film 2 and from liquid fuel on the spark electrodes. At the same time, slightly upstream of fuel film 6 and very close to the wall, PAH are detected without adjacent soot. At 36 ms aSOI, in both snapshots soot and PAH are detected in adjacent curved regions, as if being stretching out along some local streamline, which would then correspond to a temporal transition from PAH to soot. In the left image, the two signal regions slightly overlap, but in the right one, they are separated by a dark region, indicating that there might be species present that are not excited by either 532 nm or 1064 nm. In both snapshots from 45 ms aSOI, PAH and soot are only found near film 2, and this is in fact characteristic for almost all images at that timing.

From the same FOV, Figure 82 shows selected frames from a color-camera image sequence from a single combustion event. Each image is normalized to the maximum sensor read-out,

4095 counts. Where the green color channel exceeds the blue channel after the injection, both the green and the blue channel were divided by a factor of four to visually discriminate soot luminosity more clearly from the blue chemiluminescence.

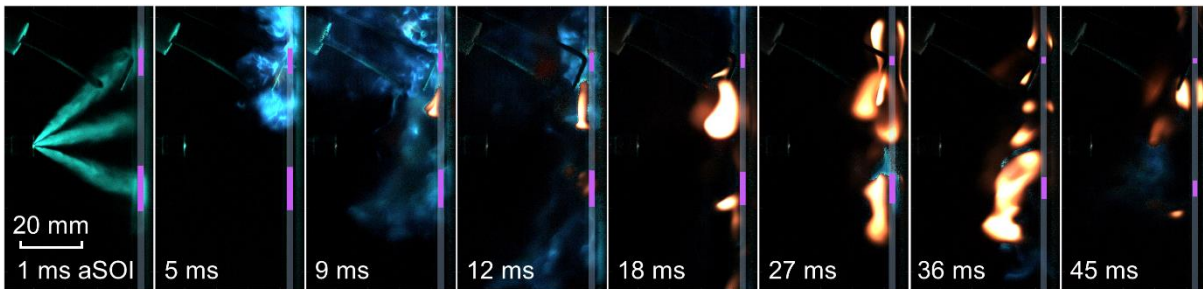


Figure 82: Sequence of high-speed images of natural soot luminosity (orange-red), Mie-scattered LED light from the spray (turquoise-green), and chemiluminescence (blue) of the flame front. $T_{\text{air}} = 381 \text{ K}$, $v_{\text{air}} = 1.8 \text{ m/s}$, $m_{\text{inj}} = 9.3 \text{ mg}$. Figure published in [97].

At 1 ms aSOI, the Mie-scattered light from the green LED localizes the spray jets and their wall impingement forming the liquid films. About 1.7 ms aSOI the spark ignites the fuel/air-mixture and a premixed turbulent flame begins propagating through the test section, as indicated by the chemiluminescence signal at 5 ms aSOI. Although some weak chemiluminescence is detected later in the sequence, the premixed phase of combustion appears to be completed after 12 ms aSOI. At 9 and 12 ms aSOI a first soot pocket is detected slightly downstream of film 2. The soot luminosity near film 2 becomes most intense at 18 ms aSOI and then decreases, while at the same time soot starts to be seen in the vicinity of film 6. From 27 to 45 ms aSOI soot is detected in various spatially separated regions, all close to the wall. Note that in contrast to the laser-based measurements, the signal here is integrated along the line of sight such that it also contains contributions from films 3 and 5. Nevertheless, the limited depth of focus renders some sooting regions sharper than others, indicating some spatial separation in the depth dimension. Overall, it is summarized that soot luminosity is detected before LII signal, mostly near the wall, somewhat downstream of the fuel films, and after the initially spray-evaporated fuel has been burned in premixed combustion.

Because of the high spatiotemporal intermittency of PAH LIF and soot LII, in addition to single shots (Figure 81), it is also useful to examine ensemble-average images of the two signals, as shown in the top row of Figure 83. Corresponding ensemble-average images from records of the high-speed color camera are shown in the bottom row of Figure 83. The normalization was the same as for the single-shot images. Following Li et al. [182], the single-shot overlap of PAH LIF with soot LII was calculated as the area in which both signals exceed a certain threshold (here, 20 counts) and then averaged at each image timing.

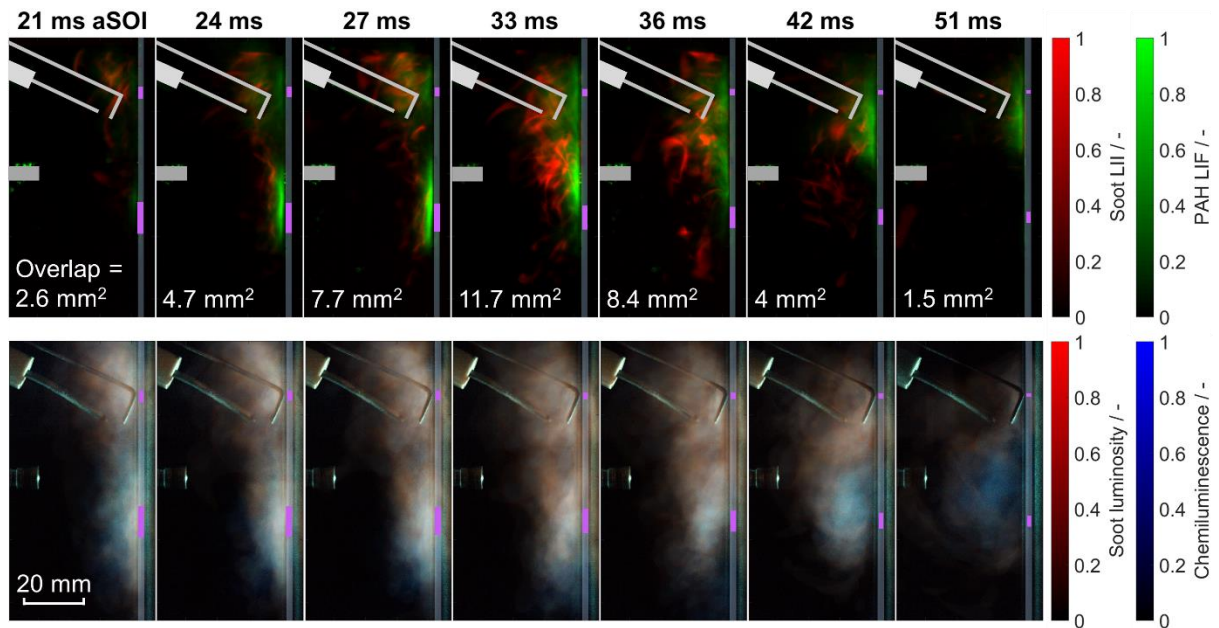


Figure 83: (Top row) ensemble-average images of PAH LIF and soot LII from 200 single shots for each image timing, (bottom row) ensemble-average images from 50 sequences of high-speed color imaging. The spatial overlap of PAH and LII, calculated according to Li et al [30], is indicated in each image in the top row. $T_{\text{air}} = 381 \text{ K}$, $v_{\text{air}} = 1.8 \text{ m/s}$, $m_{\text{inj}} = 9.3 \text{ mg}$. Figure published in [97].

First, the LIF/LII series in the top row of Figure 82 is addressed. Soot LII is first detected in the upper portion of the FOV around the spark electrodes at 21 ms aSOI, while at 24 and 27 ms aSOI, strong PAH LIF signal is detected near film 6. Very few soot filaments arise near this PAH layer, while the region of soot LII upstream is growing. At the same time, a low-intensity region of PAH LIF is found near film 2. Early soot formation in the upper portion of the FOV and PAH formation in the bottom near film 6 spatially coincide with the fuel-rich regions at that times, as seen in Section 5.2.4. At 33 ms aSOI, the soot region from the top is centered further downstream (as the fuel vapor region from the top in Figure 72) and even more intense, while PAH are now found preferentially upstream, such that on average PAH and soot are detected adjacent to each other, with PAH closer to the wall. The broadening of the PAH region, the intense LII signal, and the more extensive overlap of the PAH and soot filaments indicate increased soot formation at that time. This temporally coincides with an increased evaporation rate of fuel film 6 (see Figure 48).

In a Diesel engine, Li et al. [182] also found PAH excited at 532 and 633 nm – but not PAH excited at 355 nm – significantly overlapping with soot LII (excited at 1064 nm), indicating direct participation of the former in soot nucleation. In contrast to that work and to Aizawa et al. [179], here, on average PAH do not always visibly precede soot, e.g. near film 2 in the top region. Later, the soot LII signal first spreads towards the top and the bottom, while some soot is being transported out of the FOV at 36 ms aSOI, then the LII signal becomes weaker until almost none is detected at 51 ms aSOI. Although 20% of the mass of film 6 are left at 51 ms aSOI, neither soot nor PAH are detected nearby, but chemiluminescence is. The PAH region also shrinks at later times, but a layer of PAH is still found near film 2 at 51 ms aSOI without any adjacent soot LII. This may indicate that temperatures are not high enough anymore for soot to form from PAH. Even though the entire FOV shown here is laser-illuminated, no PAH

LIF and very little soot LII is seen towards the bottom of the FOV, indicating that PAH and soot are oxidized once they are convected far enough downstream.

The images from the color camera in the bottom row of Figure 83 show soot luminosity roughly in the same regions where LII (in the top row) also detects soot. Early soot luminosity is found in the upper part of the FOV, becoming more intense with time and covering a large area between the two pairs of fuel films around 33 ms aSOI. Compared to the LII signal, the soot luminosity covers a larger area and does not exhibit the spatial intermittency that even the ensemble-averaged LII images are showing. Surprisingly, chemiluminescence is found near the lower pair of films, number 5 and 6, and at all times, being most intensive at 42 ms aSOI. This indicates the active oxidation of either fuel, PAH, or soot, and explains the weakening of soot LII with time, and also why very little soot and no PAH are detected in the very downstream portion of the FOV. In fact, throughout the entire time series, chemiluminescence and PAH LIF spatially exclude each other, with maybe the exception of the strong PAH LIF at 24 and 27 ms aSOI that could be in front of or behind sources of chemiluminescence.

5.4.2 Comparison with CFD simulation

Figure 84 shows an image sequence of a single combustion event, captured with the high-speed color-camera viewing through the side window, and from the CFD simulation of our collaborators. Each image is processed as discussed in Section 5.4.1. The four relevant fuel-film positions on the wall (number 2+3 and 5+6 in top and bottom, respectively) are indicated from 3 ms aSOI on by magenta lines whose vertical extent and thickness are approximately proportional to those of the films. The premixed turbulent flame propagates through the test section, as indicated by the chemiluminescence signal from 2 to 12 ms aSOI. The blue volume rendering of the OH concentration in the simulation shows the early flame propagation from 2 to 5 ms aSOI in very similar regions as the experimental image sequence but spatially more extended. Note that in the simulation, OH (regardless of its electronic state) is taken as a convenient marker of active high-temperature reactions and post-flame gases, while the combustion imaging in the experiment captures light emission in the visible spectrum, mostly from electronically excited CH and from hot CO. The simulation predicts significantly more OH in the top half of the test section than in the bottom half throughout the entire time series.

Around 7 ms aSOI both the CFD and imaging find soot in multiple distinct regions in the top of the test section, in the measurement closer to films 2 and 3. The observed temporal delay between the main (premixed) combustion event and soot formation in imaging and CFD is in good agreement with previous works [96, 99, 103, 104, 209]. Then, from 12 ms aSOI soot is found as large associated agglomerates near the wall and downstream of films 2 and 3. At 18 ms aSOI, small regions of soot are also found near and downstream of films 5 and 6 in simulation and measurement while the large soot filaments in the top further grow, apparently being fed by the evaporating fuel films. The soot formation characteristics near the evaporating fuel films are consistent with the spatial distribution of the air/fuel equivalence ratio from tracer LIF (see Section 5.2.4), which indicate fuel-rich vapor plumes ($\lambda < 0.5$) emerging from the fuel films, providing a high tendency for soot formation. In contrast to the simulation, high-speed imaging also shows weak soot luminosity right next to films 5 and 6 at 30 ms aSOI. Both imaging and

the simulation indicate a reduction in spatial extent of the soot regions at 48 ms aSOI. Compared to a real SIDI engine, gas velocities are lower, and the turbulence length scales are larger in this experiment. This results in lower turbulent mixing rates of oxidizer and fuel and might lead to enhanced soot formation and increased burnout times of fuel, PAH, and soot compared to a real SIDI engine.

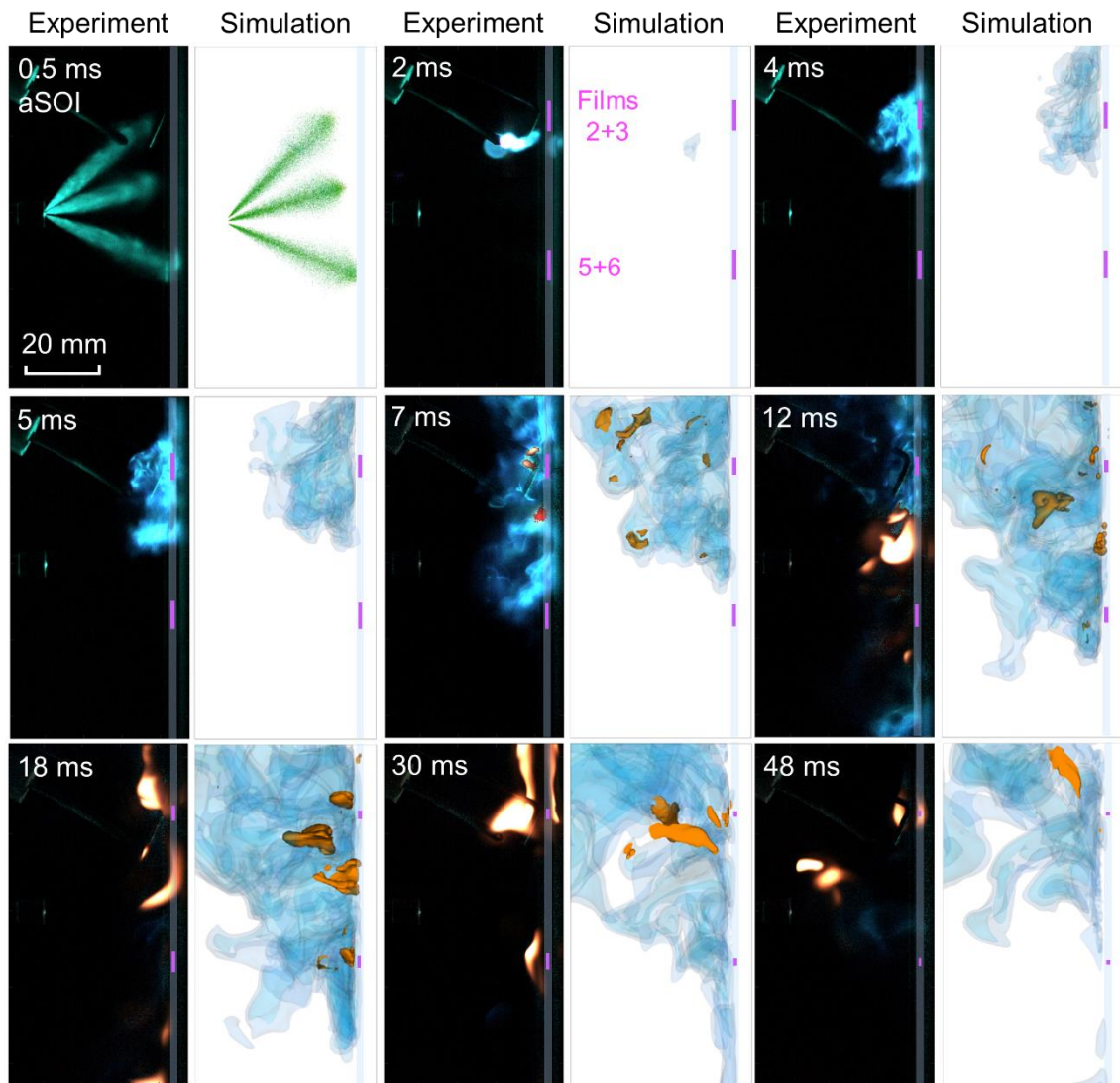


Figure 84: (left) Sequence of high-speed images of natural soot luminosity, Mie scattered LED light from the spray, and chemiluminescence of the flame front. (right) Corresponding CFD result with green fuel droplets, and qualitative line-of-sight integrating volume renderings of OH (blue) and soot volume fraction (red). The vertical magenta lines qualitatively indicate the extent of fuels films 2+3 and 5+6, see text for details. $T_{\text{air}} = 381 \text{ K}$, $v_{\text{air}} = 1.8 \text{ m/s}$, $m_{\text{inj}} = 9.3 \text{ mg}$.

5.4.3 Influence of injected mass and temperature

Figure 85a shows ensemble average images of PAH, soot, and chemiluminescence for an injected mass of 4.6 mg. Figure 85b compares the evolutions of field-wide integrated PAH LIF, soot LII, soot luminosity, and chemiluminescence for the injected masses of 4.6 and 9.3 mg. Surprisingly, throughout all images very few PAH LIF is detected. The image sequence shows soot on average very localized near film 2 and the spark electrodes. This is consistent with early

soot formation in the top for an injected mass of 9.3 mg. Apparently, soot forms rapidly from fuel vapor such that the lifetime of PAH is short, and they are not caught at the investigated times aSOI. Figure 85b additionally shows that the integrated soot LII signal is low compared to an injected mass of 9.3 mg while the integrated PAH LIF signal is approximately zero the entire time aSOI. Also, the integrated soot luminosity and chemiluminescence signals are significantly lower for the reduced injected mass. Although the flame front reaches film 6, indicated by the chemiluminescence in the bottom of Figure 85a, soot LII is not found near film 6. However, soot luminosity is found in the bottom, apparently behind or in front of the light sheet plane. Also, few chemiluminescence signal is found in that area late aSOI, indicating oxidation of fuel, PAH, or soot. Consistent with the results from soot LII, soot luminosity is detected around the spark electrodes from 18 to 36 ms aSOI. In conclusion, the lower total heat released for an injected mass of 4.6 mg, most likely comes along with lower gas temperatures in particular in the bottom, inhibiting soot formation.

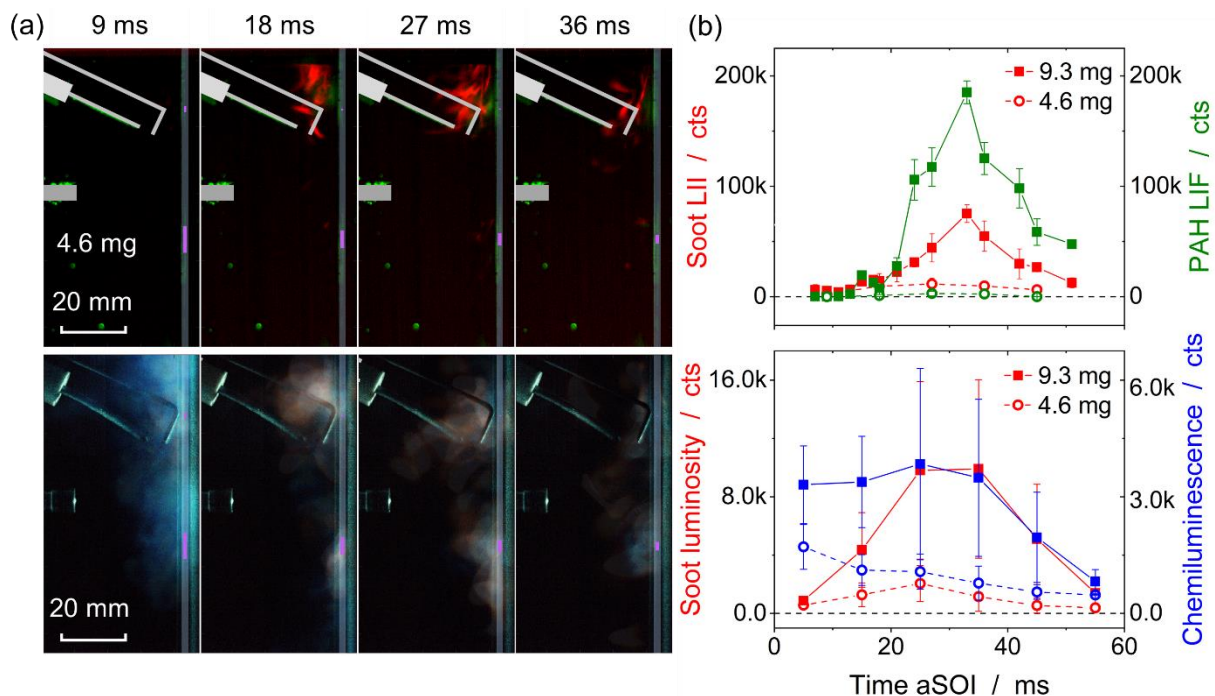


Figure 85: (a) Ensemble averages images of (top) PAH LIF/soot LII and (bottom) soot luminosity/chemiluminescence for an injected mass of 4.6 mg. (b) Evolutions of field-wide integrated signals of (top) soot LII and PAH LIF and (bottom) soot luminosity and chemiluminescence versus time aSOI. $T_w = 352$ K, $v_{air} = 1.8$ m/s, $m_{inj} = 4.6$ mg/ $m_{inj} = 9.3$ mg. Error bars indicate the standard deviation among 20 and 50 single shot images for $m_{inj} = 4.6$ mg and $m_{inj} = 9.3$ mg, respectively.

Figure 86 shows evolutions of PAH, soot, and chemiluminescence for wall temperatures of 342 and 332 K. Consistent with the previous cases, the images in Figure 86a show early soot formation in the top around 18 ms aSOI for both temperatures 342 and 332 K while for 342 K weak soot luminosity is also found near films 5 and 6. For both temperature, regions of chemiluminescence are found in the top and bottom of the test section throughout all times aSOI. However, soot luminosity downstream of film 6, indicates at 27 ms aSOI soot leaving the test section and not being oxidized. For 342 K, an intense and sudden formation of PAH

LIF becomes visible near film 6 at 27 ms aSOI with minor soot LII adjacent while for 332 K only weak PAH LIF arises at 36 ms aSOI near film 6. For a wall temperature of 332 K, the spatial extent of the flame front is reduced compared to 342 K such that a lower total heat released is expected which results in lower gas temperatures inhibiting the formation of PAH and soot, in particular in the bottom of the test section. The integrated PAH LIF signal is about a factor of four lower for the temperature 332 K than for 342 K while LII and soot luminosity, both mainly detected in the top, are of similar magnitude. Integrated chemiluminescence signals are clearly increasing with temperature until 15 ms aSOI, indicating a higher heat released from the flame front. Then, from 25 to 55 ms aSOI, the integrated chemiluminescence is of similar magnitude for 342 and 332 K. Therefore, the late oxidation of fuel, PAH, and soot appears to be unaffected by the change in temperature and the reduced soot formation. In contrast to the case at 352 K, where only PAH are found late aSOI, here soot and PAH are found near film 2 in the top of the test section at 342 and 332 K. That leads to the conclusion that the lack of LII signal around the PAH region near film 2 in the case of 352 K is not from insufficient temperature but equivalence ratio. However, the soot might also have been transported into that region.

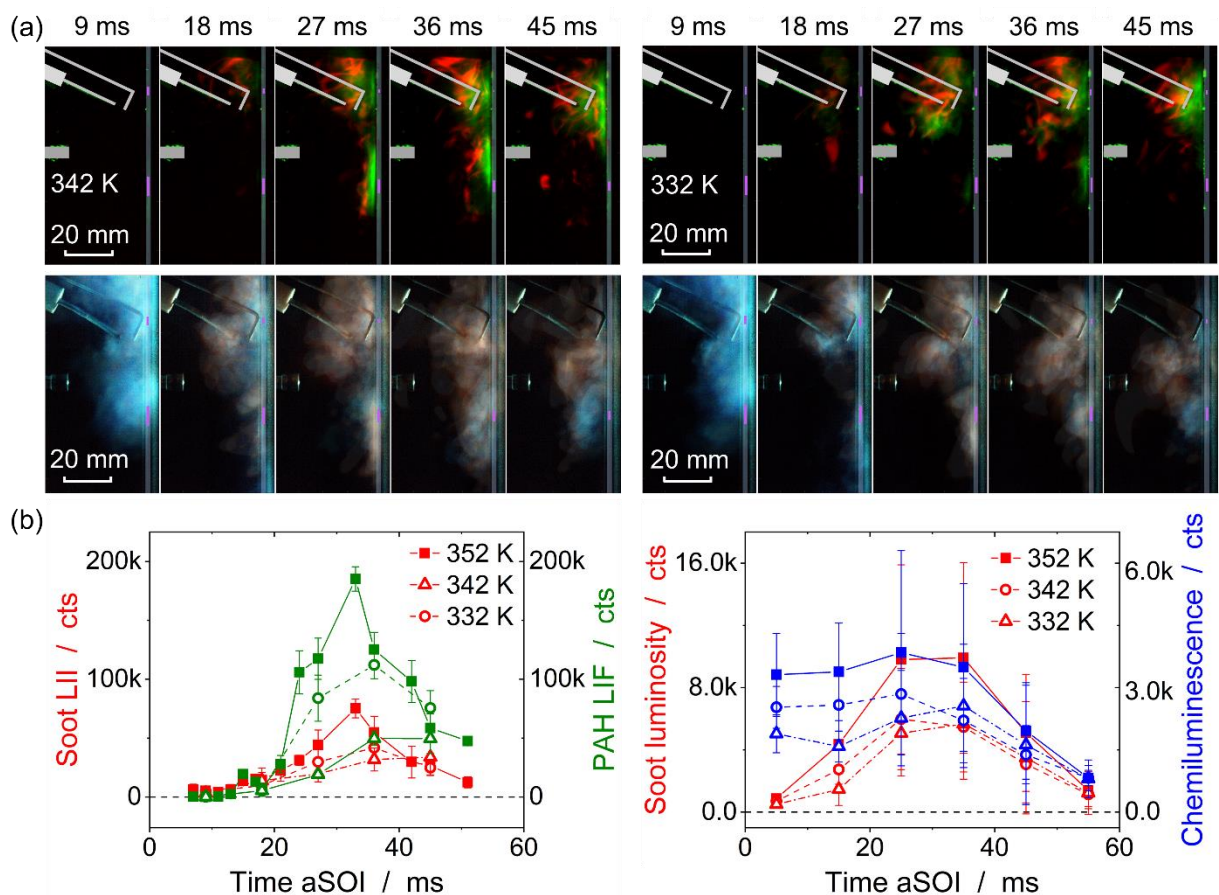


Figure 86: (a) Ensemble average images of PAH LIF/soot LII and soot luminosity/chemiluminescence for a wall temperature of (left) 342 and (right) 332 K. (b) Field-wide integrated signals of (left) soot LII and PAH LIF and (right) soot luminosity and chemiluminescence versus time aSOI. $T_w = 342$ K/332 K, $v_{air} = 1.8$ m/s, $m_{inj} = 9.3$ mg. Error bars indicate the standard deviation among 20 single shots for 332 and 342 K, respectively, and 50 single shots for 352 K.

From the previous cases, it is evident that LII signal is detected first around 18 ms aSOI for every case while soot luminosity is also found before that time. Most likely, the concentration of soot within the light sheet plane is too low to be detected because very small particles are sublimated by the high fluence laser. Table 5 shows the soot inception and extinction times determined from high-speed color combustion-sequences. The error is the relative standard deviation among 50 or 20 sequences. The emergence of soot was identified by visual inspection of the images and when the ratio of the signals in the green and blue color channels exceeded 1. Soot oxidation was considered finished when the signal vanishes into the background.

Table 5: Soot inception and extinction times.

Case			Soot inception time / ms aSOI	Soot extinction time / ms aSOI
352 K	1.8 m/s	9.3 mg	7.8 +/- 14%	76.3 +/- 18.4%
352 K	1.8 m/s	4.6 mg	7.3 +/- 21%	42.9 +/- 14%
342 K	1.8 m/s	9.3 mg	7.7 +/- 13%	127.7 +/- 21%
332 K	1.8 m/s	9.3 mg	9 +/- 27%	117.1 +/- 32%

The soot inception time seems to be unaffected by a variation in temperature and injected mass. The reason for that is most likely that soot is found first in the top of the test section where soot initiation is largely unaffected by the parameter variation. In contrast to this, the time until extinguishment increases by about 68% when the temperature decreases to 342 K and remains approximately constant when the temperature decreases further. Here, the longer lifetimes of the fuel films cause the late formation of soot. Figure 86a shows that integrated LII and soot luminosity of the cases for 342 and 332 K intersect with the trace of the case at 352 K around 45 and 57 ms aSOI, respectively, showing the persisting soot formation. The decrease in temperature tends to increase the shot-to-shot variability in the soot inception and extinction times as indicated by the increasing standard deviations. Reducing the injected mass to 4.6 mg causes a 43% lower extinction time than for an injected mass of 9.3 mg. Consistent with Figure 85, soot luminosity and LII levels are comparatively low and the fuel films have completely evaporated earlier such that it takes less time to burn out the soot.

5.4.4 Size-class dependent PAH-LIF imaging

Figure 87a shows ensemble averages of 100 single shot images of PAH LIF and soot LII in the Yale burner. The excitation wavelength and the detection filter-band are indicated in the rows and columns, respectively. The image pair “LIF + LII” and “LII” represent prompt detection and delayed detection (delay of 100 ns), respectively. Detecting laser-excited signals from the diffusion flame with prompt and delayed detection allows for discrimination of the short-lived fluorescence against the comparatively long-lived incandescence (several hundred ns). Therefore, the prompt detection captures both LIF and LII while the delayed detection shows solely LII with maybe slightly reduced intensity. Figure 87b and c show axial and radial profiles of PAH LIF and soot LII along the flame.

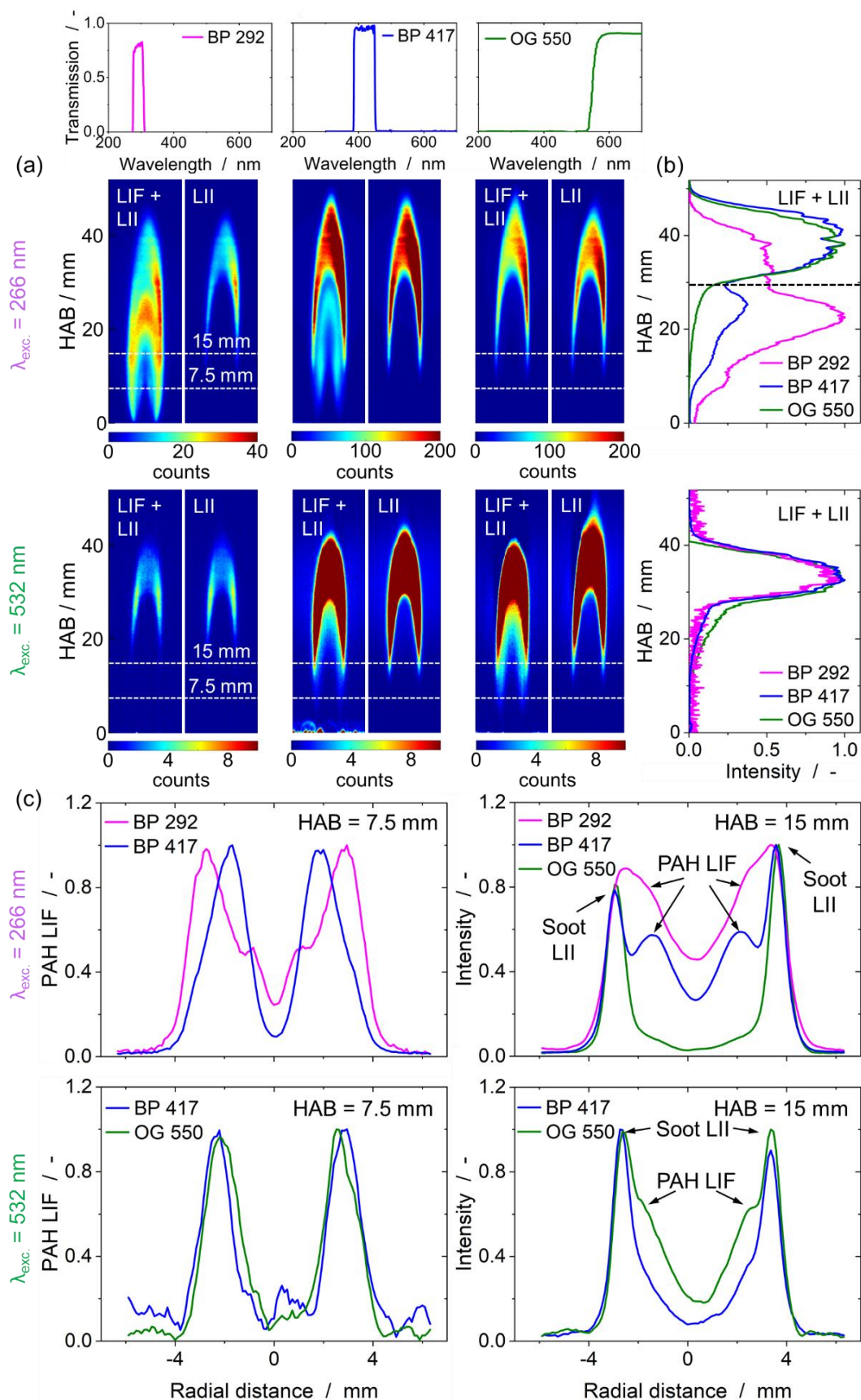


Figure 87: (a) Ensemble average images, (b) axial profiles, and (c) radial profiles at 7.5 and 15 mm HAB of PAH LIF and soot LII for varying excitation wavelengths and spectral detection-filters in the laminar diffusion flame of the Yale burner.

Excitation at 266 nm and detection in the UV (BP 292) and the blue-VIS (BP 417) clearly show PAH-LIF cones enclosed by LII signal. Note that the color scale is different for the two schemes. Excitation with 266 nm and detection with the OG 550 does not show LIF signal and thus pure LII in both images. The increased LII signal with the BP 417 and OG 550 results from the higher emissivity of LII in the VIS. The flame height still varies slightly between the images caused by fluctuations in the ethylene flow. Excitation with 532 nm and detection in the UV (BP 292) also shows solely LII in both images. In contrast to this, weak PAH LIF is detected in the VIS with the BP 417 and the OG 550, partially overlapping to the sides and to the top with soot LII.

Figure 87b shows signal profiles along the center axis of the flame with increasing HAB, extracted from the particular image with prompt detection (“LIF + LII”). Each profile is normalized to the maximum signal along the centerline. When exciting with 266 nm, the trace BP 292 indicates a plateau around 10 mm HAB and peaks around 22.5 mm HAB. The profile detected with the BP 417 shows a local maximum 25 mm HAB. Consistent with the results from the Santoro burner, both PAH-LIF profiles approximately peak at a HAB where the LII signal starts to significantly increase. The appearance of a “dark region” between the PAH LIF and soot LII signals was also reported by Vander wal et al. and Hayshida et al. and attributed to the soot nucleation region (here indicated by the dashed line around 30 mm HAB) [170, 171]. The LII signal peaks around 40 mm HAB. Excitation at 532 nm shows no such clear stratification of PAH LIF and soot LII with increasing HAB. Nevertheless, weak PAH LIF is detected with the BP 417 and even stronger with the OG 550 starting from around 15 mm HAB but interfered by the strong LII signal with further rising HAB, indicating the direct participation in soot nucleation.

The spatial separation of soot precursors and soot becomes also apparent when looking at radial profiles in the laminar diffusion flame, as shown in Figure 87c. At 7.5 mm HAB, LII signal is not detected as visualized by the images in Figure 87a so that the two plots for that height exclusively show PAH LIF. Excitation with 266 nm and detection with the BP 292 shows a first local maximum, consistent with the plateau in Figure 87b, around 1 mm away from the centerline and then peaks in a distance of around 3 mm from the centerline. Interestingly, PAH LIF excited with 266 nm and detected with the BP 417 is spatially located between the two regions around 2 mm away from the centerline. However, this spatial distance can also be caused by the slightly varying flame shape (flickering of the flame). Nevertheless, excitation with 266 nm and detection in the UV apparently visualizes two different size classes of PAH (possibly 2-3 ring and 3-4 ring PAH) indicated by the two peaks. Detection in the blue-VIS then apparently only shows a single size-class, which might be the 3-4 ring PAH. The apparent stratification of 2-3 and 3-4 ring PAH was also observed by Mannazhi et al. via excitation of PAH LIF at 266 nm and detection in the UV or blue-VIS in a premixed ethylene-air flame [210]. Exciting PAH LIF at 532 nm and detecting with the BP 417 or OG 550 shows the signals approximately overlapping, indicating the same size-class being detected, and peaking in a distance of around 2-2.5 mm from the centerline. At a HAB of 15 mm, significant contributions of PAH LIF are found in a radius of around 2 mm around the centerline while further outside PAH are consumed and vanish in the strong LII signal.

5.4.5 Transparent soot-precursor layer in fuel-film combustion

The size-dependent detection of PAH was next performed in the constant-flow facility. Figure 88 shows ensemble averages of 100 single shot images of PAH LIF at different times aSOI. The filter-transmission spectra and excitation wavelengths corresponding to the particular image series are indicated on the left side in Figure 88.

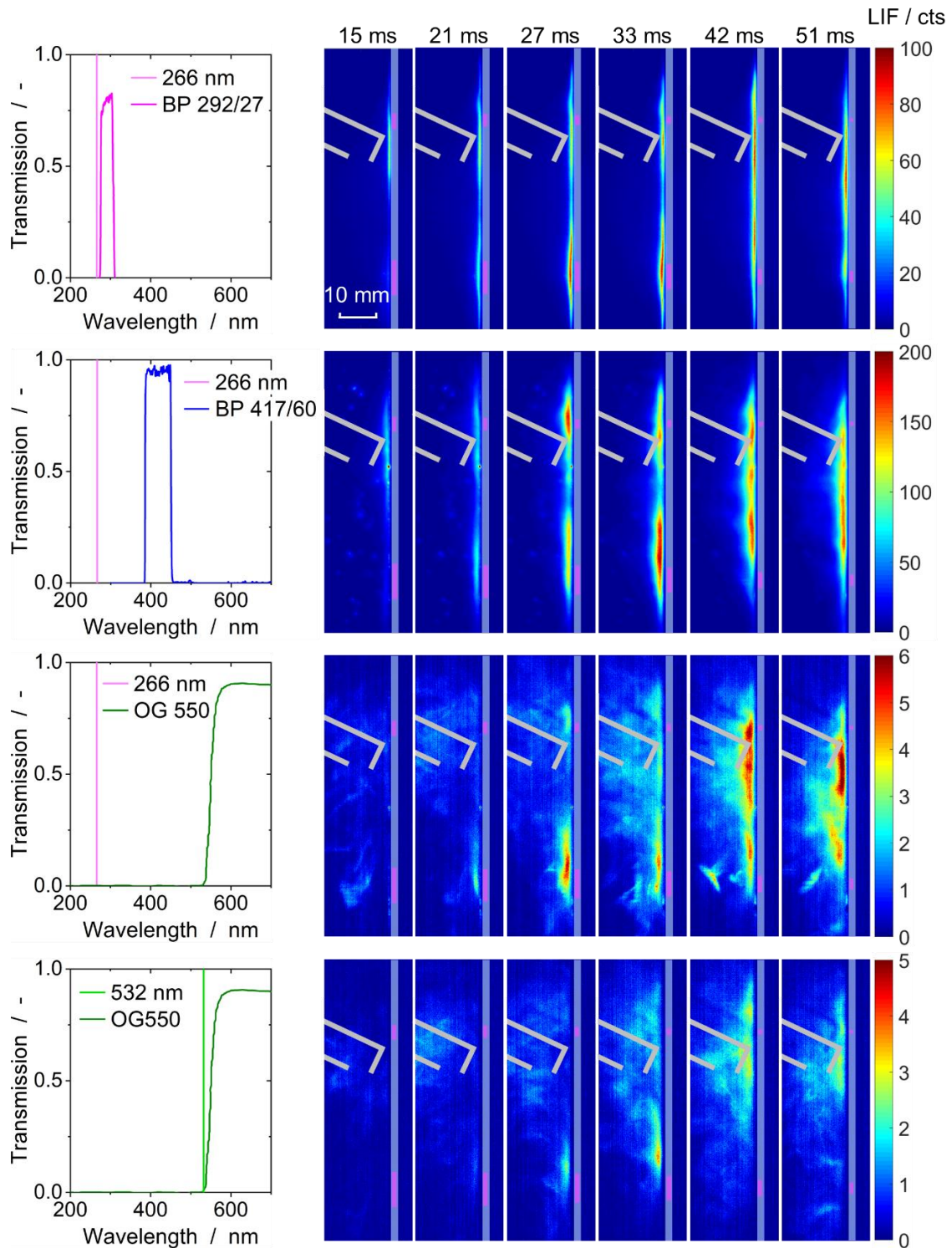


Figure 88: Ensemble average images of PAH LIF, excited at 266 nm and 532 nm and detected with different filter bands, near the evaporating fuel films 2 and 6 at different times aSOI. $T_w = 352 \text{ K}$, $v_{\text{air}} = 1.8 \text{ m/s}$, $m_{\text{inj}} = 9.3 \text{ mg}$.

The top row shows PAH LIF excited with 266 nm and detected in the UV. Throughout the entire time series, PAH LIF appears very close to the wall and the fuel-film surface. The signal spreads towards the top and bottom along the wall and only slightly towards the core of the test section. Near film 2, in the top, the signal is found earlier, already at 15 ms aSOI, and on average more intense than near film 6. The signal becomes maximal around 27-33 ms aSOI and persists with similar magnitude until 51 ms aSOI.

Switching the detection filter to the BP 417, it is found that the signal stripe is thicker and more blurred towards the core of the test section, indicating larger size classes being excited that participate in soot formation. Again, PAH LIF is found first near film 2 in the top and then appears in two intense regions, each close to either fuel film 2 or 6. Late aSOI, the two regions merge between the two fuel films. In general, PAH LIF detected in the blue-VIS is a factor of two stronger than signal detected in the UV when exciting with 266 nm which is consistent with the findings from the Yale-burner flame. PAH LIF detected in the blue VIS is expected to be even more intense when exciting with 355 nm.

Detection through the longpass filter OG 550 upon excitation at either 266 or 532 nm shows PAH LIF, soot luminosity, and weak LII signal. The contributions from LII and natural soot luminosity were found by delaying the gate and turning off the laser, respectively. However, LII and soot luminosity are always detected around 3-4 mm from the wall such that signals closer than this can be attributed to pure PAH LIF. Consistently, PAH LIF detected in the UV and blue-VIS are also located within this soot-precursor layer. In contrast to the detection in the UV or blue-VIS and consistent with Section 5.4.1, PAH onset is near film 6 and from 27 ms aSOI onward with detection by the OG 550. The images reveal that the signal becomes spatially more intermittent with increasing detection wavelength, clearly denoting the decreasing diffusivity and increasing size of the detected PAH. In contrast to the results from the Yale burner, here PAH LIF excited with 266 nm and detected with the OG 550 is prominent. Usually, LIF captured with the OG 550 is expected to be more intense when exciting with 532 nm while here it is around 50% lower here compared to excitation with 266 nm which is also in contrast to the results from the Yale burner. Most likely, the 532 nm light sheet was not properly adjusted (i.e., spatially inhomogeneous fluence distribution and low fluence in FOV).

Complementary to the laser-based imaging techniques, Figure 89 shows ensemble average images of natural combustion luminosity. As during the acquisition of the laser-based images, the camera's optical axis was aligned along the quartz wall where the fuel films evaporate from. Therefore, the distance between the wall/fuel films and flame luminosity can be derived from the image's scale with good accuracy due to the lack of perspective error. The sequence shows that the flame front quenches very close to the wall. However, the line-of-sight based measurement does not tell whether the flame only gets so close to the wall between the fuel films. In contrast to this, soot luminosity is systematically found around 3 mm away from the wall which is consistent with the results from PAH LIF in Figure 88. This finding underlines the assumption of a soot-precursor layer, transparent in the VIS, systematically existing between fuel films and soot. In contrast to chemiluminescence which is found between the wall and the soot luminosity from 12-21 ms aSOI, soot is never found close to the wall.

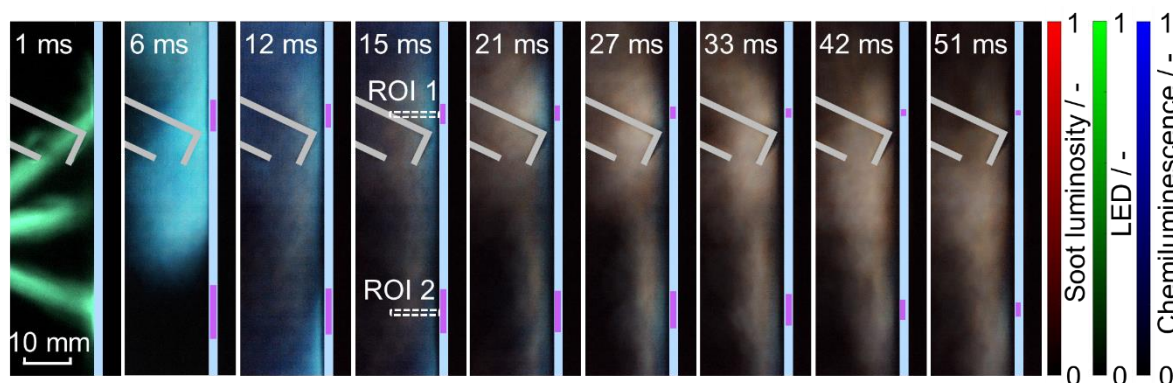


Figure 89: Ensemble-average images from 50 sequences of high-speed color combustion imaging. $T_w = 352$ K, $v_{air} = 1.8$ m/s, $minj = 9.3$ mg.

Figure 90 plots PAH LIF, excited with 266 nm, and soot luminosity, from Figure 88 and Figure 89, respectively, with increasing distance from fuel films 2 (top) and 6 (bottom) at 33 (left) and 42 (right) ms aSOI. The signals were extracted from two ROIs emerging from the centers of films 2 and 6, as indicated in the image acquired at 15 ms aSOI in Figure 89, and vertically averaged.

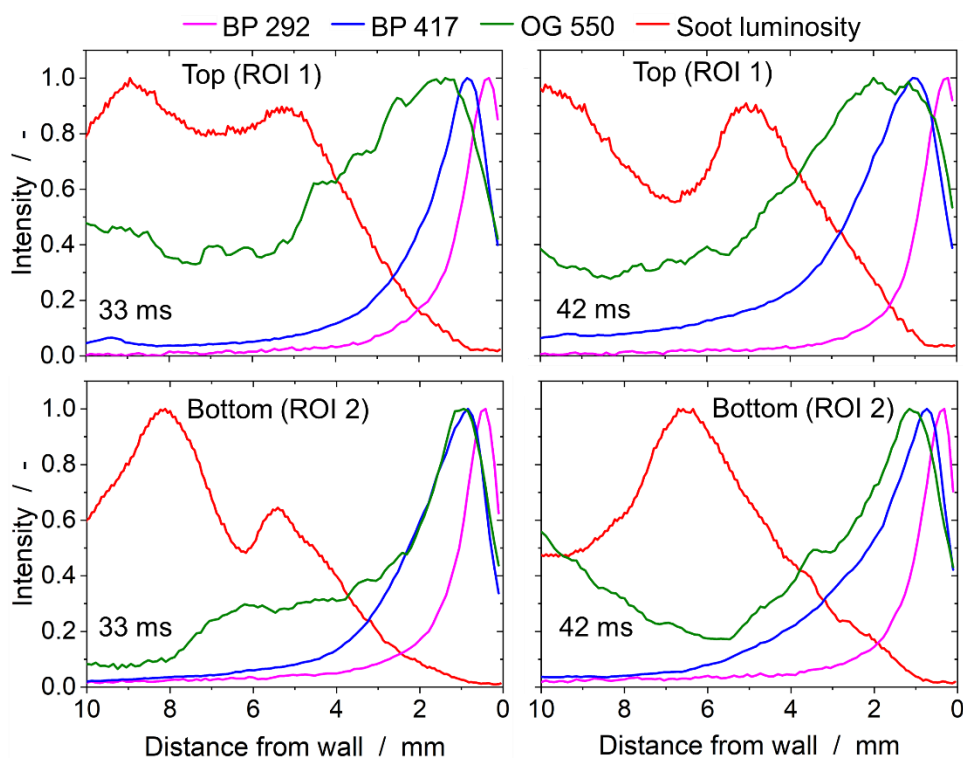


Figure 90: PAH LIF and soot luminosity with increasing distance from films 2 and 6 at 33 and 42 ms aSOI.

Overall, the signals mostly peak at different distances from the fuel film, generally the further away, the longer the detection wavelength. Apparently, small size-classes (BP 292) are quickly consumed close to the film surface, forming mid-size classes (BP 417) that then propagate further away from the fuel film. PAH LIF from mid-size classes then decreases (mid-size PAH are apparently consumed) and large PAH form (OG 550) which then fluoresce with low SNR at wavelengths > 550 nm. In contrast to the flame in the Yale burner, here the spatial profile of

PAH LIF detected in the UV (BP 292) does not exhibit two peaks, thus apparently only representing a single PAH size-class. Generally, the segregation of PAH LIF appears more pronounced near film 2 and in particular at later times aSOI, i.e., at 42 ms aSOI, when the PAH LIF region blurs out, as shown in Figure 88. Soot luminosity starts to significantly increase around 1 mm away from the wall and peaks in a distance of around 5-8 mm from the wall. The stratification of soot precursors and soot is most likely attributed to the formation of thermal and concentration boundary layers. Under similar conditions ($T_w = 363$ K, ambient pressure 1 bar), Tao et al. [141] found the thickness of the built up fuel-vapor boundary layer on the order of 1.2-1.5 mm while the thermal boundary layer was slightly thinner (~ 1 mm). This is consistent with the dimensions of the spatial stratification of soot precursors and soot from this work. Near the wall small PAH form in a region of low temperature and very fuel-rich conditions. They are transported away from the wall into a region of higher temperature where they are consumed to form large PAH which are consumed to form soot even further away from the wall in the hot burnt gas.

5.4.6 Soot formation in optically accessible gasoline engine

Together with Bosch, the diagnostics developed for simultaneous visualization of PAH LIF and soot LII were transferred to the optically accessible SIDI engine, see Figure 76 for optical layout. To the author's knowledge, this is the first time that PAH LIF was detected in a GDI engine. As these results were acquired in a measurement campaign with limited time, they are considered preliminary and more a proof of concept. Figure 91 shows the sequence of a single combustion event, captured with a high-speed color camera through the quartz cylinder-liner in the engine.

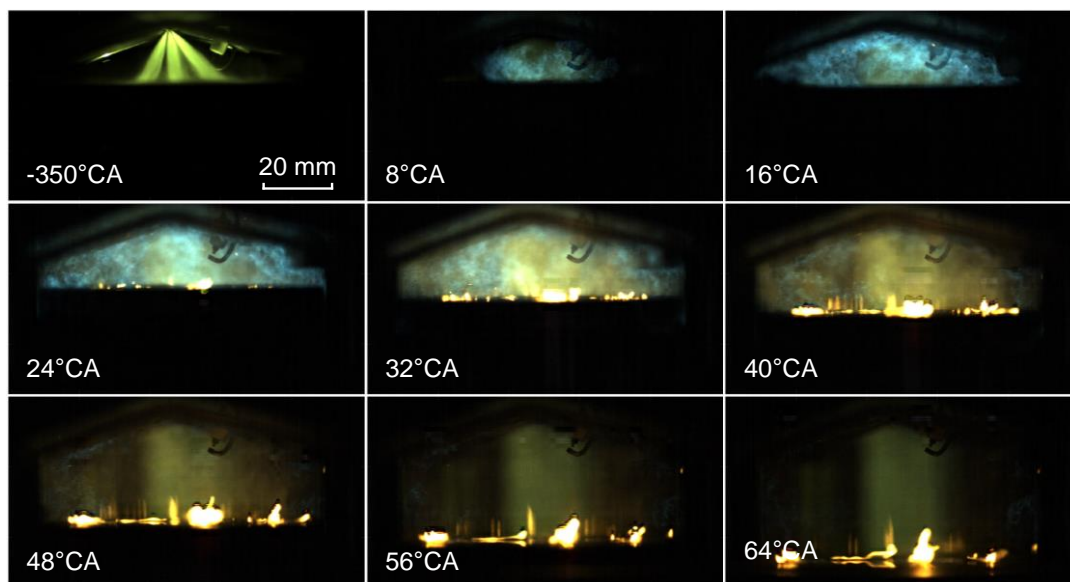


Figure 91: High-speed sequence of the combustion luminosity of a single cycle, showing the spray (turquoise-green), the flame front (blue), and soot luminosity (orange).

At -350°CA the spray is propagating through the cylinder and impinges on the piston surface, where it forms fuel films. From 8 to 32°CA the flame front propagates through the combustion

chamber, as indicated by the blue chemiluminescence. Then, from 24 to 64°CA pool fires arise near the piston surface, indicated by the soot luminosity.

For the first laser-based measurements, the 50/50 beam splitter was removed and simultaneous excitation of PAH LIF and soot LII with solely 532 nm and 1064 nm, respectively, was employed. The corresponding detection optics, as shown in Figure 76, were put in front of the cameras. Figure 92 shows single shots of PAH LIF and soot LII. Each image is normalized to the maximum signals of PAH LIF or soot LII. The comparatively long gate of the LII camera (2000 ns) leads to an interference of LII with soot luminosity. Therefore, the red color in Figure 92 comprises both soot LII and luminosity. In contrast to that, soot luminosity is not found in the PAH-LIF (green) detection. In good agreement with the flow-facility measurements, PAH and soot are mostly spatially separated from each other, indicating that the 532 nm laser does not excite significant LII signal. Throughout all images, soot always appears adjacent to PAH while PAH are also detected in some regions where soot is not apparent. Both PAH and soot are mostly found very close to the piston surface, while PAH are even closer to the surface and thus to the fuel films. Apparently, in the bottom image, acquired 40°CA, the green signal presumably corresponds to LII of soot rather than PAH LIF, indicated by the overlap of the two signals excited at 532 and 1064 nm. This is due to the focus of the green laser at this height above the piston surface, leading to locally high laser fluence.

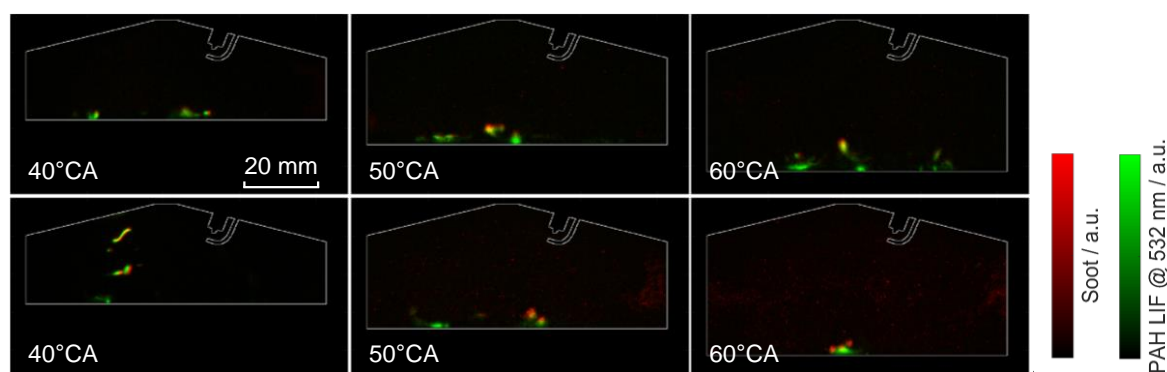


Figure 92: Single shots of PAH LIF, excited with 532 nm, and soot LII, excited with 1064 nm, from individual combustion events.

In a second measurement, simultaneous excitation with 266 and 355 nm was employed as shown in Figure 93. In both detection channels, soot luminosity was not detected due to the short gates. According to section 3.3, detection of PAH LIF, excited at 266 nm, with a longpass filter causes the LIF signal to consist of contributions from many different size-classes of PAH. In contrast to that, the detection of PAH LIF, excited with 355 nm, with a bandpass filter in the blue-VIS spectral region results in LIF mostly from PAH with three and four aromatic rings. In Figure 93, PAH LIF excited at 266 nm is detected as a very thin layer on the piston surface. It sometimes spatially overlaps with the signal from 355 nm excitation. The high SNR of PAH LIF excited with 355 nm is also consistent with the literature and the discussion in previous sections. Throughout all single shots both signals are very close to the piston surface.

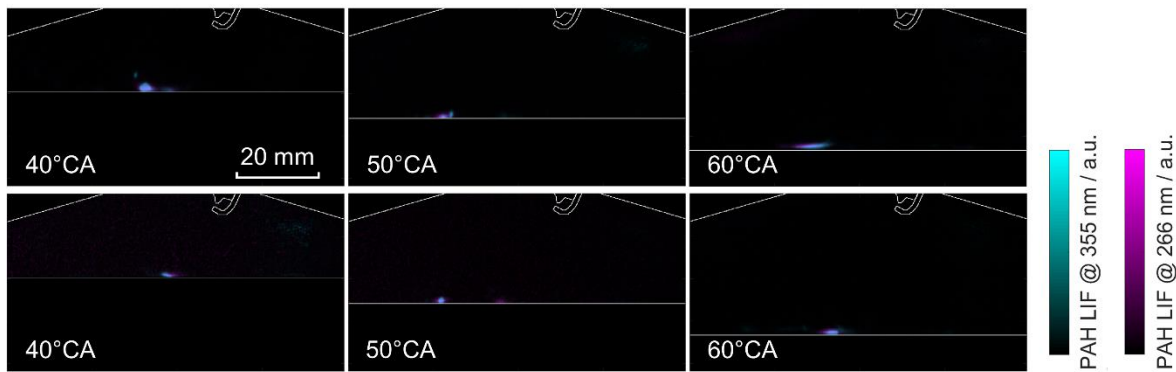


Figure 93: Single shots of PAH LIF images, excited with 266 and 355 nm, from individual combustion events.

The simultaneous visualization of PAH LIF and soot LII with four lasers and cameras according to Figure 76 is shown in Figure 94. Excitation at 266 nm did not yield any signal. This was due to camera sensitivity problems and signal attenuation beyond the second beam splitter. 40°CA, the images show PAH, excited at 355 and 532 nm, spatially overlapping on the piston surface near film 5. Soot is found on the right side and further away from the piston surface in both images. 50°CA, the PAH LIF again spatially overlaps and covers the piston surface near film 5. Here, soot is detected slightly above but adjacent to the PAH cloud. In the top image at 60°CA, PAH are found near film 6 while soot is not detected. In the bottom soot is detected above a layer of PAH, excited by 355 and 532 nm.

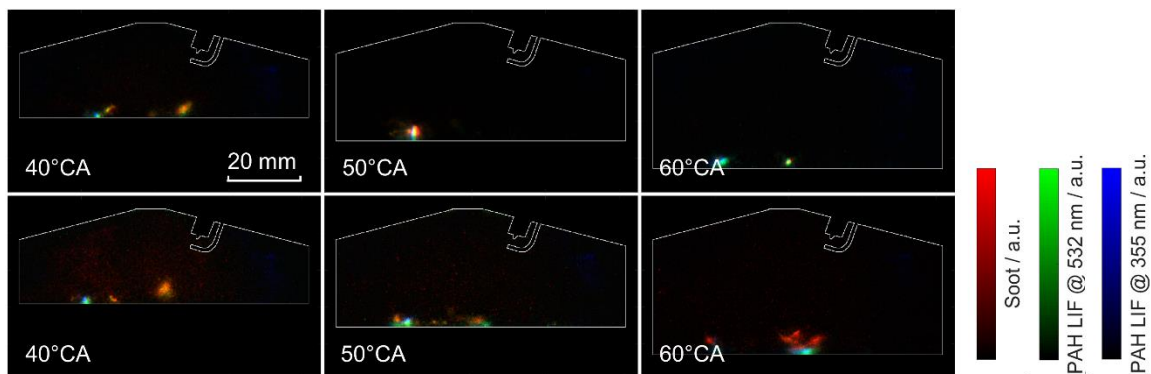


Figure 94: Single shots of PAH LIF images, excited with 355 and 532 nm, and soot LII, excited with 1064 nm, from individual combustion events.

5.5 Section conclusions

Laser diagnostics and high-speed combustion imaging were used to image fuel vapor, chemiluminescence, PAH, and soot emerging from evaporating fuel films in combustion. The diagnostics were mainly performed in the test section of a constant-flow facility which was replaced with laminar diffusion-flame burners for in-situ preliminary measurements. In proof-of-principle experiments, the laser-based diagnostic was also used in an optically accessible SIDI engine.

Tracer LIF of toluene was used to image the air/fuel ratio in the constant-flow facility. It was found that even the premixed fuel/air-mixture contains some very fuel-rich region with λ around 0.5 in the top of the test section. Therefore, when the flame front propagates through

such regions, soot formation is expected. Later, when the premixed fuel/air-mixture is transported out of the test section, fuel vapor plumes with λ even below 0.5 are emerging from the evaporating fuel films, providing a high tendency for soot formation. Interestingly, when combustion is initiated fuel vapor plumes are not visually emerging from the fuel films. This indicates that the fuel vapor pyrolytically decomposes very close to the fuel films within the hot burnt gas and grows to PAH and eventually soot.

LIF excited at 532 nm and LII excited at 1064 nm were used to simultaneously visualize PAH and soot, respectively, in the constant-flow facility during fuel-film evaporation in transient, turbulent combustion. In preliminary experiments, the technique was applied in the sooting, laminar co-flow diffusion flame on a Santoro burner. PAH LIF excited with the 532 nm sheet was linear in fluence up to about 0.01 J/cm². 0.008 J/cm² were chosen to yield maximum LIF signal yet low LII interference. The 1064 nm sheet had an average fluence of 0.5 J/cm² since the LII signal was found to saturate at that laser fluence. On the jet centerline the PAH-to-soot transition region was identified 40 mm above the nozzle.

Single shots show that PAH and soot mostly form in spatially separated but often adjacent regions with PAH closer to the fuel films. This is consistent with fuel pyrolyzing while being transported away from the evaporating films. The early formation of soot without the presence of PAH in the top of the FOV occurs most probably in a predominantly oxygen-free high-temperature pyrolysis, as the turbulent flame front has passed through this region. Later, strong PAH-LIF signal arises downstream in the lower FOV, close to lower fuel-films, while very little soot is detected in this region. The PAH layer is located between a chemiluminescence region and the fuel film, indicating that soot formation here is initiated in the vicinity of a non/partially-premixed flame. At the same time, the chemiluminescence indicates oxidation that might prevent the transition from PAH to soot. The LII signal is highest when the PAH layer moves out of the chemiluminescence region and mixes with soot from the top between the two fuel films. This and the large spatial overlap between LIF and LII signals indicate that soot formation is enhanced and that PAH excitable at 532 nm are a main contributor to soot nucleation. Ensemble-average images indicate that the spatial intermittency in the signal is much more pronounced for soot LII than for PAH LIF. Soot luminosity is detected after the premixed phase of combustion and before soot LII.

Reducing the constant-flow facility's temperature (the fuel films then survive significantly longer) results in soot formation until later times aSOI compared to the case at elevated temperature. Therefore, the lack of soot formation late aSOI at elevated temperature results from fuel-lean conditions rather than from insufficient burnt-gas temperatures. Generally, increasing the flow-facility temperature significantly shortened the time until the soot luminosity extinguished, i.e., soot was oxidized.

For one selected combustion event, high-speed images of natural combustion luminosity were compared to the CFD results. Chemiluminescence signals and the predicted OH distributions qualitatively agree, while in the CFD OH is spatially more extended and lasts much longer than visible chemiluminescence. Soot filaments appear in the vicinity of the wall films. Both the location and the spatial extent of the soot regions are well predicted by the simulation compared

to the experiment. The experiment shows in particular that soot from fuel films forms in the post-combustion region, indicated by the disappearance of visible chemiluminescence.

By varying the excitation wavelength and the detection filter-band, different size-classes of PAH were visualized via LIF in the flame of a Yale burner and the constant-flow facility. In both experiments, it was found that PAH LIF with comparatively high SNR can be detected by exciting in the UV (i.e., 266 nm) and detecting in the UV and blue-VIS. Then, PAH with 2-3 and 3-4 aromatic are expected to be detected. With less SNR, PAH LIF is detected when exciting with 266 nm or 532 nm and detecting at wavelengths longer than 550 nm. Based on the literature, the longer detection wavelength corresponds to an increasing number of aromatic rings in the detected PAH size-class. High-speed color combustion-imaging in the constant-flow facility revealed that there is a layer of a few millimeters between the fuel films and soot, which is transparent in the VIS. Taking advantage of this size-dependent excitation/detection-scheme of PAH LIF, it was found that this transparent layer consists of soot precursors. The growth of PAH was consistent with the one observed in the Yale burner, with small-size classes close to the fuel films, growing to larger size classes and eventually soot with increasing distance to the fuel films.

6 Conclusions and future work

6.1 Summary and conclusions

Multiple optical-imaging diagnostics were used to investigate the impact of evaporating fuel films on soot formation by illuminating the entire process chain from fuel-film formation over evaporation, emergence of fuel vapor, combustion, formation of PAH, to eventually soot particles. The diagnostics were mostly applied in the optically accessible test section of an atmospheric constant-flow facility, a direct-injection model experiment. Here, a GDI injector sprays fuel at high pressure into the test section. The spray evaporates and mixes with hot air, constantly flowing from top to bottom through the section at 1 bar. Some of the fuel impinges on a quartz wall on the opposite side of the injector and forms fuel films. A pair of electrodes ignites the fuel/air mixture. The flame front propagates through the test section and ignites sooting flames near the evaporating fuel films. The steady-state and transient flow fields were determined with PIV and optical-flow measurements, respectively. Significantly higher flow velocities were found when combustion is initiated.

The thickness of the fuel films was determined from quantitative tracer-LIF imaging and partially compared with results from a 3D-CFD simulation. Toluene was chosen as a tracer and iso-octane as surrogate fuel. The images reveal that the fuel films contract into thick droplets throughout the evaporation in particular on a hot wall. This leads to high spatial intermittency within the fuel-film structure, reduces the fuel-film area, potentially increasing the fuel-film lifetime. From the thickness images, the film mass and evaporation rate were derived. From LIF and CFD, it was found that the evaporation rates are highest early aSOI, most likely due to strong turbulence within the test section induced by the fuel injection. With ongoing time, LIF imaging and the CFD simulation find the evaporation rate to decrease and approach a constant level, strongly depending on the wall temperature. The quasi-steady evaporation rate indicates a constant mass transfer coefficient and fuel-vapor concentration gradient, the latter implying constant film temperature.

Combustion shows a minor effect on the fuel-film evaporation rate compared to the wall temperature in either CFD or LIF. The influence of combustion becomes more prominent for an increased injected mass. In a real SIDI engine, fuel films evaporate from a metal surface (steel or aluminum). The heat capacity of quartz is about 1.5 times higher than the one of steel. This leads to a stronger temperature decrease of the steel in the thermal boundary layer during evaporation. However, at the same time the thermal conductivity of steel is about 30 times higher than that of quartz. This presumably compensates for the lower temperature gradient between the wall and the fuel film. Aluminum has higher heat capacity and thermal conductivity than quartz, promoting a greater heat flux from the wall to the liquid. Therefore, also in an engine the fuel-film evaporation is expected to be determined by the wall temperature compared to the influences of combustion or flow velocity.

In the LDM, fuel-film and wall temperatures were determined from a heat balance around a fuel-film element and by discretizing the wall heat equation. The results show that the quartz wall does not cool down much in the impingement region early aSOI as the thermal conduction

from the bulk solid keeps the surface temperature close to the initial temperature. The fuel-film temperature rapidly approaches the wall temperature, independent of the initial film temperature and consistent with the CFD simulation. The wall temperature thus determines the fuel-film temperature, its saturation vapor pressure, and thereby also the evaporation rate. The model also indicates that the convective heat flux from the gas phase is about 10 times lower than thermal conduction from the wall. This is consistent with the results from CFD and LIF that under the current conditions, combustion has minor effect on the evaporation rate. In a real engine the air flow velocity is expected to be higher throughout the evaporation of the liquid fuel film, enhancing the convective heat transfer. A flow velocity of about 10 m/s increases the convective heat flux about a factor of five compared to the 1.8 m/s in our experiment. However, even then conductive heat flux from the wall would still be two times greater.

In a second part of this work the mixing of the gaseous fuel with air and the formation of PAH and soot were investigated. The equivalence ratio prior to combustion was imaged by tracer LIF. Throughout fuel-film evaporation, fuel-vapor plumes with air/fuel-ratios below 0.5 and thus a high tendency for soot formation are emerging towards the core of the test section. Then, the formation of soot near the evaporating fuel films was imaged by means of PAH LIF, soot LII, and high-speed combustion imaging. Preliminary in-situ measurements were done in the laminar diffusion flames of a Santoro burner and a Yale burner. Here, PAH LIF, excited with different excitation/detection-schemes, assigning different size-classes of PAH, is detected in a hollow cone region. The edges of the PAH-LIF cones are partially overlapping with regions of high soot LII signal, indicating the nucleation region where soot forms from PAH.

The comprehensive laser-based measurement technique was then applied at the optically accessible test section of the constant-flow facility to simultaneously visualize PAH and soot. Additionally, high-speed color combustion-imaging was used to visualize chemiluminescence and natural soot luminosity. Single shots of simultaneous PAH LIF, excited at 532 nm, and soot LII, excited at 1064 nm, show PAH and soot mostly in spatially well separated but adjacent regions and near the fuel films. Early soot formation in the top of the constant-flow facility occurs most probably predominantly as high-temperature pyrolysis, as the premixed flame front has left hot oxygen-depleted burnt gas in this region. In the bottom strong PAH formation without significant soot is found. The PAH layer is located between a chemiluminescence region and a fuel film, such that soot formation here is in the vicinity of a non/partially-premixed flame. The paucity of soot here results from insufficient temperatures and immediate oxidation. Then, the flow merges PAH from the bottom with soot from the top between the two fuel films and PAH LIF and soot LII become strongest. The large spatial overlap between LIF and LII signals indicate that soot formation is enhanced and that PAH excitable at 532 nm are a main contributor to soot nucleation. In average images, soot LII appears with a very high spatial intermittency while PAH form a more continuous cloud. High-speed color combustion-imaging shows that soot luminosity is detected after the premixed phase of combustion and before soot LII. The spatiotemporal evolution of the natural combustion luminosity, i.e., soot luminosity and chemiluminescence, was also compared to volume renderings of the OH concentration and f_V from a CFD simulation. Both methods predict soot formation in distinct filaments, close to the wall with the time of onset and extinguishment of soot in good agreement.

A variation of the excitation wavelength and the detection filter-band identifies different size-classes of PAH when visualizing LIF in the flame of a Yale burner and in the constant-flow facility. In both setups, PAH LIF excited in the UV (i.e., 266 nm) and detected in the UV or blue-VIS occurs with high SNR. With such a combination of excitation wavelength and detection filter-band, PAH with 2-3 and 3-4 aromatic are expected to be detected. PAH LIF excited with 266 nm or 532 nm and detected at wavelengths longer than 550 nm is detected with reduced SNR. The longer detection wavelength is most likely attributed to an increasing number of aromatic rings in the detected PAH size-class. High-speed color combustion-imaging in the constant-flow facility indicates a layer of a few millimeters, which is transparent in the VIS, between the fuel films and soot. It was found that PAH detected with different combinations of excitation wavelength and detection filter-band are located within this transparent layer. Small size-classes (attributed to detection in the UV) are found close to the fuel films, growing to larger size classes and eventually soot with increasing distance to the fuel films.

Simultaneous imaging of PAH LIF, excited at 266, 355, and 532 nm, and soot LII, excited at 1064 nm, was also done in an optically accessible engine together with Bosch. The results are qualitatively consistent regarding the spatiotemporal evolution of PAH and soot while both substances are found much closer to the wall compared to the results from the test section.

6.2 Future work

For longer injection durations, substantial evaporative cooling of the wall might occur. In such a scenario, the film temperature and evaporation rate could vary more strongly throughout the fuel-film evaporation. Suitable techniques, such as phosphor thermometry [143], for measuring the transient surface and film temperature are then required. To also investigate the magnitude of convective heat and mass transfers in more detail, the flow field during combustion needs to be acquired, which could be done by PIV measurements with solid particles. Then, heat and mass transfer coefficients could be determined based on correlations and help to assess the impact of convection.

In terms of soot formation in SIDI engines, the diagnostics for PAH LIF and soot LII with the excitation/emission-schemes developed here could be transferred to the optically accessible SIDI engine for more thorough measurements. First, by high-speed combustion imaging it should be clarified whether the transparent soot-precursor layer also exists in an engine. At high pressure, it is expected that the transition from fuel vapor to soot occurs faster and even closer to the fuel films, resulting in a much thinner layer than in the atmospheric-pressure model experiment. Then, the spatiotemporal evolution of PAH and soot can be investigated and compared to these results in terms of a layer arrangement and different size-class PAH.

Since soot formation always requires fuel-rich conditions, the air/fuel ratio λ is an important parameter. In an engine and in the absence of fuel films, the nominal air/fuel ratio is also the actual air/fuel ratio. However, when fuel films are present the nominal air/fuel ratio is not the actual one since parts of the injected fuel are not gaseous but liquid on in-cylinder surfaces. However, the fuel-film mass can be measured with tracer LIF such that also the fuel-vapor mass is known, and the actual λ can be calculated. By that, it can be checked whether soot formation

near fuel films occurs either in a region with excess oxygen (non-premixed flame) or without oxygen (pyrolysis). It would be interesting to see how the evolution of different PAH size classes and soot differs for the two regimes with different oxygen concentrations. Also, the fuel chemistry is expected to have a major impact on the soot formation tendencies of evaporating fuel films. Increasing the share of aromatics in the fuel leads to a soot onset closer to the fuel films and a shrinking of the soot-precursor layer.

Soot oxidation, which is generally not much investigated in transient turbulent combustion, could be visualized by high-speed $\text{OH}^*/\text{VIS-CL}$ or OH LIF simultaneously with soot LII or PAH LIF. Experimentally, LIF imaging of ground-state OH or at least passive imaging of chemiluminescence of electronically excited OH would also allow a more direct comparison with the combustion markers available in the CFD. This may be particularly helpful in analyzing soot or PAH oxidation. Then, it would be interesting to see whether different size classes of PAH are differently attacked by oxidizing OH^* . Also, it could be investigated to what extent high-speed imaging techniques are suitable for replacing costly laser light-sheet based techniques.

7 Bibliography

7.1 References

1. Krzyżanowski, M., Kuna-Dibbert, B., Schneider, J., *Health Effects of Transport-related Air Pollution*, Ed. 1, Copenhagen: World Health Organization Europe, 2005, pp. xiii-xvi.
 2. Faiz, A., Weaver, C.S., Walsh, M.P., *Air Pollution from Motor Vehicles: Standards and Technologies for Controlling Emissions*, Ed. 1, Washington D.C.: World Bank, 1996, pp. xiii-xiv.
 3. van Basshuysen, R., *Ottomotor mit Direkteinspritzung: Verfahren, Systeme, Entwicklung, Potenzial*, Ed. 1, Wiesbaden: Springer Fachmedien, 2007, pp. 29-74, 430.
 4. McGranahan, G., Murray, F., *Air Pollution and Health in Rapidly Developing Countries*, Ed. 1, London: Taylor & Francis, 2012, pp. 44-6.
 5. Bockhorn, H., D'Anna, A., Sarofim, A.F., Wang, H., *Combustion Generated Fine Carbonaceous Particles*, Karlsruhe: KIT Scientific Publishing, 2009.
 6. Liebl, J., Beidl, C., *Internationaler Motorenkongress 2015*, Ed. 1, Wiesbaden: Springer Fachmedien Wiesbaden, 2015, pp. 218.
 7. Spicher, U., *Direkteinspritzung im Ottomotor*, Ed. 1, Tübingen: Expert-Verlag, 2007, pp. 65, 144.
 8. Zhao, F., Lai, M.C., Harrington, D.L., *Automotive Spark-Ignited Direct-Injection Gasoline Engines*, Amsterdam: Elsevier Science, 2000, pp. 441-4.
 9. Dias Ribeiro, M., *Fuel Spray Modeling for Application in Internal Combustion Engines*, PhD thesis, São Paulo State University, São Paulo, 2019.
 10. Heywood, J., *Internal Combustion Engine Fundamentals*, New York City: McGraw-Hill Education, 1988, pp. 53-72.
 11. Kalwar, A., Agarwal, A., *Overview, Advancements and Challenges in Gasoline Direct Injection Engine Technology*, in *Advanced Combustion Techniques and Engine Technologies for the Automotive Sector*, Berlin: Springer Nature, 2019, pp. 111-47.
 12. Montanaro, A., Malaguti, S., Alfuso, S., *Wall Impingement Process of a Multi-Hole GDI Spray: Experimental and Numerical Investigation*, SAE Technical Paper 2012-01-1266, 2012.
 13. Baehr, H.D., Stephan, K., *Wärme- und Stoffübertragung*, Ed. 9, Berlin Heidelberg: Springer, 2016, pp. 121-8, 62.
 14. Ozisik, M.N., *Heat Conduction*, Ed. 2, Hoboken: Wiley, 1993, pp. 1-13.
 15. Jiji, L.M., *Heat Conduction*, Ed. 3, Berlin Heidelberg: Springer, 2009, pp. 2-3.
-

16. Martin, H., *E2 Instationäre Wärmeleitung in ruhenden Körpern*, in VDI-Wärmeatlas, Berlin Heidelberg: Springer, 2013, pp. 744-7.
 17. Baehr, H.D., Stephan, K., *Wärme- und Stoffübertragung*, Ed. 9, Berlin Heidelberg: Springer, 2016, pp. 218-33.
 18. Ozisik, M.N., *Finite Difference Methods in Heat Transfer*, London: Taylor & Francis, 1994, pp. 99-120.
 19. Baehr, H.D., Stephan, K., *Wärme- und Stoffübertragung*, Ed. 9, Berlin Heidelberg: Springer, 2016, pp. 10-27.
 20. Stephan, P., *B Grundlagen der Wärmeübertragung*, in VDI-Wärmeatlas, Berlin Heidelberg: Springer, 2013, pp. 19-28.
 21. Baehr, H.D., Stephan, K., *Wärme- und Stoffübertragung*, Ed. 9th, Berlin Heidelberg: Springer, 2016, pp. 85-9, 364-8.
 22. Bockhorn, H., D'Anna, A., Sarofim, A.F., Wang, H., *Combustion Generated Fine Carbonaceous Particles*, Karlsruhe: KIT Scientific Publishing, 2009, pp. 37-47, 189, 523-35.
 23. Bockhorn, H., *Soot Formation in Combustion*, Ed. 1, Berlin Heidelberg: Springer, 1994, pp. 3-7.
 24. Bockhorn, H., *Soot Formation in Combustion*, Ed. 1, Berlin Heidelberg: Springer, 1994, pp. 4.
 25. Harvey, R.G., *Polycyclic Aromatic Hydrocarbons: Chemistry and Carcinogenicity*, Ed. 1, Cambridge: Cambridge University Press, 1991, pp. 1-2.
 26. Agarwal, A.K., Dhar, A., Sharma, N., Shukla, P.C., *Engine Exhaust Particulates*, Ed. 1, Singapore: Springer, 2018, pp. 72-5.
 27. Richter, H., Howard, J.B., *Formation of polycyclic aromatic hydrocarbons and their growth to soot - a review of chemical reaction pathways*, Progress in Energy and Combustion Science 26 (4), 2000.
 28. Bockhorn, H., Fetting, F., Wenz, H.W., *Investigation of the formation of high molecular hydrocarbons and soot in premixed hydrocarbon-oxygen flames*, Berichte der Bunsengesellschaft für physikalische Chemie 87 (11):1067-73, 1983.
 29. Agranovski, I., *Aerosols: Science and Technology*, Ed. 1, New Jersey: Wiley, 2011.
 30. Cuoci, A., Frassoldati, A., Patriarca, D., Faravelli, T., Ranzi, E., Bockhorn, H., *Soot formation in turbulent non premixed flames*, Chemical Engineering Transactions 22:35-40, 2010.
 31. Geiler, J.N., Grzeszik, R., Quaing, S., Manz, A., Kaiser, S.A., *Development of laser-induced fluorescence to quantify in-cylinder fuel wall films*, International journal of engine research 19 (33):134-47, 2018.
-

32. Henkel, S., Beyrau, F., Hardalupas, Y., Taylor, A.M.K.P., *Novel method for the measurement of liquid film thickness during fuel spray impingement on surfaces*, Optics Express 24 (3):2542-61, 2016.
 33. Yang, H., Guo, X., Zhou, W., Chen, B., Hu, J., Su, M., Cai, X., *Investigation on liquid film of urea–water solutions with diode laser absorption spectroscopy*, Experiments in Fluids 56 (4), 2015.
 34. Einecke, S., Schulz, C., Sick, V., *Measurement of temperature, fuel concentration and equivalence ratio fields using tracer LIF in IC engine combustion*, Applied Physics B 71 (5):717-23, 2000.
 35. Hall, M.J., Koenig, M., *A fiber-optic probe to measure precombustion in-cylinder fuel-air ratio fluctuations in production engines*, Symposium (International) on Combustion 26 (2):2613-8, 1996.
 36. Schütte, M., Finke, H., Grünefeld, G., Krüger, S., Andresen, P., Stiebels, B., Block, B., Meyer, H., Hentschel, W., *Spatially Resolved Air–Fuel Ratio and Residual Gas Measurements by Spontaneous Raman Scattering in a Firing Direct Injection Gasoline Engine*, SAE Technical Paper 2000-01-1795, 2000.
 37. Espey, C., Dec, J.E., Litzinger, T.A., Santavicca, D.A., *Planar laser rayleigh scattering for quantitative vapor-fuel imaging in a diesel jet*, Combustion and Flame 109 (1):65-86, 1997.
 38. Bouvier, M., Cabot, G., Yon, J., Grisch, F., *On the use of PIV, LII, PAH-PLIF and OH-PLIF for the study of soot formation and flame structure in a swirl stratified premixed ethylene/air flame*, Proceedings of the Combustion Institute 38 (1):1851-8, 2021.
 39. Rao, L., Kook, S., *Optimisation of Image Processing Parameters for Flame Image Velocimetry (FIV) Measurement in a Single-Cylinder, Small-Bore Optical Diesel Engine*, SAE Technical Paper 2019-01-0719, 2019.
 40. Liu, Y., Tan, J., Wan, M., Yao, X., *OH* and CH* chemiluminescence characteristics in low swirl methane-air flames*, AIP Advances 10 (5):055318, 2020.
 41. Aleiferis, P.G., Rosati, M.F., *Flame chemiluminescence and OH LIF imaging in a hydrogen-fuelled spark-ignition engine*, International Journal of Hydrogen Energy 37 (2):1797-812, 2012.
 42. Geigle, K.P., O'Loughlin, W., Hadeef, R., Meier, W., *Visualization of soot inception in turbulent pressurized flames by simultaneous measurement of laser-induced fluorescence of polycyclic aromatic hydrocarbons and laser-induced incandescence, and correlation to OH distributions*, Applied Physics B 119:717-30, 2015.
 43. D'Alessio, A., D'Anna, A., D'Orsi, A., Minutolo, P., Barbella, R., Ciajolo, A., *Precursor formation and soot inception in premixed ethylene flames*, Proceedings of the Combustion Institute 24 (1):973-80, 1992.
 44. Snelling, D.R., Thomson, K.A., Smallwood, G.J., Gülder, Ö.L., *Two-dimensional imaging of soot volume fraction in laminar diffusion flames*, Applied Optics 38 (12):2478-85, 1999.
-

45. Bjørgen, K.O., Emberson, D., Lovas, T., *Diffuse Back-Illuminated Extinction Imaging of Soot: Effects of Beam Steering and Flame Luminosity*, SAE Technical Paper 2019-01-0011, 2019.
 46. Mueller, C., Martin, G., *Effects of Oxygenated Compounds on Combustion and Soot Evolution in a DI Diesel Engine: Broadband Natural Luminosity Imaging*, SAE Technical Paper 2002-01-1631, 2002.
 47. Charalampopoulos, T.T., Chang, H., *Agglomerate parameters and fractal dimension of soot using light scattering—effects on surface growth*, Combustion and Flame 87 (1):89-99, 1991.
 48. Haken, H., Wolf, H.C., *Molekülphysik und Quantenchemie: Einführung in die experimentellen und theoretischen Grundlagen*, Ed. 5, Berlin Heidelberg: Springer, 2006, pp. 299-304.
 49. Demtröder, W., *Laserspektroskopie: Grundlagen und Techniken*, Ed. 5, Berlin Heidelberg: Springer, 2007, pp. 149-51, 290, 435-7.
 50. Zhao, H., *Laser Diagnostics and Optical Measurement Techniques in Internal Combustion Engines*, Warrendale: SAE International, 2012, pp. 61-7.
 51. Sauer, M., Hofkens, J., Enderlein, J., *Handbook of Fluorescence Spectroscopy and Imaging: From Single Molecules to Ensembles*, Ed. 1, Weinheim: Wiley, 2011, pp. 1-31.
 52. Robinson, J.W., *Atomic Spectroscopy*, Ed. 2, Boca Raton: Taylor & Francis, 1996, pp. 27-8.
 53. Schulz, C., Sick, V., *Tracer-LIF diagnostics: quantitative measurement of fuel concentration, temperature and fuel/air ratio in practical combustion systems*, Progress in Energy and Combustion Science 31 (1):75-121, 2005.
 54. Fuhrmann, D., Benzler, T., Fernando, S., Endres, T., Dreier, T., Kaiser, S.A., Schulz, C., *Self-quenching in toluene LIF*, Proceedings of the Combustion Institute 36 (3):4505-14, 2017.
 55. Koban, W., Koch, J.D., Hanson, R.K., Schulz, C., *Oxygen quenching of toluene fluorescence at elevated temperatures*, Applied Physics B 80 (6):777-84, 2005.
 56. Senda, J., Ohnishi, M., Takahashi, T., Fujimoto, H., Utsunomiya, A., Wakatabe, M., *Measurement and Modeling on Wall Wetted Fuel Film Profile and Mixture Preparation in Intake Port of SI Engine*, SAE Technical Paper 1999-01-0798, 1999.
 57. Benzler, T., Endres, T., Dreier, T., Schulz, C., *Temperature, pressure, and oxygen quenching behavior of fluorescence spectra and lifetimes of gas-phase o-xylene and 1,2,4-trimethylbenzene*, Applied Physics B 124 (4):70, 2018.
 58. Koban, W., Koch, J.D., Hanson, R.K., Schulz, C., *Absorption and fluorescence of toluene vapor at elevated temperatures*, Physical Chemistry Chemical Physics 6 (11):2940-5, 2004.
-

-
59. Faust, S.M., *Characterisation of organic fuel tracers for laser-based quantitative diagnostics of fuel concentration, temperature, and equivalence ratio in practical combustion processes*, PhD thesis, University of Duisburg-Essen, Duisburg, 2013.
 60. Battin-Leclerc, F., Simmie, J.M., Blurock, E., *Cleaner Combustion: Developing Detailed Chemical Kinetic Models*, Ed. 1, London: Springer, 2013, pp. 304-13.
 61. Berlman, I.B., *Handbook of Fluorescence Spectra of Aromatic Molecules*, Ed. 2, New York and London: Academic Press, 1971, pp. 113-5.
 62. Zerbs, J., Geigle, K.P., Lammel, O., Hader, J., Stirn, R., Hader, R., Meier, W., *The influence of wavelength in extinction measurements and beam steering in laser-induced incandescence measurements in sooting flames*, Applied Physics B 96 (4):683-94, 2009.
 63. Schulz, C., Kock, B.F., Hofmann, M., Michelsen, H., Will, S., Bougie, B., Suntz, R., Smallwood, G., *Laser-induced incandescence: recent trends and current questions*, Applied Physics B 83 (3):333-54, 2006.
 64. Michelsen, H.A., Schulz, C., Smallwood, G.J., Will, S., *Laser-induced incandescence: Particulate diagnostics for combustion, atmospheric, and industrial applications*, Progress in Energy and Combustion Science 51:2-48, 2015.
 65. Goulay, F., Schrader, P.E., López-Yglesias, X., Michelsen, H.A., *A data set for validation of models of laser-induced incandescence from soot: temporal profiles of LII signal and particle temperature*, Applied Physics B 112 (3):287-306, 2013.
 66. Michelsen, H.A., Liu, F., Kock, B.F., Bladh, H., et al., *Modeling laser-induced incandescence of soot: a summary and comparison of LII models*, Applied Physics B 87 (3):503-21, 2007.
 67. Michelsen, H.A., Schrader, P.E., Goulay, F., *Wavelength and temperature dependences of the absorption and scattering cross sections of soot*, Carbon 48 (8):2175-91, 2010.
 68. Wallace, J.M., Hobbs, P.V., *Atmospheric Science: An Introductory Survey*, Ed. 2, Amsterdam: Elsevier Science, 2006, pp. 119.
 69. Bladh, H., Bengtsson, P.E., *Characteristics of laser-induced incandescence from soot in studies of a time-dependent heat- and mass-transfer model*, Applied Physics B 78 (2):241-8, 2004.
 70. Delhay, J., Bouvier, Y., Therssen, E., Black, J.D., Desgroux, P., *2D imaging of laser wing effects and of soot sublimation in laser-induced incandescence measurements*, Applied Physics B 81 (2):181-6, 2005.
 71. Bladh, H., Bengtsson, P.E., Delhay, J., Bouvier, Y., Therssen, E., Desgroux, P., *Experimental and theoretical comparison of spatially resolved laser-induced incandescence (LII) signals of soot in backward and right-angle configuration*, Applied Physics B 83 (3):423, 2006.
 72. Shaddix, C.R., Williams, T.C., *Analysis of laser focusing effect on quantification of LII images*, Proceedings of the Combustion Institute 38 (1):1729-36, 2021.
-

-
73. Bengtsson, P.E., Aldén, M., *Soot-visualization strategies using laser techniques - Laser-induced fluorescence in C2 from laser-vaporized soot and laser-induced soot incandescence*, Applied Physics B 60 (1):51-9, 1995.
 74. Vander Wal, R.L., Weiland, K.J., *Laser-induced incandescence: Development and characterization towards a measurement of soot-volume fraction*, Applied Physics B 59 (4):445-52, 1994.
 75. Goulay, F., Nemes, L., Schrader, P.E., Michelsen, H.A., *Spontaneous emission from C2(*d* 3Πg) and C3(*A* 1Πu) during laser irradiation of soot particles*, Molecular Physics 108 (7-9):1013-25, 2010.
 76. Goulay, F., Schrader, P.E., Nemes, L., Dansson, M.A., Michelsen, H.A., *Photochemical interferences for laser-induced incandescence of flame-generated soot*, Proceedings of the Combustion Institute 32 (1):963-70, 2009.
 77. Lackner, M., Palotás, Á., Winter, F., *Combustion: From Basics to Applications*, Hoboken: Wiley, 2013.
 78. Tinaut, F.V., Reyes, M., Giménez, B., Pastor, J.V., *Measurements of OH* and CH* Chemiluminescence in Premixed Flames in a Constant Volume Combustion Bomb under Autoignition Conditions*, Energy & Fuels 25 (1):119-29, 2011.
 79. Kathrotia, T., Riedel, U., Seipel, A., Moshhammer, K., Brockhinke, A., *Experimental and numerical study of chemiluminescent species in low-pressure flames*, Applied Physics B 107 (3):571-84, 2012.
 80. Lauer, M., *Determination of the Heat Release Distribution in Turbulent Flames by Chemiluminescence Imaging*, PhD thesis, Technical University of Munich, Munich, 2011.
 81. Güthe, F., Guyot, D., Singla, G., Noiray, N., Schuermans, B., *Chemiluminescence as diagnostic tool in the development of gas turbines*, Applied Physics B 107:619-36, 2012.
 82. Baehr, H.D., Stephan, K., *Wärme- und Stoffübertragung*, Ed. 9, Berlin Heidelberg: Springer, 2016, pp. 639-47.
 83. Raffel, M., Willert, C.E., Wereley, S.T., Kompenhans, J., *Particle Image Velocimetry: A Practical Guide*, Ed. 2, Berlin Heidelberg: Springer, 2007, pp. 4-16.
 84. FlowMaster DaVis 8.4 Product Manual, LaVision GmbH, Göttingen Germany, 2017. p. 17, Available from: lavisoin.de/de/downloads/manuals/.
 85. Raffel, M., Willert, C.E., Wereley, S.T., Kompenhans, J., *Particle Image Velocimetry: A Practical Guide*, Ed. 2, Berlin Heidelberg: Springer, 2007, pp. 87.
 86. Kamimoto, T., Miyairi, Y., Nagakura, K., Matsuoka, S., *Measurement of Flow Velocity in Diesel Flames by a Cross-Correlation Method*, SAE Technical Paper 820357, 1982.
 87. Eichler, H.J., Eichler, J., *Laser: Bauformen, Strahlführung, Anwendungen*, Ed. 7, Berlin Heidelberg: Springer, 2010, pp. 32-5, 148-56.
-

88. Held, G., *Introduction to Light Emitting Diode Technology and Applications*, Ed. 1, Boca Raton: CRC Press, 2016, pp. 3-5.
 89. Li, F., Nathan, A., *CCD Image Sensors in Deep-Ultraviolet: Degradation Behavior and Damage Mechanisms*, Ed. 1, Berlin Heidelberg: Springer, 2006, pp. 7-13.
 90. Imager Intense & Flow Master 3 Product Manual, LaVision GmbH, Göttingen Germany, 2007. p. 16, Available from: lavisoin.de/de/downloads/manuals/.
 91. Intensified Relay Optics - IRO Product Manual, LaVision GmbH, Göttingen Germany, 2009. pp. 10-13, Available from: lavisoin.de/de/downloads/manuals/.
 92. Nakamura, J., *Image Sensors and Signal Processing for Digital Still Cameras*, Boca Raton: CRC Press, 2017, pp. 144-51.
 93. Raffel, M., Willert, C.E., Scarano, F., Kähler, C.J., Wereley, S.T., Kompenhans, J., *Particle Image Velocimetry: A Practical Guide*, Ed. 3, Basel: Springer International Publishing, 2018, pp. 121-4.
 94. Stump, D., *Digital Cinematography: Fundamentals, Tools, Techniques, and Workflows*, London: Taylor & Francis, 2014, pp. 29-30.
 95. Hering, E., Schönfelder, G., *Sensoren in Wissenschaft und Technik: Funktionsweise und Einsatzgebiete*, Wiesbaden: Vieweg+Teubner Verlag, 2012, pp. 457.
 96. Jüngst, N., Kaiser, S.A., *Imaging of Fuel-Film Evaporation and Combustion in a Direct-Injection Model Experiment*, SAE Technical Paper 2019-01-0293, 2019.
 97. Jüngst, N., Kaiser, S.A., *Visualization of soot formation from evaporating fuel films by laser-induced fluorescence and incandescence*, Proceedings of the Combustion Institute 38 (1):1089-97, 2021.
 98. Jüngst, N., Frapolli, N., Wright, Y.M., Kaiser, S.A., Boulouchos, K., *Experimental and numerical investigation of evaporating fuel films in combustion*, Applications in Energy and Combustion Science 7:100033, 2021.
 99. Shahbaz, M.A., Jüngst, N., Grzeszik, R., Kaiser, S.A., *Endoscopic fuel film, chemiluminescence, and soot incandescence imaging in a direct-injection spark-ignition engine*, Proceedings of the Combustion Institute 38 (4):5869-77, 2021.
 100. Warey, A., Huang, Y., D. Matthews, R., Hall, M., Ng, H., *Effects of Piston Wetting on Size and Mass of Particulate Matter Emissions in a DISI Engine*, SAE Technical Paper 2002-01-1140, 2002.
 101. Drake, M.C., Fansler, T.D., Solomon, A.S., Szekely, G., *Piston fuel films as a source of smoke and hydrocarbon emissions from a wall-controlled spark-ignited direct-injection engine*, SAE Technical Paper 2003-01-0547, 2003.
 102. Ortmann, R., Arndt, S., Raimann, J., Grzeszik, R., Würfel, G., *Methods and Analysis of Fuel Injection, Mixture Preparation and Charge Stratification in Different Direct Injected SI Engines*, SAE Technical Paper 2001-01-0970, 2001.
-

-
103. Stevens, E., Steeper, R., *Piston Wetting in an Optical DISI Engine: Fuel Films, Pool Fires, and Soot Generation*, SAE Technical Paper 2001-01-1203, 2001.
 104. Stojkovic, B.D., Fansler, T.D., Drake, M.C., Sick, V., *High-speed imaging of OH* and soot temperature and concentration in a stratified-charge direct-injection gasoline engine*, Proceedings of the Combustion Institute 30 (2):2657-65, 2005.
 105. Li, J., Matthews, R.D., Stanglmaier, R.H., Roberts, C.E., Anderson, R.W., *Further Experiments on the Effects of In-Cylinder Wall Wetting on HC Emissions from Direct Injection Gasoline Engines*, SAE Technical Paper 1999-01-3661, 1999.
 106. H. Stanglmaier, R., Li, J., D. Matthews, R., *The Effect of In-Cylinder Wall Wetting Location on the HC Emissions from SI Engines*, SAE Technical Paper 1999-01-0502, 1999.
 107. Li, J., Huang, Y., Alger, T., D. Matthews, R., Hall, M., H. Stanglmaier, R., E. Roberts, C., Dai, W., W. Anderson, R., *Liquid Fuel Impingement on In-Cylinder Surfaces as a Source of Hydrocarbon Emissions From Direct Injection Gasoline Engines*, Journal of Engineering for Gas Turbines and Power 123 (3):659-68, 2001.
 108. Alger, T., Huang, Y., Hall, M., Matthews, R.D., *Liquid Film Evaporation Off the Piston of a Direct Injection Gasoline Engine*, SAE Technical Paper 2001-01-1204, 2001.
 109. Mizomoto, M., Ikai, S., Hayano, H., *Evaporation and ignition of a fuel droplet on a hot surface (Part 1, Evaporation)*, Bulletin of the JSME 21 (162):1765-71, 1978.
 110. H. Stanglmaier, R., E. Roberts, C., A. Moses, C., *Vaporization of Individual Fuel Drops on a Heated Surface: A Study of Fuel-Wall Interactions within Direct-Injected Gasoline (DIG) Engines*, SAE Technical Paper 2002-01-0838, 2002.
 111. Schulz, F., Beyrau, F., *Systematic Investigation of Fuel Film Evaporation*, SAE Technical Paper 2018-01-0310, 2018.
 112. Maligne, D., Bruneaux, G., *Time-Resolved Fuel Film Thickness Measurement for Direct Injection SI Engines Using Refractive Index Matching*, SAE Technical Paper 2011-01-1215, 2011.
 113. Lin, M.-T., Sick, V., *Is Toluene a Suitable LIF Tracer for Fuel Film Measurements?*, SAE Technical Paper 2004-01-1355, 2004.
 114. Alonso, M., Kay, P.J., Bowen, P.J., Gilchrist, R., Sapsford, S., *A laser induced fluorescence technique for quantifying transient liquid fuel films utilising total internal reflection*, Experiments in Fluids 48 (1):133-42, 2010.
 115. Kay, P.J., Bowen, P.J., Gold, M., Sapsford, S. *Development of a 2D quantitative LIF technique towards measurement of transient liquid fuel films*, in ICLASS 2006, August 27th - September 1st 2006, Kyoto, Japan.
 116. Cho, H., Min, K., *Measurement of liquid fuel film distribution on the cylinder liner of a spark ignition engine using the laser-induced fluorescence technique*, Measurement Science and Technology 14 (7):975-82, 2003.
-

-
117. Schulz, F., Schmidt, J., Beyrau, F., *Development of a sensitive experimental set-up for LIF fuel wall film measurements in a pressure vessel*, Experiments in Fluids 56:98, 2015.
 118. Schulz, F., Samenfink, W., Schmidt, J., Beyrau, F., *Systematic LIF fuel wall film investigation*, Fuel 172:284-92, 2016.
 119. Schulz, F., Beyrau, F., *The effect of operating parameters on the formation of fuel wall films as a basis for the reduction of engine particulate emissions*, Fuel 238:375-84, 2019.
 120. Xiao, D., Li, X., Hung, D., Xu, M., *Characteristics of Impinging Spray and Corresponding Fuel Film under Different Injection and Ambient Pressure*, SAE Technical Paper 2019-01-0277, 2019.
 121. Luo, H., Nishida, K., Uchitomi, S., Ogata, Y., Zhang, W., Fujikawa, T., *Effect of temperature on fuel adhesion under spray-wall impingement condition*, Fuel 234:56-65, 2018.
 122. Luo, H., Nishida, K., Ogata, Y., Zhang, W., Fujikawa, T., *Fuel adhesion characteristics under non-evaporation and evaporation conditions: Part 1-effect of injection pressure*, Fuel 240:317-25, 2019.
 123. Pan, H., Xu, M., Hung, D., Lv, H., Dong, X., Kuo, T.-W., Grover, R.O., Parrish, S.E., *Experimental Investigation of Fuel Film Characteristics of Ethanol Impinging Spray at Ultra-Low Temperature*, SAE Technical Paper 2017-01-0851, 2017.
 124. Zheng, Y., Xie, X., Lai, M.-C., VanDerWege, B. *Measurement and Simulation of DI Spray Impingements and Film Characteristics*, in ICLASS 2012, September 2nd - 6th 2012, Heidelberg, Germany.
 125. Li, X., Pan, H., Dong, X., Hung, D., Xu, M., *Spray impingement wall film breakup by wave entrainment*, Proceedings of the Combustion Institute 37 (3):3287-94, 2019.
 126. Cheng, Y.-s., Deng, K., Li, T., *Measurement and simulation of wall-wetted fuel film thickness*, International Journal of Thermal Sciences 49 (4):733-9, 2010.
 127. Almkvist, G., Denbratt, I., Josefsson, G., Magnusson, I., *Measurements of fuel film thickness in the inlet port of an SI engine by laser induced fluorescence*, SAE Technical Paper 952483, 1995.
 128. Takahashi, Y., Nakase, Y., Ichinose, H., *Analysis of the Fuel Liquid Film Thickness of a Port Fuel Injection Engine*, SAE Technical Paper 2006-01-1051, 2006.
 129. Park, S., Ghandhi, J.B., *Fuel Film Temperature and Thickness Measurements on the Piston Crown of a Direct-Injection Spark-Ignition Engine*, SAE Technical Paper 2005-01-0649, 2005.
 130. Geiler, J.N., *Bildgebende Messung der Kraftstoffwandfilmdicke durch laserinduzierte Fluoreszenz*, PhD thesis, University of Duisburg-Essen, Duisburg, 2019.
-

-
131. Liu, H., Lee, C.-F., *Numerical study on wall film formation and evaporation*, SAE Technical Paper 2014-01-1112, 2014.
 132. Köpple, F., *Untersuchung der Potentiale der numerischen Strömungsberechnung zur Prognose der Partikelemissionen in Ottomotoren mit Direkteinspritzung*, Ed. 1st, Wiesbaden: Springer Vieweg, 2015.
 133. Zhang, Y., Jia, M., Liu, H., Xie, M., *Development of an improved liquid film model for spray/wall interaction under engine-relevant conditions*, International Journal of Multiphase Flow 79:74-87, 2016.
 134. Frapolli, N., Boulouchos, K., Wright, Y.M., Geiler, J.N., Manz, A., Kaiser, S.A., *Large Eddy Simulations and Tracer-LIF Diagnostics of Wall Film Dynamics in an Optically Accessible GDI Research Engine*, SAE Technical Paper 2019-24-0131, 2019.
 135. B. Karlsson, R., B. Heywood, J., *Piston Fuel Film Observations in an Optical Access GDI Engine*, SAE Technical Paper 2001-01-2022, 2001.
 136. Köpple, F., *Untersuchung der Potentiale der numerischen Strömungsberechnung zur Prognose der Partikelemissionen in Ottomotoren mit Direkteinspritzung*, Ed. 1, Wiesbaden: Springer Vieweg, 2015, pp. 103, 5-8.
 137. Min, J., Tang, Y., *Theoretical analysis of water film evaporation characteristics on an adiabatic solid wall*, International Journal of Refrigeration 53:55-61, 2015.
 138. Oliveira, I.B., Hochgreb, S., *Detailed Calculation of Heating, Evaporation, and Reaction Processes of a Thin Liquid Layer of Hydrocarbon Fuel*, SAE Technical Paper 2000-01-0959, 2000.
 139. Liye, S., Weizheng, Z., Ti'en, Z., Zhaoju, Q., *A new approach to transient evaporating film heating modeling based on analytical temperature profiles for internal combustion engines*, International Journal of Heat and Mass Transfer 81:465-9, 2015.
 140. Yan, Y.a., Liu, H., Jia, M., Xie, M.-z., Yin, H., *A one-dimensional unsteady wall film evaporation model*, International Journal of Heat and Mass Transfer 88:138-48, 2015.
 141. Tao, M., Zhao, P., VanDerWege, B., Iyer, C., Ge, H., *Further study on wall film effects and flame quenching under engine thermodynamic conditions*, Combustion and Flame 216:100-10, 2020.
 142. Schulz, F., Schmidt, J., Kufferath, A., Samenfink, W., *Gasoline Wall Films and Spray/Wall Interaction Analyzed by Infrared Thermography*, SAE International Journal of Engines 7 (3):1165-77, 2014.
 143. Dragomirov, P., Mendieta, A., Abram, C., Fond, B., Beyrau, F., *Planar measurements of spray-induced wall cooling using phosphor thermometry*, Experiments in Fluids 59:42, 2018.
 144. Montanaro, A., Allocca, L., Meccariello, G., Lazzaro, M., *Schlieren and Mie Scattering Imaging System to Evaluate Liquid and Vapor Contours of a Gasoline Spray Impacting on a Heated Wall*, SAE Technical Paper 2015-24-2473, 2015.
-

145. Montanaro, A., Allocca, L., Lazzaro, M., Meccariello, G., *Impinging Jets of Fuel on a Heated Surface: Effects of Wall Temperature and Injection Conditions*, SAE Technical Paper 2016-01-0863, 2016.
 146. Montanaro, A., Allocca, L., Rocco, V., Costa, M., Piazzullo, D., *Transient Heat Transfer Effects on a Gasoline Spray Impact against Hot Surfaces: Experimental and Numerical Study*, SAE Technical Paper 2017-24-0107, 2017.
 147. Trost, J., Zigan, L., Leipertz, A., Sahoo, D., C Miles, P., *Characterization of four potential laser-induced fluorescence tracers for diesel engine applications*, Applied Optics 52 (33):8001-7, 2013.
 148. Faust, S., Goschütz, M., Kaiser, S., Dreier, T., Schulz, C., *A comparison of selected organic tracers for quantitative scalar imaging in the gas phase via laser-induced fluorescence*, Applied Physics B 117 (1):183-94, 2014.
 149. Desoutter, G., Cuenot, B., Habchi, C., Poinot, T., *Interaction of a premixed flame with a liquid fuel film on a wall*, Proceedings of the Combustion Institute 30 (1):259-66, 2005.
 150. Tao, M., Ge, H., VanDerWege, B., Zhao, P., *Fuel wall film effects on premixed flame propagation, quenching and emission*, International journal of engine research 21 (6):1055-66, 2018.
 151. Roque, A., Foucher, F., Lamiel, Q., Imoehl, B., Lamarque, N., Helie, J., *Impact of gasoline direct injection fuel films on exhaust soot production in a model experiment*, International journal of engine research 21 (2):367-90, 2019.
 152. Desgroux, P., Mercier, X., Thomson, K.A., *Study of the formation of soot and its precursors in flames using optical diagnostics*, Proceedings of the Combustion Institute 34 (1):1713-38, 2013.
 153. Snelling, D.R., Liu, F., Smallwood, G.J., Gülder, Ö.L., *Determination of the soot absorption function and thermal accommodation coefficient using low-fluence LII in a laminar coflow ethylene diffusion flame*, Combustion and Flame 136 (1):180-90, 2004.
 154. Crosland, B.M., Johnson, M.R., Thomson, K.A., *Analysis of uncertainties in instantaneous soot volume fraction measurements using two-dimensional, auto-compensating, laser-induced incandescence (2D-AC-LII)*, Applied Physics B 102 (1):173-83, 2011.
 155. Geigle, K.P., Hadeif, R., Meier, W., *Soot Formation and Flame Characterization of an Aero-Engine Model Combustor Burning Ethylene at Elevated Pressure*, Journal of Engineering for Gas Turbines and Power 136 (2), 2013.
 156. Dec, J.E., zur Loye, A.O., Siebers, D.L., *Soot Distribution in a D.I. Diesel Engine Using 2-D Laser-Induced Incandescence Imaging*, SAE Technical Paper 910224, 1991.
 157. Dec, J.E., Espey, C., *Ignition and Early Soot Formation in a DI Diesel Engine Using Multiple 2-D Imaging Diagnostics*, SAE Technical Paper 950456, 1995.
-

-
158. Dec, J.E., *A Conceptual Model of DI Diesel Combustion Based on Laser-Sheet Imaging*, SAE Technical Paper 970873, 1997.
 159. de Francqueville, L., Bruneaux, G., Thirouard, B., *Soot Volume Fraction Measurements in a Gasoline Direct Injection Engine by Combined Laser Induced Incandescence and Laser Extinction Method*, SAE International Journal of Engines 3 (1):163-82, 2010.
 160. Hertler, D., Stirn, R., Arndt, S., Grzeszik, R., Dreizler, A., *Investigations of soot formation in an optically accessible gasoline direct injection engine by means of laser-induced incandescence (LII)*, Applied Physics B 104 (2):399-407, 2011.
 161. Mercier, X., Carrivain, O., Irimiea, C., Faccinetto, A., Therssen, E., *Dimers of Polycyclic Aromatic Hydrocarbons: the Missing Pieces in the Soot Formation Process*, Physical Chemistry Chemical Physics 21 (16):8282-94, 2019.
 162. Bejaoui, S., Mercier, X., Desgroux, P., Therssen, E., *Laser induced fluorescence spectroscopy of aromatic species produced in atmospheric sooting flames using UV and visible excitation wavelengths*, Combustion and Flame 161 (10):2479-91, 2014.
 163. Liu, P., He, Z., Hou, G.L., Guan, B., Lin, H., Huang, Z., *The Diagnostics of Laser-Induced Fluorescence (LIF) Spectra of PAHs in Flame with TD-DFT: Special Focus on Five-Membered Ring*, The Journal of Physical Chemistry A 119 (52):13009-17, 2015.
 164. Sgro, L.A., Minutolo, P., Basile, G., D'Alessio, A., *UV-visible spectroscopy of organic carbon particulate sampled from ethylene/air flames*, Chemosphere 42 (5):671-80, 2001.
 165. Ciajolo, A., Ragucci, R., Apicella, B., Barbella, R., de Joannon, M., Tregrossi, A., *Fluorescence spectroscopy of aromatic species produced in rich premixed ethylene flames*, Chemosphere 42 (5-7):835-41, 2001.
 166. Coe, D.S., Haynes, B.S., Steinfeld, J.I., *Identification of a source of argon-ion-laser excited fluorescence in sooting flames*, Combustion and Flame 43:211-4, 1981.
 167. Wang, H., *Formation of nascent soot and other condensed-phase materials in flames*, Proceedings of the Combustion Institute 33 (1):41-67, 2011.
 168. Dobbins, R.A., Fletcher, R.A., Lu, W., *Laser microprobe analysis of soot precursor particles and carbonaceous soot*, Combustion and Flame 100 (1):301-9, 1995.
 169. Schoemaeker Moreau, C., Therssen, E., Mercier, X., Pauwels, J.F., Desgroux, P., *Two-color laser-induced incandescence and cavity ring-down spectroscopy for sensitive and quantitative imaging of soot and PAHs in flames*, Applied Physics B 78 (3):485-92, 2004.
 170. Vander Wal, R.L., Jensen, K.A., Choi, M.Y., *Simultaneous laser-induced emission of soot and polycyclic aromatic hydrocarbons within a gas-jet diffusion flame*, Combustion and Flame 109 (3):399-414, 1997.
 171. Hayashida, K., Amagai, K., Satoh, K., Arai, M., *Experimental Analysis of Soot Formation in Sooting Diffusion Flame by Using Laser-Induced Emissions*, Journal of Engineering for Gas Turbines and Power 128 (2):241-6, 2005.
-

-
172. de Andrade Oliveira, M.H., Olofsson, N.E., Johnsson, J., Bladh, H., et al., *Soot, PAH and OH measurements in vaporized liquid fuel flames*, Fuel 112:145-52, 2013.
 173. Smyth, K.C., Shaddix, C.R., Everest, D.A., *Aspects of soot dynamics as revealed by measurements of broadband fluorescence and flame luminosity in flickering diffusion flames*, Combustion and Flame 111 (3):185-207, 1997.
 174. Bennett, A., Amin, H.M.F., Cenker, E., Roberts, W.L., *Measurements of Pressure Effects on PAH Distribution and 2D Soot Volume Fraction Diagnostics in a Laminar Non-premixed Coflow Flame*, Energy & Fuels 32 (10):10974-83, 2018.
 175. Steinmetz, S.A., Fang, T., Roberts, W.L., *Soot particle size measurements in ethylene diffusion flames at elevated pressures*, Combustion and Flame 169:85-93, 2016.
 176. Kobayashi, Y., Furuhashi, T., Amagai, K., Arai, M., *Soot precursor measurements in benzene and hexane diffusion flames*, Combustion and Flame 154 (3):346-55, 2008.
 177. Hayashi, J., Hashimoto, N., Nakatsuka, N., Tainaka, K., Tsuji, H., Tanno, K., Watanabe, H., Makino, H., Akamatsu, F., *Simultaneous imaging of Mie scattering, PAHs laser induced fluorescence and soot laser induced incandescence to a lab-scale turbulent jet pulverized coal flame*, Proceedings of the Combustion Institute 37 (3):3045-52, 2019.
 178. Lemaire, R., Faccinetto, A., Therssen, E., Ziskind, M., Focsa, C., Desgroux, P., *Experimental comparison of soot formation in turbulent flames of Diesel and surrogate Diesel fuels*, Proceedings of the Combustion Institute 32 (1):737-44, 2009.
 179. Aizawa, T., Kosaka, H., Matsui, Y., *2-D Imaging of Soot Formation Process in a Transient Spray Flame by Laser-induced Fluorescence and Incandescence Techniques*, SAE Technical Paper 2002-01-2669, 2002.
 180. Bobba, M.K., Musculus, M.P.B., *Laser diagnostics of soot precursors in a heavy-duty diesel engine at low-temperature combustion conditions*, Combustion and Flame 159 (2):832-43, 2012.
 181. Leermakers, C.A.J., Musculus, M.P.B., *In-cylinder soot precursor growth in a low-temperature combustion diesel engine: Laser-induced fluorescence of polycyclic aromatic hydrocarbons*, Proceedings of the Combustion Institute 35 (3):3079-86, 2015.
 182. Li, Z., Roberts, G., Musculus, M., *Dilution and Injection Pressure Effects on Ignition and Onset of Soot at Threshold-Sooting Conditions by Simultaneous PAH-PLIF and Soot-PLII Imaging in a Heavy Duty Optical Diesel Engine*, SAE Technical Paper 2019-01-0553, 2019.
 183. Raza, M., Chen, L., Leach, F., Ding, S., *A Review of Particulate Number (PN) Emissions from Gasoline Direct Injection (GDI) Engines and Their Control Techniques*, Energies 11 (6), 2018.
 184. Transmission spectrum of 292/27 nm single-band bandpass filter, Semrock Inc., Rochester USA, semrock.com/filterdetails.aspx?id=ff01-292/27-25, accessed Sept. 2018.
-

-
185. Transmission spectrum of 266 nm ultrastEEP longpass edge filter, Semrock Inc., Rochester USA, semrock.com/filterdetails.aspx?id=lp02-266ru-25, accessed Sept. 2018.
 186. Bracco, F.V., *Modeling of Engine Sprays*, SAE Technical Paper 850394, 1985.
 187. Sirignano, W.A., *Fluid Dynamics and Transport of Droplets and Sprays*, Ed. 1st, Cambridge: Cambridge University Press, 1999.
 188. Torres, D., O'Rourke, P., Amsden, A.A., *Efficient multicomponent fuel algorithm*, *Combustion Theory and Modelling* 7 (1):66-86, 2003.
 189. Bai, C., Gosman, A.D., *Development of Methodology for Spray Impingement Simulation*, SAE Technical Paper 950283, 1995.
 190. Bai, C., Gosman, A.D., *Mathematical Modelling of Wall Films Formed by Impinging Sprays*, SAE Technical Paper 960626, 1996.
 191. Pitzer, K.S., *The Thermodynamics of n-Heptane and 2,2,4-Trimethylpentane, Including Heat Capacities, Heats of Fusion and Vaporization and Entropies*, *Journal of the American Chemical Society* 62 (5):1224-7, 1940.
 192. Majer, V., Svoboda, V., Hála, S., Pick, J., *Temperature dependence of heats of vaporization of saturated hydrocarbons C5-C8; Experimental data and an estimation method*, *Collection of Czechoslovak Chemical Communications* 44 (3):637-51, 1979.
 193. Willingham, C.B., Taylor, W.J., Pignocco, J.M., Rossini, F.D., *Vapor Pressures and Boiling Points of Some Paraffin, Alkylcyclopentane, Alkylcyclohexane, and Alkylbenzene Hydrocarbons*, *Journal of Research of the National Bureau of Standards* 35 (3):219-44, 1945.
 194. Stephan, K., Laesecke, A., *The Thermal Conductivity of Fluid Air*, *Journal of Physical and Chemical Reference Data* 14 (1):227-34, 1985.
 195. Blanke, W., Biermann, M., Dammermann, W., German, S., et al., *Thermophysikalische Stoffgrößen*, Ed. 1st, Berlin Heidelberg: Springer, 1989, pp. 292.
 196. Abdulagatov, I.M., Emirov, S.N., Tsomaeva, T.A., Gairbekov, K.A., Askerov, S.Y., Magomedova, N.A., *Thermal conductivity of fused quartz and quartz ceramic at high temperatures and high pressures*, *Journal of Physics and Chemistry of Solids* 61 (5):779-87, 2000.
 197. Smith, G.D., *Numerical Solution of Partial Differential Equations: Finite Difference Methods*, Ed. 3rd, Oxford: Clarendon Press, 1986.
 198. Li, Z., Qiao, Z., Tang, T., *Numerical Solution of Differential Equations*, Ed. 1st, Cambridge: Cambridge University Press, 2017.
 199. Hildenbrand, S., Staudacher, S., Brüggemann, D., Beyrau, F., Weikl, M.C., Seeger, T., Leipertz, A., *Numerical and experimental study of the vaporization cooling in gasoline direct injection sprays*, *Proceedings of the Combustion Institute* 31 (2):3067-73, 2007.
-

-
200. Yale Coflow Diffusion Flames, Yale University, New Haven USA, guilford.eng.yale.edu/yalecoflowflames/burner.html, accessed May 2020.
 201. Smooke, M.D., Hall, R.J., Colket, M.B., Fielding, J., Long, M.B., McEnally, C.S., Pfefferle, L.D., *Investigation of the transition from lightly sooting towards heavily sooting co-flow ethylene diffusion flames*, Combustion Theory and Modelling 8 (3):593-606, 2004.
 202. McEnally, C.S., Schaffer, A.M., Long, M.B., Pfefferle, L.D., Smooke, M.D., Colket, M.B., Hall, R.J., *Computational and experimental study of soot formation in a coflow, laminar ethylene diffusion flame*, Symposium (International) on Combustion 27 (1):1497-505, 1998.
 203. Koban, W., Koch, J., Hanson, R., Schulz, C., *Toluene LIF at elevated temperatures: implications for fuel-air ratio measurements*, Applied Physics B 80 (2):147-50, 2005.
 204. Lee, S.-Y., Turns, S.R., Santoro, R.J., *Measurements of soot, OH, and PAH concentrations in turbulent ethylene/air jet flames*, Combustion and Flame 156 (12):2264-75, 2009.
 205. Santoro, R.J., Semerjian, H.G., Dobbins, R.A., *Soot particle measurements in diffusion flames*, Combustion and Flame 51:203-18, 1983.
 206. Desgroux, P., Mercier, X., Lefort, B., Lemaire, R., Therssen, E., Pauwels, J.F., *Soot volume fraction measurement in low-pressure methane flames by combining laser-induced incandescence and cavity ring-down spectroscopy: Effect of pressure on soot formation*, Combustion and Flame 155 (1):289-301, 2008.
 207. Mannazhi, M., Török, S., Gao, J., Bengtsson, P.-E., *Soot maturity studies in methane-air diffusion flames at elevated pressures using laser-induced incandescence*, Proceedings of the Combustion Institute 38 (1):1217-24, 2021.
 208. Yale Coflow Diffusion Flames, Yale University, New Haven USA, guilford.eng.yale.edu/yalecoflowflames/sooting.html, accessed Oct. 2020.
 209. Storch, M., Zigan, L., Wensing, M., Will, S., *Systematic Investigation of the Influence of Ethanol Blending on Sooting Combustion in DISI Engines Using High-Speed Imaging and LII*, SAE Technical Paper 2014-01-2617, 2014.
 210. Mannazhi, M., Bergqvist, S., Török, S., Cuong Le, T.K., Bengtsson, P.E. *Influence of potassium chloride on PAH concentration during soot formation; A laser induced fluorescence study using excitation at 266 nm and 532 nm*, in 38th International Symposium on Combustion, January 24th - January 29th 2021, Adelaide, Australia.
-

7.2 Contributions of the author

7.2.1 Journal articles

- [96] N. Jüngst, S.A. Kaiser, *Imaging of Fuel-Film Evaporation and Combustion in a Direct-Injection Model Experiment*, SAE Technical Paper 2019-01-0293, 2019.
- [97] N. Jüngst, S.A. Kaiser, *Visualization of soot formation from evaporating fuel films by laser-induced fluorescence and incandescence*, Proceedings of the Combustion Institute 38 (1):1089-97, 2021.
- [98] N. Jüngst, N. Frapolli, Y. M. Wright, K. Boulouchos, S.A. Kaiser, *Experimental and numerical investigation of evaporating fuel films in combustion*, Applications in Energy and Combustion Science, 7:100033, 2021.
- [99] M.A. Shahbaz, N. Jüngst, R. Grzeszik, S.A. Kaiser, *Endoscopic fuel film, chemiluminescence, and soot incandescence imaging in a direct-injection spark-ignition engine*, Proceedings of the Combustion Institute 38 (4):5869-77, 2021.

7.2.2 Conference contributions

Papers (including oral presentation):

N. Jüngst, S.A. Kaiser, *Visualization of soot formation from evaporating fuel films by laser-induced fluorescence and incandescence*, in 29. Deutscher Flammentag, September 17th – 18th 2019, Bochum, Germany.

Oral presentations:

N. Jüngst, S.A. Kaiser, *Imaging of Fuel-Film Evaporation and Combustion in a Direct-Injection Model Experiment*, in SAE World Congress Experience 2019, April 9th – 11th 2019, Detroit, MI, USA.

Jüngst, N., Kaiser, S.A., *Imaging of evaporating fuel films in combustion, soot precursors, and soot by laser-induced fluorescence and incandescence*, in 2019 Gordon Research Seminar – Laser Diagnostics in Energy and Combustion Science, June 22nd – 23rd 2019, Les Diablerets, Switzerland.

Jüngst, N., Kaiser, S.A., *Experimentelle und numerische Untersuchung von verdampfenden Flüssigfilmen*, in Thermodynamik-Kolloquium 2019, September 30th – October 2nd 2019, Duisburg, Germany.

Posters:

Jüngst, N., Schulz C., Kaiser, S.A., *Multi-diagnostic imaging of evaporating fuel wall-films in combustion as a source of PAH and soot*, in 2017 Gordon Research Seminar and Conference – Laser Diagnostics in Combustion, August 5th – 11th 2017, West Dover, VT, USA.

Jüngst, N., Kaiser, S.A., *Multi-diagnostic imaging of evaporating fuel wall-films in combustion as a source of PAH and soot*, in 8th International Workshop on Laser-Induced Incandescence (LII), June 10th – 13th 2018, Tutzing, Germany.

Jüngst, N., Kaiser, S.A., *Multi-diagnostic imaging of evaporating fuel wall-films in combustion as a source of PAH and soot*, in 37th International Symposium on Combustion, July 29th – August 3rd 2018, Dublin, Ireland.

Jüngst, N., Kaiser, S.A., *Imaging of evaporating fuel films in combustion, soot precursors, and soot by laser-induced fluorescence and incandescence*, in 2019 Gordon Research Seminar and Conference – Laser Diagnostics in Energy and Combustion Science, June 22nd - 28th 2019, Les Diablerets, Switzerland.

7.2.3 Supervised theses

Stradmann, S., *Untersuchung der Kraftstoffwandbenetzung durch Benzindirekteinspritzung in einem optisch zugänglichen Strömungskanal*, master's thesis, University of Duisburg-Essen, 2017.

Ceylan, F., *Visualisierung von Kraftstoffeinspritzung und -verbrennung in einem Strömungskanal durch Schlieren-Messtechnik*, bachelor's thesis, University of Duisburg-Essen, 2018.

Liu, R., *Untersuchung der Rußbildung während der Verdampfung und Verbrennung von Kraftstoff-Wandfilmen durch laserinduzierte Inkandescenz und Fluoreszenz*, master's thesis, University of Duisburg-Essen, 2018.

Kock, M., *Simultane Visualisierung von Ruß und Rußvorläufern durch laserinduzierte Inkandescenz und Fluoreszenz bei der Verbrennung von Kraftstoffwandfilmen*, master's thesis, University of Duisburg-Essen, 2018.

Drechnowicz, S., *Aufbau eines Brenners mit laminarer Diffusionsflamme und Charakterisierung durch optische Messtechnik*, bachelor's thesis, University of Duisburg-Essen, 2019.

Bogdanski, J., *Entwicklung eines Modells zur Verdampfung von Kraftstoffwandfilmen*, master's thesis, University of Duisburg-Essen, 2019.

Laichter, J., *Bildgebende Untersuchung der Flüssigfilmbildung und des Strömungsfeldes bei der Wassereinspritzung in einem Windkanal*, master's thesis, University of Duisburg-Essen, 2019.

8 Appendices

A1 Spherical tridiagonal matrices for the Crank-Nicholson method

$$A_M = \begin{pmatrix} 2M + M & -M & \cdots & 0 \\ -M & & & \\ \vdots & \ddots & & \vdots \\ 0 & \cdots & -M & 2M + M \end{pmatrix} \quad (62)$$

$$B_M = \begin{pmatrix} 2 - M & M & \cdots & 0 \\ M & 2 - 2M & & \\ \vdots & & \ddots & \vdots \\ 0 & \cdots & 2 - 2M & M \\ & & M & 2 - M \end{pmatrix} \quad (63)$$

$$T^n = \begin{pmatrix} T_1^n \\ T_2^n \\ \vdots \\ T_{l-1}^n \\ T_l^n \end{pmatrix}, T^{n+1} = \begin{pmatrix} T_1^{n+1} \\ T_2^{n+1} \\ \vdots \\ T_{l-1}^{n+1} \\ T_l^{n+1} \end{pmatrix}, b^n = \begin{pmatrix} MT_1^n \\ 0 \\ \vdots \\ 0 \\ MT_l^n \end{pmatrix} \quad (64)$$

A2 Processing parameters for PIV and optical flow

1. PIV			
		PIV	Optical flow
Vector calculation parameters	Iterations	Multi-pass (decreasing size)	
	Interrogation window properties		Start: 32 x 32, 50% overlap, 3 passes End: 24 x 24, 50% overlap, 3 passes
	Other options	High accuracy mode for final pass	
Correlation function	All initial pass(es)	Standard I1*I2 (via FFT, no zero-padding)	
	Final pass(es)	Standard I1*I2 (via FFT, no zero-padding)	
Multi-pass postprocessing			Delete vector if peak ratio $Q < 1.5$
	1 × median filter: remove & iteratively replace		Remove if diff. to avg. $> 2 * \text{Stdev}$ of neighbors (Re)insert if diff. to avg. $< 3 * \text{Stdev}$ of neighbors
	Denoising		3 x 3
Vector postprocessing	1 × median filter: universal outlier detection		Remove if residual > 2 , filter region: 3 × 3 (Re)insert if residual < 0.1 , min number of vectors: 5
	Delete vector		If correlation value < 0.7 If peak ratio $Q < 2$
2. Smooth and fill up			
Vector postprocessing			Fill-up empty spaces (interpolation)
			Smoothing: optimal
			Make mask permanent
3. Remove spurious vectors			
Vector postprocessing	1 × median filter: universal outlier detection		Remove if residual > 2 , filter region: 11 × 11 (Re)insert if residual < 2 , min number of vectors: 1

DuEPublico

Duisburg-Essen Publications online

UNIVERSITÄT
DUISBURG
ESSEN

Offen im Denken

ub | universitäts
bibliothek

Diese Dissertation wird via DuEPublico, dem Dokumenten- und Publikationsserver der Universität Duisburg-Essen, zur Verfügung gestellt und liegt auch als Print-Version vor.

DOI: 10.17185/duepublico/74816

URN: urn:nbn:de:hbz:464-20210916-102607-7

Alle Rechte vorbehalten.